

2012-01-01

Analysis Of Aerosol Particle Size Distributions Observed During Aerose V Campaign

Mariana Guereque

University of Texas at El Paso, guereque@gmail.com

Follow this and additional works at: https://digitalcommons.utep.edu/open_etd



Part of the [Atmospheric Sciences Commons](#)

Recommended Citation

Guereque, Mariana, "Analysis Of Aerosol Particle Size Distributions Observed During Aerose V Campaign" (2012). *Open Access Theses & Dissertations*. 2097.

https://digitalcommons.utep.edu/open_etd/2097

This is brought to you for free and open access by DigitalCommons@UTEP. It has been accepted for inclusion in Open Access Theses & Dissertations by an authorized administrator of DigitalCommons@UTEP. For more information, please contact lweber@utep.edu.

ANALYSIS OF AEROSOL PARTICLE SIZE DISTRIBUTIONS OBSERVED DURING
AEROSE V CAMPAIGN

MARIANA GÜEREQUE

Department of Geological Sciences

APPROVED:

Thomas E. Gill, Ph.D., Co-Chair

Rosa M. Fitzgerald, Ph.D., Co-Chair

Philip C. Goodell, Ph.D.

Vernon R. Morris, Ph.D.

Benjamin C. Flores, Ph.D.
Interim Dean of the Graduate School

Copyright ©

By

Mariana Güereque

2012

Dedication

I'd like to dedicate this thesis to my husband Moises Macias, for all of the assistance, guidance and patience throughout this journey. To the rest of my family I would like to thank them for their encouragement and support.

ANALYSIS OF AEROSOL PARTICLE SIZE DISTRIBUTIONS OBSERVED DURING
AEROSE V CAMPAIGN

by

MARIANA GÜEREQUE, B.S. ENVIRONMENTAL SCIENCE

THESIS

Presented to the Faculty of the Graduate School of

The University of Texas at El Paso

in Partial Fulfillment

of the Requirements

for the Degree of

MASTER OF SCIENCE

Department of Geological Sciences

THE UNIVERSITY OF TEXAS AT EL PASO

May 2012

Acknowledgements

The author wishes to express her gratitude to NOAA Educational Partnership Program for Minority Serving Institutions (EPP/MSI) Cooperative Agreement NA17AE1623 for their support on this work. Also, to the NOAA Center for Atmospheric Science (NCAS) at Howard University and its researchers for their guidance and suggestions, as well as to the rest of the members from the AEROSE V and AEROSE VI expeditions. I would like to thank the members of the Environmental Physics Lab at the University of Texas at El Paso who offered opinions and a friendly ear to my ideas.

Special thanks to the members of my committee for agreeing to participate and lend their support to my research. Dr. Fitzgerald for her unwavering support and her pragmatism, Dr. Gill for his guidance and his feedback, Dr. Morris for his words of wisdom and his knowledge, and Dr. Goodell for his candidness and willingness to participate in the madness.

Abstract

The African continent is the principal contributor of mineral aerosols into the atmosphere. It is also a significant source of carbonaceous aerosols resulting from rampant biomass burning activities. Both aerosol types have a profound impact on climate change and are an important factor in climate modeling, regional weather forecasting, as well as health-impact studies. Due to their importance, it is beneficial to characterize the transport and evolution of these aerosols from their origins in Africa, across the Atlantic Ocean and into the Americas. In-situ aerosol number distributions were collected during the 2009 Aerosols and Ocean Science Expeditions (AEROSE) V campaign, in the tropical Atlantic Ocean. For the purpose of establishing air mass type, HYSPLIT 7-day backward trajectories were generated from July 12, 2009 to August 4, 2009 on a daily basis, on 6-hour intervals: at 00hrs, 06hrs, 12hrs and 18hrs; at five different elevations: 10m, 100m, 500m, 1000m and 500m. This amounted to a total of four hundred and forty trajectories. This research presented statistical analysis of air mass occurrences per regimen type for 6-hour intervals contrasted with daily averaged air mass types. To do so, each trajectory was backtracked to their source region and air type regimen was established according to NAAPS/FLAMBE/MODIS forecasts and datasets

Table of Contents

| | Page |
|---|------|
| Acknowledgments | v |
| Abstract | vi |
| Table of Contents | vii |
| List of Tables | viii |
| List of Figures | ix |
| Chapter 1: Introduction | 1 |
| Chapter 2: Background Information | 6 |
| Chapter 3: Methods and Materials | 10 |
| Chapter 4: Results and Discussion | 22 |
| Chapter 5: Conclusion..... | 63 |
| References | 65 |
| Glossary | 73 |
| Appendix | 74 |
| Curriculum Vita | 140 |

List of Tables

| | Page |
|---|------|
| Table 1: Sampling channels per CLIMET instrument..... | 15 |
| Table 2: CLIMET sampling channels analyzed for this research | 17 |
| Table 3: HYSPLIT back-trajectories receptor sites..... | 32 |
| Table 4: Meteorological GDAS files..... | 33 |
| Table 5: Resulting HYSPLIT backward trajectory files..... | 35 |
| Table 6: NAAPS/FLAMBE forecasts (.kml files) | 36 |
| Table 7: Six-hour interval predominant source regimen..... | 38 |
| Table 8: 6-hr interval Event Type Numerical Values | 40 |
| Table 9: 6-hr interval HYSPLIT source-region plots | 40 |
| Table 10: Daily averaged predominant source regimen..... | 46 |
| Table 11: Daily averaged HYSPLIT source-region plots | 47 |
| Table 12: Daily averaged Event Type Numerical Values | 48 |
| Table 13: Corresponding Figure for Percentage-Comparison Plots..... | 54 |
| Table 14: Correlation and Covariance Comparison | 58 |
| Table 15: Corresponding Figure for Percentage Comparisons | 59 |
| Table 16: Comparison between 6-hour readings and average values at 10m..... | 60 |
| Table 17: Comparison between 6-hour readings and average values at 100m..... | 60 |
| Table 18: Comparison between 6-hour readings and average values at 500m..... | 61 |
| Table 19: Comparison between 6-hour readings and average values at 1000m..... | 61 |
| Table 20: Comparison between 6-hour readings and average values at 5000m..... | 62 |

List of Figures

| | Page |
|--|------|
| Figure 1: RHB track during AEROSE V..... | 4 |
| Figure 2: Image of the RHB ship | 11 |
| Figure 3: Image of CLIMET instruments..... | 12 |
| Figure 4: CLIMET sampling setup | 16 |
| Figure 5: CI-500 Time Series | 22 |
| Figure 6: CI-550 Time Series | 23 |
| Figure 7: CI-500 Evolution of daily averaged number concentrations | 24 |
| Figure 8: CI-550 Evolution of daily averaged number concentrations | 25 |
| Figure 9: CI-500 daily averaged size distributions across sampling ranges | 26 |
| Figure 10: CI-550 daily averaged size distributions across sampling ranges | 27 |
| Figure 11: CI-500 histogram of daily averaged number size distributions per bin size. | 28 |
| Figure 12: CI-550 histogram of daily averaged number size distributions per bin size. | 29 |
| Figure 13: CI-500 Percentages across bin sizes | 30 |
| Figure 14: CI-550 Percentages across bin sizes | 31 |
| Figure 15: 6-hr interval Daily evolution of air mass types at source site for 10m..... | 41 |
| Figure 16: 6-hr interval Percentage of air mass type occurrence 10m | 41 |
| Figure 17: 6-hr interval Daily evolution of air mass types at source site for 100m | 42 |
| Figure 18: 6-hr interval Percentage of air mass type occurrence 100m | 42 |
| Figure 19: 6-hr interval Daily evolution of air mass types at source site for 500m | 43 |
| Figure 20: 6-hr interval Percentage of air mass type occurrence 500m | 43 |

| | |
|---|----|
| Figure 21: 6-hr interval Daily evolution of air mass types at source site for 1000m | 44 |
| Figure 22: 6-hr interval Percentage of air mass type occurrence 1000m | 44 |
| Figure 23: 6-hr interval Daily evolution of air mass types at source site for 5000m | 45 |
| Figure 24: 6-hr interval Percentage of air mass type occurrence 5000m | 45 |
| Figure 25: Daily averaged evolution of air mass types at source site for 10m | 49 |
| Figure 26: Daily averaged Percentage of air mass type occurrence 10m | 49 |
| Figure 27: Daily averaged evolution of air mass types at source site for 100m | 50 |
| Figure 28: Daily averaged Percentage of air mass type occurrence 100m | 50 |
| Figure 29: Daily averaged evolution of air mass types at source site for 500m | 51 |
| Figure 30: Daily averaged Percentage of air mass type occurrence 500m | 51 |
| Figure 31: Daily averaged evolution of air mass types at source site for 1000m | 52 |
| Figure 32: Daily averaged Percentage of air mass type occurrence 1000m | 52 |
| Figure 33: Daily averaged evolution of air mass types at source site for 5000m | 53 |
| Figure 34: Daily averaged Percentage of air mass type occurrence 5000m | 53 |
| Figure 35: Comparison between 6-hour readings and averaged values at 10m | 55 |
| Figure 36: Comparison between 6-hour readings and averaged values at 100m | 55 |
| Figure 37: Comparison between 6-hour readings and averaged values at 500m | 56 |
| Figure 38: Comparison between 6-hour readings and averaged values at 1000m | 56 |
| Figure 39: Comparison between 6-hour readings and averaged values at 5000m | 57 |
| Figure 40: HYSPLIT 7-day backward trajectory for 071209 | 74 |
| Figure 41: HYSPLIT 7-day backward trajectory for 071309 | 75 |
| Figure 42: HYSPLIT 7-day backward trajectory for 071409 | 76 |
| Figure 43: HYSPLIT 7-day backward trajectory for 071509 | 77 |

| | |
|---|----|
| Figure 44: HYSPLIT 7-day backward trajectory for 071609 | 78 |
| Figure 45: HYSPLIT 7-day backward trajectory for 071709 | 79 |
| Figure 46: HYSPLIT 7-day backward trajectory for 072009 | 80 |
| Figure 47: HYSPLIT 7-day backward trajectory for 072109 | 81 |
| Figure 48: HYSPLIT 7-day backward trajectory for 072209 | 82 |
| Figure 49: HYSPLIT 7-day backward trajectory for 072309 | 83 |
| Figure 50: HYSPLIT 7-day backward trajectory for 072409 | 84 |
| Figure 51: HYSPLIT 7-day backward trajectory for 072509 | 85 |
| Figure 52: HYSPLIT 7-day backward trajectory for 072609 | 86 |
| Figure 53: HYSPLIT 7-day backward trajectory for 072709 | 87 |
| Figure 54: HYSPLIT 7-day backward trajectory for 072809 | 88 |
| Figure 55: HYSPLIT 7-day backward trajectory for 072909 | 89 |
| Figure 56: HYSPLIT 7-day backward trajectory for 073009 | 90 |
| Figure 57: HYSPLIT 7-day backward trajectory for 073109 | 91 |
| Figure 58: HYSPLIT 7-day backward trajectory for 080109 | 92 |
| Figure 59: HYSPLIT 7-day backward trajectory for 080209 | 93 |
| Figure 60: HYSPLIT 7-day backward trajectory for 080309 | 94 |
| Figure 61: HYSPLIT 7-day backward trajectory for 080409 | 95 |
| Figure 62: NAAPS/FLAMBE forecast and HYSPLIT trajectories for 071209 - 00hrs..... | 96 |
| Figure 63: NAAPS/FLAMBE forecast and HYSPLIT trajectories for 071209 - 06hrs..... | 96 |
| Figure 64: NAAPS/FLAMBE forecast and HYSPLIT trajectories for 071209 - 12hrs..... | 97 |
| Figure 65: NAAPS/FLAMBE forecast and HYSPLIT trajectories for 071209 - 18hrs..... | 97 |
| Figure 66: NAAPS/FLAMBE forecast and HYSPLIT trajectories for 071309 - 00hrs..... | 98 |

| | |
|---|-----|
| Figure 67: NAAPS/FLAMBE forecast and HYSPLIT trajectories for 071309 - 06hrs..... | 98 |
| Figure 68: NAAPS/FLAMBE forecast and HYSPLIT trajectories for 071309 - 12hrs..... | 99 |
| Figure 69: NAAPS/FLAMBE forecast and HYSPLIT trajectories for 071309 - 18hrs..... | 99 |
| Figure 70: NAAPS/FLAMBE forecast and HYSPLIT trajectories for 071409 - 00hrs... | 100 |
| Figure 71: NAAPS/FLAMBE forecast and HYSPLIT trajectories for 071409 - 06hrs... | 100 |
| Figure 72: NAAPS/FLAMBE forecast and HYSPLIT trajectories for 071409 - 12hrs... | 101 |
| Figure 73: NAAPS/FLAMBE forecast and HYSPLIT trajectories for 071409 - 18hrs... | 101 |
| Figure 74: NAAPS/FLAMBE forecast and HYSPLIT trajectories for 071509 - 00hrs... | 102 |
| Figure 75: NAAPS/FLAMBE forecast and HYSPLIT trajectories for 071509 - 06hrs... | 102 |
| Figure 76: NAAPS/FLAMBE forecast and HYSPLIT trajectories for 071509 - 12hrs... | 103 |
| Figure 77: NAAPS/FLAMBE forecast and HYSPLIT trajectories for 071509 - 18hrs... | 103 |
| Figure 78: NAAPS/FLAMBE forecast and HYSPLIT trajectories for 071609 - 00hrs... | 104 |
| Figure 79: NAAPS/FLAMBE forecast and HYSPLIT trajectories for 071609 - 06hrs... | 104 |
| Figure 80: NAAPS/FLAMBE forecast and HYSPLIT trajectories for 071609 - 12hrs... | 105 |
| Figure 81: NAAPS/FLAMBE forecast and HYSPLIT trajectories for 071609 - 18hrs... | 105 |
| Figure 82: NAAPS/FLAMBE forecast and HYSPLIT trajectories for 071709 - 00hrs... | 106 |
| Figure 83: NAAPS/FLAMBE forecast and HYSPLIT trajectories for 071709 - 06hrs... | 106 |
| Figure 84: NAAPS/FLAMBE forecast and HYSPLIT trajectories for 071709 - 12hrs... | 107 |
| Figure 85: NAAPS/FLAMBE forecast and HYSPLIT trajectories for 071709 - 18hrs... | 107 |
| Figure 86: NAAPS/FLAMBE forecast and HYSPLIT trajectories for 072009 - 00hrs... | 108 |
| Figure 87: NAAPS/FLAMBE forecast and HYSPLIT trajectories for 072009 - 06hrs... | 108 |
| Figure 88: NAAPS/FLAMBE forecast and HYSPLIT trajectories for 072009 - 12hrs... | 109 |
| Figure 89: NAAPS/FLAMBE forecast and HYSPLIT trajectories for 072009 - 18hrs... | 109 |

| | |
|---|-----|
| Figure 90: NAAPS/FLAMBE forecast and HYSPLIT trajectories for 072109 - 00hrs... | 110 |
| Figure 91: NAAPS/FLAMBE forecast and HYSPLIT trajectories for 072109 - 06hrs... | 110 |
| Figure 92: NAAPS/FLAMBE forecast and HYSPLIT trajectories for 072109 - 12hrs... | 111 |
| Figure 93: NAAPS/FLAMBE forecast and HYSPLIT trajectories for 072109 - 18hrs... | 111 |
| Figure 94: NAAPS/FLAMBE forecast and HYSPLIT trajectories for 072209 - 00hrs... | 112 |
| Figure 95: NAAPS/FLAMBE forecast and HYSPLIT trajectories for 072209 - 06hrs... | 112 |
| Figure 96: NAAPS/FLAMBE forecast and HYSPLIT trajectories for 072209 - 12hrs... | 113 |
| Figure 97: NAAPS/FLAMBE forecast and HYSPLIT trajectories for 072209 - 18hrs... | 113 |
| Figure 98: NAAPS/FLAMBE forecast and HYSPLIT trajectories for 072309 - 00hrs... | 114 |
| Figure 99: NAAPS/FLAMBE forecast and HYSPLIT trajectories for 072309 - 06hrs... | 114 |
| Figure 100: NAAPS/FLAMBE forecast and HYSPLIT trajectories for 072309 - 12hr... | 115 |
| Figure 101: NAAPS/FLAMBE forecast and HYSPLIT trajectories for 072309 - 18hrs. | 115 |
| Figure 102: NAAPS/FLAMBE forecast and HYSPLIT trajectories for 072409 - 00hrs. | 116 |
| Figure 103: NAAPS/FLAMBE forecast and HYSPLIT trajectories for 072409 - 06hrs. | 116 |
| Figure 104: NAAPS/FLAMBE forecast and HYSPLIT trajectories for 072409 - 12hrs. | 117 |
| Figure 105: NAAPS/FLAMBE forecast and HYSPLIT trajectories for 072409 - 18hrs. | 117 |
| Figure 106: NAAPS/FLAMBE forecast and HYSPLIT trajectories for 072509 - 00hrs. | 118 |
| Figure 107: NAAPS/FLAMBE forecast and HYSPLIT trajectories for 072509 - 06hrs. | 118 |
| Figure 108: NAAPS/FLAMBE forecast and HYSPLIT trajectories for 072509 - 12hrs. | 119 |
| Figure 109: NAAPS/FLAMBE forecast and HYSPLIT trajectories for 072509 - 18hrs. | 119 |
| Figure 110: NAAPS/FLAMBE forecast and HYSPLIT trajectories for 072609 - 00hrs. | 120 |
| Figure 111: NAAPS/FLAMBE forecast and HYSPLIT trajectories for 072609 - 06hrs. | 120 |
| Figure 112: NAAPS/FLAMBE forecast and HYSPLIT trajectories for 072609 - 12hrs. | 121 |

Figure 113: NAAPS/FLAMBE forecast and HYSPLIT trajectories for 072609 - 18hrs.121

Figure 114: NAAPS/FLAMBE forecast and HYSPLIT trajectories for 072709 - 00hrs.122

Figure 115: NAAPS/FLAMBE forecast and HYSPLIT trajectories for 072709 - 06hrs.122

Figure 116: NAAPS/FLAMBE forecast and HYSPLIT trajectories for 072709 - 12hrs.123

Figure 117: NAAPS/FLAMBE forecast and HYSPLIT trajectories for 072709 - 18hrs.123

Figure 118: NAAPS/FLAMBE forecast and HYSPLIT trajectories for 072809 - 00hrs.124

Figure 119: NAAPS/FLAMBE forecast and HYSPLIT trajectories for 072809 - 06hrs.124

Figure 120: NAAPS/FLAMBE forecast and HYSPLIT trajectories for 072809 - 12hrs.125

Figure 121: NAAPS/FLAMBE forecast and HYSPLIT trajectories for 072809 - 18hrs.125

Figure 122: NAAPS/FLAMBE forecast and HYSPLIT trajectories for 072909 - 00hrs.126

Figure 123: NAAPS/FLAMBE forecast and HYSPLIT trajectories for 072909 - 06hrs.126

Figure 124: NAAPS/FLAMBE forecast and HYSPLIT trajectories for 072909 - 12hrs.127

Figure 125: NAAPS/FLAMBE forecast and HYSPLIT trajectories for 072909 - 18hrs.127

Figure 126: NAAPS/FLAMBE forecast and HYSPLIT trajectories for 073009 - 00hrs.128

Figure 127: NAAPS/FLAMBE forecast and HYSPLIT trajectories for 073009 - 06hrs.128

Figure 128: NAAPS/FLAMBE forecast and HYSPLIT trajectories for 073009 - 12hrs.129

Figure 129: NAAPS/FLAMBE forecast and HYSPLIT trajectories for 073009 - 18hrs.129

Figure 130: NAAPS/FLAMBE forecast and HYSPLIT trajectories for 073109 - 00hrs.130

Figure 131: NAAPS/FLAMBE forecast and HYSPLIT trajectories for 073109 - 06hrs.130

Figure 132: NAAPS/FLAMBE forecast and HYSPLIT trajectories for 073109 - 12hrs.131

Figure 133: NAAPS/FLAMBE forecast and HYSPLIT trajectories for 073109 - 18hrs.131

Figure 134: NAAPS/FLAMBE forecast and HYSPLIT trajectories for 080109 - 00hrs.132

Figure 135: NAAPS/FLAMBE forecast and HYSPLIT trajectories for 080109 - 06hrs.132

Figure 136: NAAPS/FLAMBE forecast and HYSPLIT trajectories for 080109 - 12hrs.133

Figure 137: NAAPS/FLAMBE forecast and HYSPLIT trajectories for 080109 - 18hrs.133

Figure 138: NAAPS/FLAMBE forecast and HYSPLIT trajectories for 080209 - 00hrs.134

Figure 139: NAAPS/FLAMBE forecast and HYSPLIT trajectories for 080209 - 06hrs.134

Figure 140: NAAPS/FLAMBE forecast and HYSPLIT trajectories for 080209 - 12hrs.135

Figure 141: NAAPS/FLAMBE forecast and HYSPLIT trajectories for 080209 - 18hrs.135

Figure 142: NAAPS/FLAMBE forecast and HYSPLIT trajectories for 080309 - 00hrs.136

Figure 143: NAAPS/FLAMBE forecast and HYSPLIT trajectories for 080309 - 06hrs.136

Figure 144: NAAPS/FLAMBE forecast and HYSPLIT trajectories for 080309 - 12hrs.137

Figure 145: NAAPS/FLAMBE forecast and HYSPLIT trajectories for 080309 - 18hrs.137

Figure 146: NAAPS/FLAMBE forecast and HYSPLIT trajectories for 080409 - 00hrs.138

Figure 147: NAAPS/FLAMBE forecast and HYSPLIT trajectories for 080409 - 06hrs.138

Figure 148: NAAPS/FLAMBE forecast and HYSPLIT trajectories for 080409 - 12hrs.139

Figure 149: NAAPS/FLAMBE forecast and HYSPLIT trajectories for 080409 - 18hrs.139

Chapter 1: Introduction

Atmospheric aerosols

In their 2001 report, the Intergovernmental Panel on Climate Change (IPCC), described atmospheric aerosols as “one of the largest uncertainties in climate change studies” (IPCC, 2001; Tanré et al. 2009). To this day, atmospheric aerosol interactions are not yet fully understood due to their complex characteristics. However, it has been established that continental mineral dust is the largest natural source of particulate aerosol mass (Heintzenberg, 2009).

It is also known that of all the various aerosol types, sea-salt and mineral dust are the most abundant of aerosol species (Tanré et al. 2009). The latter plays a key role in the Earth's radiative budget by backscattering a considerable portion of the solar radiation (Tanré et al. 2009). Thus, mineral dust significantly impacts the climate system by altering the global energy balance, "forcing" the climate to change (IPCC, 2001). Such interaction is described in literature as a "*climate forcing*" mechanism (Cess, 1985). Climate forcing by aerosols depends on the aerosol properties. The climate forcing is a function of aerosol size distribution. If the area-weighted mean radius, r_{eff} , which is a single parameter that can describe the size dependence, is greater than about 2 μm , the global average greenhouse effect of the aerosols exceeds the albedo effect, causing a surface heating. The aerosol climate forcing is less sensitive to other characteristics of the size distribution, the aerosol composition, and the altitude of the aerosols (Lacis et al., 1992).

Sources

More mineral dust originates from North Africa than any other region of the world, and more dust is deposited into the North Atlantic than any other ocean basin (Shao et al., 2011). The sources of these aerosols moving across the Atlantic are varied and their origin is closely tied to their composition, which ultimately will determine their behavior. It is important to determine the origin of these aerosols, so that we may understand how they behave and thus impact our health, the climate, and the various meteorological processes that shape the weather and deeply influence our daily lives.

According to Moulin and Chiapello (2006), “dust emissions in Sahel and Atlantic dust exports have regularly increased since 1965”. This is of special importance due to the fact that more than 30% of the African continent is covered by deserts (Thomas et al., 2005). Some of the world’s great deserts are located in Africa, such as the Sahara, the Kalahari, and the Namib; all sources of sandstorms and dust aerosols. Desert sandstorms alone are an important source of aerosols to the Atlantic Ocean. Polymenakou et al. 2008 states “estimated that dust flux from the Saharan- Sahel region to the atmosphere is approximately 1 billion tons/year.”

Importance

From the health perspective, it is important to determine the particle sizes of the aerosols coming across the Atlantic into the US Eastern seaboard due to the implications they may have on its population. It has been determined that those particle sizes that have a diameter measuring less than 10 microns are inhalable (Ganor et al.,

2009), which is considered a major health hazard (Dockery et al., 1993; Schwartz, 1994; Prospero, 1999; Annesi-Maesano et al., 2007). It is also possible for pathogens to participate in transcontinental transport due to their presence in small particles (Polymenakou et al. 2008).

From a policy standpoint, there is also a need to better represent the influence of aerosol particles in atmospheric processes so that adequate regulations pertaining to each industry may be enacted. (Chin et al. 2009).

Purpose

The purpose of the proposed research is to analyze the microphysical properties of aerosols within the air masses encountered during the AEROSE V expedition according to their particle number size distributions. Statistical and graphical analysis of these aerosol distributions encountered during the expeditions is used to make this classification. In order to validate the obtained results, HYSPLIT back-trajectories to aerosol source areas as well as NAAPS model outputs of aerosol type are utilized to determine their accuracy.

The datasets to be used in this study were collected during the AEROSE V campaign. The AEROSE V campaign took place from July 13 to August 10, 2009, on a cruise track from Barbados to Key West, Florida (Figure 1).

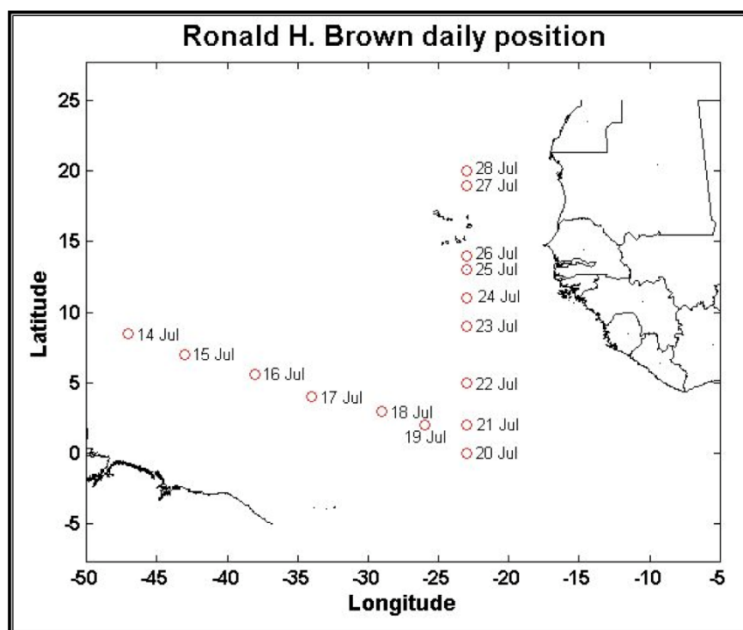


Figure (1): The image reflects the location of the ship Ronald H. Brown (RHB) on a daily basis during AEROSE V. Courtesy of Dr. Nick Nalli.

Characterization of the air masses is completed by utilizing the particle size distributions provided by the CI-500 and CI-550 Laser Particle Counters.

Data collected out in the field, such as the AEROSE datasets, are referred to as in-situ measurements. Unfortunately, they are often time-consuming, as well as expensive, to acquire them since they require traveling to the source-site and spending time performing the survey. These datasets may also be inaccurate, due to human method-produced error and measurement-device miscalibration, both of which contribute to the in-situ data-collection error. Therefore, in situ data is considered as ground reference data, since it must be acknowledged that it may contain errors. For this reason, the findings from this research, i.e. the aerosol classification scheme, are

verified against remotely sensed data- in this instance, NASA MODIS satellite Fire products. Remotely sensed data is defined as information collected from a distance by aerial platforms and sensors (Jensen, 2005).

Chapter 2: Background Information

Mineral particles travel from continent to continent when the proper meteorological conditions exist (Chun et al. 2001). Such conditions are influenced by synoptic-scale disturbances, natural and anthropogenic pollution, and other factors, and thus, to the present day, the accurate monitoring of atmospheric aerosols has been an extremely difficult task (Dubovik et al. 2002). Detailed and accurate data about the dynamic optical properties of these aerosols are incomplete. Although aerosols are one of the most important factors in climate change, due to these limitations their role is not very well understood (Dubovik et al. 2002).

Monitoring of aerosols may be achieved by the use of remote sensing techniques, which provide a nonintrusive measurement of particles and offer global coverage (Dubovik et al. 2002). However, such techniques are affected by factors that are difficult to account for, such as the physical properties (i.e. reflection, refraction, absorption) of the aerosols encountered; and the data obtained has limited accuracy (Kaufman et al. 1997; King et al. 1999). In addition, the conversion of satellite radiances to aerosol and ozone distributions requires a large number of assumptions (Bates et al. 2001). Even though data collected in situ cannot achieve the coverage provided by satellites, they provide detailed and accurate aerosol physical, chemical and optical information (Bates et al. 2001) that can be used for the analysis of climate. According to Colbeck (2008), in-situ measurements are the least invasive and the measurements obtained by optical techniques are made without moving a sample from a flowing aerosol stream. This is important because it guarantees the integrity of the

data, and it assures that the measurements taken are not being altered by removing or adding anything from the aerosols being measured.

The optical properties of aerosols present clear information about a limited set of physical and chemical features of the aerosol. For this reason, optical aerosol models utilize the following confined set of aerosol parameters: particle size (particle size distribution), composition (complex index of refraction), and shape (sphericity) (Dubovik et al. 2002). Therefore, it is important to conduct further research and analysis of the aerosol physical properties in conjunction with and to validate optical measurements.

One way to obtain reliable in-situ surface aerosol data over a large geographical area such as the ocean is the use of a research ship. Previous ocean-borne research expeditions such as the Aerosols99 (Bates et al. 2001), the AEROSE campaigns (Morris et al. 2006, Nalli et al. 2005, Nalli et al. 2011), and ground- and aircraft-based expeditions such as the SHADE (Tanré et al., 2003) and the SAMUM-1 field campaign (Heintzenberg, 2009) have proven to be great sources for measuring properties of aerosols.

SAMUM-1

According to Heintzenberg (2009), SAMUM-1 provided ‘the first radiative closure experiment near the dust source’. It took place over Southeast Morocco and its primary focus was to characterize the optical and physical properties of mineral dust emanated from the Sahara.

SHADE

The purpose of the Saharan Dust Experiment (SHADE) was to enhance direct radiative effect calculations by exploring the effects of mineral dust and its microphysical and optical properties (Tanré et al. 2003).

AEROSE

Aerosol and Ocean Science Expeditions (AEROSE) are a series of trans-Atlantic intensive atmospheric field campaigns conducted aboard the NOAA (National Oceanic and Atmospheric Administration) ship Ronald H. Brown (RHB) (Morris et al., 2006). The purpose of the AEROSE expeditions is to gather physical, biological, and chemical data across the Atlantic. AEROSE campaigns have sought to obtain a suite of complementary measurements to study the transport of aerosols from the African continent across the Atlantic Ocean. More specifically, they seek to analyze the “impacts of Saharan dust outbreaks on the ocean, atmosphere, biosphere, and on satellite radiometric observations” (Nalli et al., 2005)

The first expedition was AEROSE-I in 2004. Six more expeditions have taken place since, with the most recent being AEROSE-VII, which took place in the spring of

2011. The in-situ datasets collected on the AEROSE expeditions are important because they can help us understand the impacts these aerosols have on health and climate, as well as on the meteorological processes that take place out at sea, which shape the larger-scale regional weather.

Chapter 3: Methods and Materials

The purpose of this research is to analyze the temporal and spatial evolution of aerosol number distributions during AEROSE V by examining size separated number concentrations and their correlation to the predominant regimen at their source site as determined by HYSPLIT backward trajectories, NAAPS model projections and MODIS fire locations.

This research presents statistical results based on the analysis of aerosol size distributions measured over a period of 22 sampling days (July 12 – August 4, 2009) during the AEROSE V campaign. Lapses in data acquisition were either a result of sensor malfunction or an obligatory data-collection shutdown upon entrance into the Brazilian exclusive economic zones (EEZ) (Nalli et al., 2011).

The Ronald H. Brown (Figure 2) ship is equipped with a centralized data acquisition and logging network that acquires and stores data from the various sensors throughout the ship. This system is referred to as SCS, or the Ship's Computer System data, and it automatically generates for every cruise a set of files with standardized datasets. <http://www.moc.noaa.gov/rb/science/equipment.html>



Figure (2): Pictured is the Ronald H. Brown ship from the NOAA research fleet.

The SCS, the RHB's main data-storage system, can incorporate data from every sensor connected to it; hence it can generate files with various combinations of datasets. The OCEAN-OBS_001.elg, OCEAN-OBS_002.elg, OBS_001.elg and OBS_002.elg files were selected from the pool of pre-set (automated) SCS files, since they encompassed the set of variables pertinent to this research, such as latitude, longitude and time. A detailed description of the sensors and instruments that collected the aforementioned datasets can be found in the instrumentation section of this thesis.

Instrumentation

CLIMET CI-500 and CI-550

Particle-size distribution datasets were collected with CLIMET CI-500 and CI-550 laser particle counters (LPC) (Figure 3). In an LPC, particles pass through a sensing zone that is illuminated by a laser (Esparza, 2011). The light scattered by each aerosol particle is detected over a range of angles and converted to an electronic pulse that is a complex but generally increasing function of particle size (Baron and Willeke, 2001). These instruments utilize a size-selective sampling approach, where the particles are sorted into size bins (Esparza et al., 2011). Both the CI-500 and CI-550 instruments size and count particles in six differentiated channels (Table 1). The instruments sampled every fifteen minutes, for a total volume of 0.028 m^3 of air, the equivalent to one cubic foot of air in each sample.



Figure (3) – The CLIMET CI-500 to the right, and the CI-550 on the left.

IMET sensors

The IMET sensors refer to a number of onboard sensors developed by Woods Hole Oceanographic Institute (WHOI) in Woods Hole, Massachusetts. (<http://www.moc.noaa.gov/rb/science/calibration.html>). The IMET set are calibrated on a yearly basis, and the output data is already in calibrated values. The location of the relative humidity and temperature IMET sensors is listed as 9.6m above the water line. <http://www.moc.noaa.gov/rb/science/equipment.html>.

Position datasets are provided by the Trimble GPS Precise Positioning GPS (P-Code) navigation system (<http://www.moc.noaa.gov/rb/science/scs-sensor.html>), and the time is obtained from a precision UTC clock onboard the ship (<http://www.moc.noaa.gov/rb/science/equipment.html>). For the purpose of this research, these datasets were acquired from the OCEAN-OBS_001.elg, OCEAN-OBS_002.elg, OBS_001.elg and OBS_002.elg files from the RHB's Ship's Computer System (SCS). The original resolution for the position datasets was continuous, 10 seconds sampling.

Temporal scale

The temporal scale is set to Coordinated Universal Time (UTC), or 'Zulu' time. The instrumentation and sensors collected data setting the time zone to UTC. Time depictions followed by a 'Z' (i.e. 12:00Z) denote time in UTC zone.

Models

HYSPLIT

The HYSPLIT (Hybrid Single-Particle Lagrangian Integrated Trajectory) model (Draxler and Hess, 1998) was used to generate the backward trajectories of the air masses to establish their origins and aid in their classifications. The HYSPLIT model was designed for quick response to atmospheric emergencies, diagnostic case studies, or climatological analyses using previously gridded meteorological data. In this instance, we were interested in its diagnostic capabilities, given that it can be used to calculate trajectories and air concentrations for analytical studies (Draxler and Hess, 1998). This model can be very helpful when investigating long-range transport, since it provides the capability to determine the location of an air mass or a contaminant's plume.

NAAPS Global Aerosol Model

The NAAPS (Navy Aerosol Analysis and Prediction System) Global Aerosol Model, from the Naval Research Laboratory (NRL) was selected to facilitate this research due to its global, multi-component aerosol analysis and modeling capabilities. The NAAPS Global Aerosol Model products use global meteorological fields from the Navy Operational Global Atmospheric Prediction System (NOGAPS) (Hogan and Rosmond, 1991; Hogan and Brody 1993). The Naval Research Laboratory (NRL) (Zhang and Reid, 2009) generates these products, and they can distinguish between clean air, polluted air, smoke or dust. Such feature was essential for our task of classifying the air masses encountered by the RHB during the AEROSE cruise.

Methodology

CLIMET datasets

During the expedition, datasets were collected using the CLIMET CI-500 and CLIMET CI-550, depicted in the image (Figure 3). Each monitor aerosols in six particle size ranges (given in microns), as Table 1 depicts. Both instruments use the same sampling method, sampling cycle, and sampling volume. The only differences between the two are the particle size ranges. The LPC's were set-up to sample every 15 minutes, taking a total volume of 0.028 m^3 of air. The instruments were placed inside a repurposed shipping container, which was retrofitted with power lines to maintain the instrumentation continuously taking samples without the need of battery power (Figure 4).

Table 1 – The CI-500 and CI-550 instruments size and count particles in six differentiated channels as shown on the table below.

| Instrument | Sampling size-bins per instrument (units in μm) | | | | | |
|------------|---|-----------|-----------|-----------|------------|--------|
| CI-500 | 0.3 – 0.5 | 0.5 – 0.7 | 0.7 – 1.2 | 1.2 – 5.0 | 5.0 – 10.0 | 10.0 + |
| CI-550 | 0.3 – 0.5 | 0.5 – 1.0 | 1.0 – 3.0 | 3.0 – 5.0 | 5.0 – 10.0 | 10.0 + |

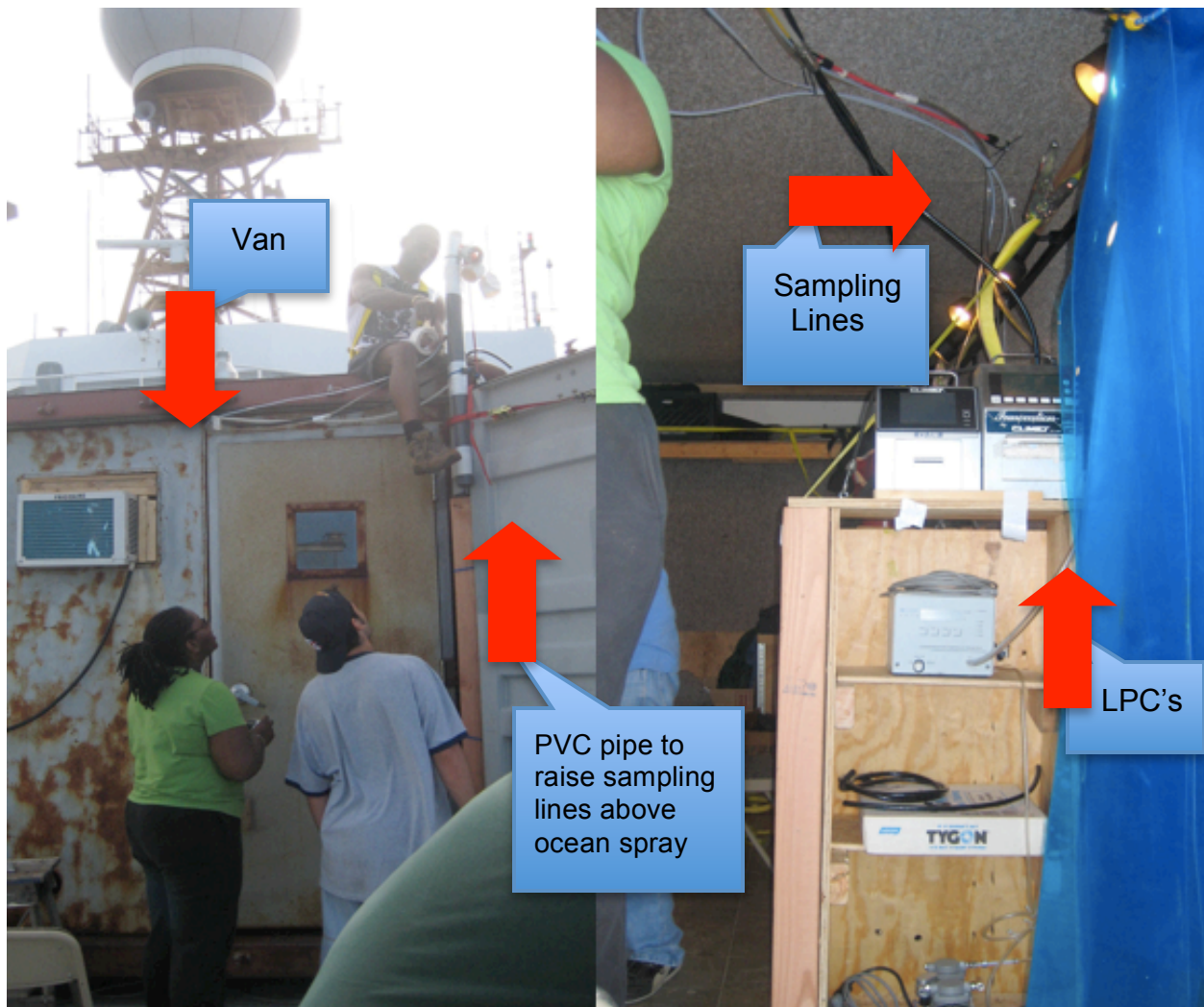


Figure (4) – The CLIMET (LPC) instruments were placed inside a repurposed shipping container, which was retrofitted with power lines to maintain the instrumentation continuously taking samples without the need of battery power

Drops in data proved frequent, mostly due to water in the sampling lines from a big splash or excessive ambient humidity that generated condensation in the lines. To fix the condensation issues as well as any clogs in the sampling lines, flushing was conducted with nitrogen and/or air on the instruments as well as on the lines.

The output from the LPC's is a comma-delimited ASCII file that was transferred to Excel spreadsheets to facilitate analysis. During the quality control and assurance

processes (QA and QC), the identified blocks of data plagued by clogging issues in the sampling lines were edited out in separate files, to maintain the integrity of the datasets. Datasets were subsequently resolved to half-hour averages, in order to allow for comparison with the meteorological datasets, and other instrumentation onboard the RHB. Two channels of data were dropped for each LPC, leaving four channels per instrument, for a total of eight. Table 2 depicts the sampling channels analyzed for this research.

Table 2 – The table below depicts the sampling channels analyzed for this research.

| Instrument | Sampling channels analyzed (units in μm) | | | |
|-------------------|---|-----------|-----------|-----------|
| CI-500 | 0.3 – 0.5 | 0.5 – 0.7 | 0.7 – 1.2 | 1.2 – 5.0 |
| CI-550 | 0.3 – 0.5 | 0.5 – 1.0 | 1.0 – 3.0 | 3.0 – 5.0 |

HYSPLIT Backward Trajectories

The HYSPLIT backward trajectories are a helpful tool since they project the path of an air mass from a user-specified receptor site to its source, back in time and space.

This research employed the PC Windows-based HYSPLIT version 4.9.

For this research, backward trajectories were generated as supporting data. Their role was to aid in the identification of a determined air mass, in order to resolve if an agreement existed between the regimens (dust, marine, smoke) suggested by the corresponding measured aerosol number distributions, and the regimen suggested by the source of the air mass.

In order to generate the backward trajectories, the desired receptor sites, trajectories' heights, model run-time, and necessary gridded meteorological datasets were established. The gridded meteorological datasets used to create the backward trajectories were Global Data Analysis System (GDAS) archived datasets from the NOAA Air Resource Laboratory (ARL). Such datasets were obtained through the FTP option within the HYSPLIT model's GUI, and incorporated into the HYSPLIT model to generate the backward trajectories. The residence time of aerosols in the troposphere is assumed to be on the order of 7 days (Ganguly et al., 2005; Verma et al., 2007); consequently 7-days backward trajectories were generated, equivalent to 168 hours of the model's run time. The receptor sites for the HYSPLIT model were selected by identifying the location (latitude and longitude) of the ship for 00:00Z hours, 06:00Z hours, 12:00Z hours and 18:00Z hours for each day, from July 12 – August 4, 2009. The temporal scale was set to Coordinated Universal Time (UTC).

The elevations for the backward trajectories were picked as follows: the 10m, 100m, and 500m heights were chosen given that they are generally associated to short range transport within the marine boundary layer. Respectively, the 1000m and 5000m elevations were selected due to the fact that they are usually associated to air masses involved in long-range transport. This was of critical importance to this research, as it would aid in discerning the source region of the air parcels encountered deep into the Atlantic Ocean.

NAAPS-FLAMBE *.kml product

The NAAPS model was chosen to complement the aerosol number distribution and meteorological datasets, as well as the HYSPLIT simulations due to the before mentioned model's capability "of predicting the distribution of dust, smoke and sulfur tropospheric aerosols", as stated by Naval Research

Laboratory's (NRL) FAQ webpage found at

http://www.nrlmry.navy.mil/flambe/ge_faq.html

For this research, the NAAPS-FLAMBE kml product files were selected since they provide a compelling view in 2D, with the help of Google Earth, of the concentrations of dust, smoke and sulfur tropospheric aerosols, as well as the locations of fires. This was useful because it presented this research the opportunity of contrasting the predictions of the model with the in-situ aerosol number distributions, and the origin of the air masses highlighted by the HYSPLIT backward trajectories with the locations of fires. An area experiencing possible smoke, according to the NAAPS predictions, could be correlated to an air mass that originated, according to HYSPLIT backward trajectories, in an area experiencing a fire, according to the MODIS predictions.

The NAAPS-FLAMBE kml files were downloaded from

http://www.nrlmry.navy.mil/aerosol/kml/older_flambe_world_kml/. These datasets

incorporated NAAPS Global Aerosol Model products; MODIS (MODerate Resolution Imaging Spectroradiometer) satellite data; and FLAMBE (Fire Locating and Modeling of Burning Emissions) datasets.

According to the documentation found under the 'Description of NAAPS Plots' at

http://www.nrlmry.navy.mil/aerosol_web/Docs/globaer_plots.html, the NAAPS Global Aerosol Model product depicts “the dust optical depth, sulfate optical depth and smoke optical depth as contour bands, at a wavelength of 0.55 microns for all NAAPS components: sulfate, dust, and smoke”. These components are differentiated by the color shades assigned to each. Red and orange shades are used to identify sulfate contours, yellow and green shades are used for dust contours, and blue shades are used for smoke contours.

As for the MODIS satellite data, the datasets are described as “RGB color composites that are made of 0.1-degree (Lat/Lon) gridded MODIS product. Red, green and blue colors are assigned to the channel 1 (620 – 670nm), 4 (545 – 565nm), and 3 (459 – 479nm) of MODIS data respectively”, according to the description given at http://www.nrlmry.navy.mil/flambe/ge_faq.html. The University of Maryland generates the MODIS fire products from Terra and Aqua. <http://www.nrlmry.navy.mil/flambe/>

Finally, the following description of FLAMBE can be found at http://www.nrlmry.navy.mil/flambe/ge_faq.html. “FLAMBE is a program to model biomass burning emissions, transport, and radiative effects in a global prognostic meteorology model. Initiated by the US Navy, National Aeronautics and Space Administration (NASA), National Oceanic and Atmospheric Administration (NOAA), and the University of Alabama, FLAMBE “is a multi-disciplinary program drawing from a broad range of expertise and resources.” The FLAMBE program is further described in Reid et al. (2009).

The NAAPS-FLAMBE kml files incorporate all of these datasets, as well as

others available from NOGAPS Fleet Numerical Meteorology and Oceanography Center (FNMOC) (<https://www.fnmoc.navy.mil/>) to provide a global depiction of air masses from severe dust events (which correlate to dust contour areas), air masses from heavily industrialized regions (which correlate to sulfur contour areas) and air masses resulting from biomass burning (which correlates to smoke areas); as well as the location of fires from the MODIS fire products from Terra and Aqua generated by the University of Maryland. <http://www.nrlmry.navy.mil/flambe/>

Chapter 4: Results and Discussion

Instrumentation

Figure 5 depicts the size-segregated particle-number concentrations observed during the AEROSE V campaign; from July 17th to August 3rd 2009, with the CI-500 instrument. The number concentration for the 0.3 to 0.5 μm range, the smallest measured by the instrument, remained stable until July 24th, when it decreased sharply, remaining stable for the rest of the expedition. Particles within the 0.5 to 0.7 μm range dominated from early on until a shift was observed on July 26, 2009. By July 28th, particle sizes ranging from 0.7 to 1.2 μm became dominant until July 31st. The largest measured particle sizes, in the 1.2 to 5.0 μm range, increased substantially during the same period, from July 28th to July 31st. Number concentrations reached the maximum during this same period, specifically on July 29th.

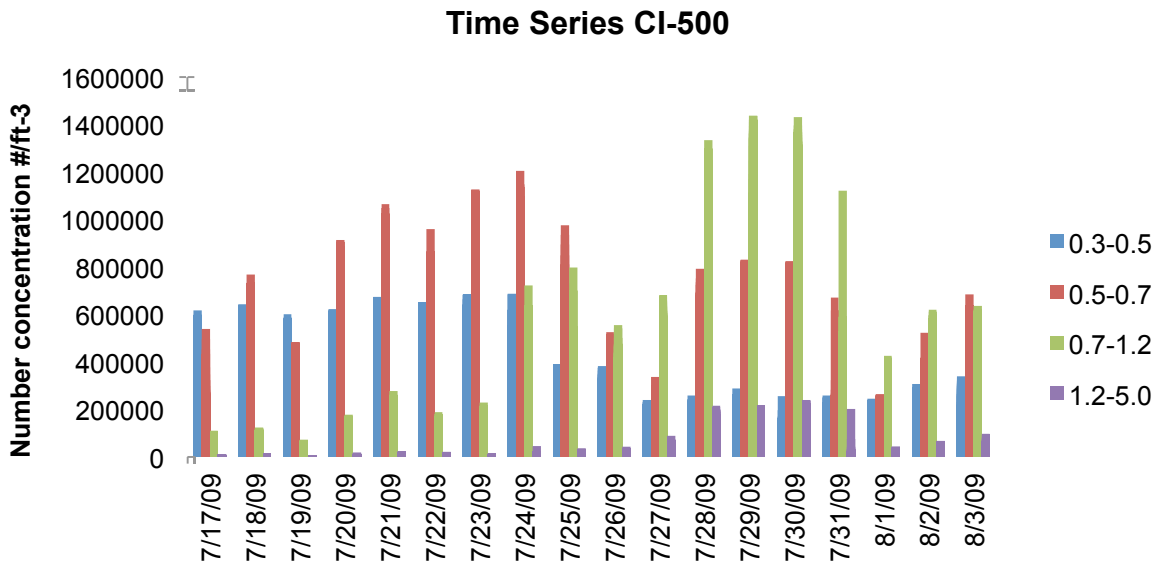


Figure (5) - CI-500 time series variation of aerosol number concentrations

The CI-550 size-segregated particle-number concentrations are depicted in Figure 6. The 0.3 to 0.5 μm range, the smallest measured by the instrument, exhibited the maximum concentrations of all the ranges, specifically for the day of July 20th. For the 0.5 to 1.0 μm range concentrations increased steadily until July 25th, then dropped sharply by July 26th only to increase again by the next day and exhibit the largest concentrations ranging on July 28th, lasting until August 1st.

The 1.0 to 3.0 μm range showed a low concentration of particles up until July 23rd, and began incrementing by July 24th remaining steady until July 27th. From July 28th to July 29th, the largest particle concentrations can be observed until July 29th. The largest measured particle size, from 3.0 to 5.0 μm , exhibited the lowest number concentration of aerosols, bordering on the negligible until July 28, when a sharp and considerable increment was observed, then dropped back into low number concentrations by August 1st, and remained steady up to August 4th.

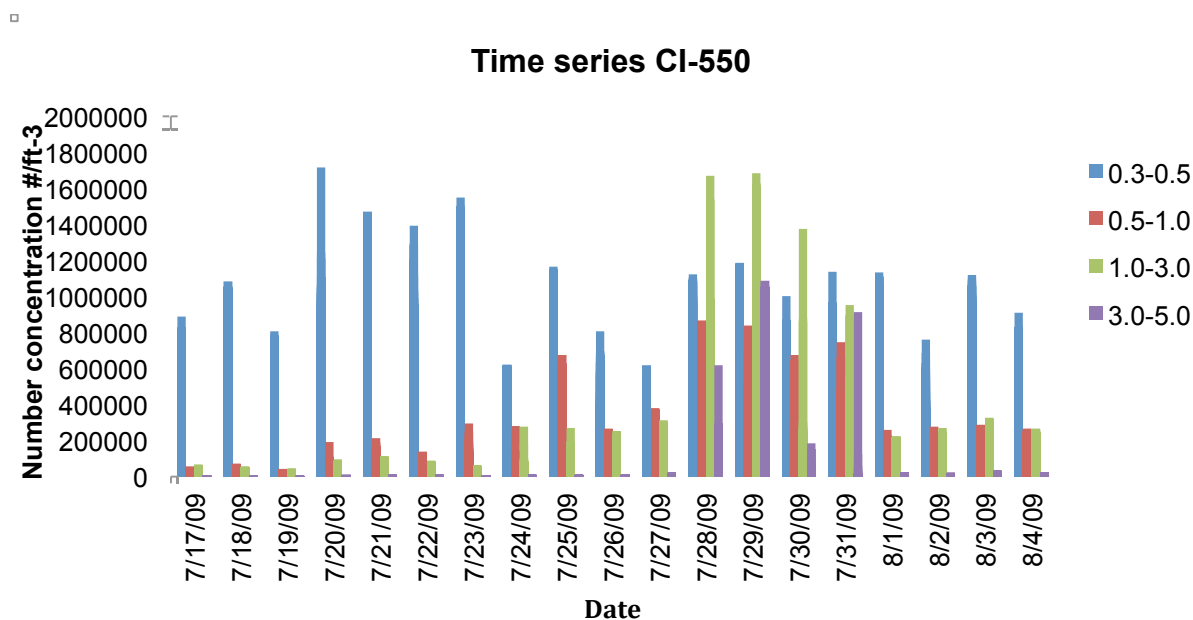


Figure (6) - CI-550 time series variation of aerosol number concentrations

Figure 7 and Figure 8 depict the daily averaged particle number distributions (#particles/ft⁻³) for the CI-550 and Ci-500 instruments, respectively, for each day. These smooth-line scatter plots show the number concentration of particles across size ranges. The size ranges for Figure 7, and Figure 8, are as follows: below the 1.0 µm range, above the 1.0 µm range and below the 10.0 µm range. This plotting method was chosen since it highlights the particle size range where the maximum peak was measured for each day.

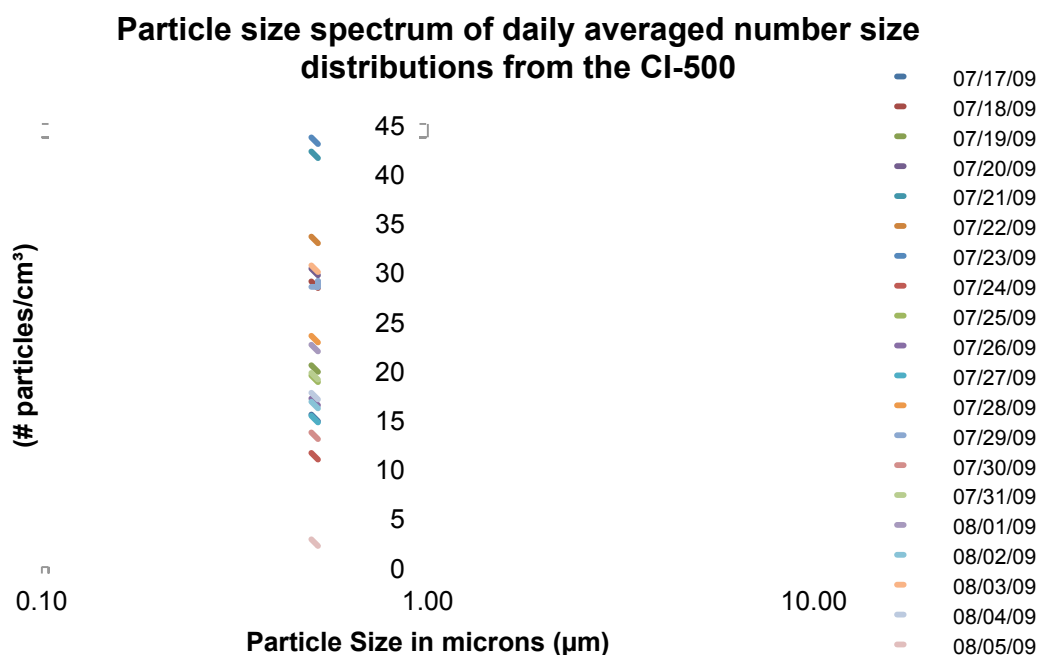


Figure (7) – Evolution of daily averaged number concentrations (#particles/cm⁻³) across the particle size spectrum.

It is apparent from Figure 7 that the particle size distributions measured by the CI-500 peak below the 1.0 µm range, for all days except 07/29/09. The particle size ranges measured by this instrument were established in Table 2 as follows:

| | | | |
|--------------|--------------|--------------|--------------|
| 0.3 – 0.5 µm | 0.5 – 0.7 µm | 0.7 – 1.2 µm | 1.2 – 5.0 µm |
|--------------|--------------|--------------|--------------|

In contrast to Figure 7, Figure 8 evidences that the particle size distributions measured by the CI-550 peak at several different particle size ranges. The particle size ranges measured by this instrument were established in Table 2 as follows:

0.3 – 0.5 μm

0.5 – 1.0 μm

1.0 – 3.0 μm

3.0 – 5.0 μm

A total of 18 days were plotted in Figure 8. For 9 days, it peaked above the 1.0 μm range and below the 10.0 μm range, and for the remaining 9 days it peaked below the 1.0 μm range. This shows a 50/50 split across the two ranges in this particle size spectrum.

□

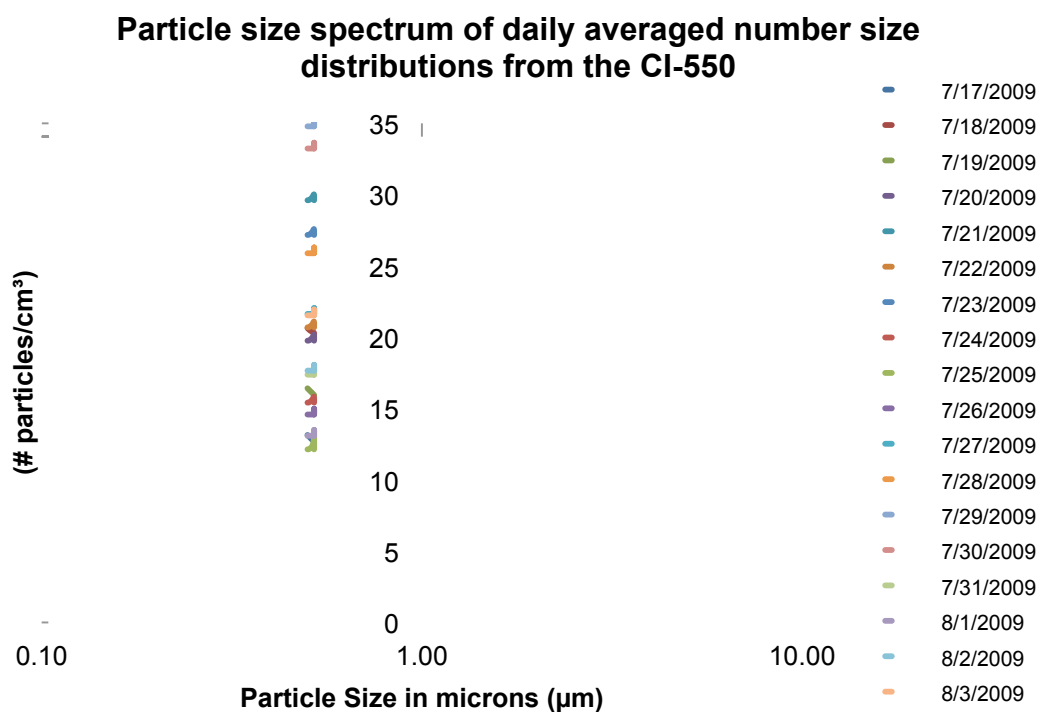


Figure (8) – Evolution of daily averaged number concentrations (#particles/ cm^{-3}) across the particle size spectrum.

It is established from examining both figures that Figure 7 showcases a sampling prevalence of particles smaller than the 1.2 – 5.0 μm range, while Figure 8 does not exhibit an obvious sampling prevalence of a particular particle-size range.

In Figure 9 and Figure 10, the daily averaged number size distributions are further broken down into the four sampling ranges chosen per instrument for this research. The intent was to identify each instrument's sampling ability within each particular sampling range. For this purpose, radar plots were chosen to better represent the behavior of number concentrations within each sampling range. The particle size ranges measured by both instruments were established in Table 2.

It is observed from Figure 9 that the CI-500 measured the highest particle size concentrations for the 0.5 – 0.7 μm sampling range, and the lowest for the 1.2 – 5.0 μm range.

□

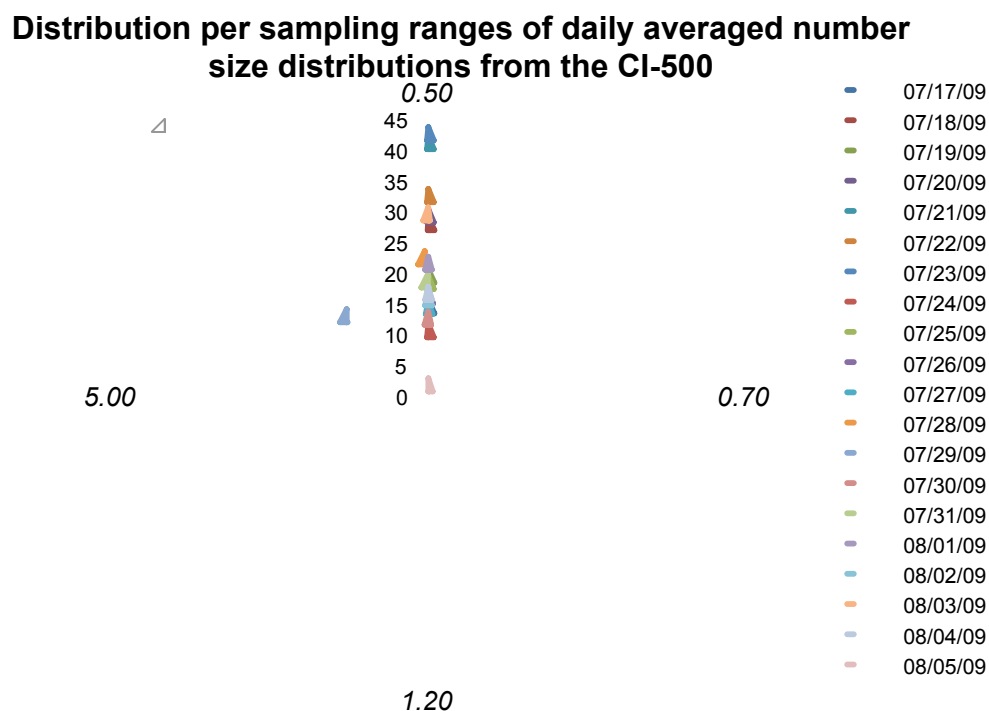


Figure (9) – Daily averaged number size distributions ($\#particles/cm^3$) across CI-500 sampling ranges

In Figure 10, the CI-550 measured the highest particle size concentrations for the 1.0 – 3.0 μm sampling range, closely followed by number of particles measured within the 0.5 – 1.0 μm sampling range. The lowest concentrations were measured for the 3.0 – 5.0 μm range.

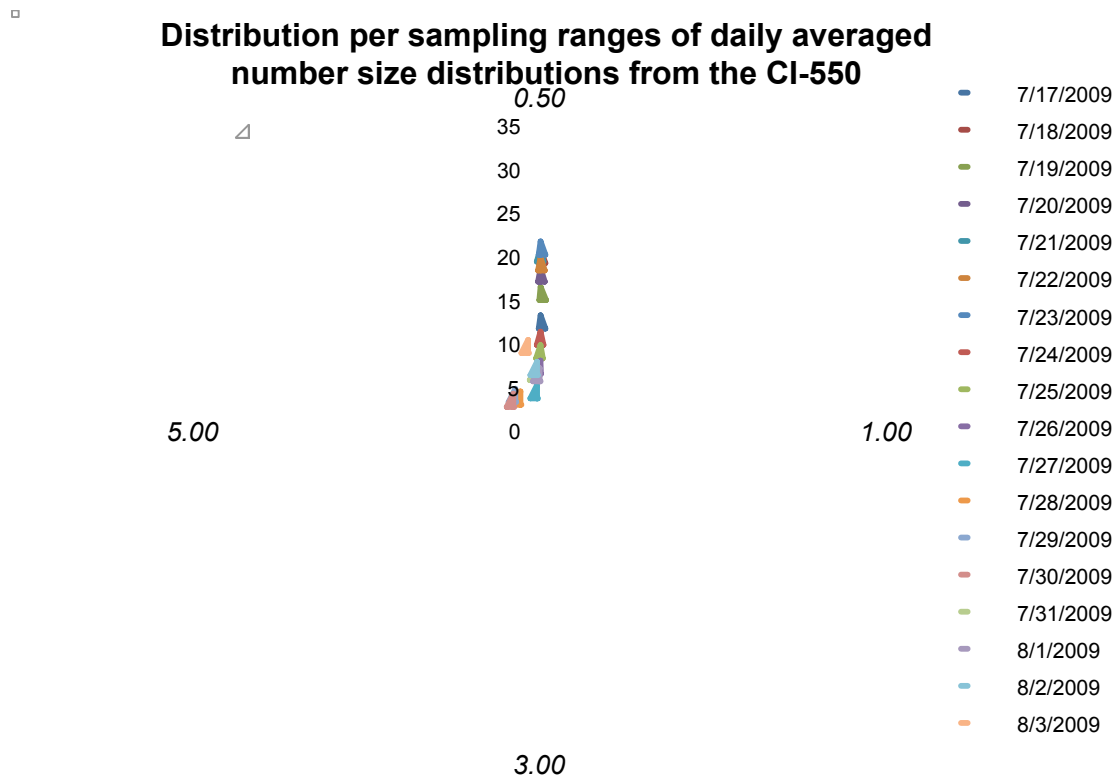


Figure (10) – Daily averaged number size distributions ($\# \text{particles}/\text{cm}^{-3}$) across CI-550 sampling ranges

To further examine the evolution of number concentrations per instrument across sampling ranges, histograms of daily averaged number size distributions were plotted by bin size. This allotted this research the opportunity to establish variations in number concentrations on a daily basis per bin size-range in a clearer manner than the radar plots from Figure 9 and Figure 10. The histogram plots are also to be contrasted with the radar plots to verify the sampling ability predicted by the first, and determine if an agreement between the two plotting methods is established.

Figure 11 illustrates the fact that the highest number concentrations for the CI-500 were measured for the 0.5 – 0.7 μm sampling range, and the lowest for the 1.2 – 5.0 μm range. This is in agreement with the observations made from Figure 9, and the assumption can be made that the CI-500 sampling ability is geared towards the smallest particle size ranges.

□

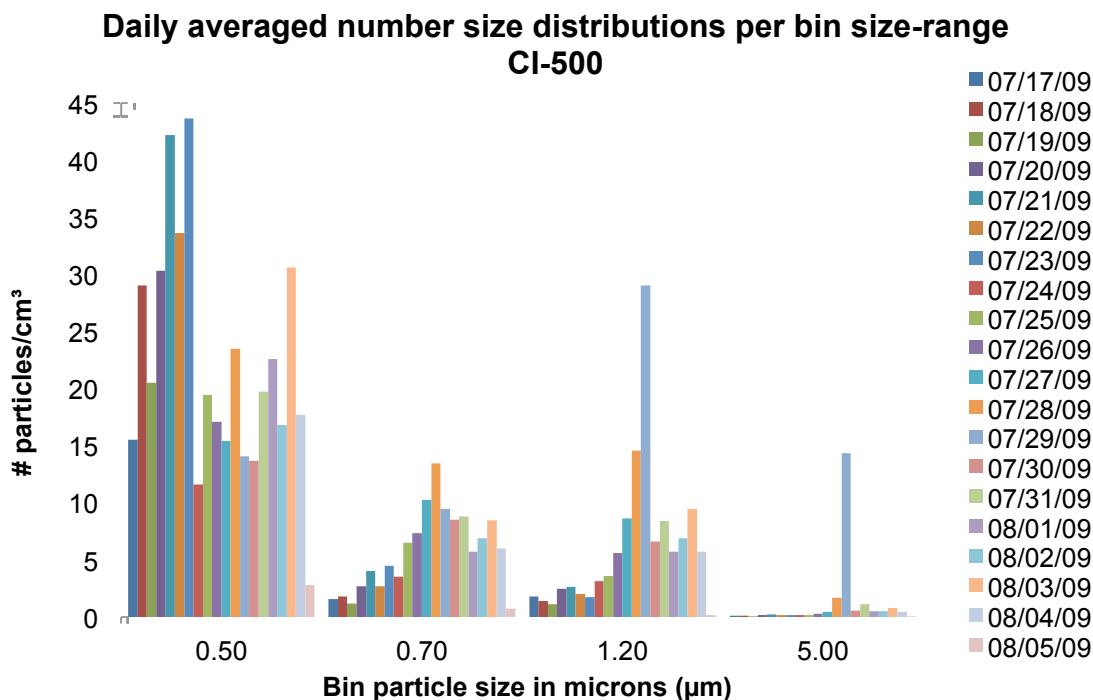


Figure (11) – Histogram of daily averaged number size distributions per bin size

In contrast, Figure 12 demonstrates that number size distributions for the CI-500 instrument were at its highest concentration for the 1.0 – 3.0 μm sampling range, closely followed by number of particles measured within the 0.5 – 1.0 μm sampling range. The lowest concentrations were measured for the 3.0 – 5.0 μm range, the bin size focused on the sampling of the largest particles. There is an agreement with the observations

made from radar plot in Figure 10, therefore it may be established that the CI-550 sampling capability is geared towards the mid particle size ranges.

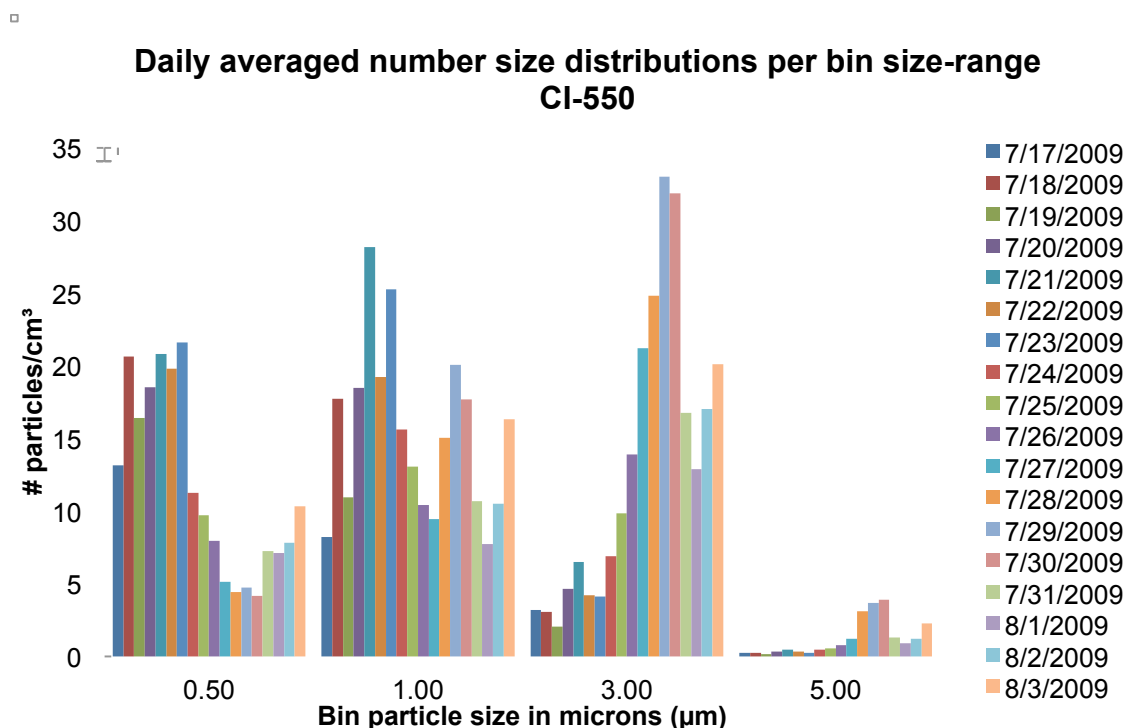


Figure (12) – Histogram of daily averaged number size distributions per bin size

After establishing an agreement between the two plotting methods by comparing them and obtaining similar results, it is verified that the sampling capability predicted by the radar plots is confirmed by the histogram plots.

Now, in order to establish the distribution of particle size concentrations across sampling ranges in a more qualitative manner, percentages for each of the four bin sizes per instrument were calculated. The results are shown in Figure 13 and Figure 14.

The percentages across bin sizes for the CI-500 instrument are plotted in Figure 13. As a reminder, it was established In Table 2 that the sampling ranges for this instrument are as follows:

0.3 – 0.5 μm

0.5 – 0.7 μm

0.7 – 1.2 μm

1.2 – 5.0 μm

From the percentage plot in Figure 13 it is demonstrated in a quantitative manner that the highest number concentrations were assured for the 0.3 – 0.5 μm sampling range, corresponding to an overwhelming 82% of all the sampled particles.

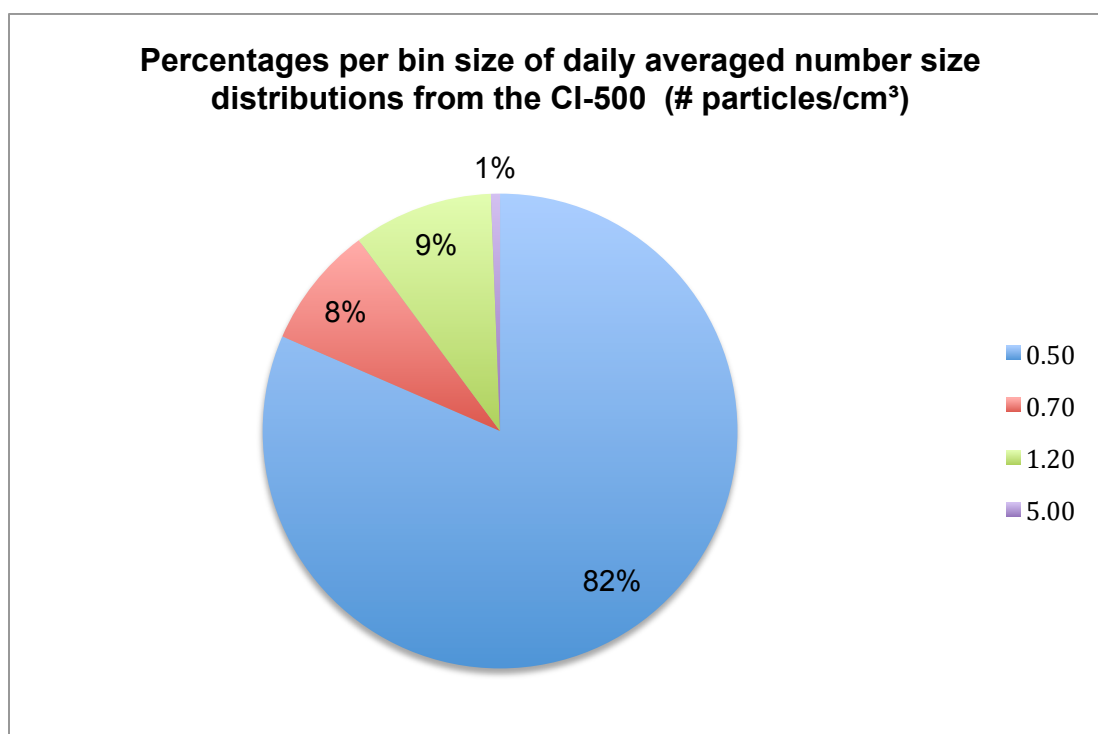


Figure (13) - Percentages across bin sizes for the CI-500

Figure 14 depicts the percentages across bin sizes for the CI-550 instrument. From Table 2, the sampling ranges for this instrument are as follows:

0.3 – 0.5 μm

0.5 – 1.0 μm

1.0 – 3.0 μm

3.0 – 5.0 μm

From the percentage plot in Figure 14 it is demonstrated in a quantitative manner that the highest number concentrations were measured for the 0.3 – 0.5 μm sampling range at 53%, followed by 33% from the 1.0 – 3.0 μm sampling range.

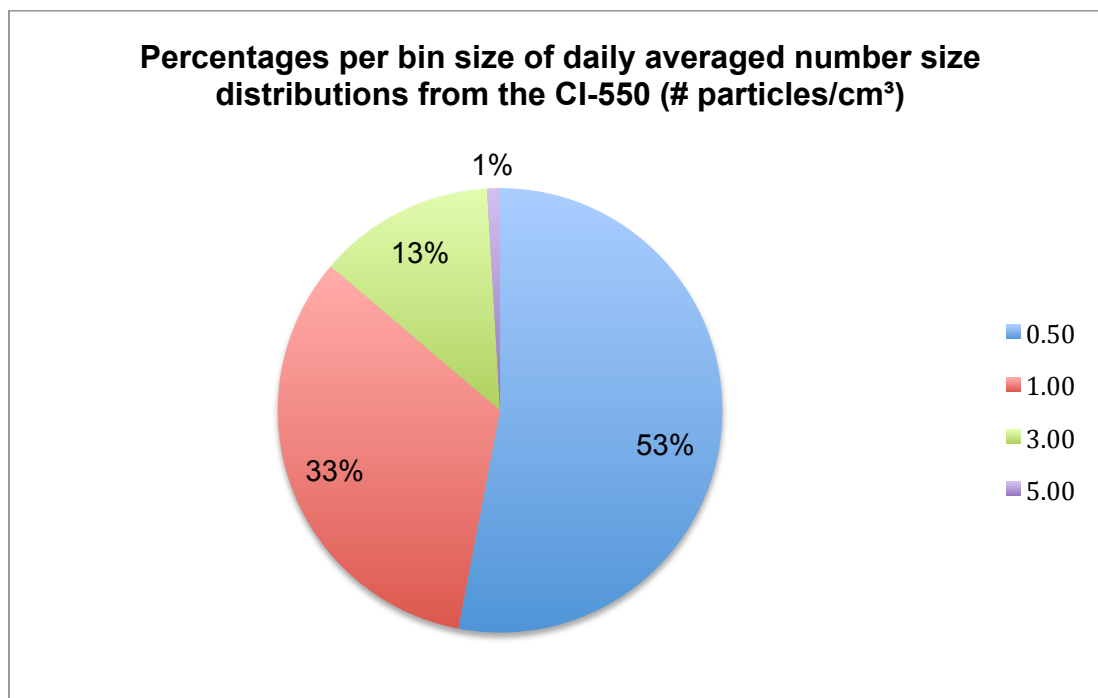


Figure (14) - Percentages across bin sizes for the CI-550

To summarize, there was an overall agreement between the observations made across Figure 7, Figure 9, Figure 11 and Figure 13 regarding the CI-500 instrument and its capability toward sampling smaller particle sizes, in this instance across the 0.3 – 0.5 μm sampling range. In addition, Figure 8, Figure 10, Figure 12 and Figure 14, related to the CI-550 and its preferred sampling range, did not show a clear-cut agreement. For this instrument, it was determined that there was no overwhelming sampling range, although preference toward the 1.0 – 3.0 μm sampling range was noted, closely followed by the 0.5 – 1.0 μm sampling range. HYSPLIT Backward Trajectories

HYSPLIT backward trajectories were generated using the GUI interface for HYSPLIT model version 4.9. Four HYSPLIT back-trajectories receptor sites were chosen for each day, at 0, 6, 12 and 18 UTC time (Table 3). The purpose was to

insulate the resulting trajectories from the influence of specific chemical and physical phenomena such as wind speed variations, photosynthesis, to name a few, linked to spatial variations throughout the day.

Table 3 – A total of four HYSPLIT back-trajectories receptor sites were chosen for each day, at 0, 6, 12 and 18 UTC time, with the exception of 07/18/09 and 07/19/09 due to an incursion into the Brazilian EEZ.

| Date | 0 hour | | 6 hours | | 12 hours | | 18 hours | |
|----------|----------|-----------|----------|-----------|----------|-----------|----------|-----------|
| | Latitude | Longitude | Latitude | Longitude | Latitude | Longitude | Latitude | Longitude |
| 07/12/09 | 12.45 | -58.25 | 12.11 | -57.25 | 11.76 | -56.26 | 11.40 | -55.22 |
| 07/13/09 | 11.05 | -54.21 | 10.70 | -53.22 | 10.34 | -52.20 | 9.97 | -51.14 |
| 07/14/09 | 9.60 | -50.09 | 9.21 | -48.97 | 8.81 | -47.83 | 8.41 | -46.70 |
| 07/15/09 | 8.01 | -45.55 | 7.61 | -44.42 | 7.20 | -43.28 | 6.80 | -42.16 |
| 07/16/09 | 6.42 | -41.07 | 6.03 | -39.99 | 5.65 | -38.91 | 5.26 | -37.81 |
| 07/17/09 | 4.86 | -36.67 | 4.47 | -35.59 | 4.10 | -34.56 | 3.75 | -33.56 |
| 07/18/09 | 3.41 | -32.60 | 0.00 | 0.00 | 0.00 | 0.00 | 0.00 | 0.00 |
| 07/19/09 | 1.07 | -26.02 | 0.00 | 0.00 | 0.00 | 0.00 | 0.00 | 0.00 |
| 07/20/09 | 0.84 | -25.40 | 0.49 | -24.42 | 0.14 | -23.41 | 0.00 | -22.99 |
| 07/21/09 | 1.24 | -22.99 | 2.47 | -23.00 | 3.73 | -23.01 | 4.08 | -23.01 |
| 07/22/09 | 4.07 | -23.00 | 4.50 | -23.00 | 5.11 | -23.00 | 5.93 | -23.00 |
| 07/23/09 | 6.54 | -23.00 | 7.35 | -23.00 | 8.00 | -23.00 | 8.84 | -23.00 |
| 07/24/09 | 9.50 | -23.00 | 10.26 | -23.00 | 11.00 | -23.00 | 11.49 | -23.00 |
| 07/25/09 | 11.50 | -23.00 | 12.22 | -23.00 | 13.00 | -23.00 | 13.82 | -23.00 |
| 07/26/09 | 14.50 | -23.00 | 15.37 | -22.77 | 16.08 | -22.60 | 16.92 | -22.80 |
| 07/27/09 | 17.56 | -23.00 | 18.39 | -23.00 | 19.00 | -23.00 | 19.84 | -23.00 |
| 07/28/09 | 20.47 | -23.12 | 20.46 | -23.12 | 20.42 | -23.17 | 20.44 | -23.72 |
| 07/29/09 | 20.41 | -25.02 | 20.37 | -26.35 | 20.33 | -27.69 | 20.29 | -29.05 |
| 07/30/09 | 20.25 | -30.40 | 20.22 | -31.72 | 20.18 | -33.07 | 20.14 | -34.42 |
| 07/31/09 | 20.10 | -35.75 | 20.06 | -37.00 | 20.03 | -37.86 | 20.04 | -37.85 |
| 08/01/09 | 19.99 | -38.89 | 19.94 | -40.20 | 19.88 | -41.56 | 19.83 | -42.90 |
| 08/02/09 | 19.76 | -44.21 | 19.70 | -45.52 | 19.64 | -46.81 | 19.59 | -48.09 |
| 08/03/09 | 19.53 | -49.41 | 19.47 | -50.71 | 19.41 | -51.98 | 19.36 | -53.24 |
| 08/04/09 | 19.30 | -54.52 | 19.25 | -55.77 | 19.19 | -57.09 | 19.13 | -58.34 |

In order to determine the temporal and spatial position of the ship and generate the information contained in Table 3, the RHB's Ship's Computer System was accessed. Files OCEAN-OBS_001.elg, OCEAN-OBS_002.elg, OBS_001.elg and OBS_002.elg

were obtained. Their resolution is of 10 seconds continuous sampling, and these datasets were sifted to determine the coordinates at the 00hrs, 06hrs, 12hrs and 18hrs.

Global Data Analysis System (GDAS) archived datasets with 0.5-degree resolution and hybrid (h) vertical coordinates were used to provide the necessary meteorological data to the HYSPLIT model (Table 4).

Table 4 - Weekly meteorological GDAS files used for HYSPLIT backward trajectories

| Global Data Analysis System (GDAS) datasets |
|---|
| gdas1.jul09.w1 |
| gdas1.jul09.w2 |
| gdas1.jul09.w3 |
| gdas1.jul09.w4 |
| gdas1.jul09.w5 |
| gdas1.jul09.w6 |

HYSPLIT backward trajectories were generated for AEROSE V dates for which data was available. The dates correspond to July 12 to August 4th, 2009. The ensuing quality control and assurance processes (QA and QC) revealed data blackouts for July 18 and July 19, 2009. These were imposed upon entry into the Brazilian exclusive economic zones (EEZ) and remained for the duration of the RHB stay within such zones. Since no data was available for all of July 18th and 19th; it was determined that there was no need to generate HYSPLIT trajectories for those days. At 22 days selected, and four trajectories generated per day at 6-hour intervals, a total of eighty-eight 7-day HYSPLIT backward-trajectory files were generated for this research (Table 5). The name for each of the eighty-eight files, sorted by its corresponding day and hour can be observed in detail in Table 5.

In addition, for each of the eighty-eight receptor sites, backward trajectories were generated at five different heights (10m, 100m, 500m, 1000m and 5000m). This corresponds to 440 HYSPLIT backward trajectories. The fact that short-range transport within the marine boundary layer takes place below the 1000m is the reasoning behind the selection of the 10m, 100m, and 500m heights. To contrast, heights associated with long-range transport, such as the 1000m and 5000m heights were also selected.

All of the resulting eighty-eight HYSPLIT backward trajectory files, each with its corresponding five heights, can be observed in the Appendix section of this thesis spanning from Figure 40 to Figure 61. To maximize space, each page depicts the four 6-hour intervals generated for each day. At the upper left corner: 00hrs, upper right corner: 06hrs, lower left corner: 12hrs, and lower right corner: 18hrs. Additionally, all of the 6-hour intervals show the five different heights plotted for every one of them. Each color corresponds to a specific trajectory height: red 10m, blue 100m, green 500m, cyan 1000m and magenta 5000m

The backward trajectories were created in Adobe (.PDF), GIS (.SHP), and Google Earth (.KML) output formats. This methodology allowed for the HYSPLIT backward trajectories to be superimposed with NAAPS/FLAMBE forecasts and MODIS fire-location files in .KML format using Google Earth. This technique proved advantageous since it allowed for the opportunity to determine the predominant regimen to which air masses backtracked their source.

Table5 - Resulting eighty-eight HYSPLIT backward trajectory files

| Date of data coverage | HYSPLIT 7 day backward trajectory file name | | | |
|--------------------------|---|--------------------------------------|--------------------------------------|--------------------------------------|
| | 00hrs | 06hrs | 12hrs | 18hrs |
| 07/12/09 | HYSPLITtraj071209-00hr-corrected.kmz | HYSPLITtraj071209-06hr-corrected.kmz | HYSPLITtraj071209-12hr-corrected.kmz | HYSPLITtraj071209-18hr-corrected.kmz |
| 07/13/09 | HYSPLITtraj071309-00hr-corrected.kmz | HYSPLITtraj071309-06hr-corrected.kmz | HYSPLITtraj071309-12hr-corrected.kmz | HYSPLITtraj071309-18hr-corrected.kmz |
| 07/14/09 | HYSPLITtraj071409-00hr-corrected.kmz | HYSPLITtraj071409-06hr-corrected.kmz | HYSPLITtraj071409-12hr-corrected.kmz | HYSPLITtraj071409-18hr-corrected.kmz |
| 07/15/09 | HYSPLITtraj071509-00hr-corrected.kmz | HYSPLITtraj071509-06hr-corrected.kmz | HYSPLITtraj071509-12hr-corrected.kmz | HYSPLITtraj071509-18hr-corrected.kmz |
| 07/16/09 | HYSPLITtraj071609-00hr-corrected.kmz | HYSPLITtraj071609-06hr-corrected.kmz | HYSPLITtraj071609-12hr-corrected.kmz | HYSPLITtraj071609-18hr-corrected.kmz |
| 07/17/09 | HYSPLITtraj071709-00hr-corrected.kmz | HYSPLITtraj071709-06hr-corrected.kmz | HYSPLITtraj071709-12hr-corrected.kmz | HYSPLITtraj071709-18hr-corrected.kmz |
| 07/18/09 | NO DATA | NO DATA | NO DATA | NO DATA |
| 07/19/09 | NO DATA | NO DATA | NO DATA | NO DATA |
| 07/20/09 | HYSPLITtraj072009-00hr-corrected.kmz | HYSPLITtraj072009-06hr-corrected.kmz | HYSPLITtraj072009-12hr-corrected.kmz | HYSPLITtraj072009-18hr-corrected.kmz |
| 07/21/09 | HYSPLITtraj072109-00hr-corrected.kmz | HYSPLITtraj072109-06hr-corrected.kmz | HYSPLITtraj072109-12hr-corrected.kmz | HYSPLITtraj072109-18hr-corrected.kmz |
| 07/22/09 | HYSPLITtraj072209-00hr-corrected.kmz | HYSPLITtraj072209-06hr-corrected.kmz | HYSPLITtraj072209-12hr-corrected.kmz | HYSPLITtraj072209-18hr-corrected.kmz |
| 07/23/09 | HYSPLITtraj072309-00hr-corrected.kmz | HYSPLITtraj072309-06hr-corrected.kmz | HYSPLITtraj072309-12hr-corrected.kmz | HYSPLITtraj072309-18hr-corrected.kmz |
| 07/24/09 | HYSPLITtraj072409-00hr-corrected.kmz | HYSPLITtraj072409-06hr-corrected.kmz | HYSPLITtraj072409-12hr-corrected.kmz | HYSPLITtraj072409-18hr-corrected.kmz |
| 07/25/09 | HYSPLITtraj072509-00hr-corrected.kmz | HYSPLITtraj072509-06hr-corrected.kmz | HYSPLITtraj072509-12hr-corrected.kmz | HYSPLITtraj072509-18hr-corrected.kmz |
| 07/26/09 | HYSPLITtraj072609-00hr-corrected.kmz | HYSPLITtraj072609-06hr-corrected.kmz | HYSPLITtraj072609-12hr-corrected.kmz | HYSPLITtraj072609-18hr-corrected.kmz |
| 07/27/09 | HYSPLITtraj072709-00hr-corrected.kmz | HYSPLITtraj072709-06hr-corrected.kmz | HYSPLITtraj072709-12hr-corrected.kmz | HYSPLITtraj072709-18hr-corrected.kmz |
| 07/28/09 | HYSPLITtraj072809-00hr-corrected.kmz | HYSPLITtraj072809-06hr-corrected.kmz | HYSPLITtraj072809-12hr-corrected.kmz | HYSPLITtraj072809-18hr-corrected.kmz |
| 07/29/09 | HYSPLITtraj072909-00hr-corrected.kmz | HYSPLITtraj072909-06hr-corrected.kmz | HYSPLITtraj072909-12hr-corrected.kmz | HYSPLITtraj072909-18hr-corrected.kmz |
| 07/30/09 | HYSPLITtraj073009-00hr-corrected.kmz | HYSPLITtraj073009-06hr-corrected.kmz | HYSPLITtraj073009-12hr-corrected.kmz | HYSPLITtraj073009-18hr-corrected.kmz |
| 07/31/09 | HYSPLITtraj073109-00hr-corrected.kmz | HYSPLITtraj073109-06hr-corrected.kmz | HYSPLITtraj073109-12hr-corrected.kmz | HYSPLITtraj073109-18hr-corrected.kmz |
| 08/01/09 | HYSPLITtraj080109-00hr-corrected.kmz | HYSPLITtraj080109-06hr-corrected.kmz | HYSPLITtraj080109-12hr-corrected.kmz | HYSPLITtraj080109-18hr-corrected.kmz |
| 08/02/09 | HYSPLITtraj080209-00hr-corrected.kmz | HYSPLITtraj080209-06hr-corrected.kmz | HYSPLITtraj080209-12hr-corrected.kmz | HYSPLITtraj080209-18hr-corrected.kmz |
| 08/03/09 | HYSPLITtraj080309-00hr-corrected.kmz | HYSPLITtraj080309-06hr-corrected.kmz | HYSPLITtraj080309-12hr-corrected.kmz | HYSPLITtraj080309-18hr-corrected.kmz |
| 08/04/09 | HYSPLITtraj080409-00hr-corrected.kmz | HYSPLITtraj080409-06hr-corrected.kmz | HYSPLITtraj080409-12hr-corrected.kmz | HYSPLITtraj080409-18hr-corrected.kmz |

Table 6 – Downloaded NAAPS/FLAMBE forecasts with its corresponding date.

| NAAPS/MODIS-fire file name | Date of data coverage | HYSPLIT .kml file corresponding date |
|-------------------------------|--------------------------|---|
| 20090706_fire_global.kml | 07/06/09 | 07/12/09 |
| 20090707_fire_global.kml | 07/07/09 | 07/13/09 |
| 20090708_fire_global.kml | 07/08/09 | 07/14/09 |
| 20090709_fire_global.kml | 07/09/09 | 07/15/09 |
| 20090710_fire_global.kml | 07/10/09 | 07/16/09 |
| 20090711_fire_global.kml | 07/11/09 | 07/17/09 |
| 20090712_fire_global.kml | 07/12/09 | 07/18/09 |
| 20090713_fire_global.kml | 07/13/09 | 07/19/09 |
| 20090714_fire_global.kml | 07/14/09 | 07/20/09 |
| 20090715_fire_global.kml | 07/15/09 | 07/21/09 |
| 20090716_fire_global.kml | 07/16/09 | 07/22/09 |
| 20090717_fire_global.kml | 07/17/09 | 07/23/09 |
| 20090718_fire_global.kml | 07/18/09 | 07/24/09 |
| 20090719_fire_global.kml | 07/19/09 | 07/25/09 |
| 20090720_fire_global.kml | 07/20/09 | 07/26/09 |
| 20090721_fire_global.kml | 07/21/09 | 07/27/09 |
| 20090722_fire_global.kml | 07/22/09 | 07/28/09 |
| 20090723_fire_global.kml | 07/23/09 | 07/29/09 |
| 20090724_fire_global.kml | 07/24/09 | 07/30/09 |
| 20090725_fire_global.kml | 07/25/09 | 07/31/09 |
| 20090726_fire_global.kml | 07/26/09 | 08/01/09 |
| 20090727_fire_global.kml | 07/27/09 | 08/02/09 |
| 20090728_fire_global.kml | 07/28/09 | 08/03/09 |
| 20090729_fire_global.kml | 07/29/09 | 08/04/09 |

Table 6 depicts the name of each downloaded forecast, and the name of the file specifies the date to which this forecast corresponds to. NAAPS/FLAMBE forecasts were obtained from the following website:

http://www.nrlmry.navy.mil/aerosol/kml/older_flambe_world_kml/.

Each of the four hundred and forty four backward trajectories generated for this research were backtracked from receptor site to source region. Image prints from Google Earth of the resulting eighty-eight NAAPS/FLAMBE forecast and MODIS fire-location files, superimposed with the HYSPLIT 7-day backward-trajectory files, each with its corresponding five heights, can be observed in the Appendix section of this thesis, spanning from Figure 62 to Figure 149.

In order to facilitate analysis and fulfill the purposes of this research, it was determined which regimen (dust, marine, smoke) was predominant at the source of the HYSPLIT trajectory, according to the NAAPS/FLAMBE forecasts, and compiled into Table 7.

Table 7 shows the regimen for all four hundred and forty backward trajectories, at each 6-hour interval, at 00hrs, 06hrs 12hrs and 18hrs, for all corresponding five heights (at 10m, 100m, 500m, 1000m and 5000m).

The first column of the table depicts the name of the NAAPS/FLAMBE forecast that was paired to the corresponding trajectory. Note that there is a 7-day displacement between the NAAPS/FLAMBE forecast date and the trajectory date. This is due to the fact that the trajectories are 7-day backward trajectories, hence the resultant displacement.

In order to quantitatively assess the results brought forward in Table 7, a series of line plots and percentage plots were generated, corresponding to Figure 15, through Figure 24.

Table 7 (split in two pages) - Predominant regimen (dust, marine, smoke) according to the HYSPLIT source region as backtracked to NAAPS forecasts, depicting the regimen for every six hours, at 00hrs, 06hrs 12hrs and 18hrs, for each corresponding height (at 10m, 100m, 500m, 1000m and 5000m).

| Predicted by NAAPS/FLAMBE for THIS date MODIS kml file for date below | date below BACKTRACKS to date in left column HYSPLIT kml file for date below | HYSPLIT 7-day backward trajectory height in meters (m) | | | | |
|---|---|---|---------|---------|---------|---------|
| | | 10m | 100m | 500m | 1000m | 5000m |
| | | red | blue | green | cyan | magenta |
| 07/06/09 | 7/12/2009 - 00hrs | dust | dust | dust | dust | dust |
| | 7/12/2009 - 06hrs | dust | dust | dust | dust | dust |
| | 7/12/2009 - 12hrs | dust | dust | dust | dust | dust |
| | 7/12/2009 - 18hrs | dust | dust | dust | dust | dust |
| 07/07/09 | 7/13/2009 - 00hrs | dust | dust | dust | dust | dust |
| | 7/13/2009 - 06hrs | dust | dust | dust | dust | dust |
| | 7/13/2009 - 12hrs | dust | dust | dust | dust | dust |
| | 7/13/2009 - 18hrs | dust | dust | dust | dust | dust |
| 07/08/09 | 7/14/2009 - 00hrs | dust | dust | dust | dust | dust |
| | 7/14/2009 - 06hrs | dust | dust | dust | marine | dust |
| | 7/14/2009 - 12hrs | dust | dust | marine | dust | dust |
| | 7/14/2009 - 18hrs | marine | marine | marine | dust | dust |
| 07/09/09 | 7/15/2009 - 00hrs | marine | marine | dust | marine | dust |
| | 7/15/2009 - 06hrs | marine | marine | dust | marine | dust |
| | 7/15/2009 - 12hrs | smoke | smoke | marine | dust | marine |
| | 7/15/2009 - 18hrs | smoke | smoke | marine | dust | dust |
| 07/10/09 | 7/16/2009 - 00hrs | marine | marine | marine | dust | dust |
| | 7/16/2009 - 06hrs | marine | marine | marine | smoke | dust |
| | 7/16/2009 - 12hrs | marine | marine | marine | marine | dust |
| | 7/16/2009 - 18hrs | marine | marine | marine | smoke | dust |
| 07/11/09 | 7/17/2009 - 00hrs | marine | marine | dust | dust | dust |
| | 7/17/2009 - 06hrs | marine | marine | dust | dust | dust |
| | 7/17/2009 - 12hrs | marine | marine | smoke | smoke | dust |
| | 7/17/2009 - 18hrs | marine | smoke | smoke | smoke | dust |
| 07/12/09 | 07/18/09 | NO DATA | NO DATA | NO DATA | NO DATA | NO DATA |
| 07/13/09 | 07/19/09 | NO DATA | NO DATA | NO DATA | NO DATA | NO DATA |
| 07/14/09 | 7/20/2009 - 00hrs | marine | marine | smoke | smoke | dust |
| | 7/20/2009 - 06hrs | marine | marine | smoke | smoke | smoke |
| | 7/20/2009 - 12hrs | marine | marine | smoke | smoke | smoke |
| | 7/20/2009 - 18hrs | marine | marine | dust | dust | smoke |
| 07/15/09 | 7/21/2009 - 00hrs | marine | marine | marine | marine | smoke |
| | 7/21/2009 - 06hrs | marine | marine | marine | smoke | smoke |
| | 7/21/2009 - 12hrs | marine | marine | marine | smoke | marine |
| | 7/21/2009 - 18hrs | marine | marine | marine | smoke | marine |
| 07/16/09 | 7/22/2009 - 00hrs | marine | marine | marine | marine | smoke |
| | 7/22/2009 - 06hrs | marine | smoke | marine | smoke | marine |
| | 7/22/2009 - 12hrs | marine | marine | marine | smoke | smoke |
| | 7/22/2009 - 18hrs | marine | marine | marine | smoke | smoke |
| 07/17/09 | 7/23/2009 - 00hrs | smoke | marine | smoke | smoke | smoke |
| | 7/23/2009 - 06hrs | smoke | smoke | smoke | smoke | dust |
| | 7/23/2009 - 12hrs | marine | smoke | smoke | smoke | dust |
| | 7/23/2009 - 18hrs | marine | marine | smoke | dust | dust |
| 07/18/09 | 7/24/2009 - 00hrs | marine | marine | smoke | smoke | dust |
| | 7/24/2009 - 06hrs | smoke | marine | smoke | smoke | dust |
| | 7/24/2009 - 12hrs | smoke | marine | marine | dust | dust |
| | 7/24/2009 - 18hrs | dust | marine | dust | dust | dust |

Table 7 (CONTINUED from previous page) - Predominant regimen (dust, marine, smoke) according to the HYSPLIT source region as backtracked to NAAPS forecasts, depicting the regimen for every six hours, at 00hrs, 06hrs 12hrs and 18hrs, for each corresponding height (at 10m, 100m, 500m, 1000m and 5000m).

| Predicted by NAAPS/FLAMBE for THIS date MODIS kml file for date below | date below BACKTRACKS to date in left column HYSPLIT kml file for date below | HYSPLIT 7-day backward trajectory height in meters (m) | | | | |
|---|---|---|--------|--------|-------|---------|
| | | 10m | 100m | 500m | 1000m | 5000m |
| | | red | blue | green | cyan | magenta |
| 07/19/09 | 7/25/2009 - 00hrs | dust | dust | dust | dust | dust |
| | 7/25/2009 - 06hrs | dust | dust | dust | dust | dust |
| | 7/25/2009 - 12hrs | marine | marine | dust | dust | dust |
| | 7/25/2009 - 18hrs | marine | marine | dust | dust | dust |
| 07/20/09 | 7/26/2009 - 00hrs | marine | marine | dust | dust | dust |
| | 7/26/2009 - 06hrs | marine | marine | marine | dust | dust |
| | 7/26/2009 - 12hrs | marine | marine | marine | dust | dust |
| | 7/26/2009 - 18hrs | marine | marine | marine | dust | dust |
| 07/21/09 | 7/27/2009 - 00hrs | marine | marine | marine | dust | dust |
| | 7/27/2009 - 06hrs | marine | marine | marine | dust | dust |
| | 7/27/2009 - 12hrs | marine | marine | marine | dust | dust |
| | 7/27/2009 - 18hrs | marine | marine | marine | dust | dust |
| 07/22/09 | 7/28/2009 - 00hrs | marine | marine | dust | dust | dust |
| | 7/28/2009 - 06hrs | marine | marine | marine | dust | dust |
| | 7/28/2009 - 12hrs | marine | marine | marine | dust | dust |
| | 7/28/2009 - 18hrs | marine | marine | dust | dust | smoke |
| 07/23/09 | 7/29/2009 - 00hrs | marine | marine | marine | dust | dust |
| | 7/29/2009 - 06hrs | marine | marine | marine | dust | dust |
| | 7/29/2009 - 12hrs | marine | marine | marine | dust | dust |
| | 7/29/2009 - 18hrs | marine | marine | marine | dust | dust |
| 07/24/09 | 7/30/2009 - 00hrs | marine | marine | marine | dust | dust |
| | 7/30/2009 - 06hrs | marine | marine | marine | dust | dust |
| | 7/30/2009 - 12hrs | dust | marine | marine | dust | dust |
| | 7/30/2009 - 18hrs | dust | dust | marine | dust | dust |
| 07/25/09 | 7/31/2009 - 00hrs | dust | dust | dust | dust | dust |
| | 7/31/2009 - 06hrs | dust | dust | dust | dust | dust |
| | 7/31/2009 - 12hrs | dust | dust | dust | dust | dust |
| | 7/31/2009 - 18hrs | dust | dust | dust | dust | dust |
| 07/26/09 | 8/1/2009 - 00hrs | dust | marine | dust | smoke | dust |
| | 8/1/2009 - 06hrs | dust | marine | dust | dust | dust |
| | 8/1/2009 - 12hrs | marine | marine | dust | dust | dust |
| | 8/1/2009 - 18hrs | marine | marine | dust | dust | dust |
| 07/27/09 | 8/2/2009 - 00hrs | marine | marine | marine | dust | dust |
| | 8/2/2009 - 06hrs | marine | marine | marine | dust | dust |
| | 8/2/2009 - 12hrs | marine | marine | marine | dust | dust |
| | 8/2/2009 - 18hrs | marine | marine | dust | dust | dust |
| 07/28/09 | 8/3/2009 - 00hrs | dust | dust | marine | dust | dust |
| | 8/3/2009 - 06hrs | dust | dust | dust | dust | dust |
| | 8/3/2009 - 12hrs | dust | dust | dust | dust | dust |
| | 8/3/2009 - 18hrs | dust | dust | dust | dust | dust |
| 07/29/09 | 8/4/2009 - 00hrs | dust | dust | dust | dust | marine |
| | 8/4/2009 - 06hrs | dust | dust | marine | dust | marine |
| | 8/4/2009 - 12hrs | dust | dust | marine | dust | marine |
| | 8/4/2009 - 18hrs | dust | dust | dust | dust | marine |

The line plots allowed this research the ability of representing in a visual manner the evolution of the air mass types over the duration of the AEROSE V campaign (Table 9). By assigning a specific numerical value to each event type (Table 8), the transitions from one event type to the next became apparent.

Table 8 - Corresponding Numerical Values Assigned to Event Type

| Event Type | Numerical Value |
|------------|-----------------|
| No Data | 0 |
| Dust | 1 |
| Marine | 2 |
| Smoke | 3 |

This methodology also revealed in a graphic manner which type of air mass tended to dominate at each elevation. In order to validate the findings from the line plots in a quantifiable manner, percentage plots were generated for each elevation (Table 9).

Table 9 - 6-hr interval HYSPLIT source-region plots

| 6-hr interval HYSPLIT source-region plots | | |
|---|------------------|-----------|
| Line Plots | Percentage Plots | Elevation |
| Figure 15 | Figure 16 | 10m |
| Figure 17 | Figure 18 | 100m |
| Figure 19 | Figure 20 | 500m |
| Figure 21 | Figure 22 | 1000m |
| Figure 23 | Figure 24 | 5000m |

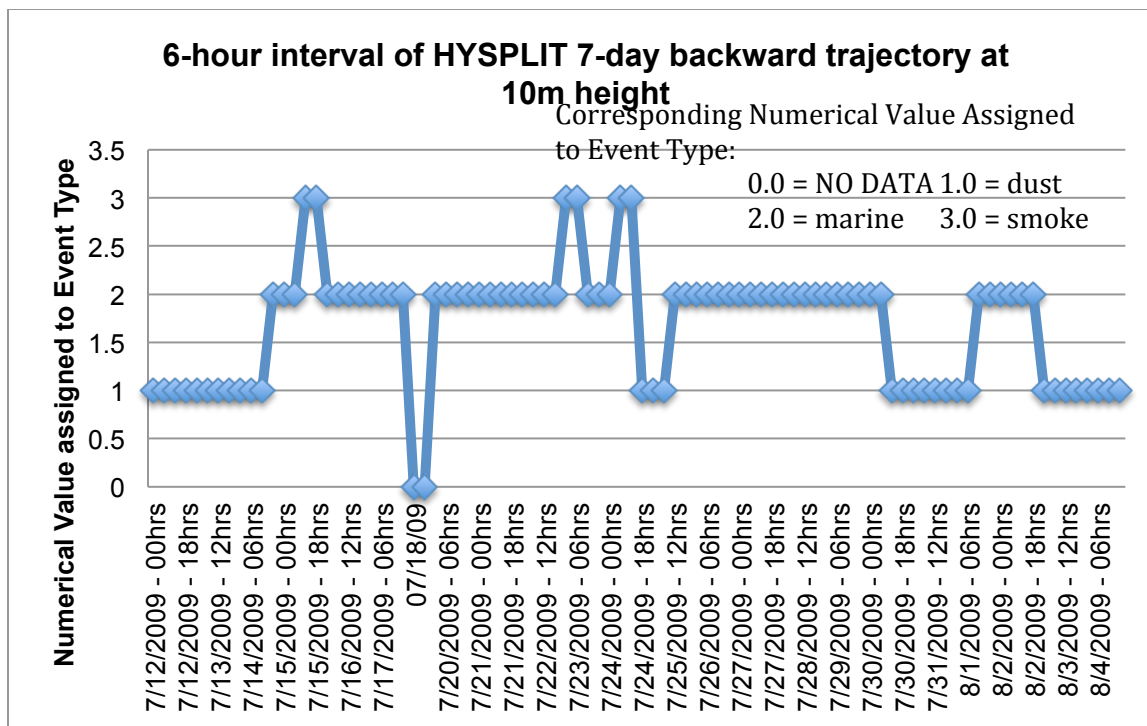


Figure (15) – Evolution over time of air mass types at HYSPLIT trajectory's source at 10m height.

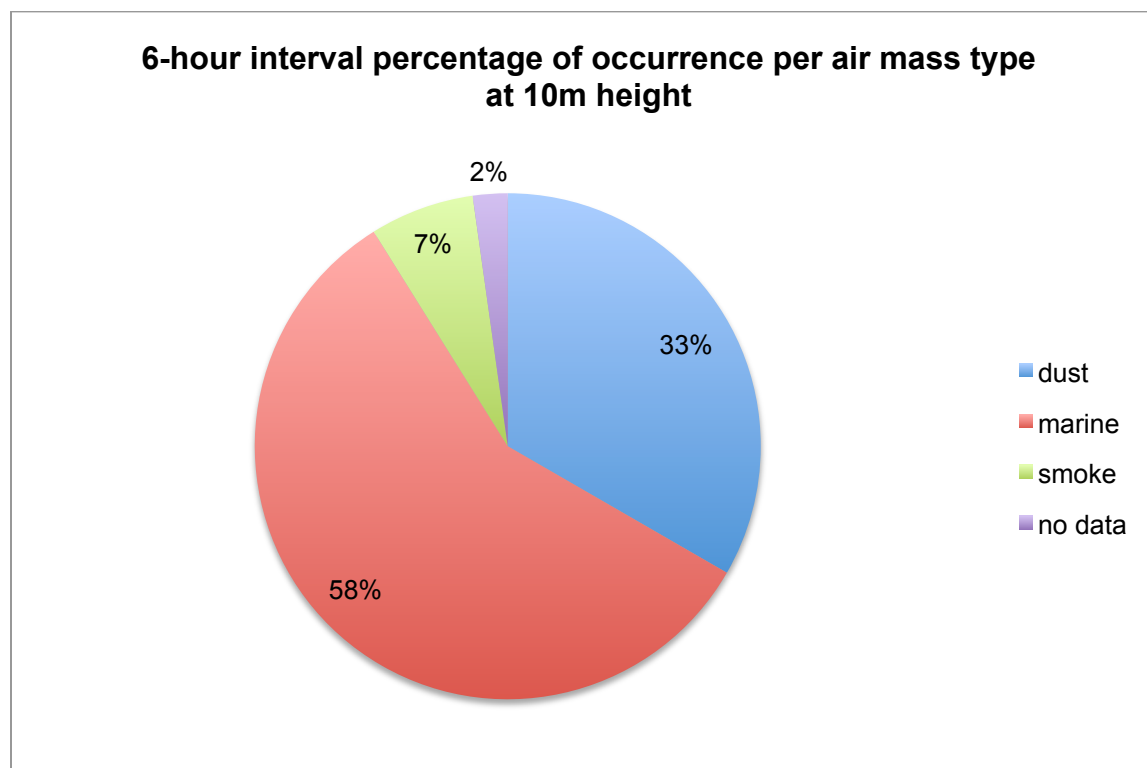


Figure (16) – Percentage of air mass occurrence for 6-hr interval HYSPLIT source-region plots for 10m elevation.

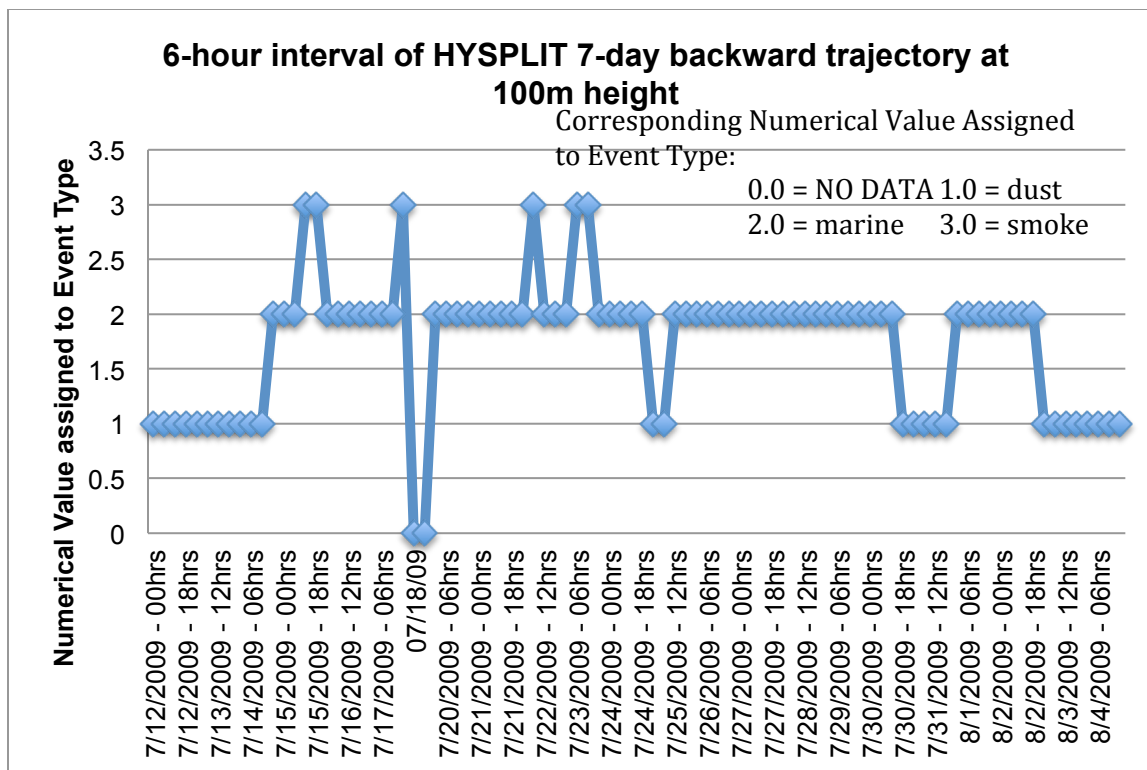


Figure (17) - Evolution over time of air mass types at HYSPLIT trajectory's source at 100m height.

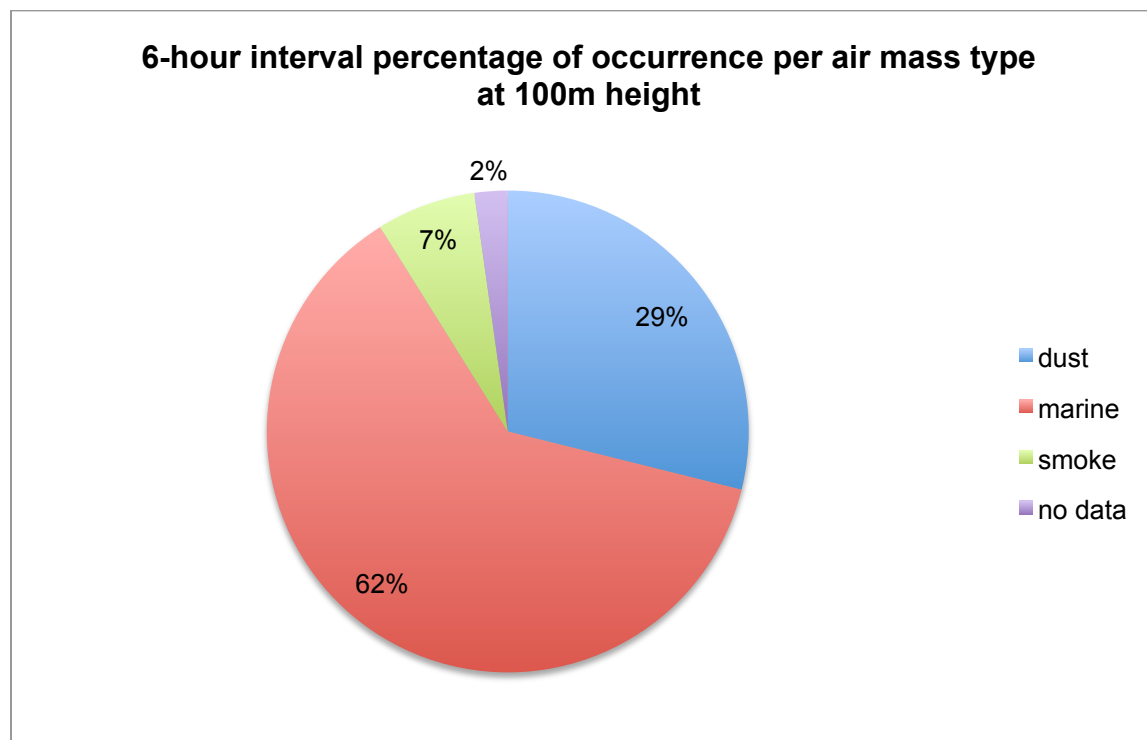


Figure (18) – Percentage of air mass occurrence for 6-hr interval HYSPLIT source-region plots for 100m elevation.

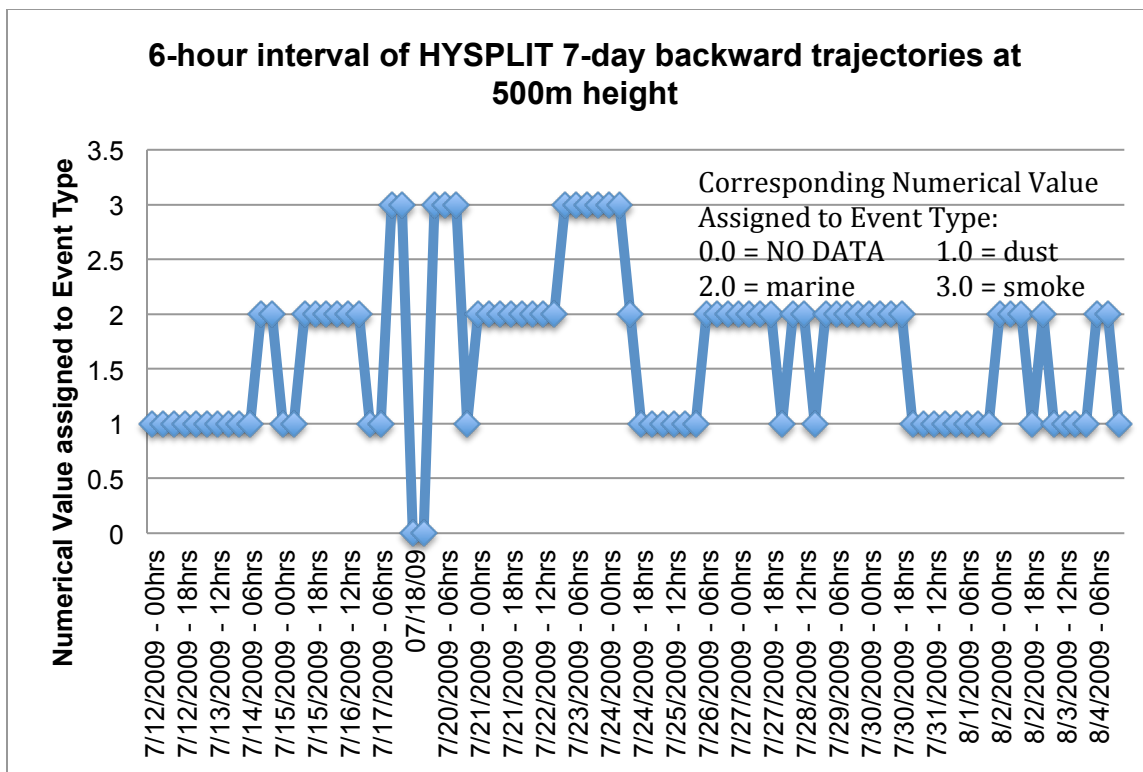


Figure (19) – Evolution over time of air mass types at HYSPLIT trajectory's source at 500m height.

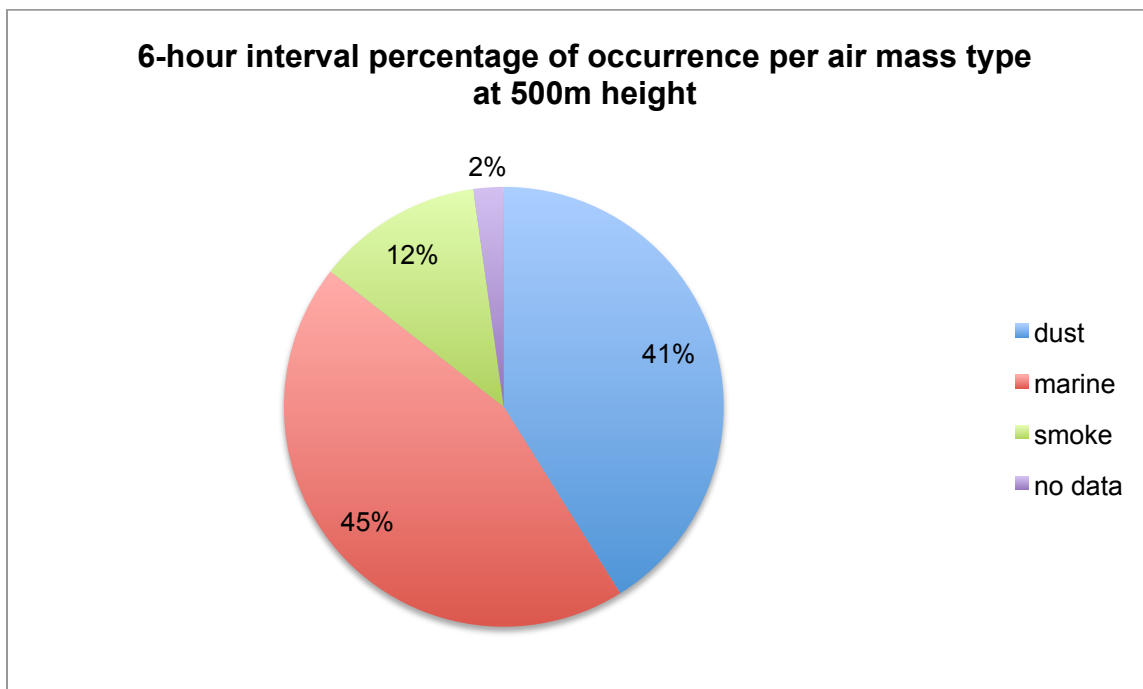


Figure (20) – Percentage of air mass occurrence for 6-hr interval HYSPLIT source-region plots for 500m elevation.

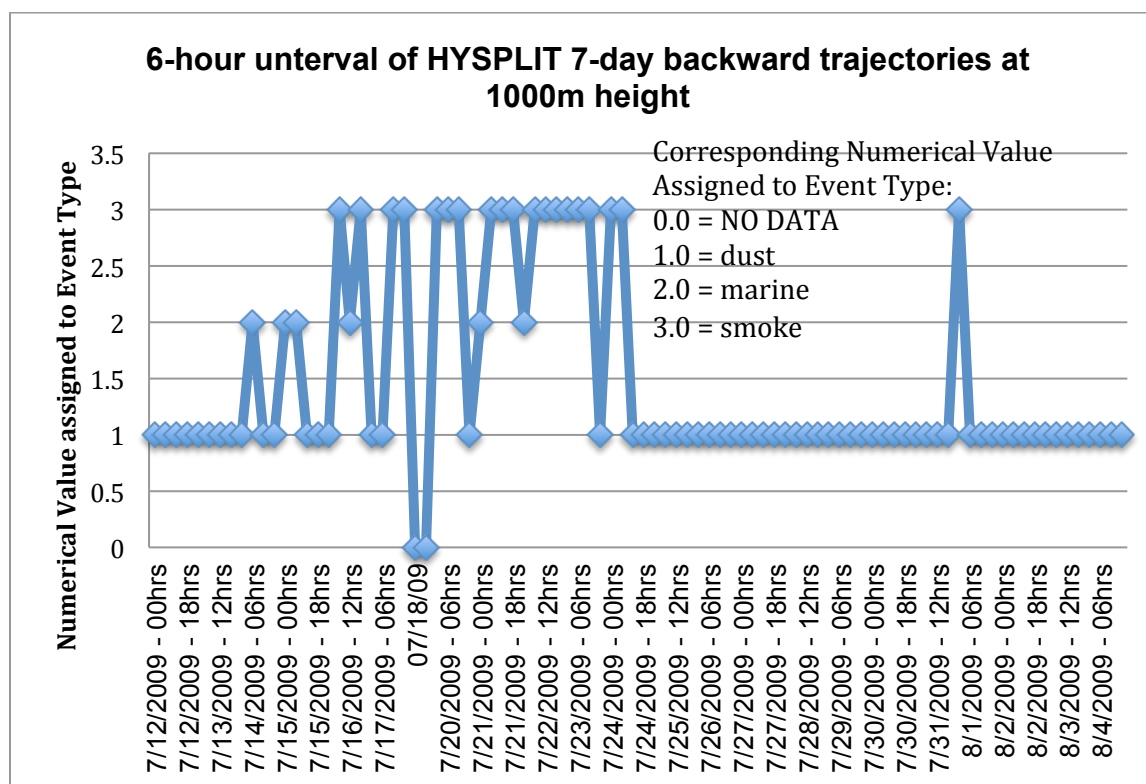


Figure (21) - Evolution over time of air mass types at HYSPLIT trajectory's source at 1000m height.

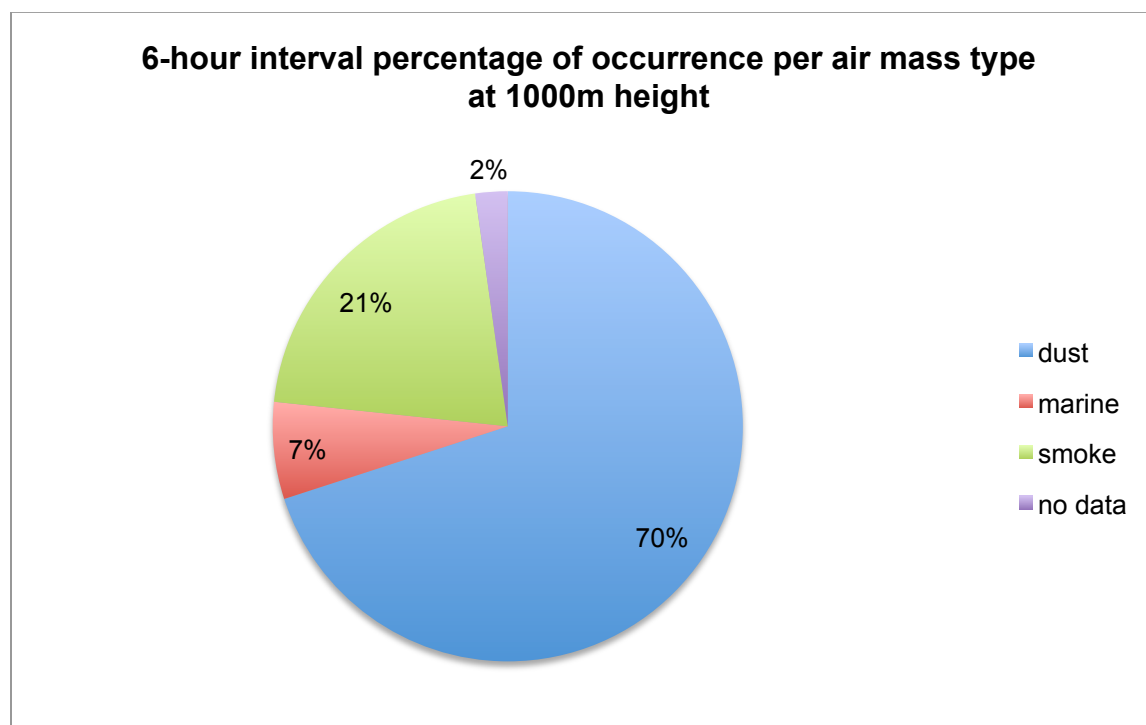


Figure (22) – Percentage of air mass occurrence for 6-hr interval HYSPLIT source-region plots for 1000m elevation.

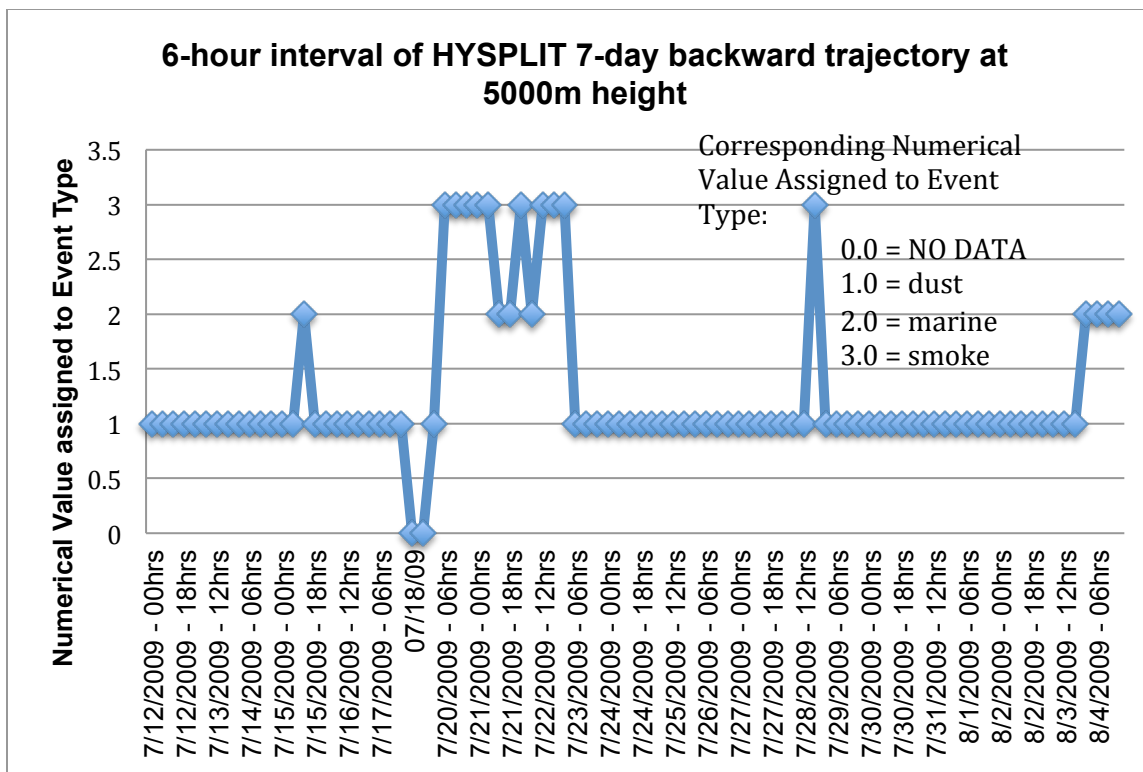


Figure (23) - Evolution over time of air mass types at HYSPLIT trajectory's source at 5000m height.

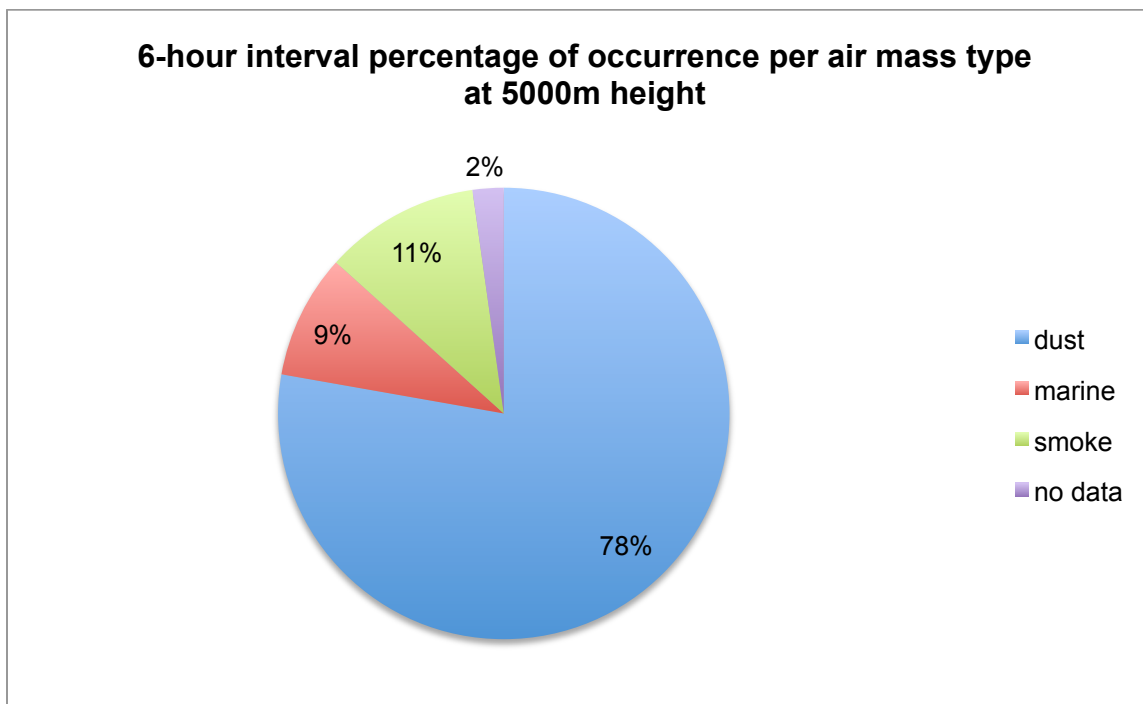


Figure (24) – Percentage of air mass occurrence for 6-hr interval HYSPLIT source-region plots for 5000m elevation.

In contrast to Table 7, Table 10 depicts the daily averaged predominant regimen (dust, marine, smoke) according to the HYSPLIT source region as backtracked to NAAPS forecasts, for each corresponding height (at 10m, 100m, 500m, 1000m and 5000m). There were a total of 22 days with available data, and the air mass types were established at five different heights, for a total of 110 resulting daily averaged air mass types.

Table 10 - Daily averaged predominant regimen (dust, marine, smoke) according to the HYSPLIT source region as backtracked to NAAPS forecasts, for each corresponding height (at 10m, 100m, 500m, 1000m and 5000m).

| predicted by NAAPS /FLAMBE for THIS date MODIS kml file for date below | date below BACKTRACKS to date in left column HYSPLIT kml file for date below | HYSPLIT 7-day backward trajectory height in meters (m) | | | | |
|--|---|--|--------------|-------------|-------------|---------|
| | | 10m | 100m | 500m | 1000m | 5000m |
| | | red | blue | green | cyan | magenta |
| 07/06/09 | 07/12/09 | dust | dust | dust | dust | dust |
| 07/07/09 | 07/13/09 | dust | dust | dust | dust | dust |
| 07/08/09 | 07/14/09 | dust | dust | dust/marine | dust | dust |
| 07/09/09 | 07/15/09 | marine/smoke | marine/smoke | dust/marine | dust/marine | dust |
| 07/10/09 | 07/16/09 | marine | marine | marine | smoke | dust |
| 07/11/09 | 07/17/09 | marine | marine | dust/smoke | dust/smoke | dust |
| 07/12/09 | 07/18/09 | no data | no data | no data | no data | no data |
| 07/13/09 | 07/19/09 | no data | no data | no data | no data | no data |
| 07/14/09 | 07/20/09 | marine | marine | smoke | smoke | smoke |
| 07/15/09 | 07/21/09 | marine | marine | marine | smoke | dust |
| 07/16/09 | 07/22/09 | marine | marine | marine | smoke | smoke |
| 07/17/09 | 07/23/09 | marine/smoke | marine/smoke | smoke | smoke | dust |
| 07/18/09 | 07/24/09 | smoke | marine | smoke | dust/smoke | dust |
| 07/19/09 | 07/25/09 | dust/marine | dust/marine | dust | dust | dust |
| 07/20/09 | 07/26/09 | marine | marine | marine | dust | dust |
| 07/21/09 | 07/27/09 | marine | marine | marine | dust | dust |
| 07/22/09 | 07/28/09 | marine | marine | dust/marine | dust | dust |
| 07/23/09 | 07/29/09 | marine | marine | marine | dust | dust |
| 07/24/09 | 07/30/09 | dust/marine | marine | marine | dust | dust |
| 07/25/09 | 07/31/09 | dust | dust | dust | dust | dust |
| 07/26/09 | 08/01/09 | dust/marine | marine | dust | dust | dust |
| 07/27/09 | 08/02/09 | marine | marine | marine | dust | dust |
| 07/28/09 | 08/03/09 | dust | dust | dust | dust | dust |
| 07/29/09 | 08/04/09 | dust | dust | dust/marine | dust | marine |

To contrast the findings established from Figures 15 through Figure 24, where the regimen type was analyzed for each 6-hr interval (for a total of 440 different air mass types); the daily averages for the regimen types computed in Table 10 were plotted in a similar manner. The main purpose was to determine and quantify the possible differences between the two methodologies, therefore a series of clustered-column plots and percentage plots were generated, corresponding to Figure 25, through Figure 34.

As it was the case with the 6-hr interval findings, the results from the daily averaged HYSPLIT source-region clustered-column plots were validated in a quantifiable manner by also generating percentage plots for each elevation.

In Table 11 there is the breakdown of which figure corresponds to each plotting methodology, as well as the elevation.

Table 11 - Daily averaged HYSPLIT source-region plots

| Daily averaged HYSPLIT source-region plots | | |
|--|------------------|-----------|
| Clustered-Column Plots | Percentage Plots | Elevation |
| Figure 25 | Figure 26 | 10m |
| Figure 27 | Figure 28 | 100m |
| Figure 29 | Figure 30 | 500m |
| Figure 31 | Figure 32 | 1000m |
| Figure 33 | Figure 34 | 5000m |

The clustered-column plots were chosen to directly contrast the line plots, since this method also proved to be advantageous by affording a visual representation of the evolution of the air mass types throughout the AEROSE V campaign. Specific numerical values were also assigned to each event type in order to assist in the graphical representation of the transitions from one regimen to the next. The numerical values for each air mass type are depicted in Table 12.

Due to the fact that these were daily averages, in some instances there was no dominant regimen but instead a split between two air mass types. For these situations, additional categories were created to encompass all of the possible variations.

Table 12 - Corresponding Numerical Values Assigned to Event Type

| Event Type | Numerical Value |
|--------------|-----------------|
| No Data | 0 |
| Dust | 1 |
| Marine | 2 |
| Smoke | 3 |
| Dust/Marine | 4 |
| Marine/Smoke | 5 |
| Dust/Smoke | 6 |

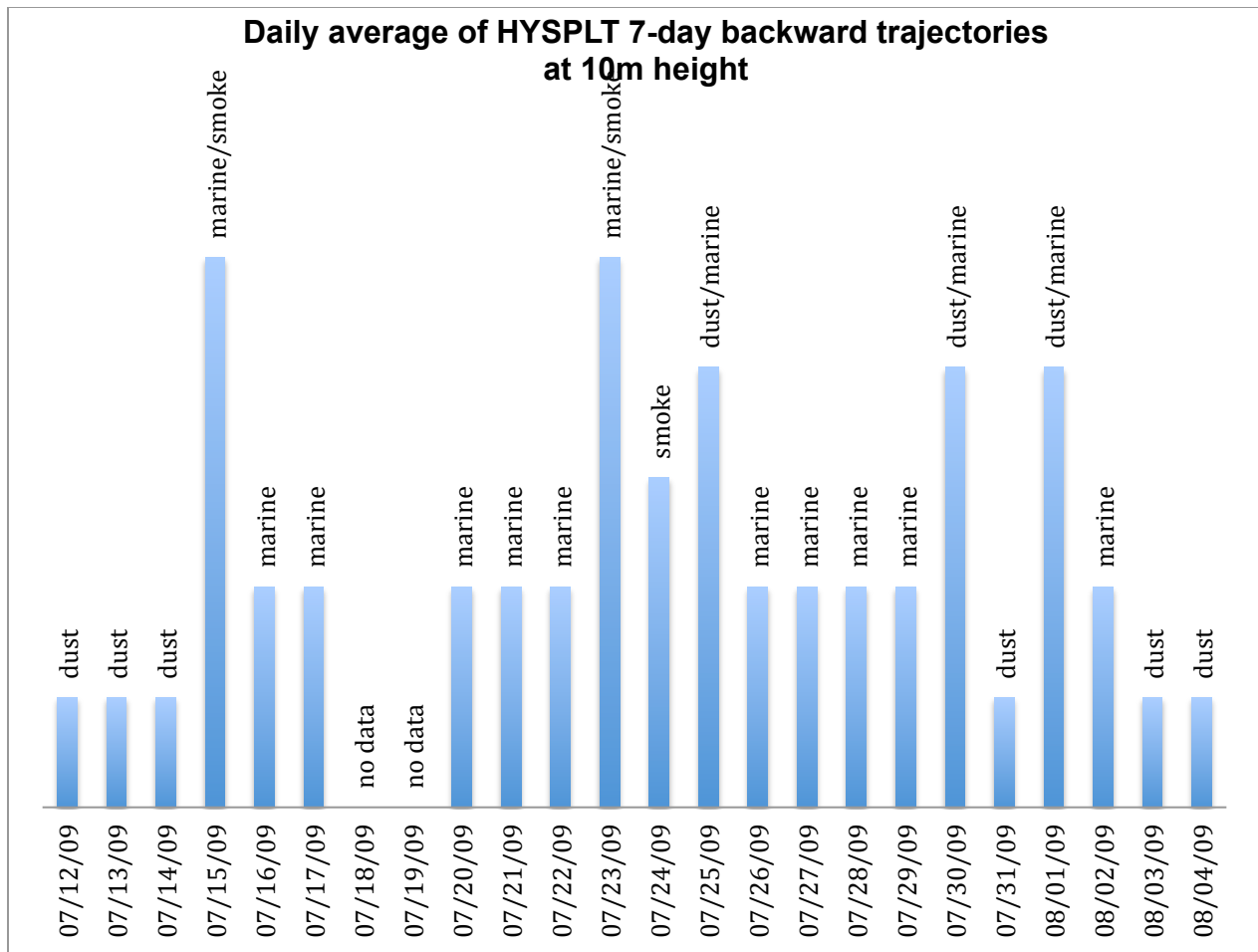


Figure (25) – Daily averaged evolution over time of air mass types at HYSPLIT trajectory's source at 10m height.

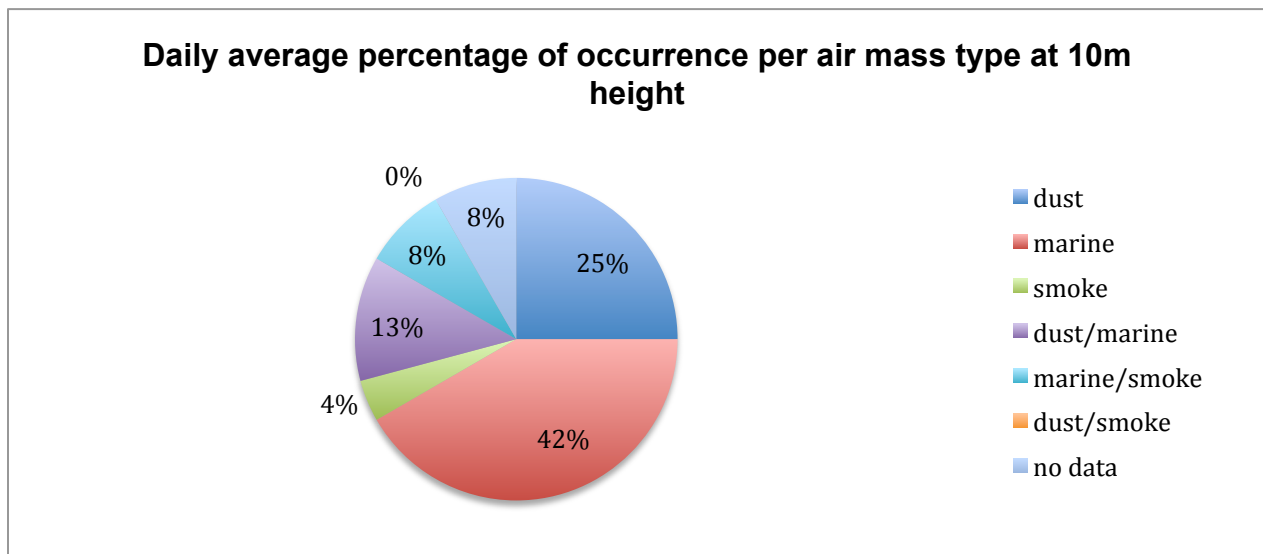


Figure (26) – Percentage of air mass occurrence for daily averaged HYSPLIT source-region plots for 10m elevation.

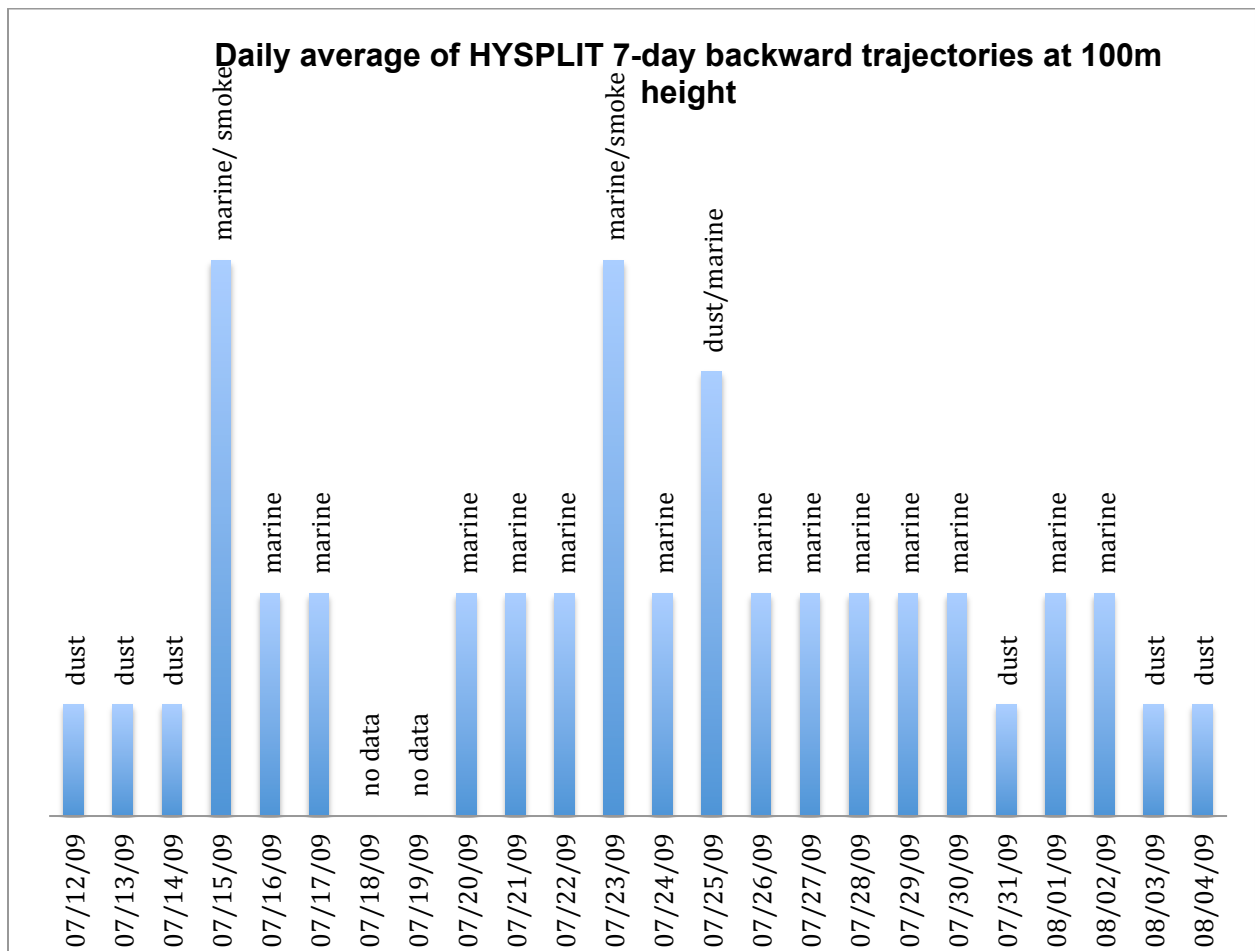


Figure (27) – Daily averaged evolution over time of air mass types at HYSPLIT trajectory's source at 100m height.

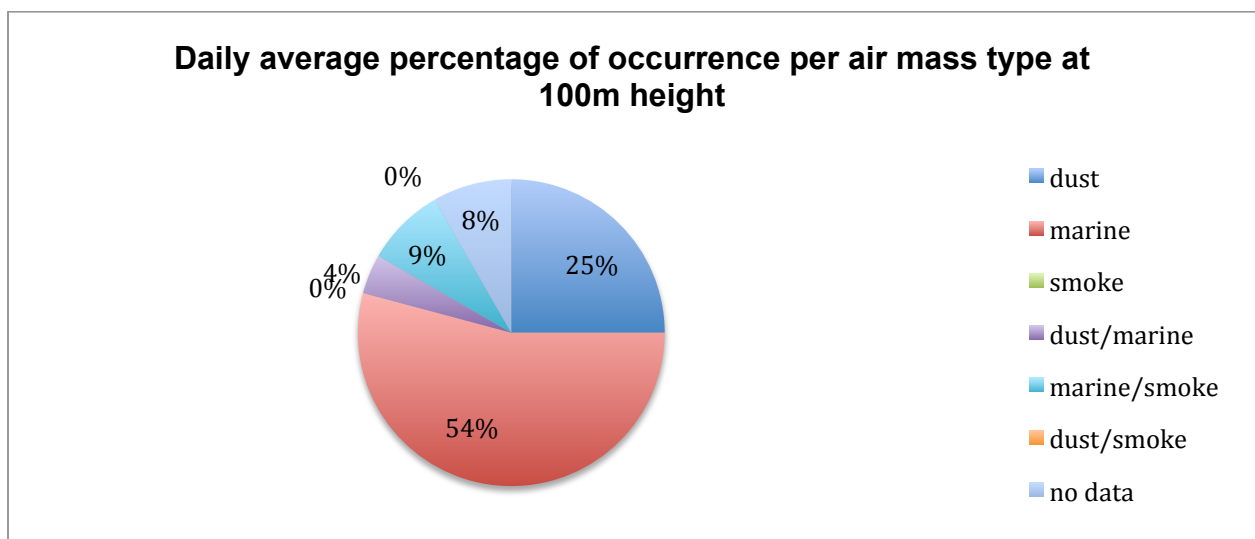


Figure (28) – Percentage of air mass occurrence for daily averaged HYSPLIT source-region plots for 100m elevation.

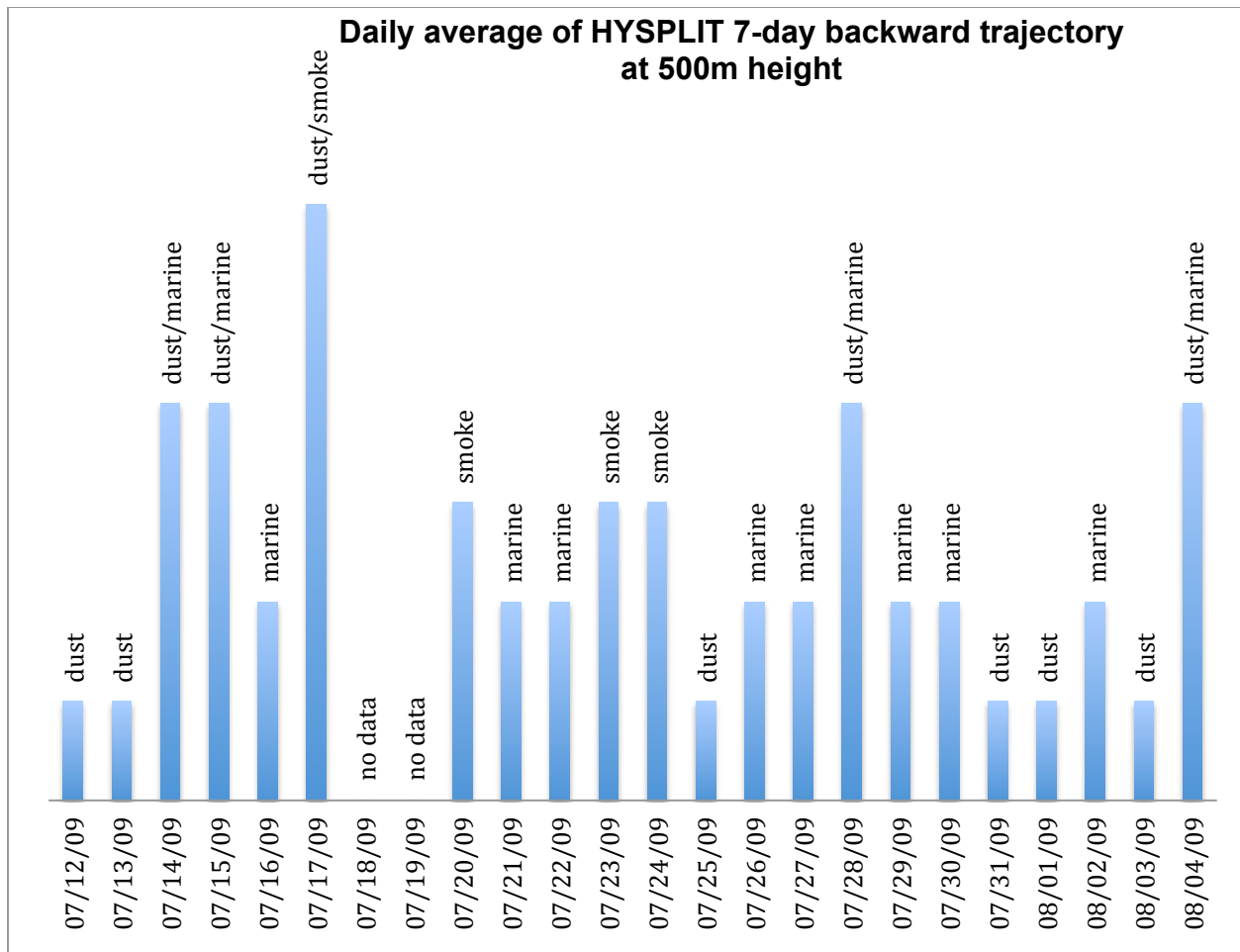


Figure (29) – Daily averaged evolution over time of air mass types at HYSPLIT trajectory's source at 500m height.

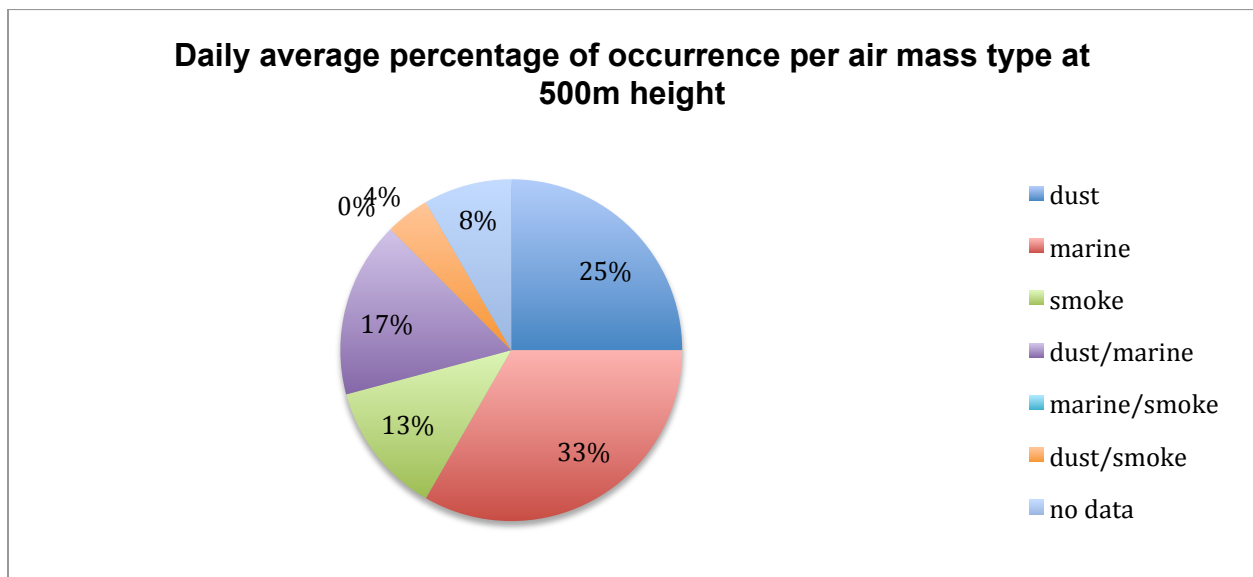


Figure (30) – Percentage of air mass occurrence for daily averaged HYSPLIT source-region plots for 500m elevation.

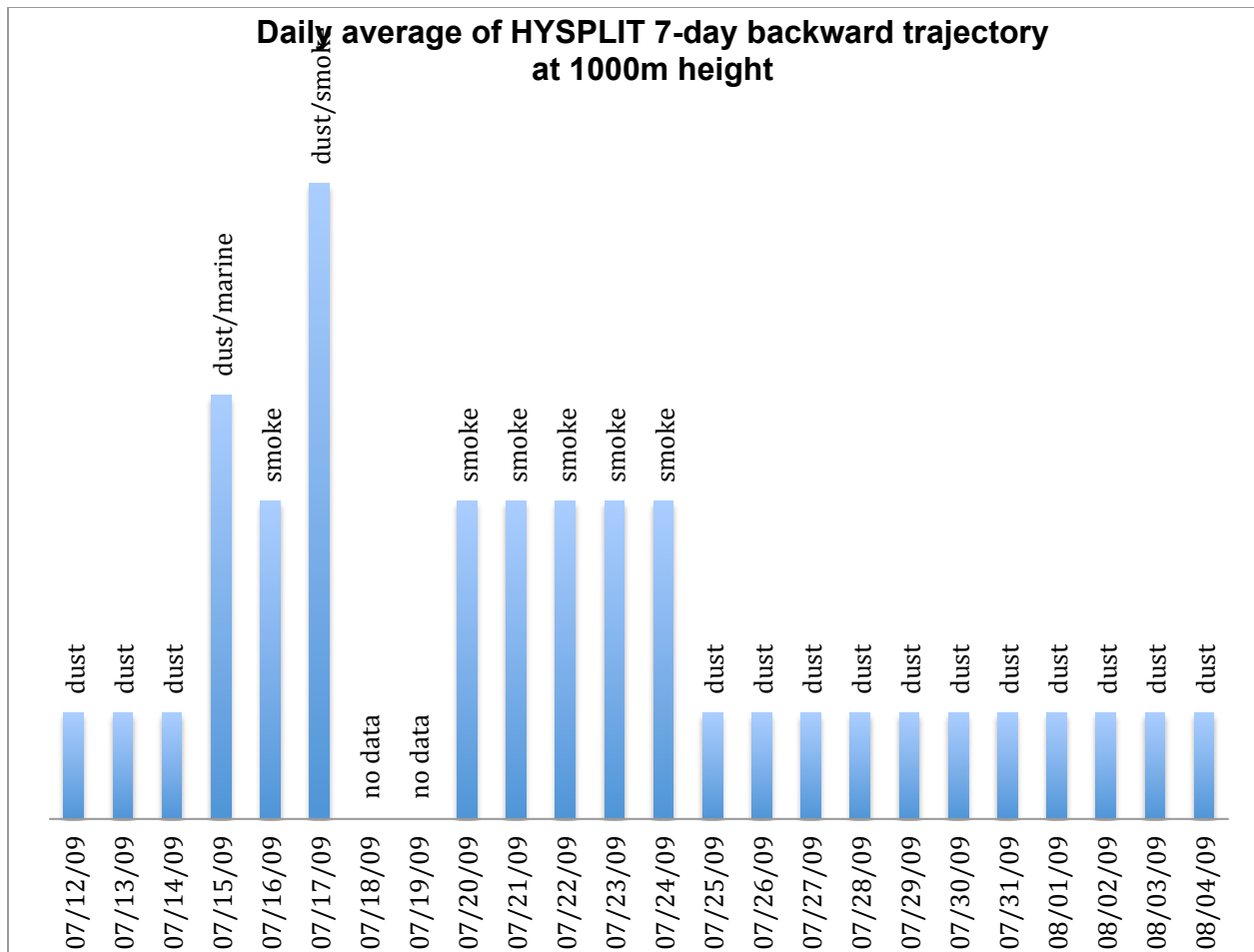


Figure (31) – Daily averaged evolution over time of air mass types at HYSPLIT trajectory's source at 1000m height.

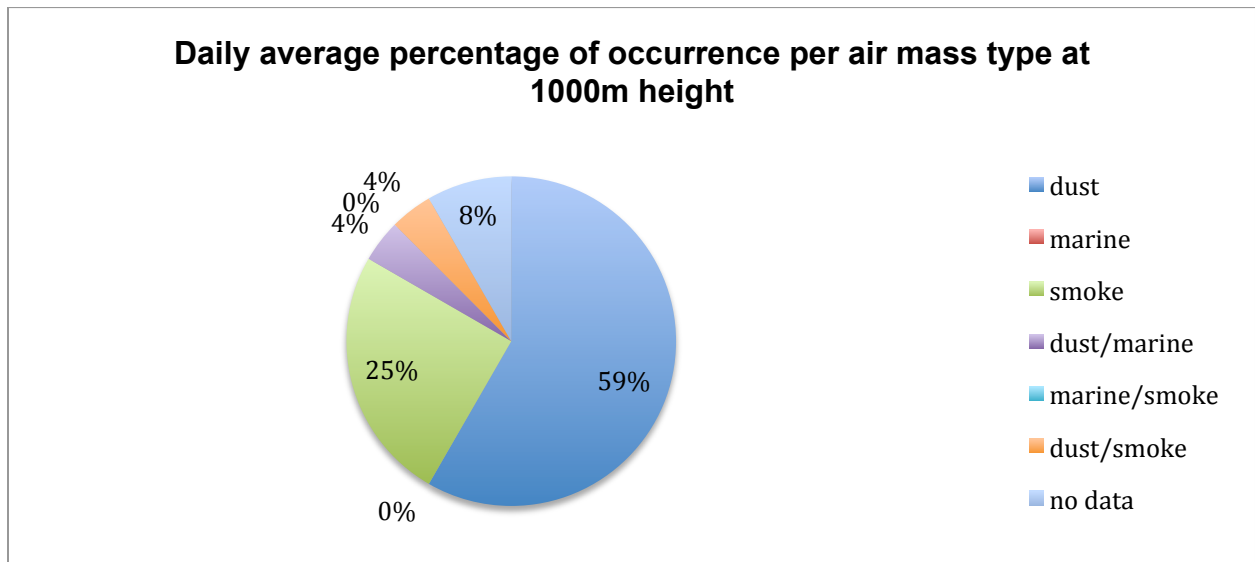


Figure (32) – Percentage of air mass occurrence for daily averaged HYSPLIT source-region plots for 1000m elevation.

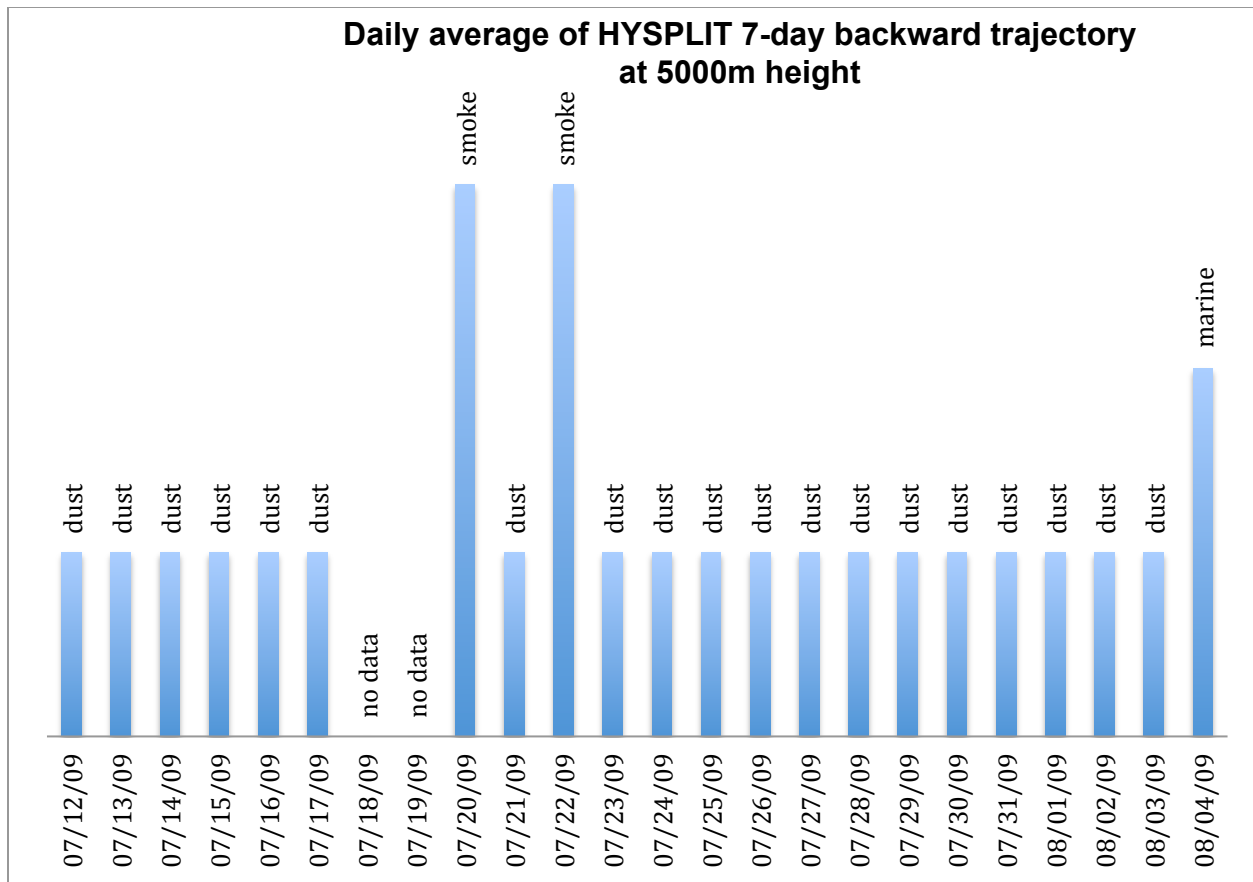


Figure (33) – Daily averaged evolution over time of air mass types at HYSPLIT trajectory's source at 5000m height.

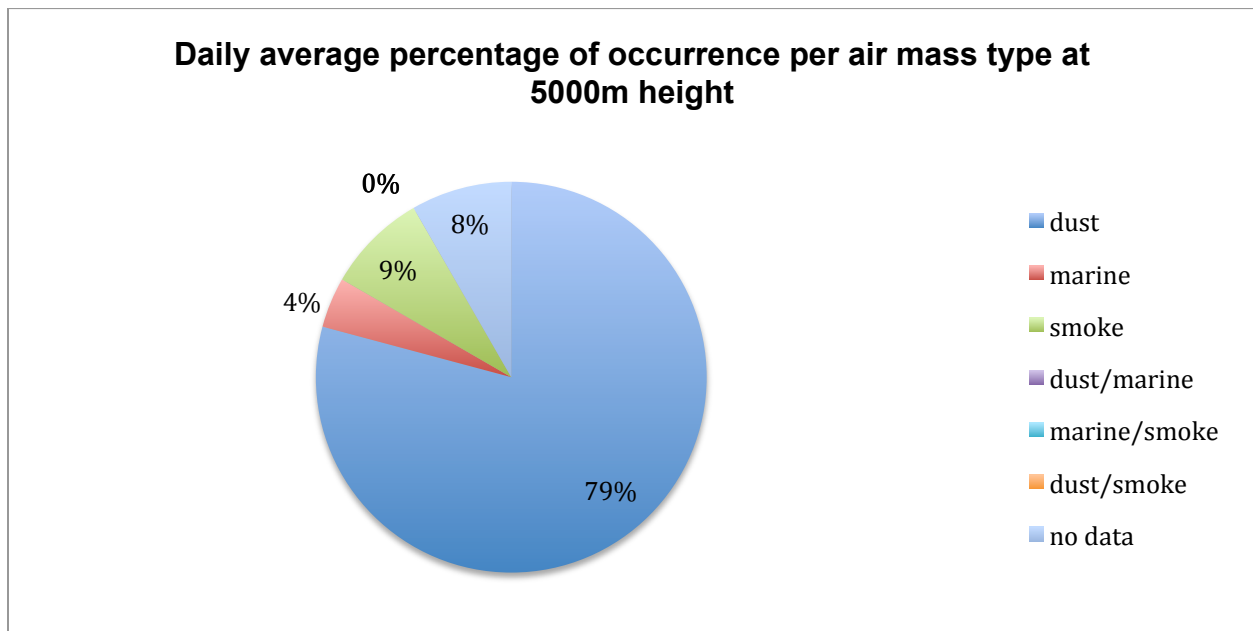


Figure (34) – Percentage of air mass occurrence for daily averaged HYSPLIT source-region plots for 5000m elevation.

As it was mentioned earlier, the reasoning behind analyzing air mass type regimes by two different methodologies, the 6-hr interval being the first (for a total of 440 different air mass types analyzed); and the daily averaged regimen types (for a total of 110 air mass types) was to contrast the findings to determine and quantify the possible differences between the two methodologies.

To establish the difference between the 6-hr interval findings and the daily averaged findings, the resulting percentages of air mass type occurrences from each method were plotted against each other, per each elevation. The results are found in Figure 35 through Figure 39 as depicted in Table 13.

Table 13 - Corresponding Figure for Percentage Comparisons Plots of 6-hour readings vs. Daily averaged values

| Percentage Comparison Plots of 6-hour readings vs. Daily averaged values | |
|--|-----------|
| Corresponding Figure | Elevation |
| Figure 35 | 10m |
| Figure 36 | 100m |
| Figure 37 | 500m |
| Figure 38 | 1000m |
| Figure 39 | 5000m |

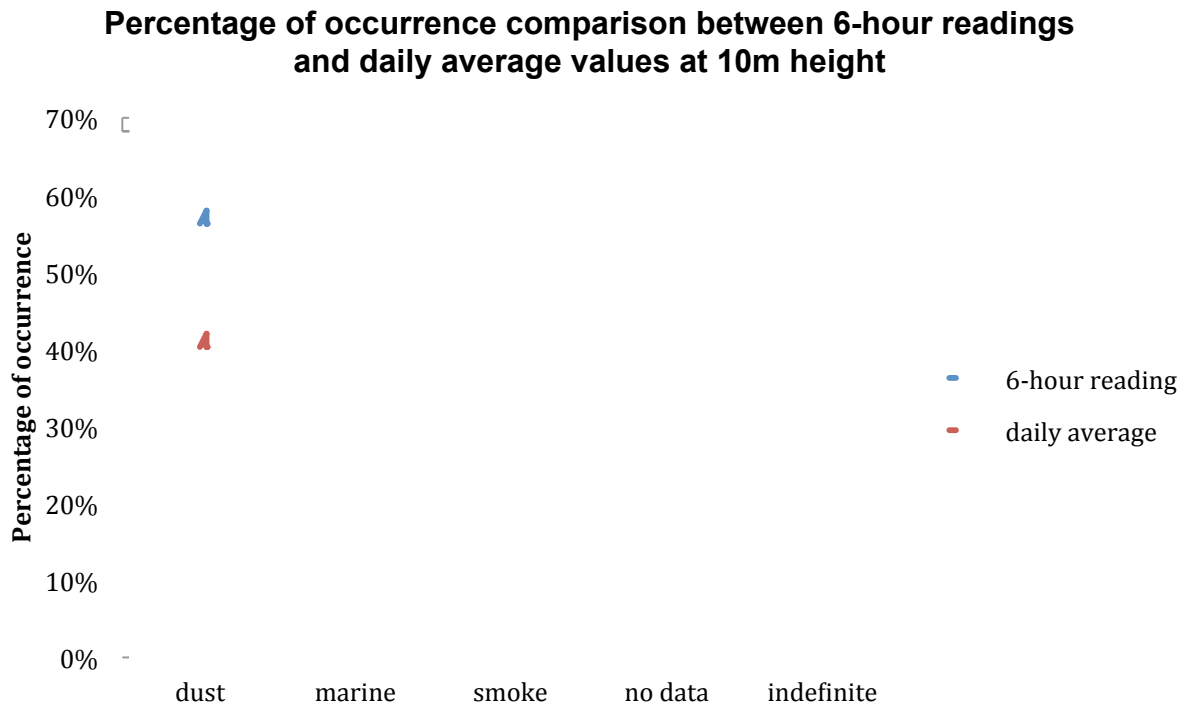


Figure (35) – 6hr-interval vs. daily averaged percentages of occurrence per regimen type at 10m

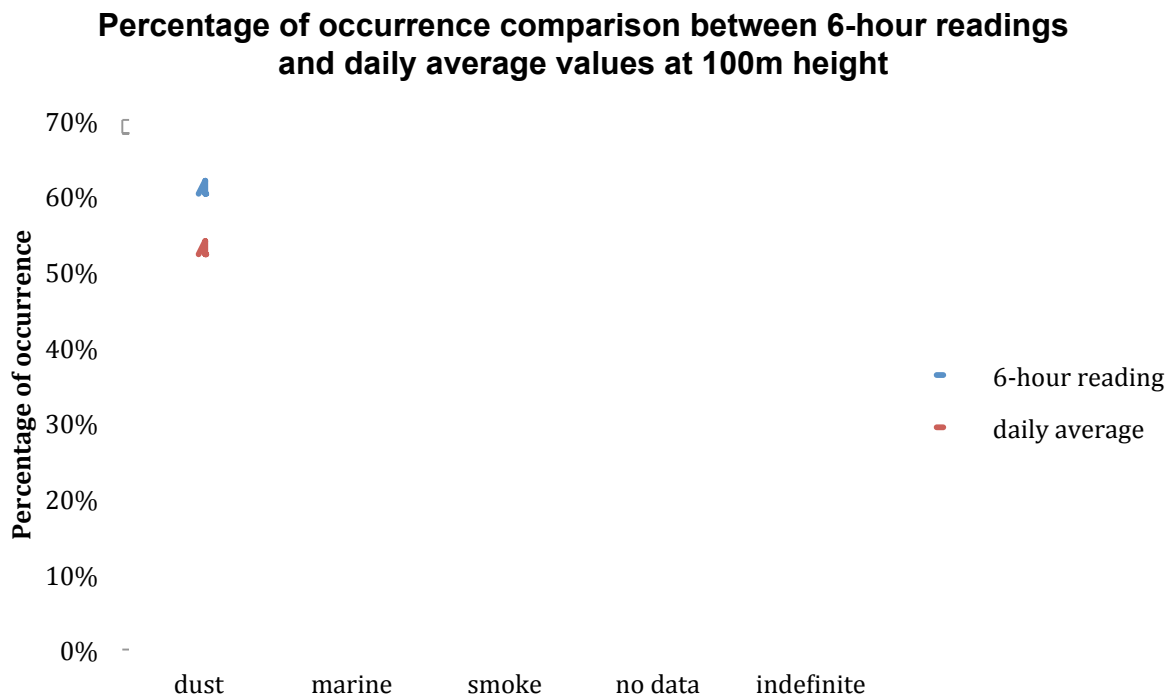


Figure (36) — 6hr-interval vs. daily averaged percentages of occurrence per regimen type at 100m

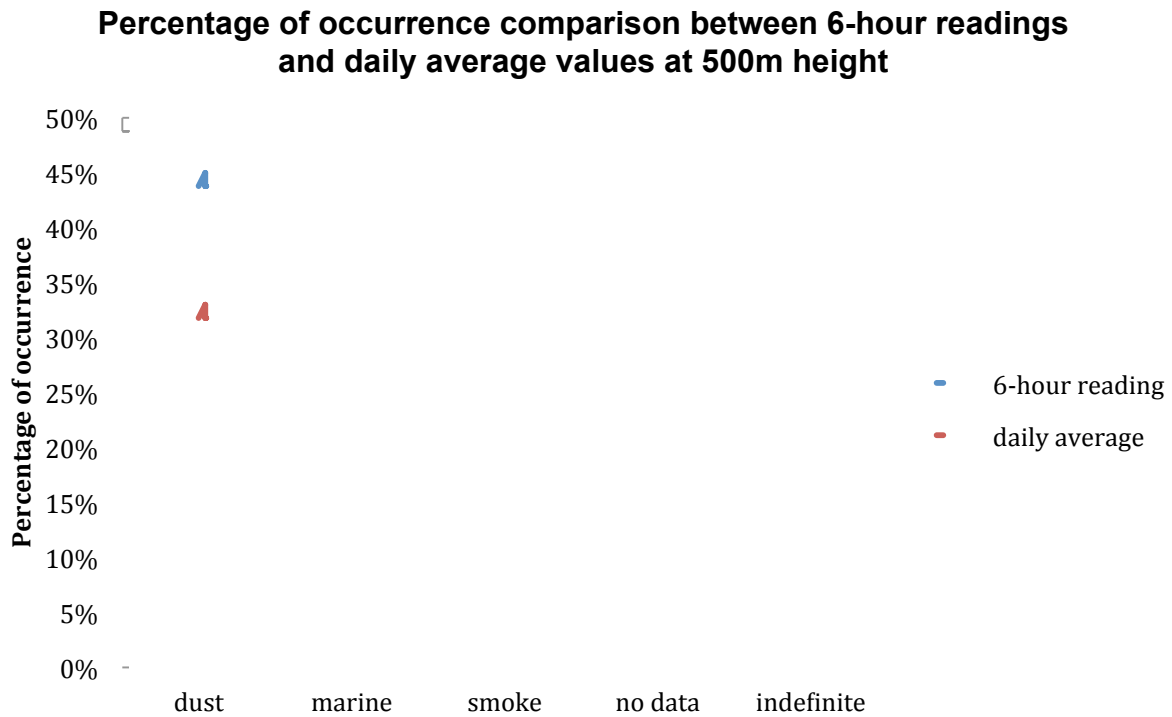


Figure (37) — 6hr-interval vs. daily averaged percentages of occurrence per regimen type at 500m

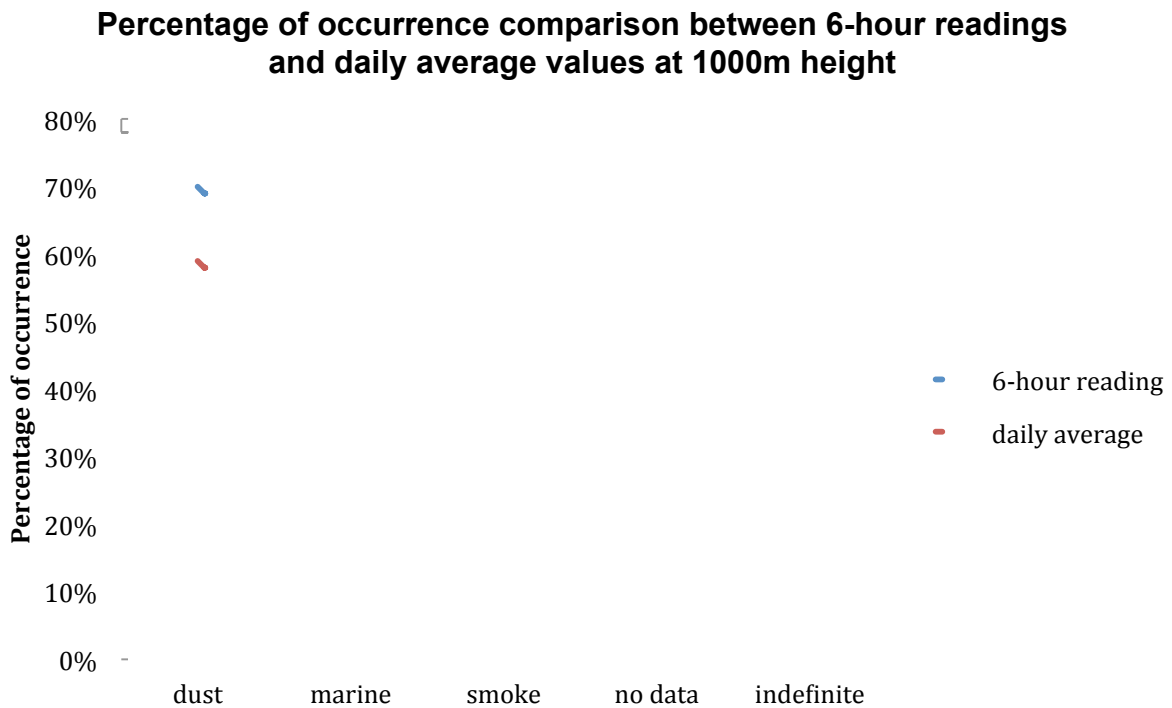


Figure (38) — 6hr-interval vs. daily averaged percentages of occurrence per regimen type at 1000m

□

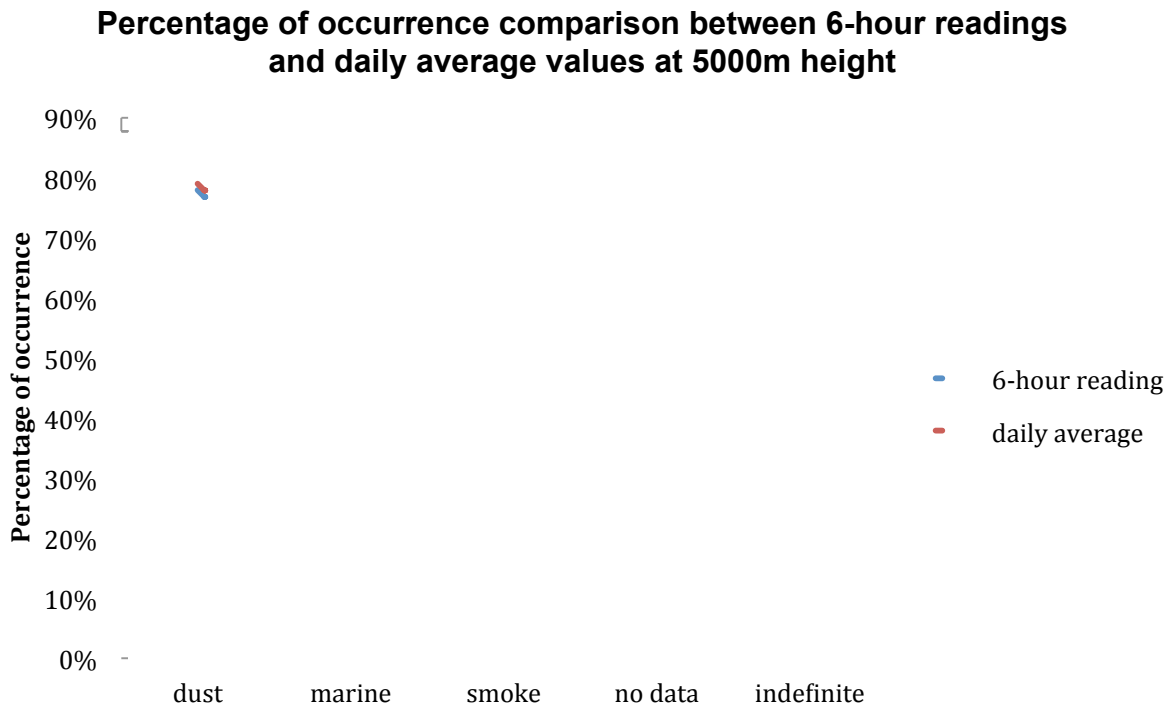


Figure (39) — 6hr-interval vs. daily averaged percentages of occurrence per regimen type at 5000m

It was established by analyzing Figure 35 through Figure 39 that although the curves did not match exactly, they tended to follow the same general behavior. The closest resemblance for the percentage comparison between the 6-hour readings and the daily averaged values was observed at the 5000m elevation plot, followed by the 1000m and the 100m elevation plots. The biggest difference was observed at the 500m elevation plot.

Once the percentage comparisons between the 6-hour readings and the daily averaged values were plotted in Figure 35 through Figure 39, it was established that a more quantitative method was required to contrast both methods. Correlation and covariance coefficients were calculated between the 6-hr percentage of occurrence

readings and the daily averaged percentage of occurrence values. This approach removed the interpretation factor in trying to quantify the differences between both methodologies by assigning a numerical value to the agreement between them. The results are listed in Table 14

Table 14 - Correlation and covariance coefficients between 6-hour readings and average values for each height

| Correlation and Covariance Coefficients per Elevation between 6-hour readings and Daily averaged values | | |
|--|-------------|------------|
| Elevation | Correlation | Covariance |
| 10m | 0.864 | 0.033 |
| 100m | 0.948 | 0.052 |
| 500m | 0.804 | 0.017 |
| 1000m | 0.970 | 0.067 |
| 5000m | 0.992 | 0.108 |

In accordance with the observations from Figure 35 through Figure 39, analysis of Table confirmed the findings from Figure 35 through Figure 39. The highest agreement was established by the correlation coefficients for the 5000m elevation, followed by the 1000m elevation. The worst correlation was established for the 500m elevation.

The corresponding percentages per air mass type, for each of the two methods, and per each elevation, were assembled into Tables. This allowed for a quick comparison of air mass types as determined by each of the methodologies. The purpose was to establish the transition elevations from one regimen to the next, as well as to quantify the air mass prediction agreement between both methodologies. Table 15 lists the resulting five tables, from Table 16 through Table 20, by their respective elevation.

Table 15 - Corresponding Figure for Percentage Comparisons between 6-hour readings and Daily averaged values

| Percentage Comparison between 6-hour readings and Daily averaged values | |
|---|-----------|
| Corresponding Table | Elevation |
| Table 16 | 10m |
| Table 17 | 100m |
| Table 18 | 500m |
| Table 19 | 1000m |
| Table 20 | 5000m |

Table 16 - Comparison of occurrence between 6-hour readings and average values at 10m height in percentage

| Origin | 6-hour reading | Daily average |
|------------|----------------|---------------|
| Dust | 33% | 25% |
| Marine | 58% | 42% |
| Smoke | 7% | 4% |
| No data | 2% | 8% |
| Indefinite | 0% | 21% |

Table 17 - Comparison of occurrence between 6-hour readings and average values at 100m height in percentage

| Origin | 6-hour reading | Daily average |
|------------|----------------|---------------|
| Dust | 29% | 25% |
| Marine | 62% | 54% |
| Smoke | 7% | 0% |
| No data | 2% | 8% |
| Indefinite | 0% | 13% |

Table 18 – Comparison of occurrence between 6-hour readings and average values at 500m height in percentage

| Origin | 6-hour reading | Daily average |
|------------|----------------|---------------|
| Dust | 41% | 25% |
| Marine | 45% | 33% |
| Smoke | 12% | 13% |
| No data | 2% | 8% |
| Indefinite | 0% | 21% |

Table 19 - Comparison of occurrence between 6-hour readings and average values at 1000m height in percentage

| Origin | 6-hour reading | Daily average |
|------------|----------------|---------------|
| Dust | 70% | 59% |
| Marine | 7% | 0% |
| Smoke | 21% | 25% |
| No data | 2% | 8% |
| Indefinite | 0% | 8% |

Table 20 - Comparison of occurrence between 6-hour readings and average values at 5000m height in percentage

| Origin | 6-hour reading | Daily average |
|------------|----------------|---------------|
| Dust | 78% | 79% |
| Marine | 9% | 4% |
| Smoke | 11% | 9% |
| No data | 2% | 8% |
| Indefinite | 0% | 0% |

Analysis of Table 16 through Table 20 revealed that marine type air masses dominate within the boundary layer. In this instance, at elevations of 10m, 100m and 500m. The last elevation zone could be described as a transition zone, since a shift from marine air mass type to dust air mass type begins to take place as evidenced by the percentage occurrence listed in Table 18. Dust air mass types dominate the elevations associated with long range transport, at the 1000m and 5000m elevations.

Chapter 5: Conclusions

Given that the CI-500 and the CI-550 cover different particle size ranges, a one to one assessment would be inadequate. Nonetheless, useful information can still be garnered from a comparison between the two instruments. The CI-500 exhibited a higher sensitivity to smaller particles. Such sensitivity is evidenced by a comparison of both time series (Figure CI-500 and Figure CI-550), where one can observe that both instruments detect roughly the same combined number of particles below the 1.0 μm and 1.2 μm thresholds. Yet, the CI-500 splits the particles across two size ranges, the 0.3 – 0.5 μm and the 0.5 – 0.7 μm , while the CI-550 lumps the majority of the particles under the 0.3 – 0.5 μm range. In contrast, the CI-550 displayed a higher sensitivity to larger particle-size ranges.

Analysis and comparison of CI-500 and CI-550 collected datasets confirmed in a quantitative manner that the sampling of the CI-500 instrument is geared toward the smaller particle spectrum, while the CI-550 has a higher sensitivity toward mid size particles.

Analysis of 440 HYSPLIT 7-day backward trajectories indicated that at lower elevations, specifically at 10m and 100m heights, the trajectories mainly backtracked to marine source regions, closely followed by dust source regions.

It was also established that HYSPLIT backward trajectories at higher elevations, particularly at 1000m and 5000m heights backtracked to dust, closely followed by smoke.

More over, HYSPLIT backward trajectories at middle elevation, such as 500m may be described as transition regions. This is due to the fact that they showed to have initiated a transition from a marine source region to a dust source region.

Ultimately, similar results were observed from both HYSPLIT sampling methods: those described throughout this research as the daily averages vs. the 6-hr readings.

The best correlations between both HYSPLIT sampling methods were observed at the 5000m height and the 1000m. Consequently, the worst correlations were noted at the 500m height and the 10m height. Therefore, an argument may be established that better correlations are to be obtained from higher elevations, while worst correlations will be the resultant from lower elevations.

Finally, both HYSPLIT sampling methods, the daily averages as well as the 6-hr readings, were deemed reliable, although a particular method may be preferred depending on user necessities.

References

- Annesi-Maesano, I., Moreau, D., Caillaud, D., Lavaud, F., Le Moullec, Y., Taytard, A., Pauli, G., and Charpin, D., 2007, Residential proximity fine particles related to allergic sensitisation and asthma in primary school children, *Respiratory Medicine*, v. 101, no. 8, pp. 1721-1729, doi: 10.1016/j.rmed.2007.02.022. (<http://www.sciencedirect.com/science/article/pii/S0954611107000996>)
- Baron, P.A. and Willeke, K., 2001, *Aerosol Measurement: Principles, Techniques and Applications*: John Wiley and Sons, Inc. (New York), 1131 p.
- Bates, T.S., Quinn, P.K., Coffman, D.J., Johnson, J.E., Miller, T.L., Covert, D.S., Wiedensohler, A., Leinert, S., Nowak, A., and Neusüs, C., 2001, Regional physical and chemical properties of the marine boundary layer aerosol across the Atlantic during Aerosols99: An overview, *Journal of Geophysical Research*, v. 106, pp. 20,767-20,782.
- Cess, R. D., Potter, G. L., Ghan, S. J., and Gates, W. L., 1985, The Climatic Effects of Large Injections of Atmospheric Smoke and Dust: A Study of Climate Feedback Mechanisms With One- and Three-Dimensional Climate Models, *Journal of Geophysical Research*, v. 90, no. D7, pp. 12,937 -12,950, doi: 10.1029/JD090iD07p12937.

- Chin, M., Kahn, R. A., Remer, L. A., Yu, H., Rind, D., Feingold, G., Quinn, P. K., Schwartz, S.E., Streets, D. G., Decola, P., and Halthore, R., Atmospheric Aerosol Properties and Climate Impacts, in: US Climate Change Science Program Synthesis and Assessment Product 2.3, 2009, 128pp.
- Chun, Y., Kim, J.Y., Choi, J.C., Boo, K.O., Oh, S.N., and Lee, M., 2001, Characterization of number size distribution of aerosol during Asian dust period in Korea: Atmospheric Environment, v. 35, p. 2715-2721.
- Colbeck, I., 2008, Environmental Chemistry of Aerosols: Blackwell Publishing Ltd. (Oxford), 255 p.
- Dockery, D., Pope, C. A., Xu, X., Spengler, J., Ware, J., Fay, M., Ferris, B., and Speizer, F., 1993, An association between air pollution and mortality in six U.S. cities, New England Journal of Medicine, v. 329, pp. 1753-1759.
- Draxler, R.R, and Hess, G.D., 1998, An overview of the Hysplit-4 modeling system for trajectories, dispersion, and deposition, Australian Meteorology Magazine, v. 47, pp. 295-308.
- Dubovik, O., Holben, B., Eck, T. F., Smirnov, A., Kaufman, Y.J., King, M. D., Tanré, D., and Slutsker, I., 2002, Variability of absorption and optical properties of key aerosol types observed in worldwide locations, Journal of the Atmospheric Sciences, v. 59, pp. 590-608.

Esparza, A. E., 2011, Aerosol characterization in El Paso-Juarez airshed using optical methods, ETD Collection for University of Texas, El Paso. Paper AAI3489978.
<http://digitalcommons.utep.edu/dissertations/AAI3489978>

Esparza, A. E., Fitzgerald, R. M., Gill, T. E., and Polanco, J., 2011, Use of Light Extinction Method and Inverse Modeling to Study Aerosols in the Paso del Norte Airshed, *Atmospheric Environment*, v. 45, pp. 7360-7369.

Formenti, P., W. Elbert, W. Maenhaut, J. Haywood, and Andreae, M. O., 2003, Chemical composition of mineral dust aerosol during the Saharan Dust Experiment (SHADE) airborne campaign in the Cape Verde region, September 2000, *Journal of Geophysical Research*, v. 108, no. D18, pp. 8576, doi: 10.1029/2002JD002648.

Ganguly, D., Jayaraman, A., and Gadhavi, H., 2005, In situ ship cruise measurements of mass concentration and size distribution of aerosols over Bay of Bengal and their radiative impacts, *Journal of Geophysical Research*, v. 110, no. D06205, doi: 10.1029/2004JD005325.

Ganor, E., Stupp, A., and Alpert, P., 2009, A method to determine the effect of mineral dust aerosols on air quality, *Atmospheric Environment*, v. 43, 5463–5468.

Heintzenberg, J., 2009, The SAMUM-1 experiment over southern Morocco: Overview and introduction, *Tellus B*, v. 61, no. 1, pp. 2-11. doi: 10.1111/j.16000889.2008.00403.x

Hinds, W.C., 1998, *Aerosol Technology: Properties, Behavior, and Measurement of Airborne Particles*, John Wiley and Sons, Inc., New York, 483 pp.

Hogan, T. F., and L. R. Brody, 1991, Sensitivity studies of the Navy's global forecast model parameterizations and evaluation of improvements to NOGAPS, *Monthly Weather Review*, v. 121, pp. 2373-2395.

Hogan, T. F., and T. E. Rosmond, 1991, The description of the Navy operational global atmospheric prediction system's spectral forecast model, *Monthly Weather Review*, v. 119, pp. 1786-1815.

IPCC, 2001: *Climate Change 2001, The Scientific Basis*. Contribution of Working Group I to the Third Assessment Report of the Intergovernmental Panel on Climate Change [Houghton, J.T., Y. Ding, D.J. Griggs, M. Noguer, P.J. van der Linden, X. Dai, K. Maskell, and C.A. Johnson (eds.)]; Cambridge University Press, Cambridge, United Kingdom and New York, NY, USA, 881 pp.

Jensen, J. R., 2005, *Introductory Digital Image Processing: A Remote Sensing Perspective*, Prentice Hall PTR, (Upper Saddle River, NJ), pp. 526.

Kaufman, Y. J., Tanré, D., Gordon, H. R., Nakajima, T., Lenoble, J., Frouin, R., Grassl, H., Herman, B. M., King, M.D., and Teillet, P.M., 1997, Passive remote sensing of tropospheric aerosol and atmospheric correction for the aerosol effect, *Journal of Geophysical Research*, v. 102, pp. 16,971 - 16,988.

King, M.D., Kaufman, Y.J., Tanré, D. and T. Nakajima, T., 1999, Remote sensing of tropospheric aerosols from space: Past, present and future, *Bulletin of the American Meteorological Society*, v. 80, no. 11, pp. 2,229-2,259.

Lacis, A.E., Hansen, J. E., and Sato, M., 1992, Climate forcing by stratospheric aerosols, *Geophysical Research Letters*, v. 19, no. 15, pp. 1607–1610.

Morris, V., Clemente-Colón, P., Nalli, N.R., Joseph, E., Armstrong, R.A., Detrés, Y., Goldberg, M.D., Minnett, P.J., and Lumpkin, R., 2006, Measuring trans-Atlantic aerosol transport from Africa: *EOS*, v. 87 no. 50, pp. 565-571.

Nalli, N.R., Clemente-Colón, P., Morris, V., Joseph, E., Szczodrak, M., Minnett, P.J., Shannahoff, J., Goldberg, M.D., Barnet, C.D., Wolf, W.W., Feltz, W.F., and Knuteson, R.O., 2005, Profile Observations of the Saharan Air Layer During AEROSE 2004, *Geophysical Research Letters*, v. 32, no. L05815, doi: 10.1029/2004GL022028.

Nalli, N. R., Joseph, E., Morris, V., Barnet, C.D., Wolf, W.W., Wolfe, D., Minnett, P.J., Szczodrak, M., Izaguirre, M. A., Lumpkin, R., Xie, H., Smirnov, A., King, T. S., and Wei, J., 2011, Multiyear Observations of the Tropical Atlantic Atmosphere: Multidisciplinary Applications of the NOAA Aerosols and Ocean Science Expeditions, *Bulletin of the American Meteorological Society*, v. 92, no. 6, pp. 765–789, doi: 10.1175/2011BAMS2997.1.

Polymenakou, P.N., Manolis, M., Euripides, G.S., and Anastasios, T., 2008, Particle size distribution of airborne microorganisms and pathogens during an intense African dust event in the Eastern Mediterranean, *Environmental Health Perspectives*, v.116, pp. 292–296.

Prospero, J., 1999, Long-term measurements of the transport of African mineral dust to the southeastern United States: Implications for regional air quality, *Journal of Geophysical Research*, v. 104, no. D13, pp. 15,917 - 15,927.

Reid, J., Hyer, E., Prins, E., Westphal, D. L., Zhang, J., Wang, J., Christopher, S., Curtis, C., Schmidt, C., Eleuterio, D., Richardson, K., and Hoffman, J., 2009, Global monitoring and forecasting of biomass-burning smoke: Description of and lessons from the Fire Locating and Modeling of Burning Emissions (FLAMBE) program, *IEEE Journal of Selected Topics in Applied Earth Observations in Remote Sensing*, v. 2, pp. 144–161.

- Schwartz, J., 1994, Air Pollution and Daily Mortality: A Review and Meta Analysis, Environmental Research, v. 64, no. 1, pp. 36-52, ISSN 0013-9351, doi: 10.1006/enrs.1994.1005.
(<http://www.sciencedirect.com/science/article/pii/S001393518471005X>)
- Shao, Y., Wyrwoll, K. H., Chappell, A., Huang, J., Lin, J., McTainsh, G. H., Mikami, M., Tanaka, T.Y., Wang, X., and Yoon, S., 2011, Dust cycle: An emerging core theme in Earth system science, Aeolian Research, vol. 2, pp. 181- 204.
- Tanré, D., Haywood, J., Pelon, J., Leon, J. F., Chatenet, B., Formenti, P., Francis, P., Goloub, P., Highwood, E. J., and Myhre, G., Measurement and modeling of the Saharan dust radiative impact: Overview of the Saharan Dust Experiment (SHADE), Journal of Geophysical Research, v. 108, no. D18, 8574, doi: 10.1029/2002JD003273, 2003.
- Thomas, D.S.G., Knight, M., Wiggs, G.F.S., 2005, Remobilization of southern African desert dune systems by twenty-first century global warming, Nature v. 435, pp. 1218–1221
- Verma, S., Venkataraman, C., Boucher, O., Ramachandran, S., 2007. Source evaluation of aerosols measured during the Indian Ocean experiment using combined chemical transport and back trajectory modelling, Journal of Geophysical Research, v. 112, no. D11210, [doi: 10.1029/2006JD007698](https://doi.org/10.1029/2006JD007698).

Wang, J., Christopher, S. A., Nair, U. S., Reid, J. S., Prins, E. M., Szykman, J., and Hand, J. L., 2006, Mesoscale modeling of Central American smoke transport to the United States: 1. "Top-down" assessment of emission strength and diurnal variation impacts, *Journal of Geophysical Research*, v. 111, no. D05S17, doi: 10.1029/2005JD006416.

Zhang, J. and Reid, J.S., 2009, An analysis of clear sky and contextual biases using an operational over ocean MODIS aerosol product: *Geophysical Research Letters*, v. 36, no. L15824, doi: 10.1029/2009GL038723.

Glossary

AEROSE - Aerosols and Ocean Science Expeditions

ARL - NOAA Air Resource Laboratory

EEZ – Exclusive economic zone

FLAMBE - Fire Locating and Modeling of Burning Emissions

GDAS - Global Data Analysis System

HYSPLIT - HYbrid Single-Particle Lagrangian Integrated Trajectory model

ITCZ – Inter-tropical convergence zone

LPC – Laser particle counter

MODIS - MODerate Resolution Imaging Spectroradiometer

NAAPS - Navy Aerosol Analysis and Prediction System

NOAA - National Oceanic and Atmospheric Administration

NOGAPS - Navy Operational Global Atmospheric Prediction System

NRL - Naval Research Laboratory

RHB - Ronald H. Brown, a NOAA research vessel.

SAL - Saharan Air Layer

SCS- Ship's Computer System

TSG – Thermosalinograph

UTC - Coordinated Universal Time, also known as Zulu time.

Appendix

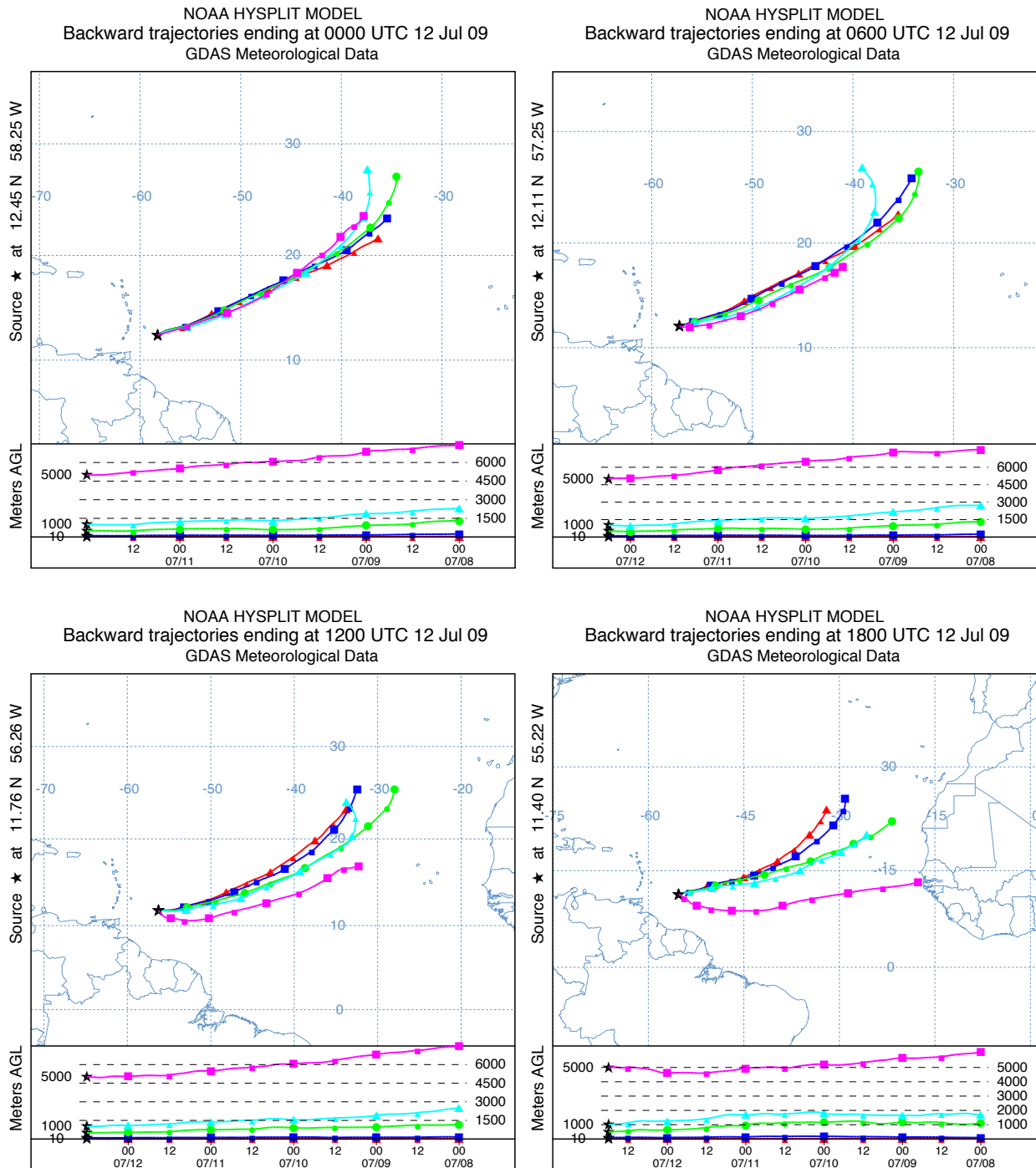


Figure (40) – 7-day backward trajectories; each color corresponds to trajectory height: red 10m, blue 100m, green 500m, cyan 1000m and magenta 5000m.

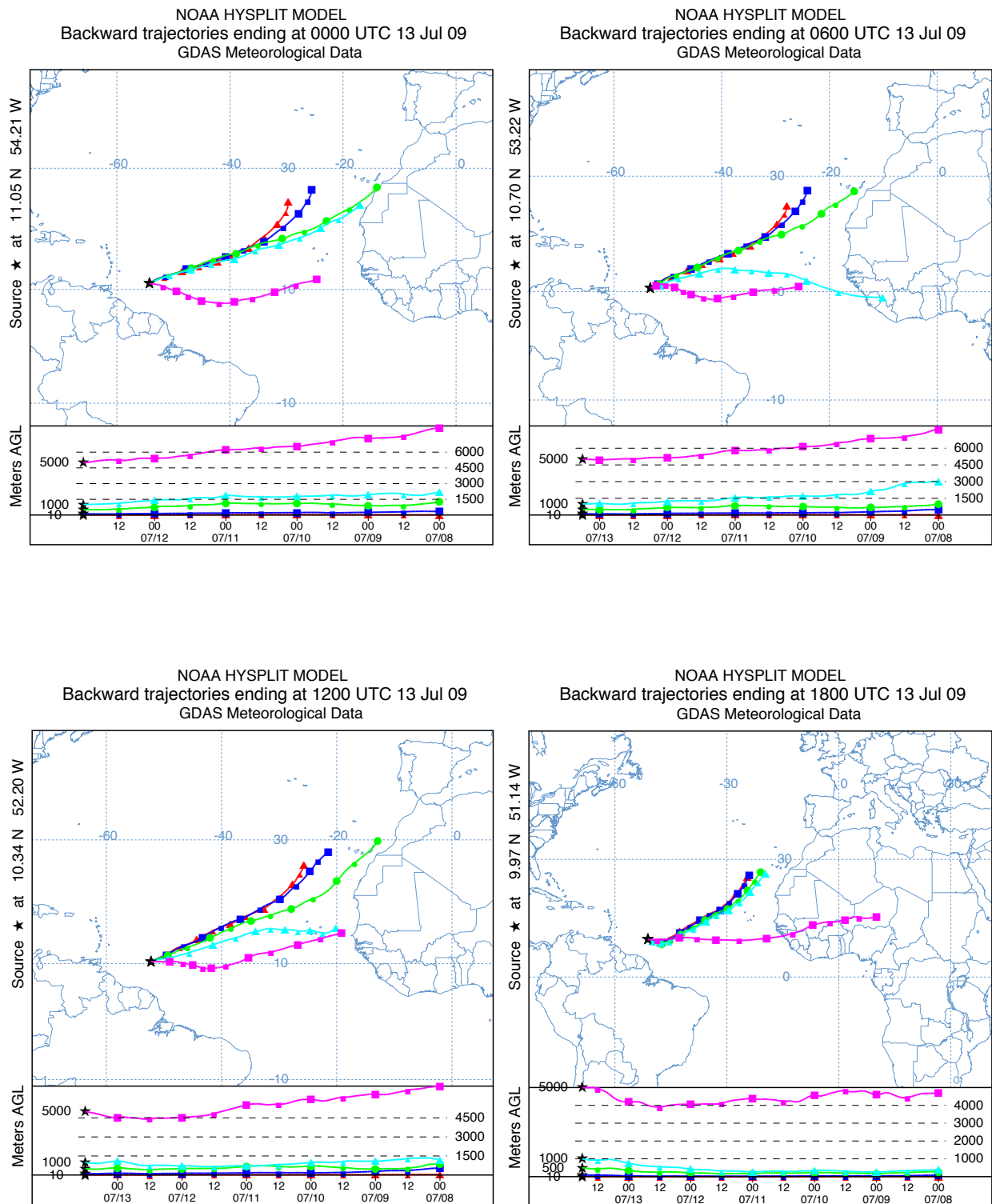


Figure (41) – 7-day backward trajectories; each color corresponds to trajectory height: red 10m, blue 100m, green 500m, cyan 1000m and magenta 5000m.

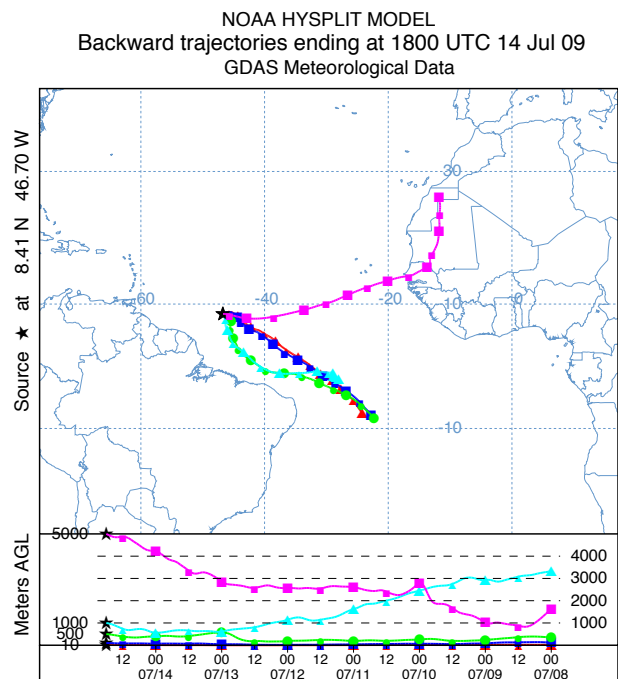
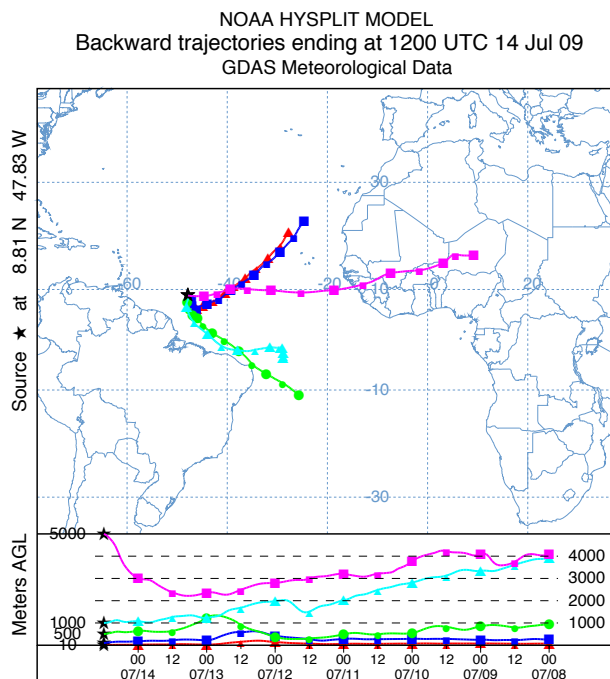
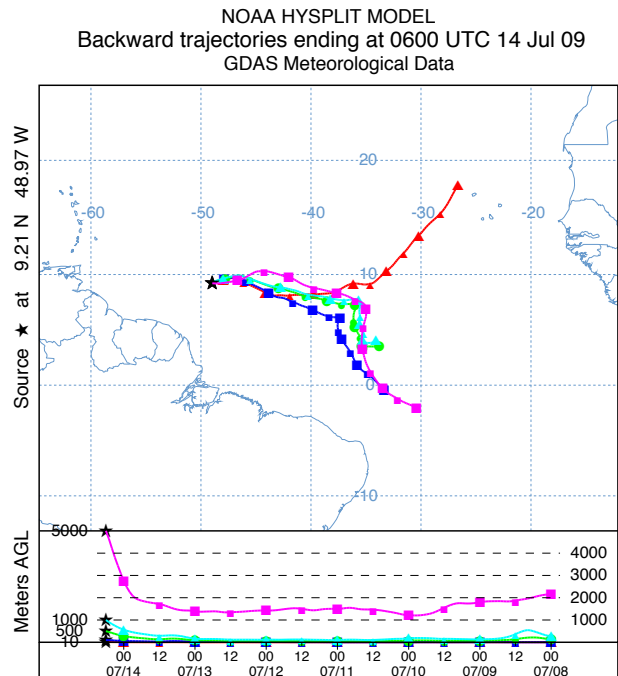
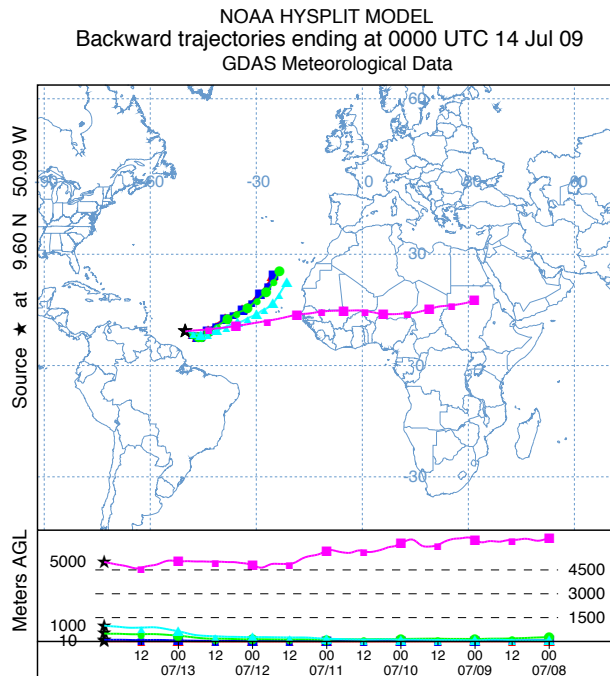


Figure (42) – 7-day backward trajectories; each color corresponds to trajectory height: red 10m, blue 100m, green 500m, cyan 1000m and magenta 5000m.

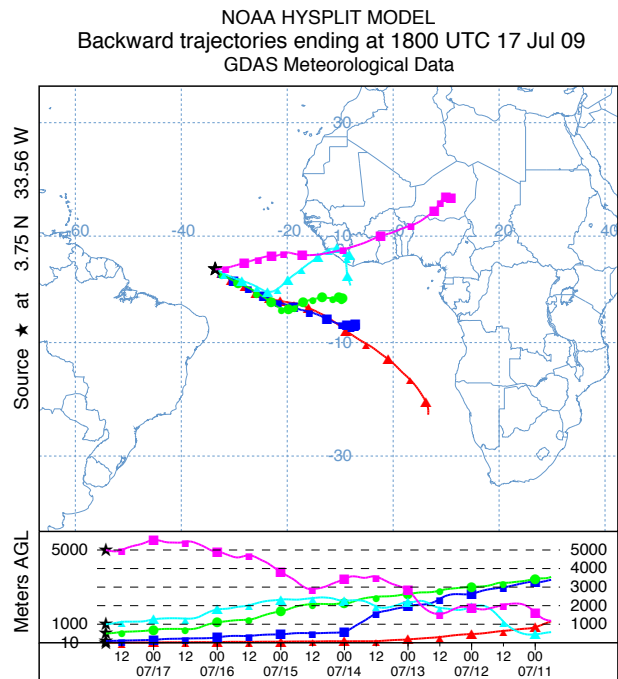
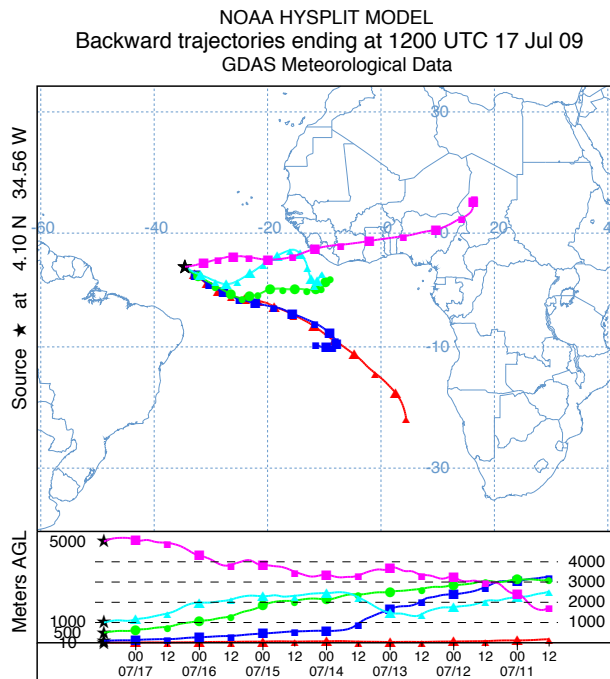
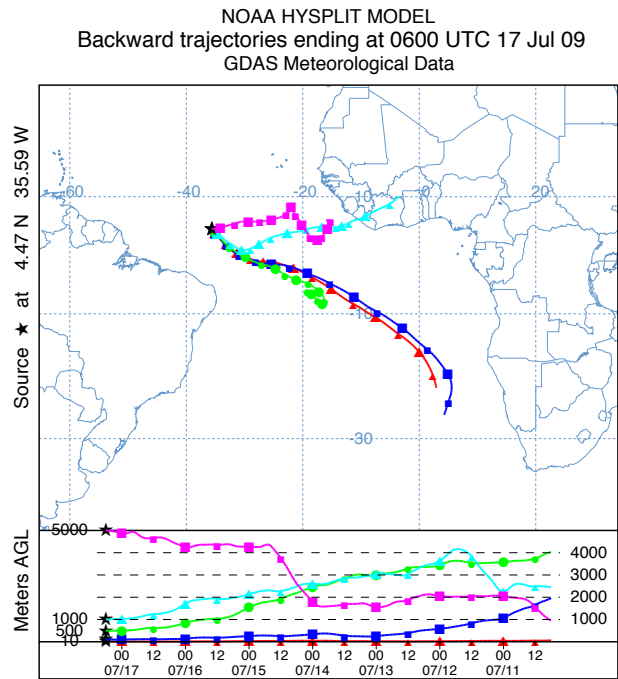
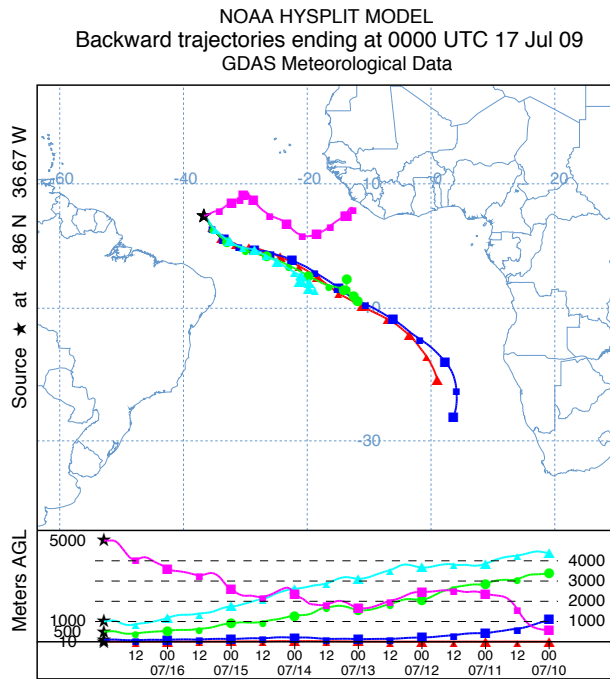


Figure (45) – 7-day backward trajectories; each color corresponds to trajectory height: red 10m, blue 100m, green 500m, cyan 1000m and magenta 5000m.

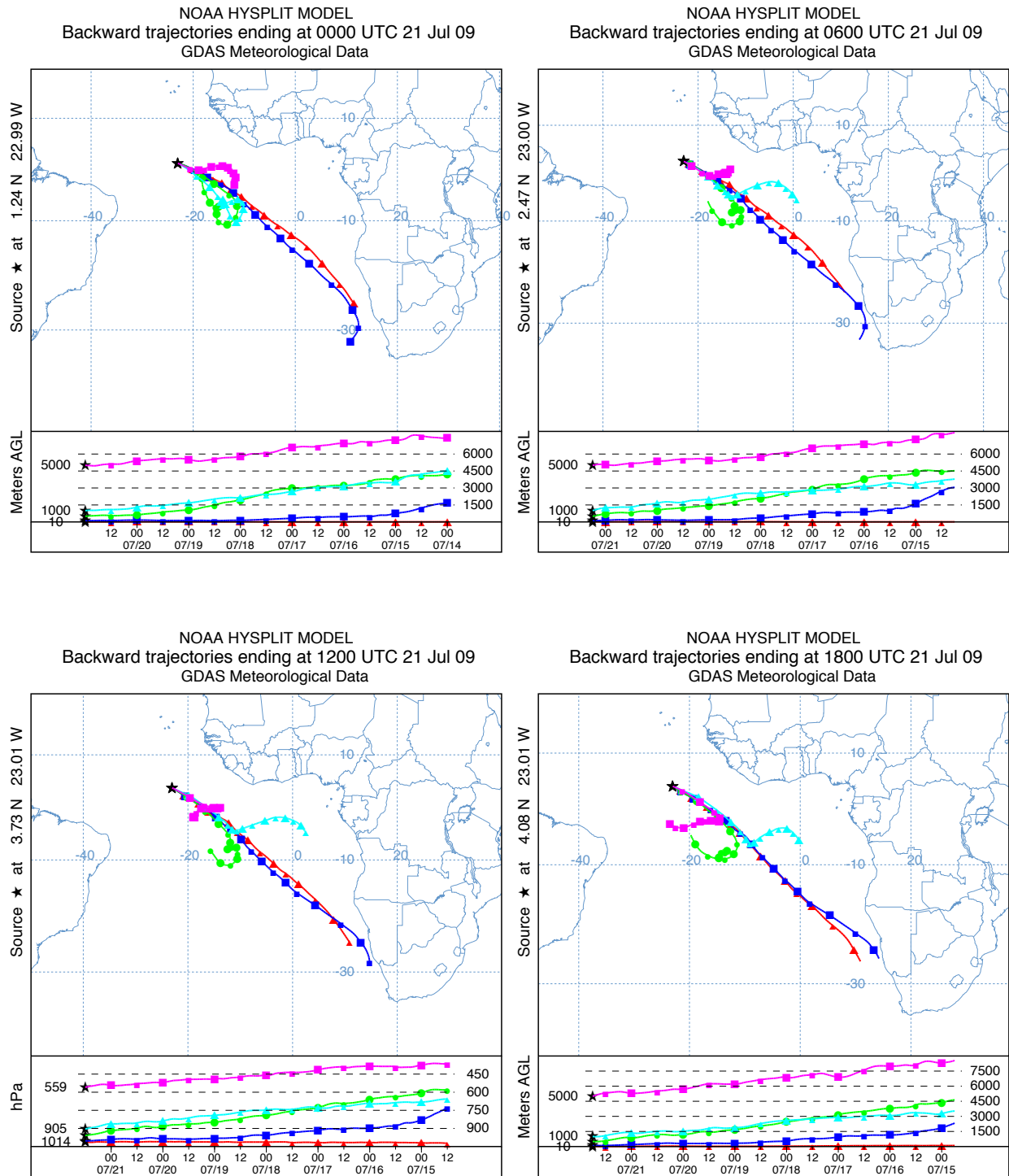


Figure (47) – 7-day backward trajectories; each color corresponds to trajectory height: red 10m, blue 100m, green 500m, cyan 1000m and magenta 5000m.

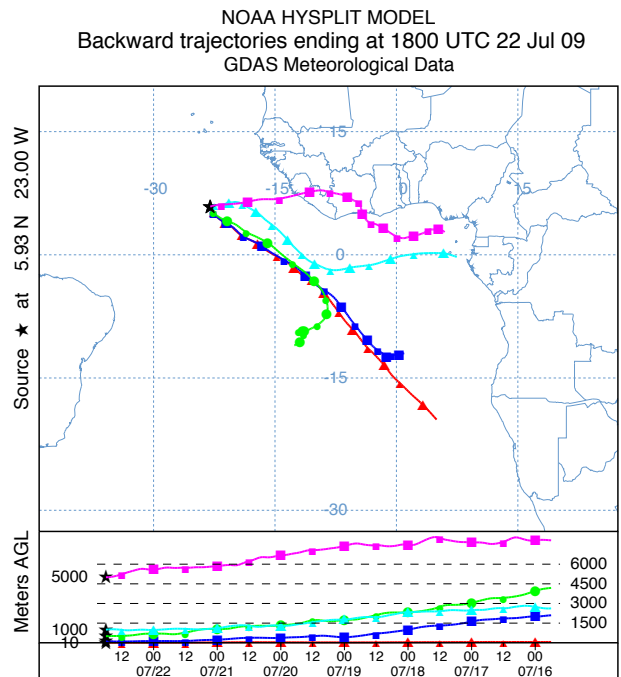
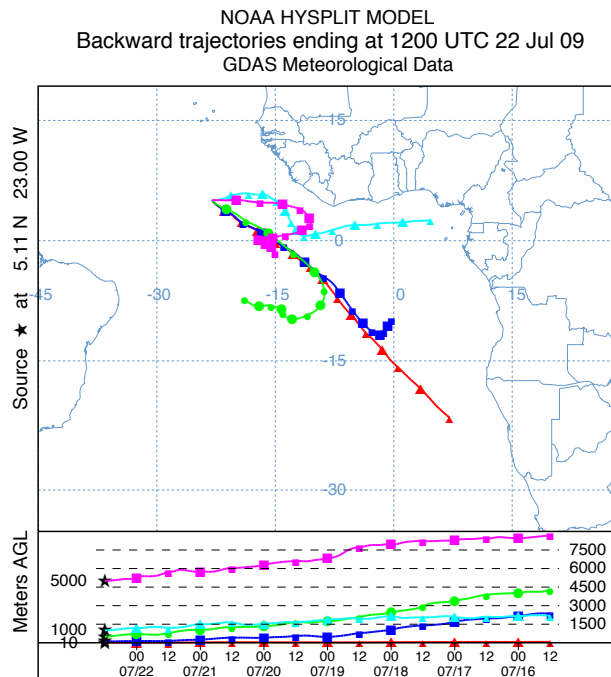
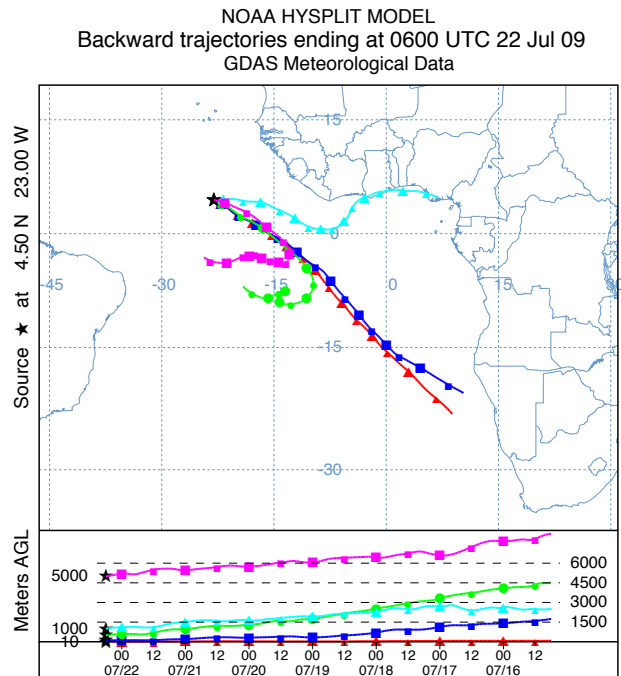
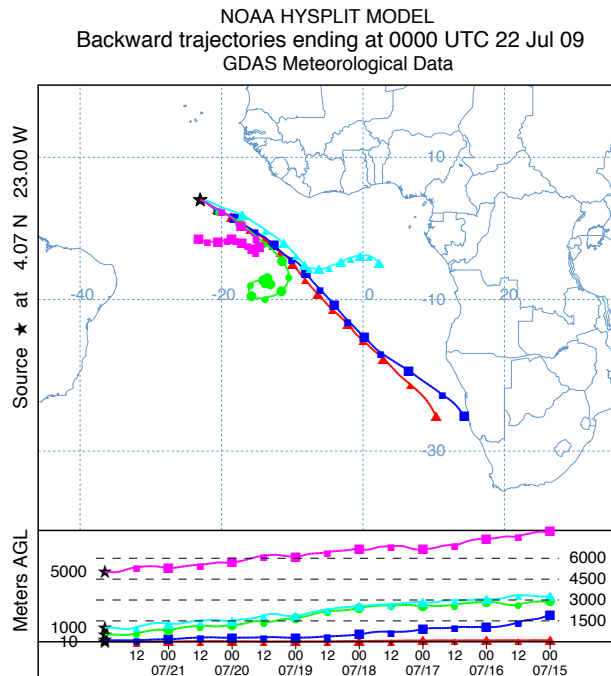


Figure (48) – 7-day backward trajectories; each color corresponds to trajectory height: red 10m, blue 100m, green 500m, cyan 1000m and magenta 5000m.

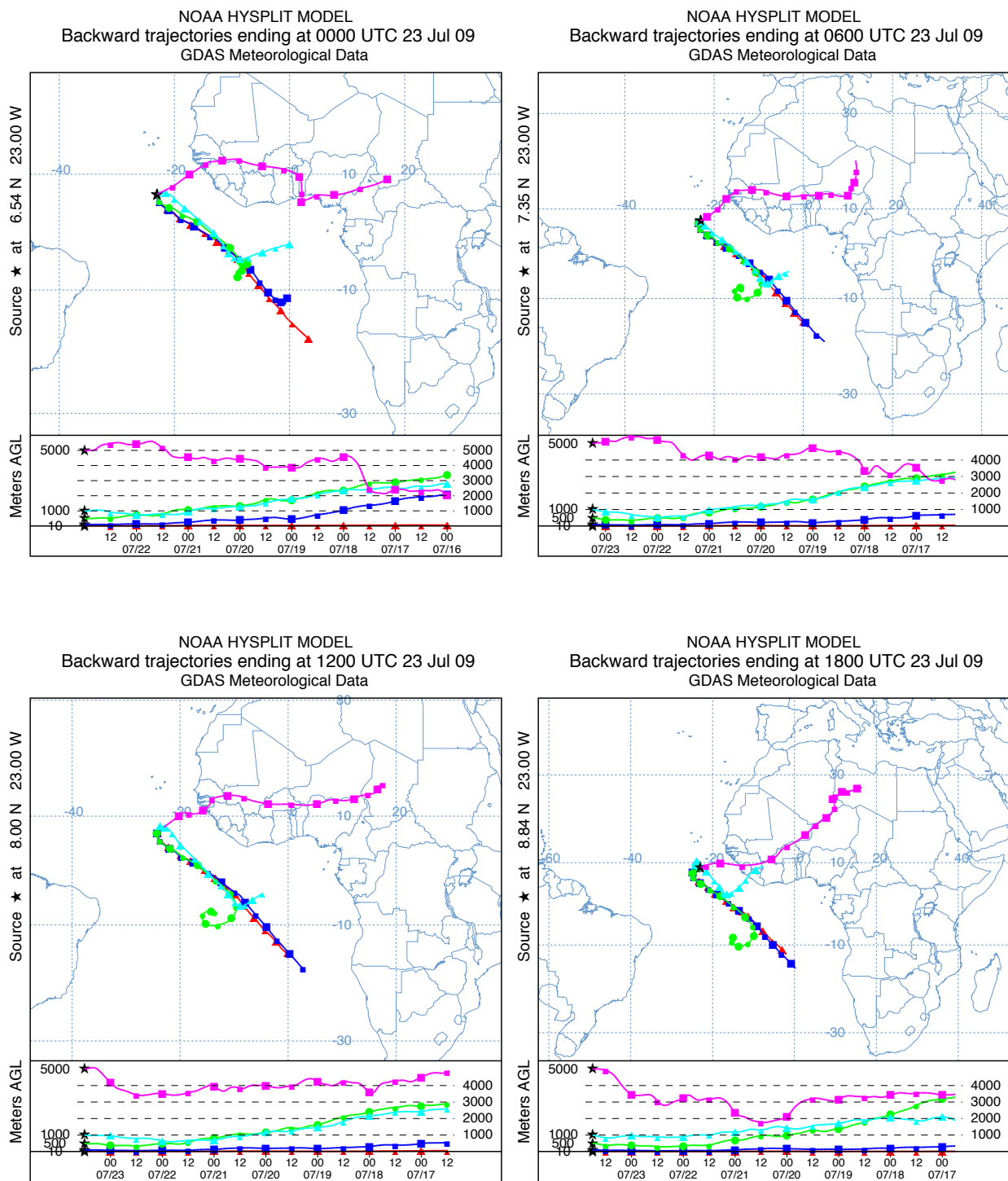


Figure (49) – 7-day backward trajectories; each color corresponds to trajectory height: red 10m, blue 100m, green 500m, cyan 1000m and magenta 5000m.

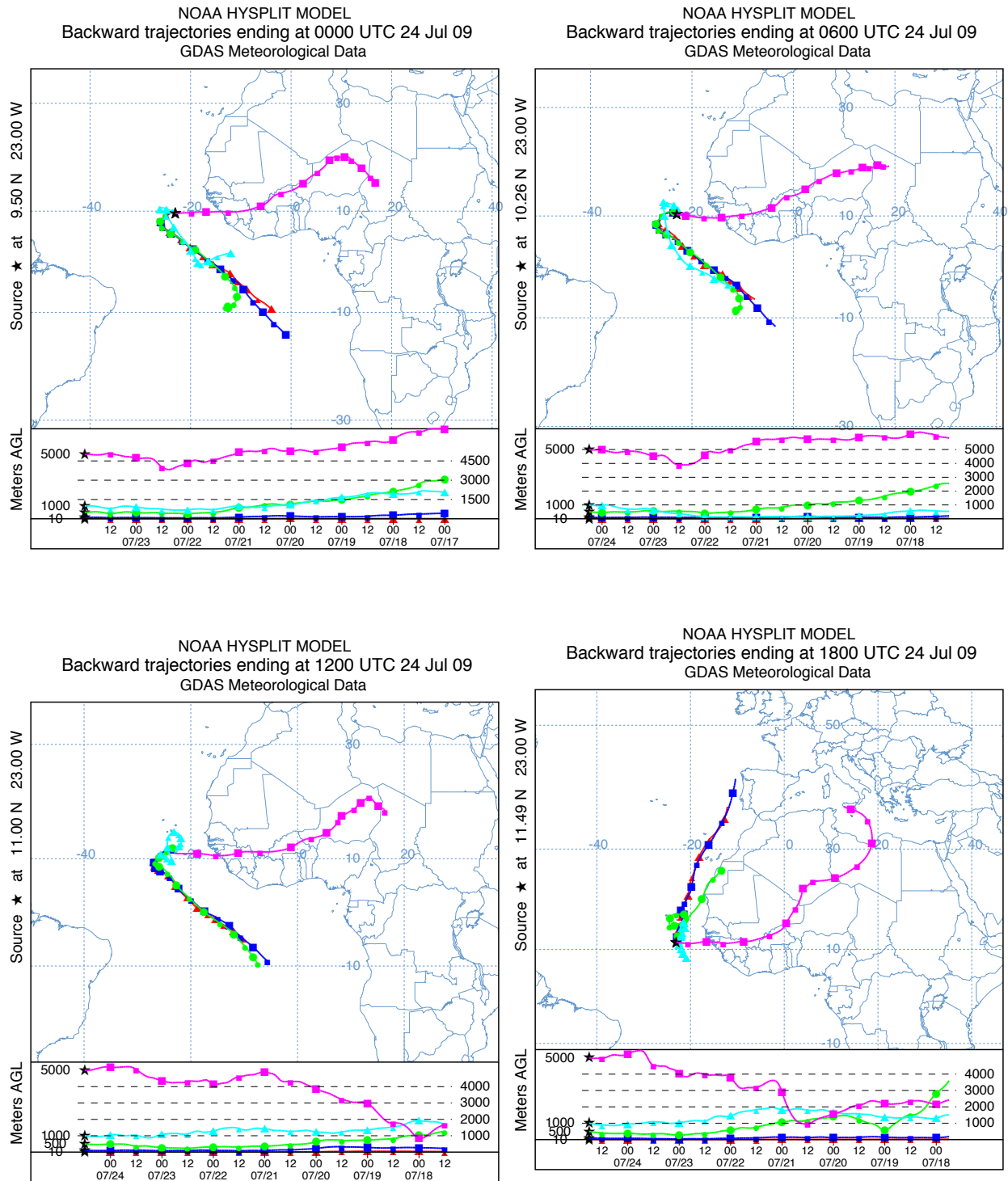


Figure (50) – 7-day backward trajectories; each color corresponds to trajectory height: red 10m, blue 100m, green 500m, cyan 1000m and magenta 5000m.

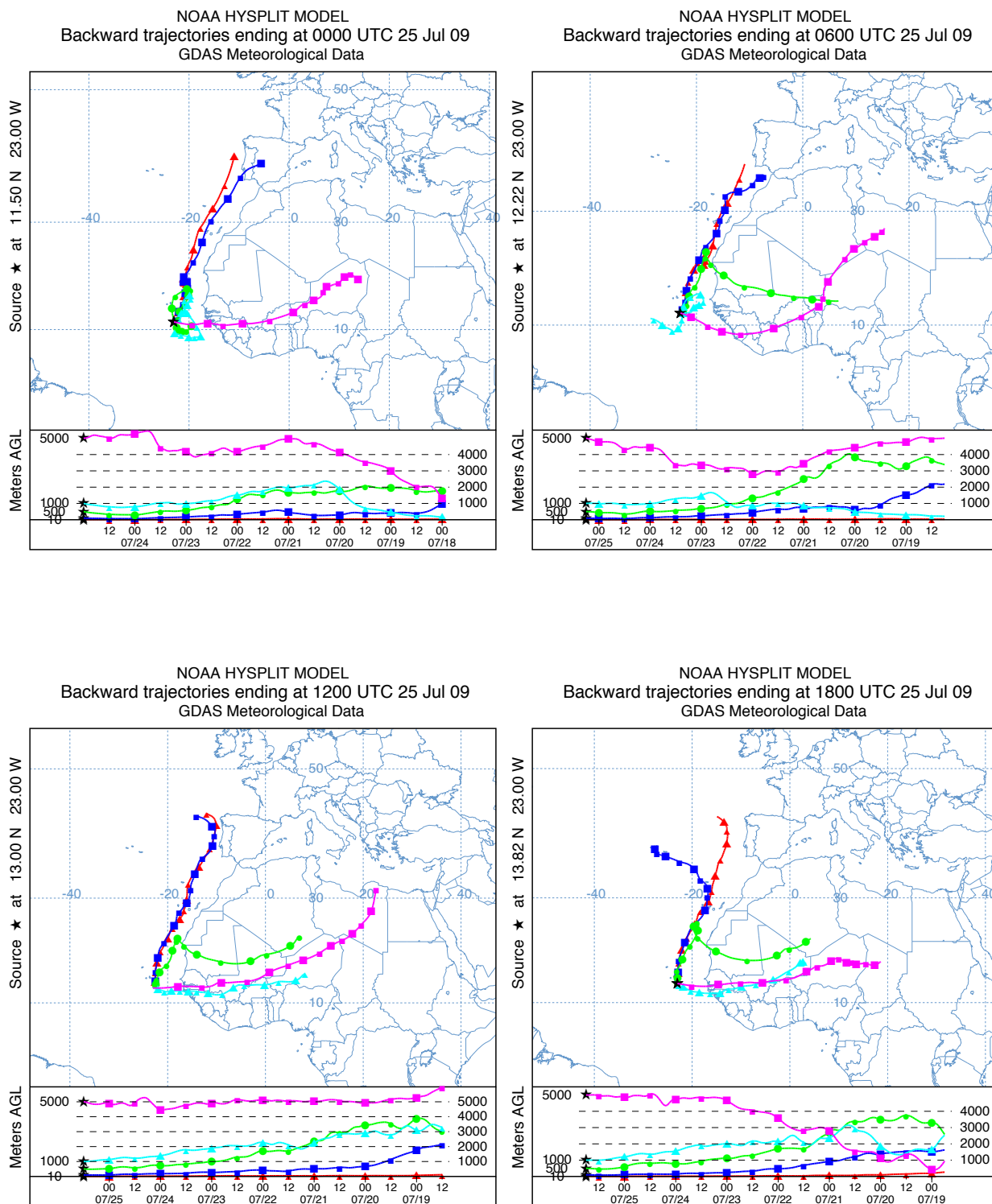


Figure (51) – 7-day backward trajectories; each color corresponds to trajectory height: red 10m, blue 100m, green 500m, cyan 1000m and magenta 5000m.

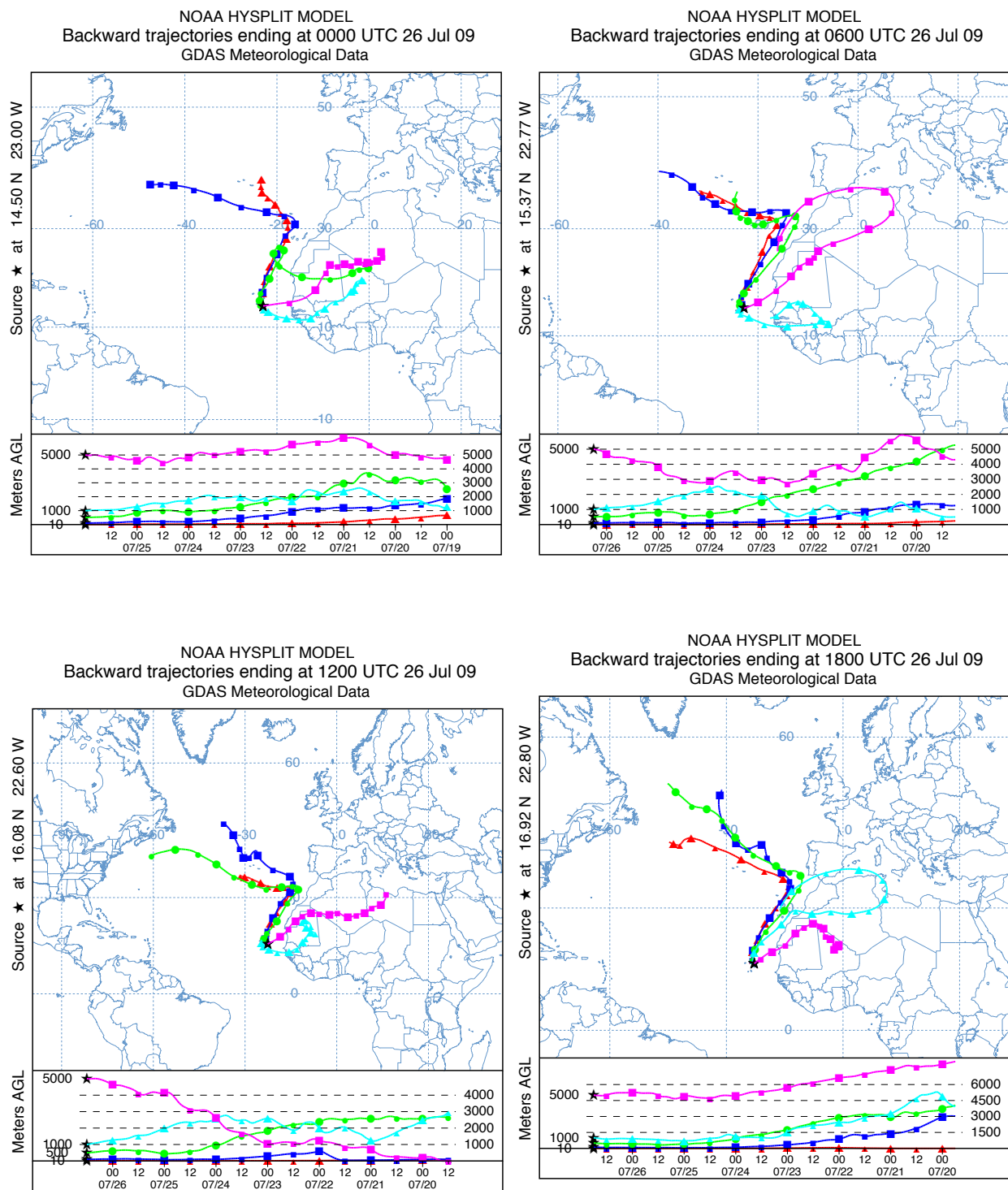


Figure (52) – 7-day backward trajectories; each color corresponds to trajectory height: red 10m, blue 100m, green 500m, cyan 1000m and magenta 5000m.

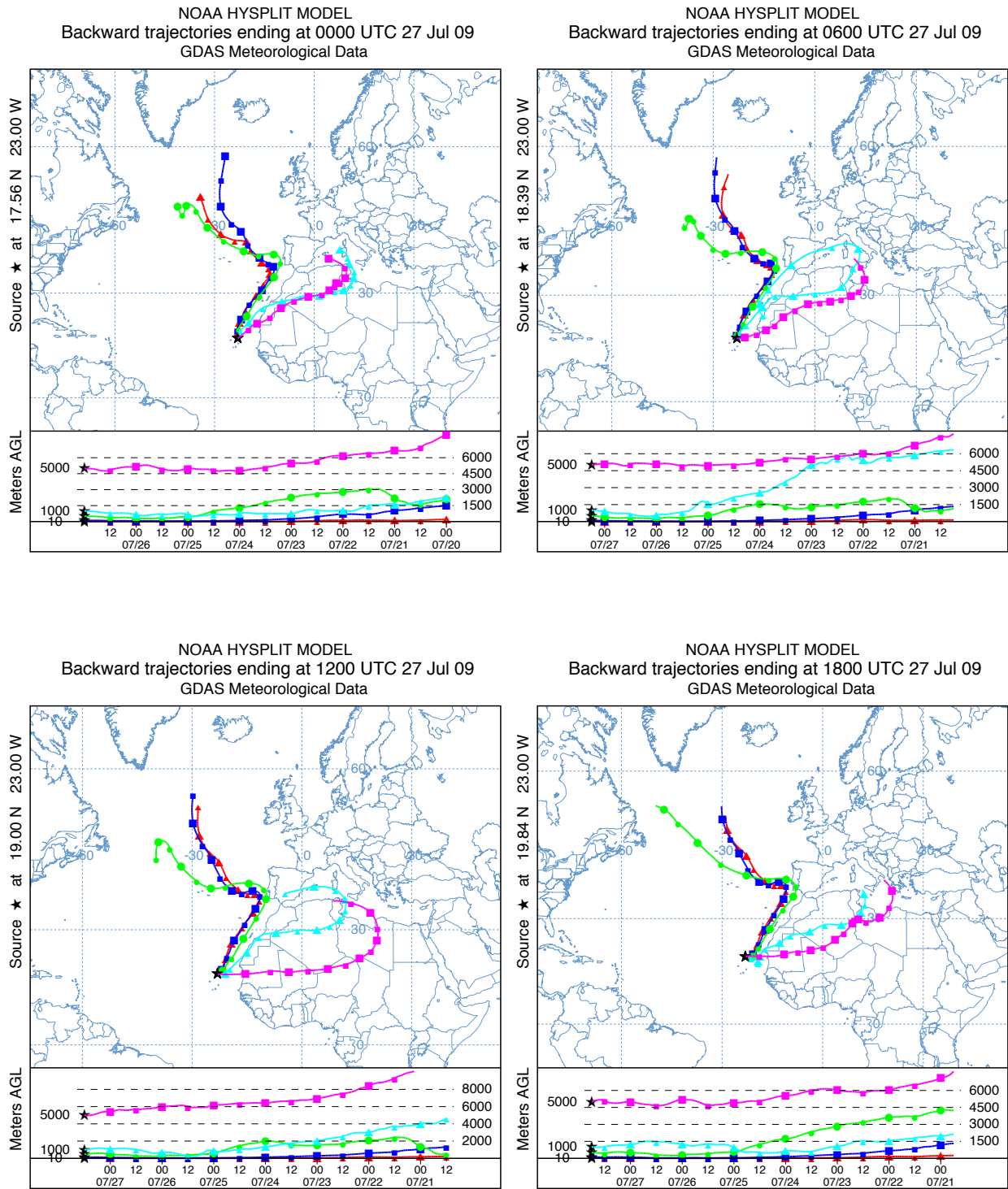


Figure (53) – 7-day backward trajectories; each color corresponds to trajectory height: red 10m, blue 100m, green 500m, cyan 1000m and magenta 5000m.

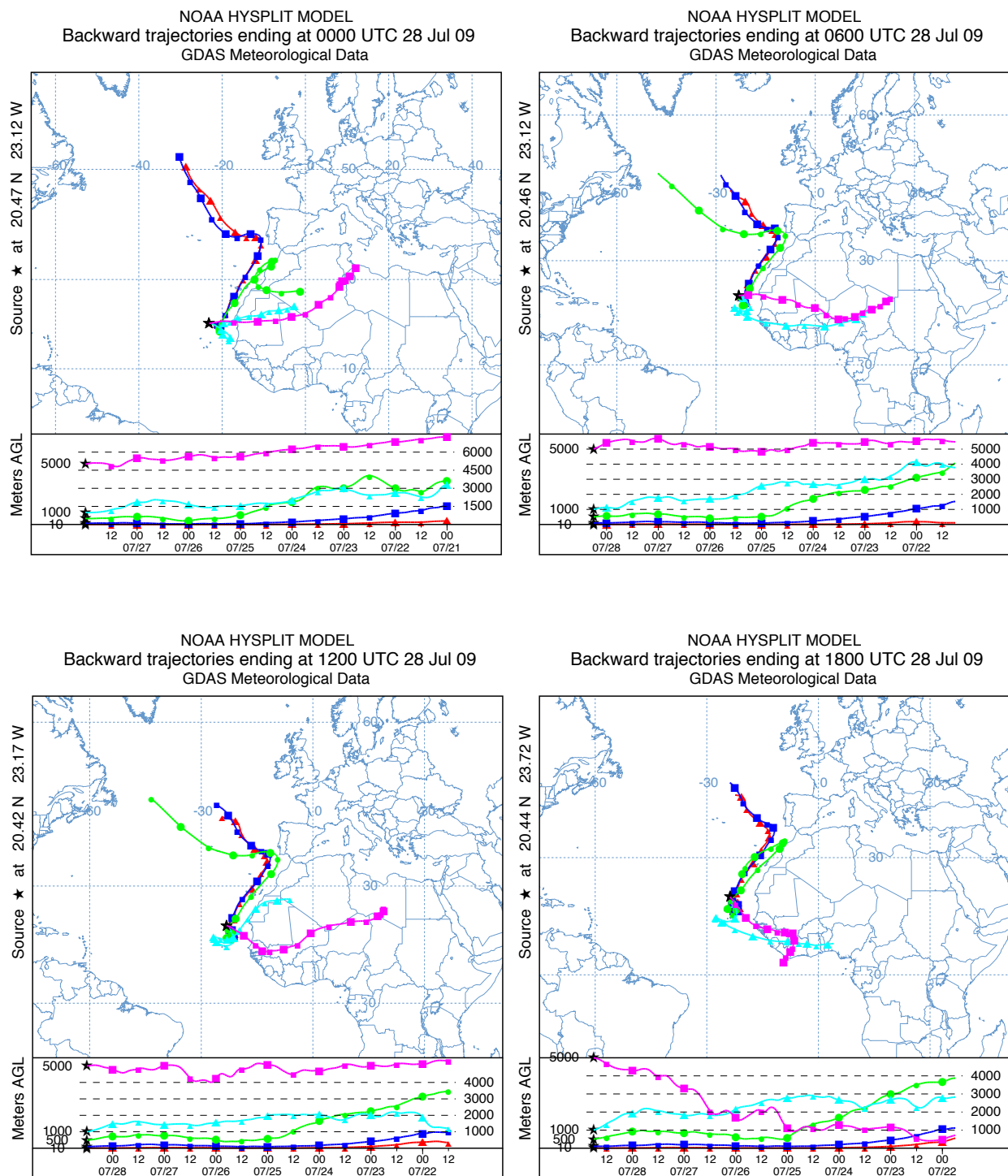


Figure (54) – 7-day backward trajectories; each color corresponds to trajectory height: red 10m, blue 100m, green 500m, cyan 1000m and magenta 5000m.

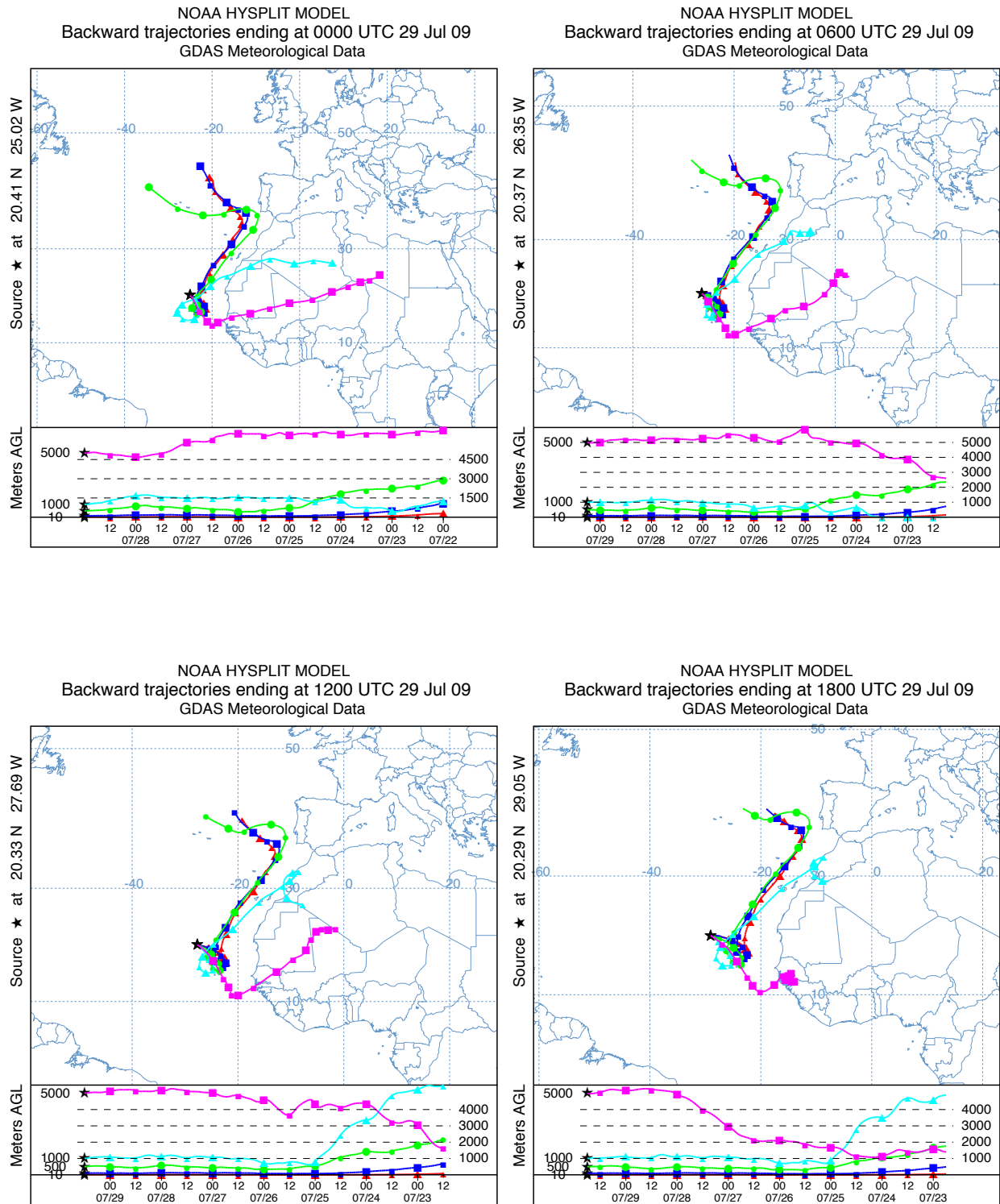


Figure (55) – 7-day backward trajectories; each color corresponds to trajectory height: red 10m, blue 100m, green 500m, cyan 1000m and magenta 5000m.

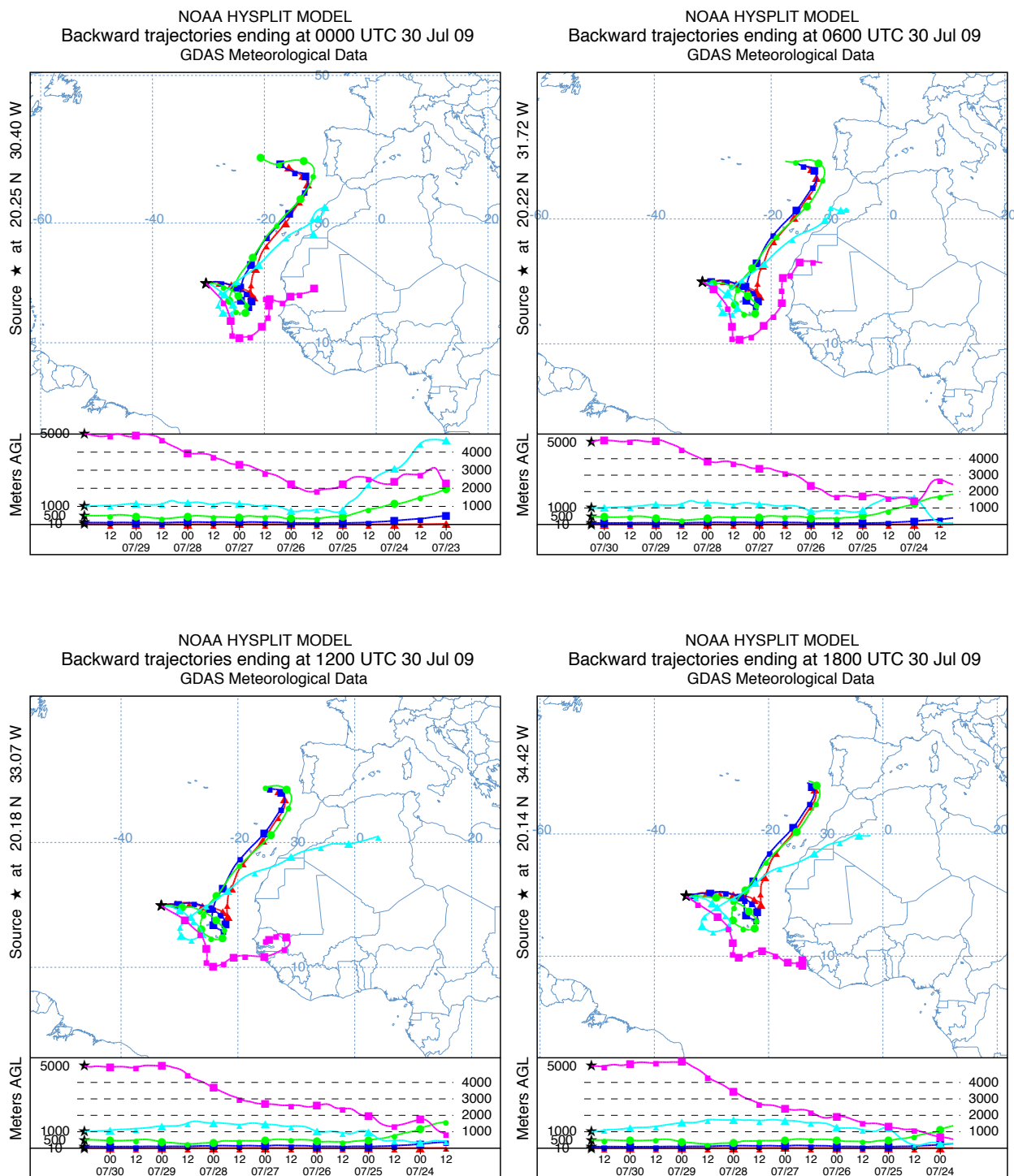


Figure (56) – 7-day backward trajectories; each color corresponds to trajectory height: red 10m, blue 100m, green 500m, cyan 1000m and magenta 5000m.

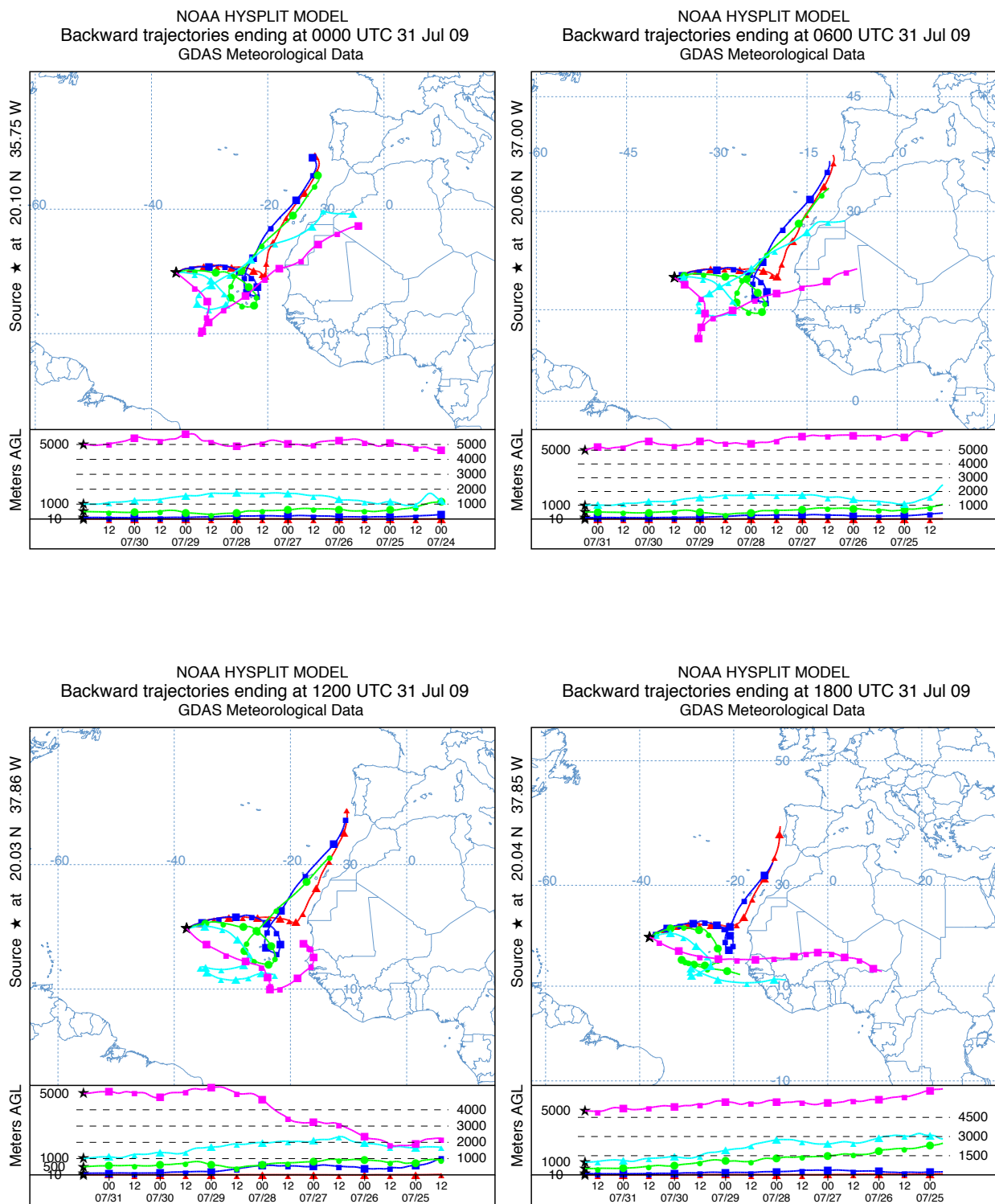


Figure (57) – 7-day backward trajectories; each color corresponds to trajectory height: red 10m, blue 100m, green 500m, cyan 1000m and magenta 5000m.

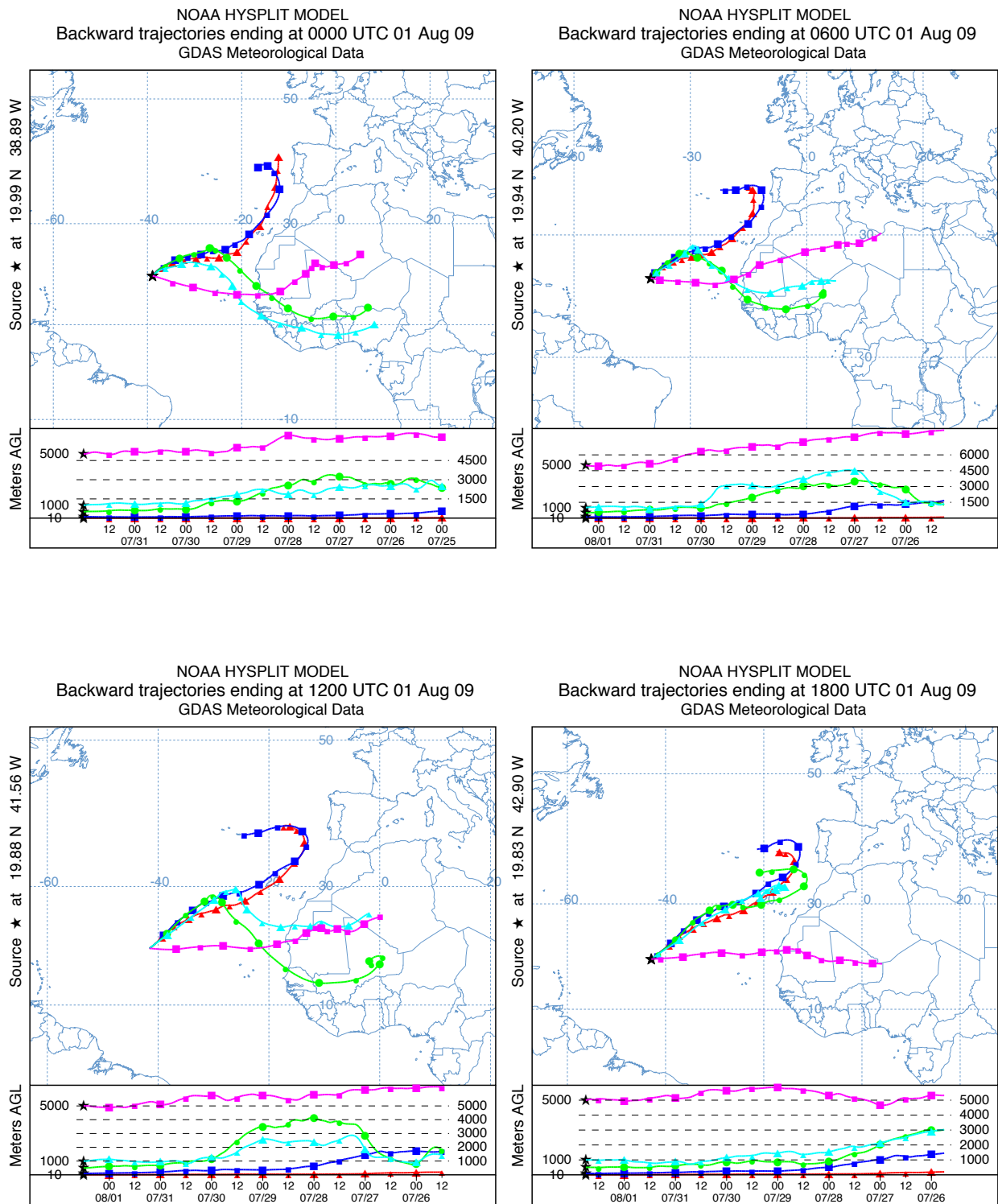


Figure (58) – 7-day backward trajectories; each color corresponds to trajectory height: red 10m, blue 100m, green 500m, cyan 1000m and magenta 5000m.

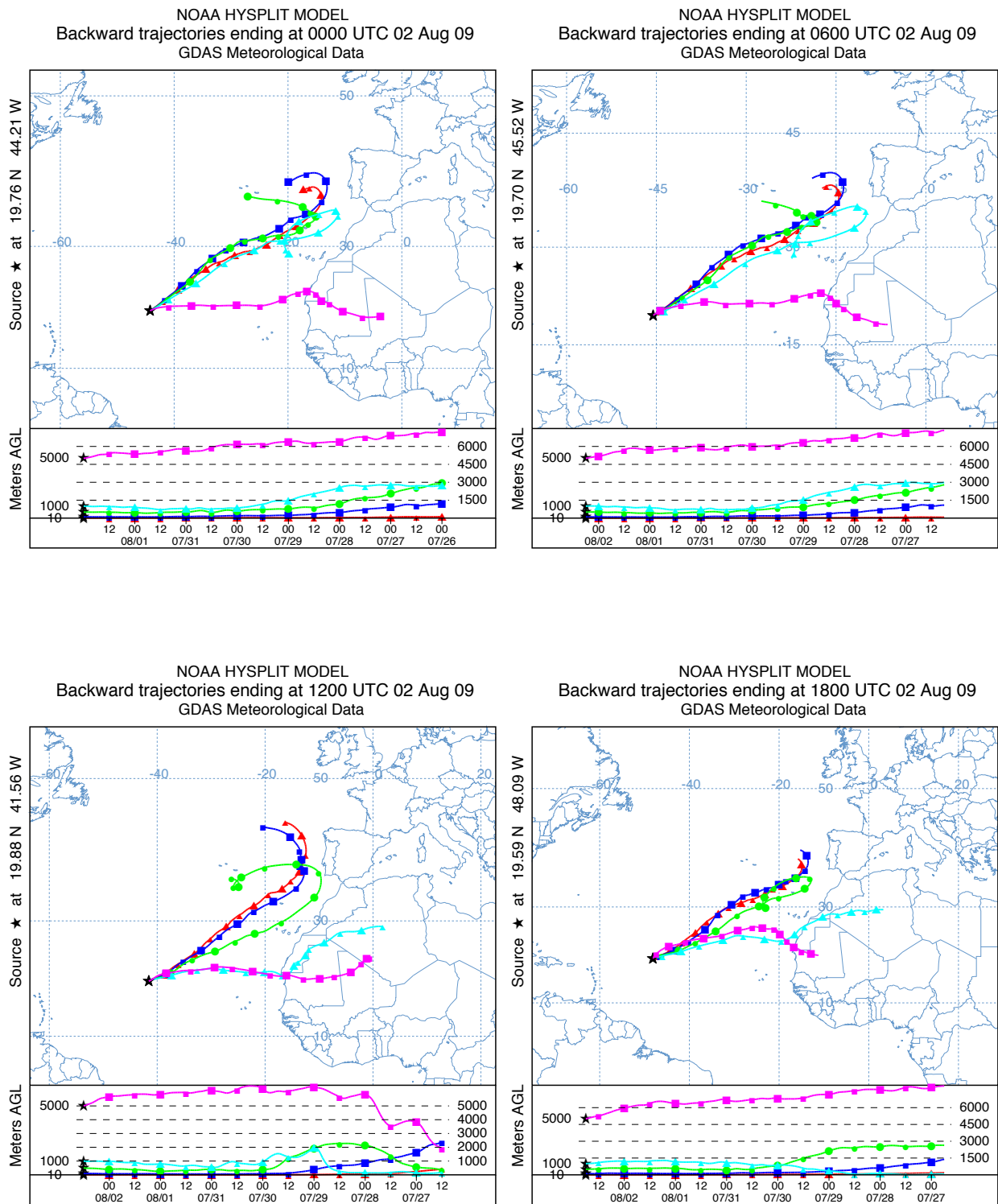


Figure (59) – 7-day backward trajectories; each color corresponds to trajectory height: red 10m, blue 100m, green 500m, cyan 1000m and magenta 5000m.

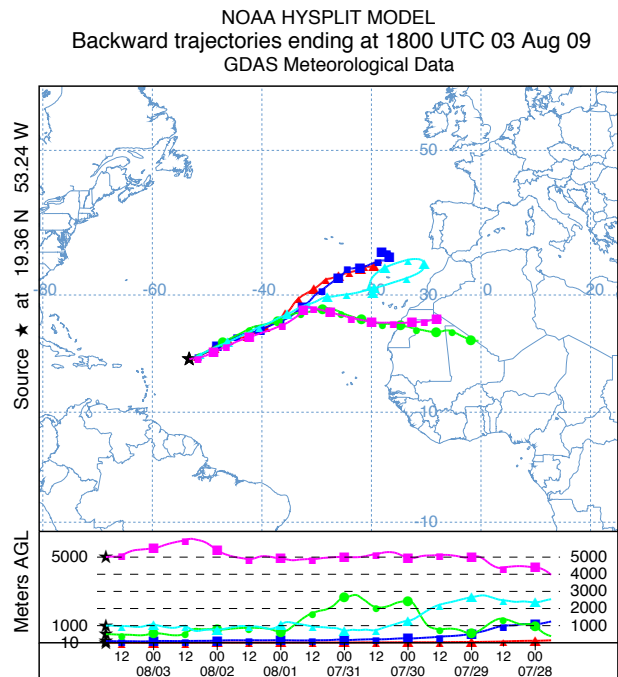
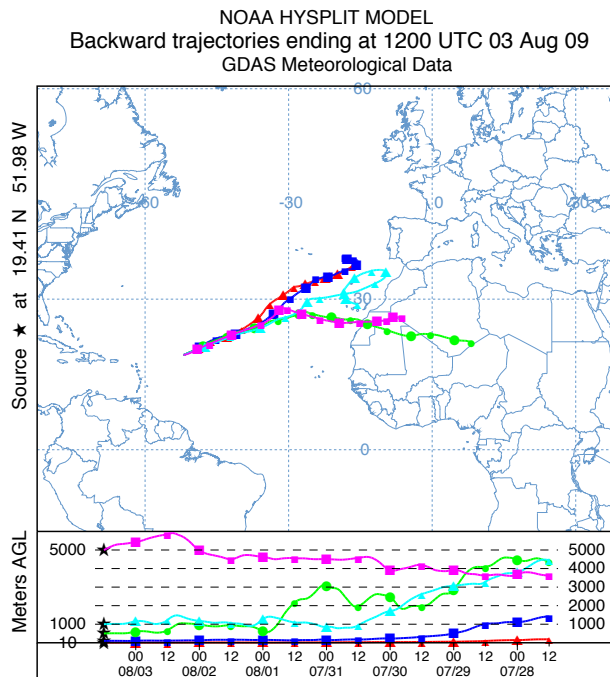
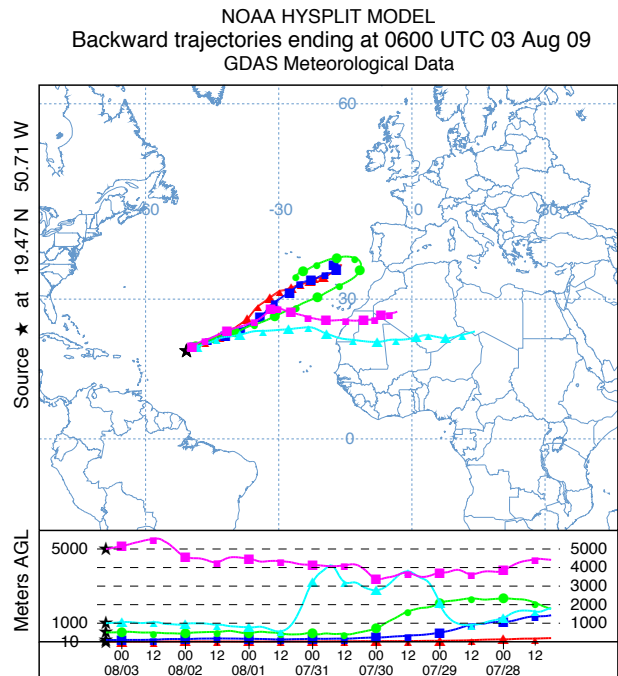
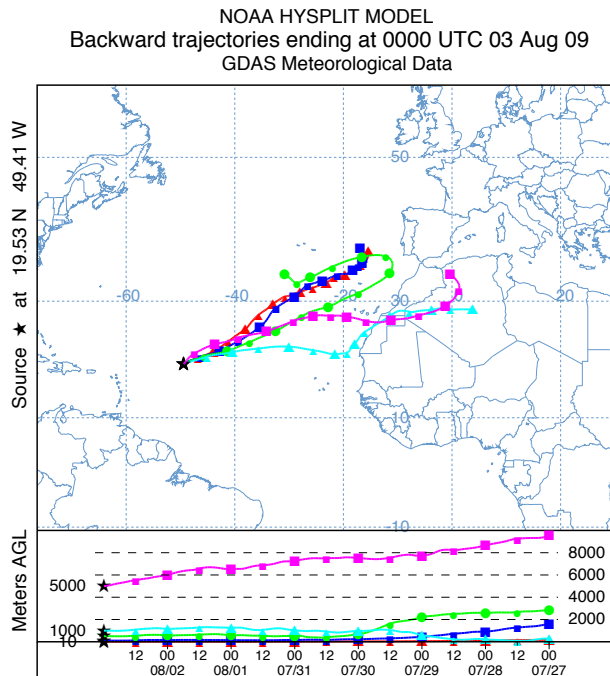


Figure (60) – 7-day backward trajectories; each color corresponds to trajectory height: red 10m, blue 100m, green 500m, cyan 1000m and magenta 5000m.

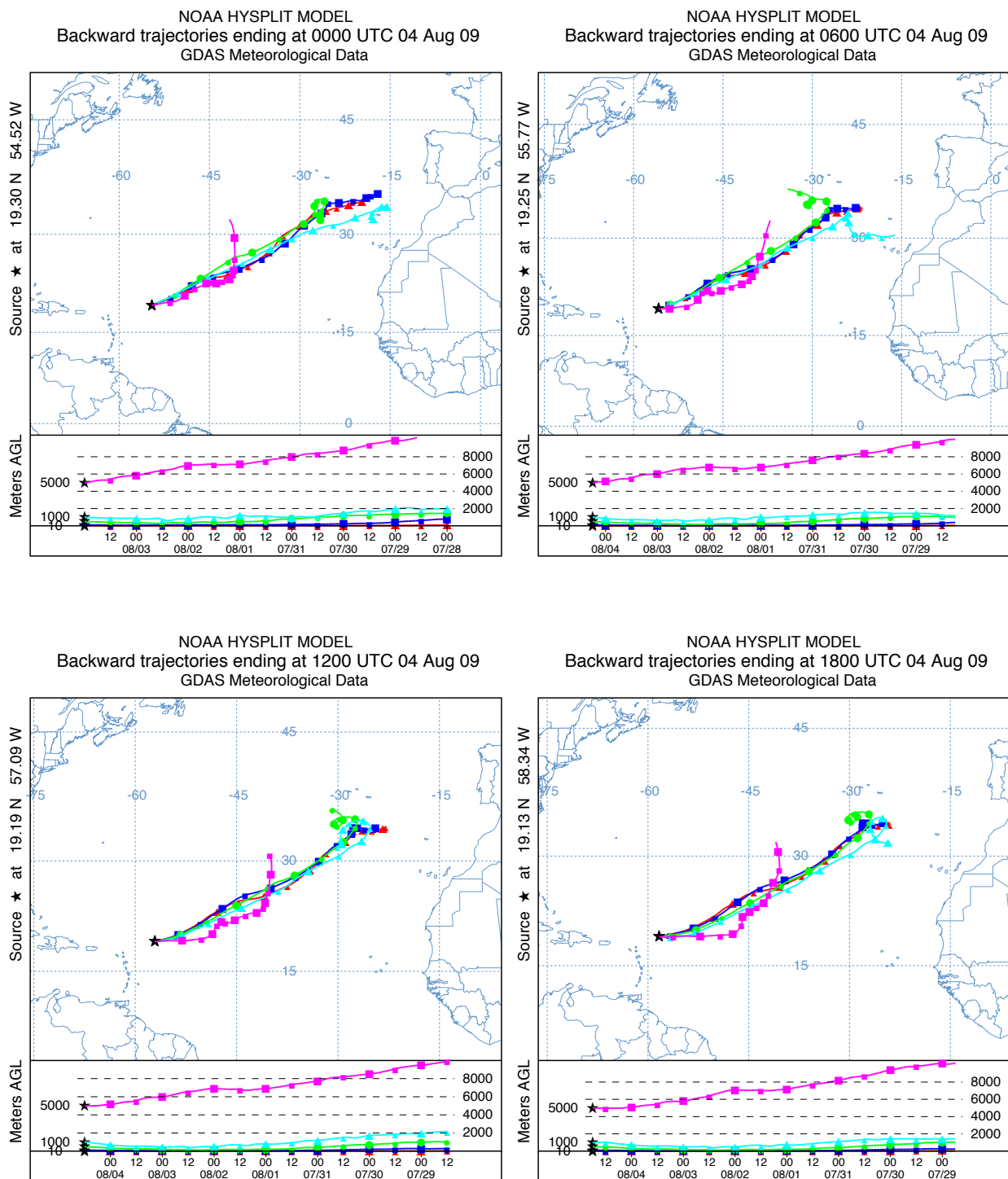


Figure (61) – 7-day backward trajectories; each color corresponds to trajectory height: red 10m, blue 100m, green 500m, cyan 1000m and magenta 5000m.

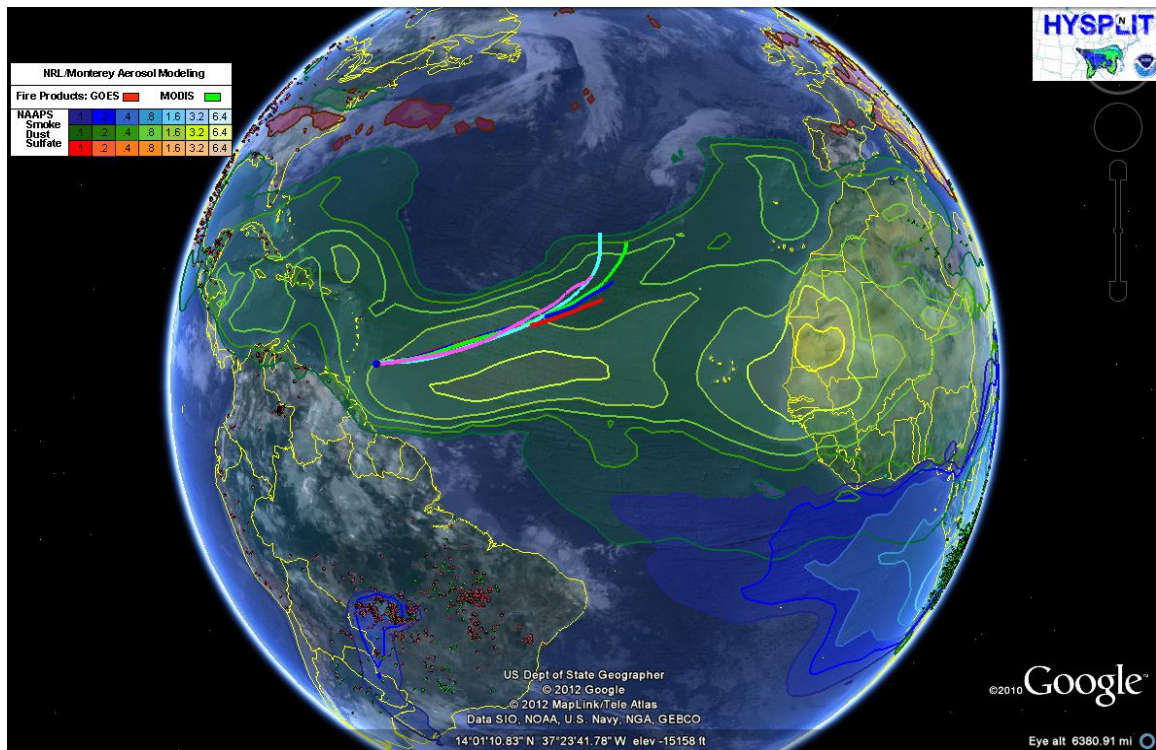


Figure (62) – NAAPS/FLAMBE forecast and HYSPLIT trajectories for 071209 - 00hrs

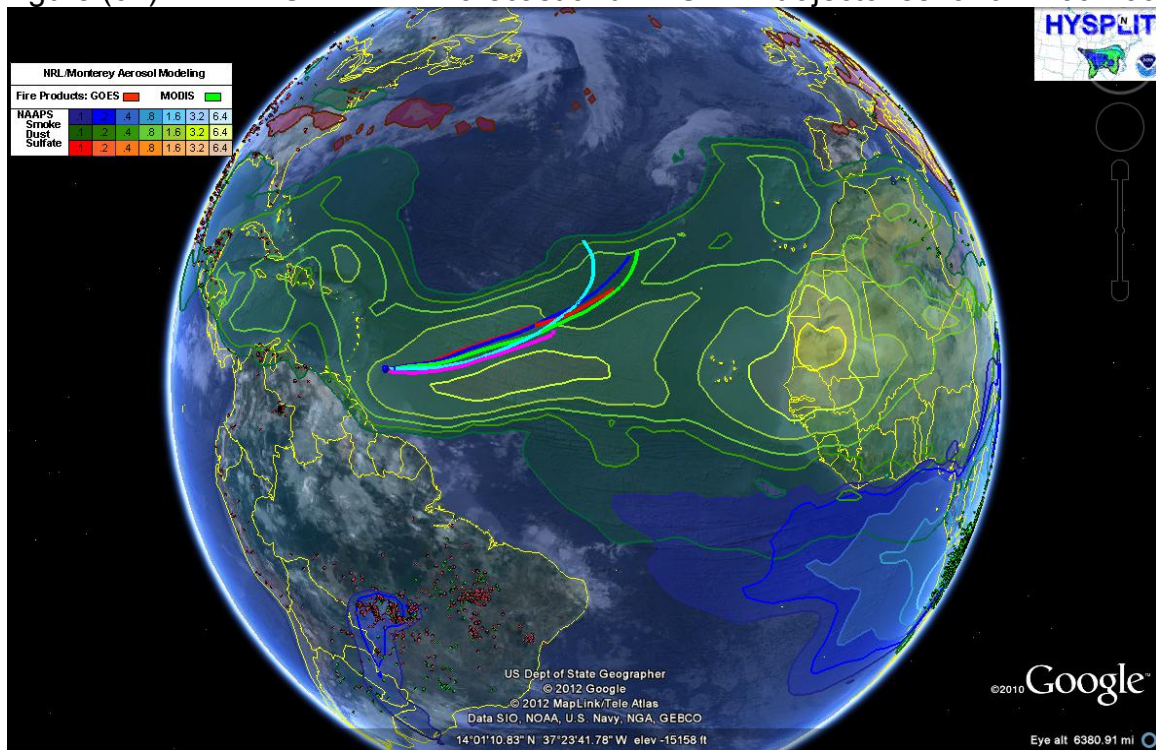


Figure (63) – NAAPS/FLAMBE forecast and HYSPLIT trajectories for 071209 – 06hrs

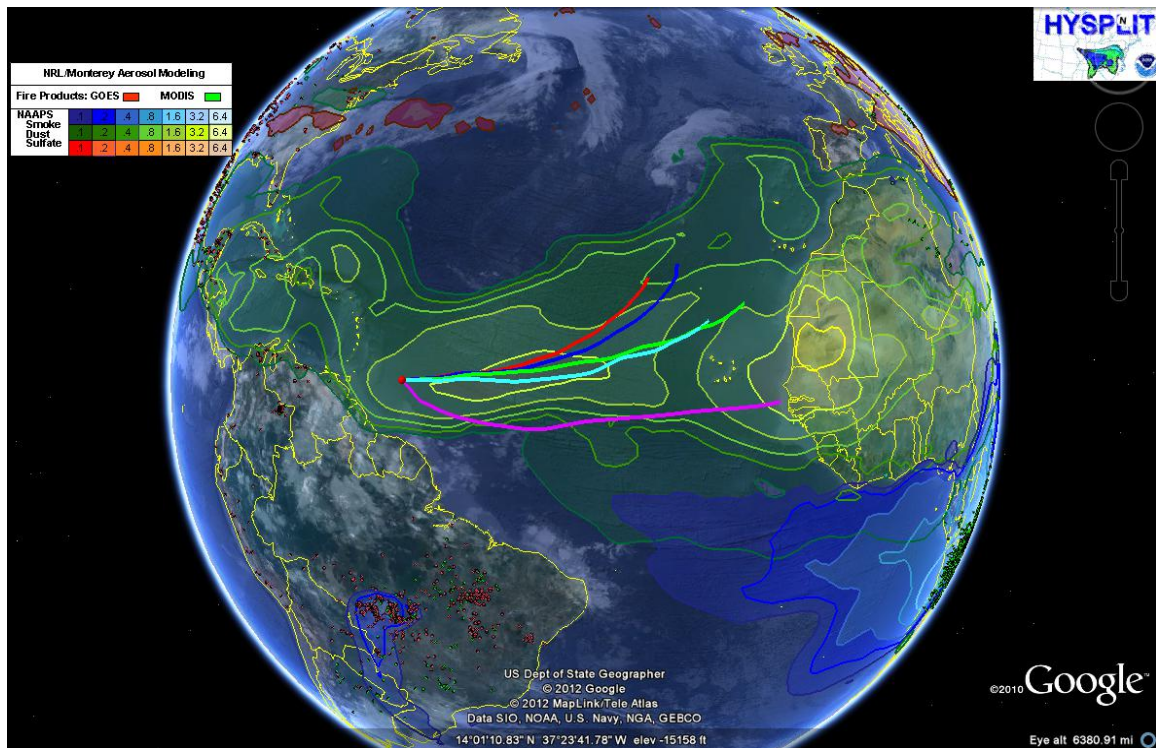


Figure (64) – NAAPS/FLAMBE forecast and HYSPLIT trajectories for 071209 – 12hrs

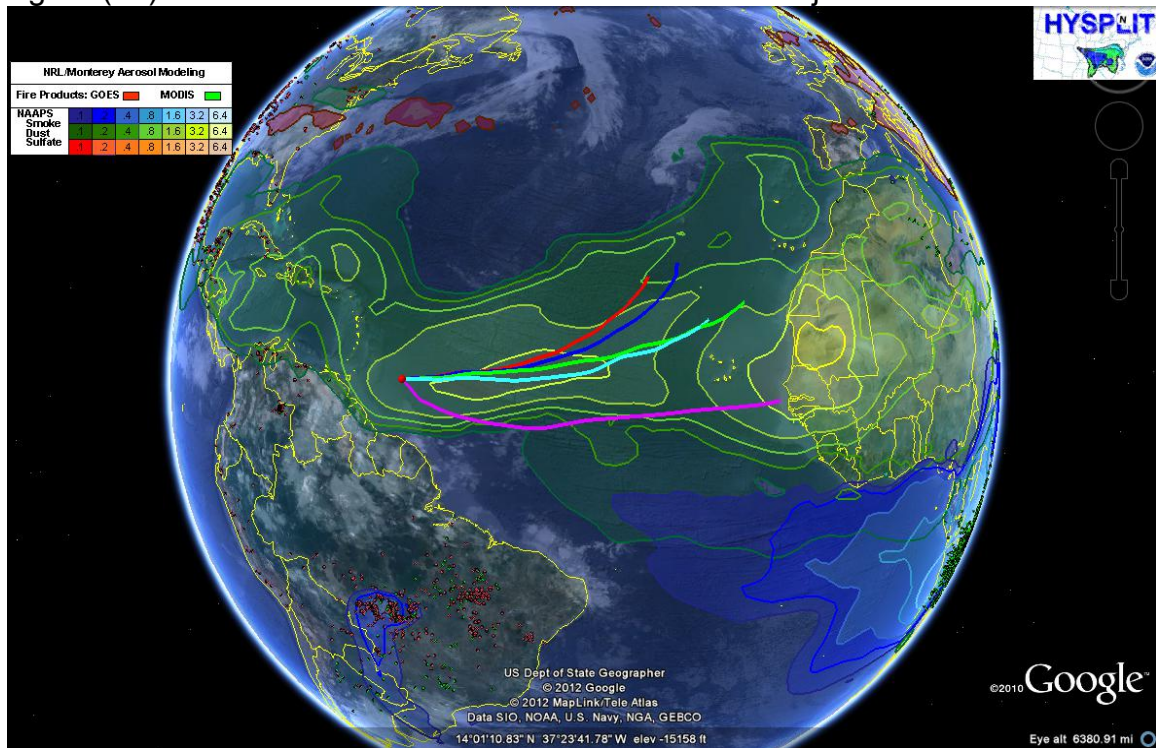


Figure (65) – NAAPS/FLAMBE forecast and HYSPLIT trajectories for 071209 – 18hrs

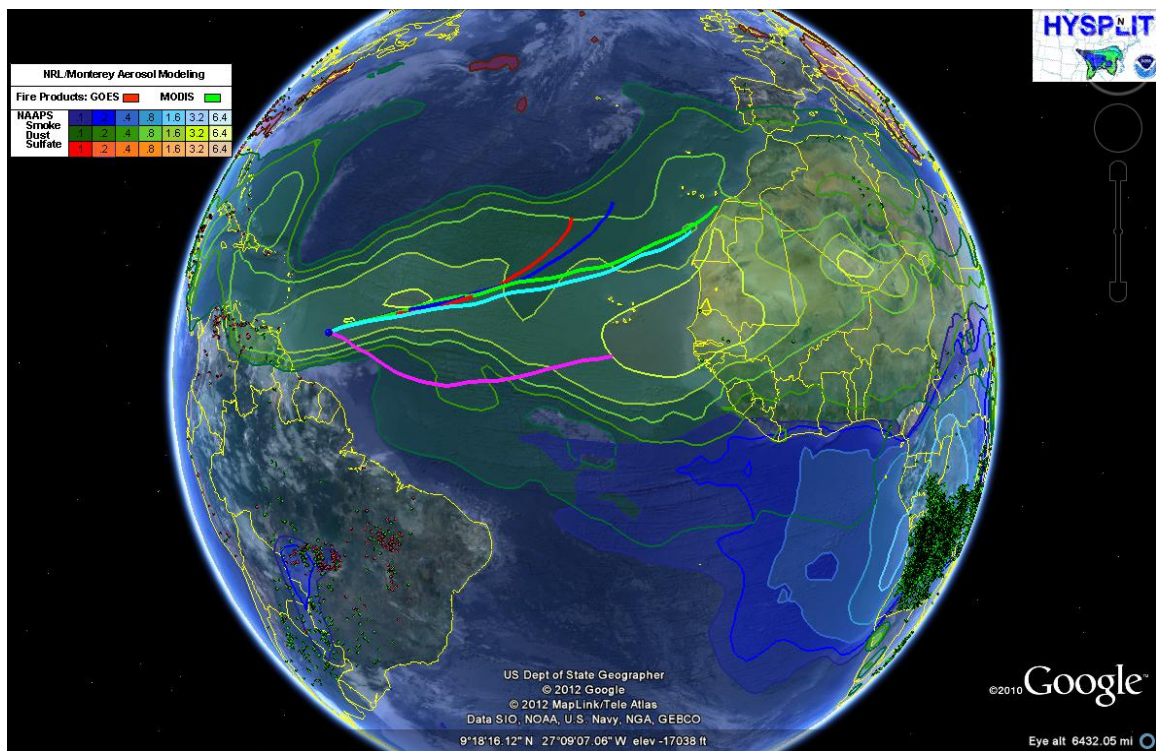


Figure (66) – NAAPS/FLAMBE forecast and HYSPLIT trajectories for 071309 – 00hrs

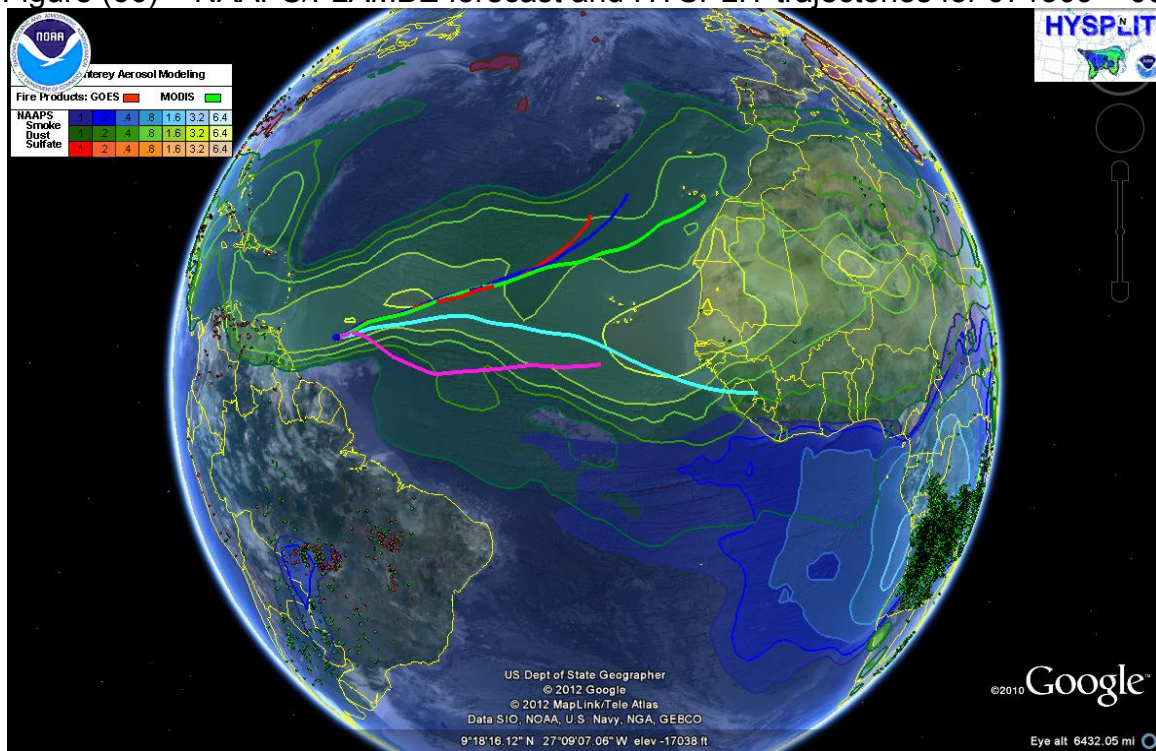


Figure (67) – NAAPS/FLAMBE forecast and HYSPLIT trajectories for 071309 – 06hrs

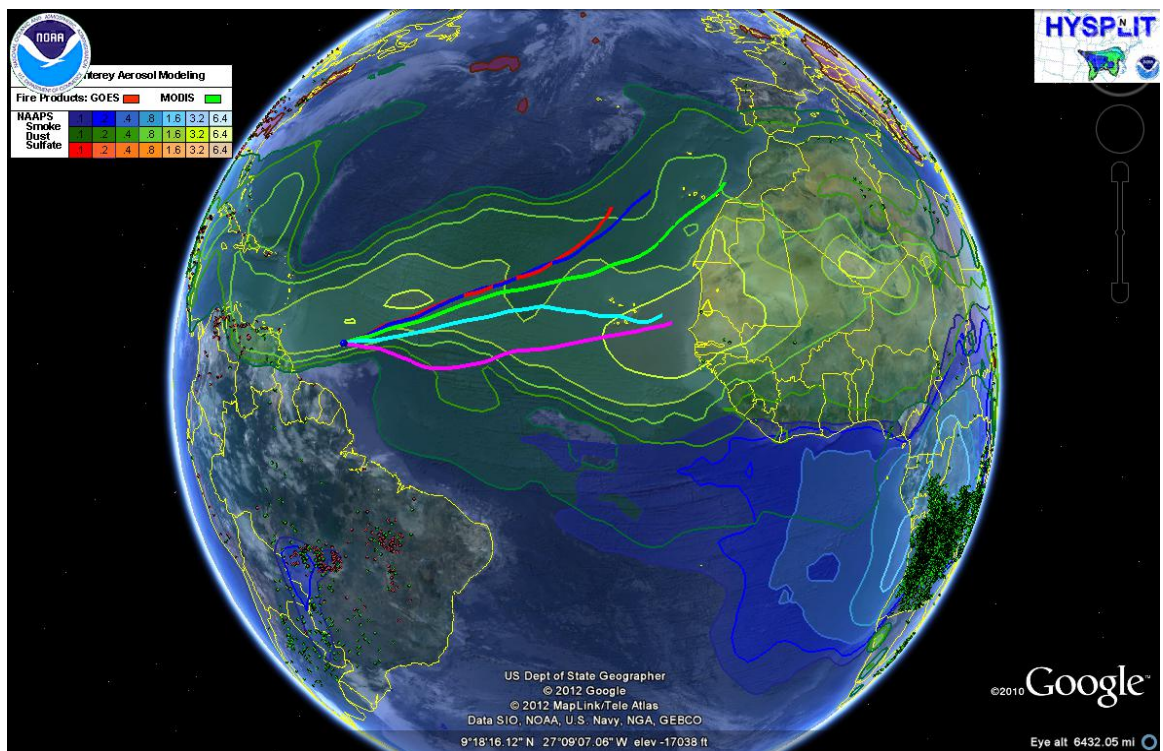


Figure (68) – NAAPS/FLAMBE forecast and HYSPLIT trajectories for 071309 – 12hrs

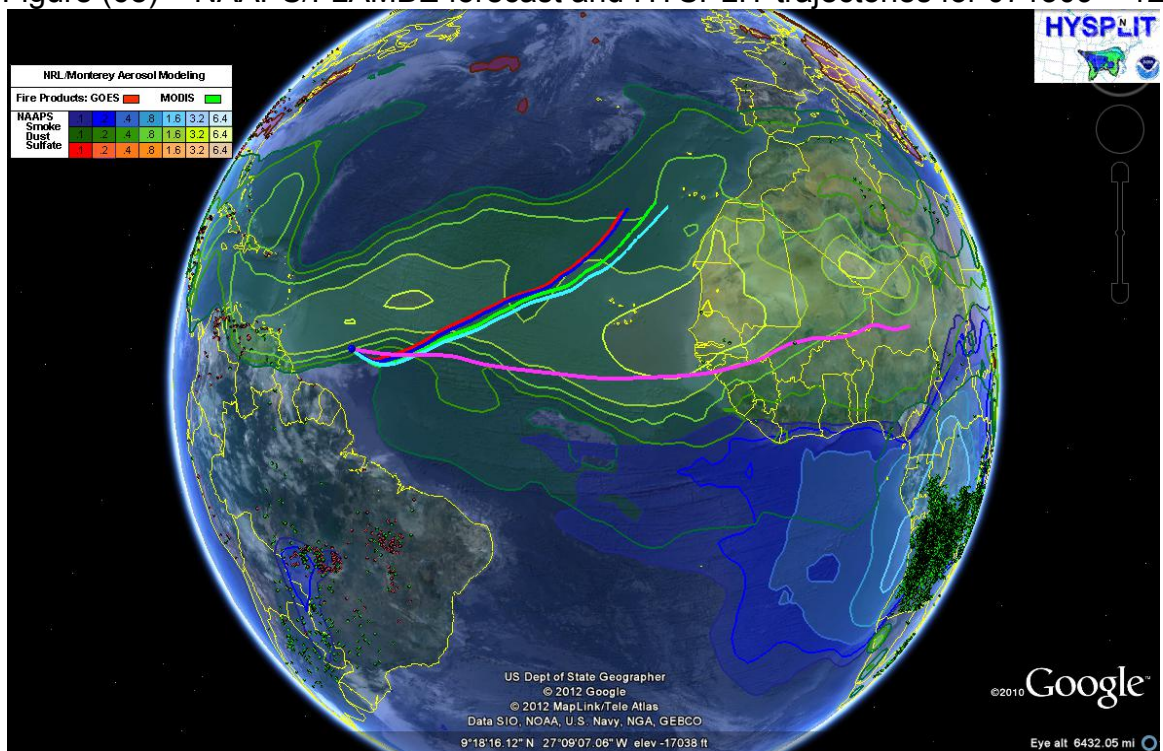


Figure (69) – NAAPS/FLAMBE forecast and HYSPLIT trajectories for 071309 – 18hrs

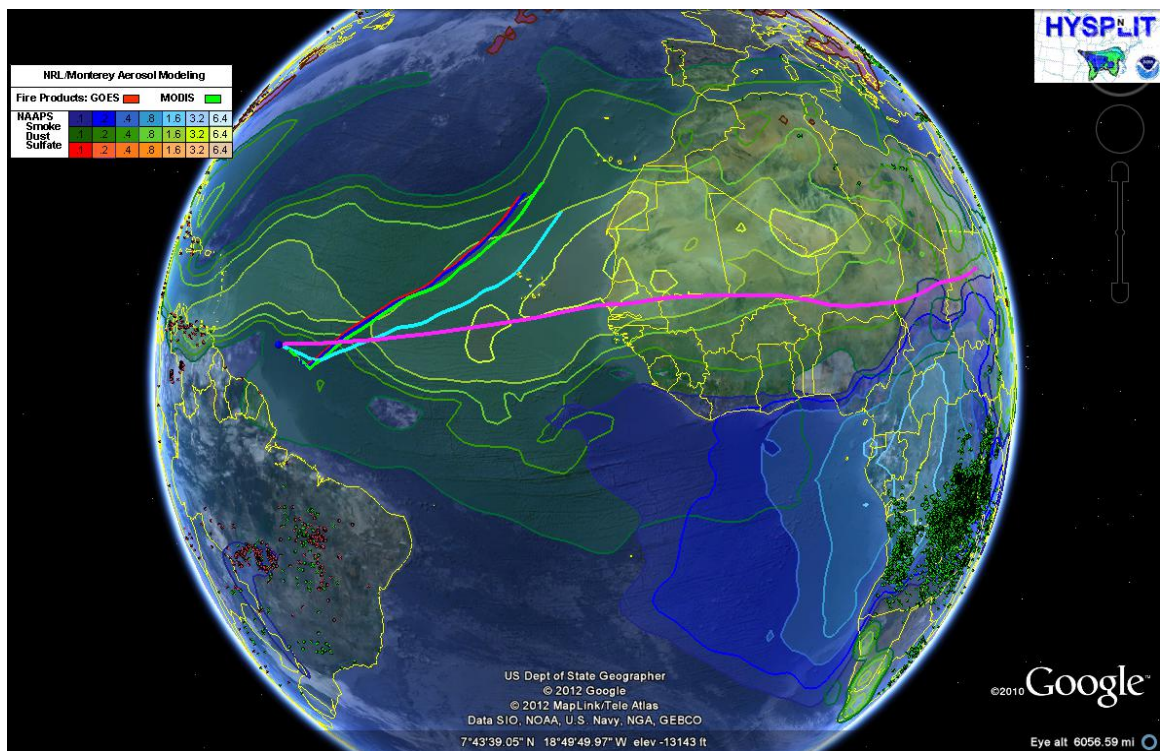


Figure (70) – NAAPS/FLAMBE forecast and HYSPLIT trajectories for 071409 – 00hrs

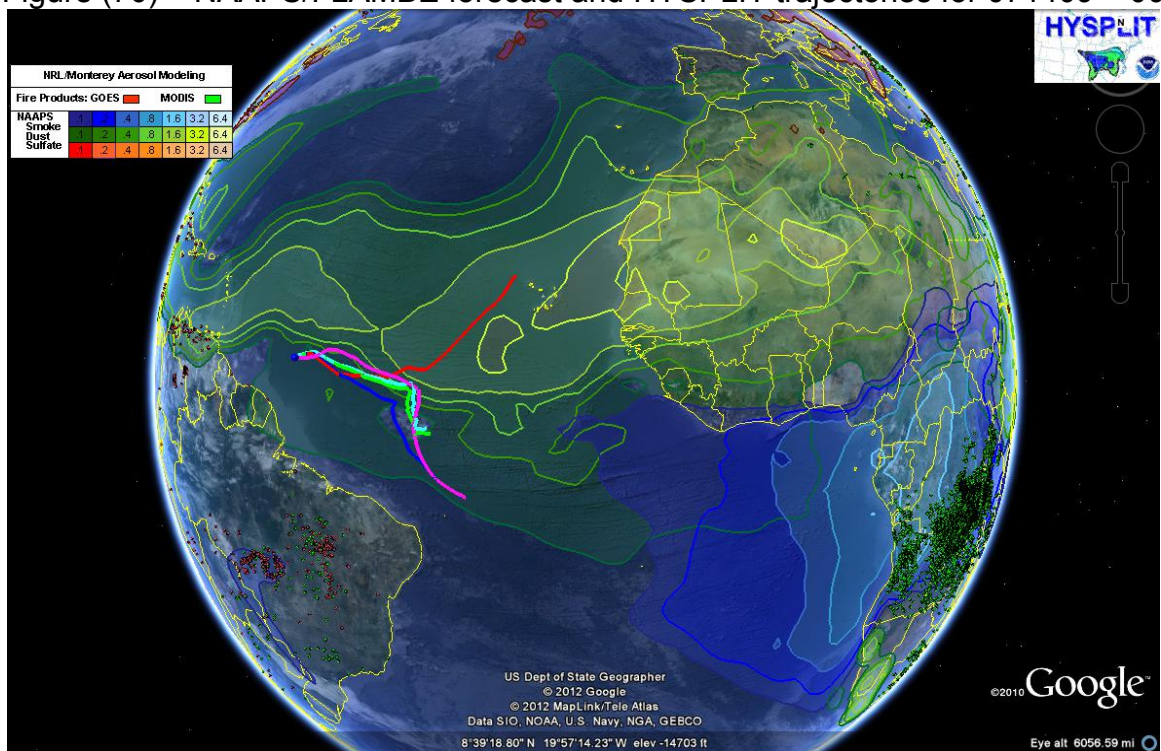


Figure (71) – NAAPS/FLAMBE forecast and HYSPLIT trajectories for 071409 – 06hrs

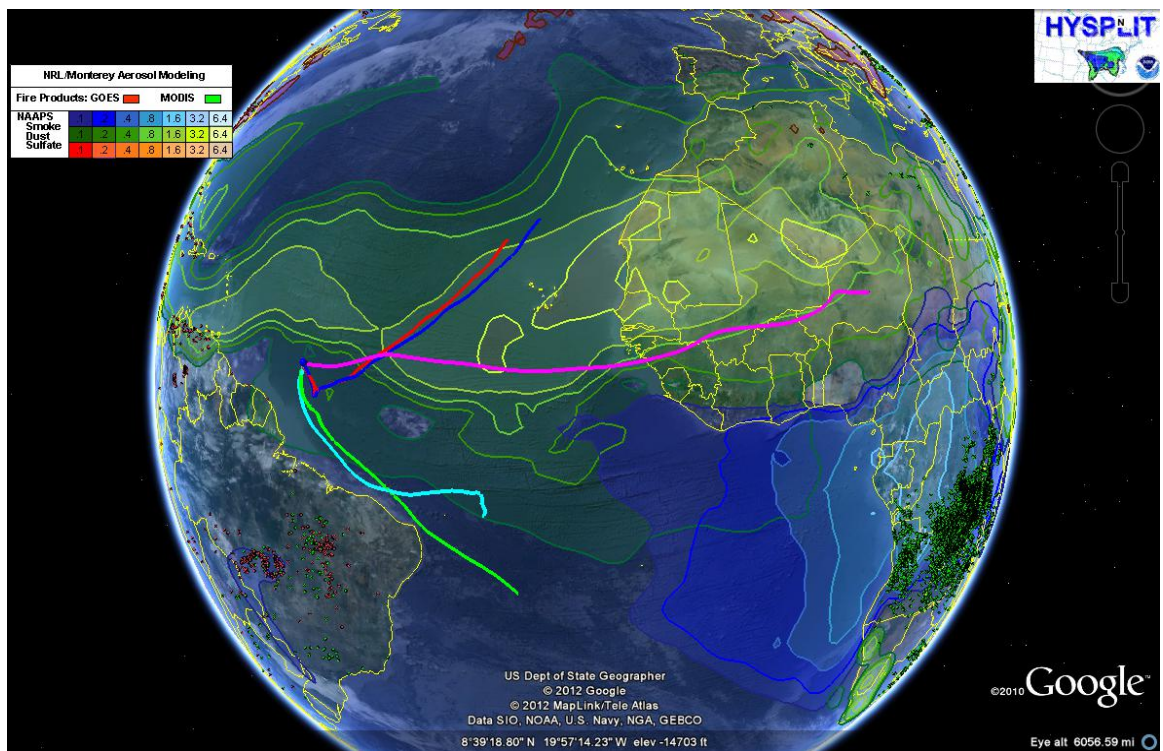


Figure (72) – NAAPS/FLAMBE forecast and HYSPLIT trajectories for 071409 – 12hrs

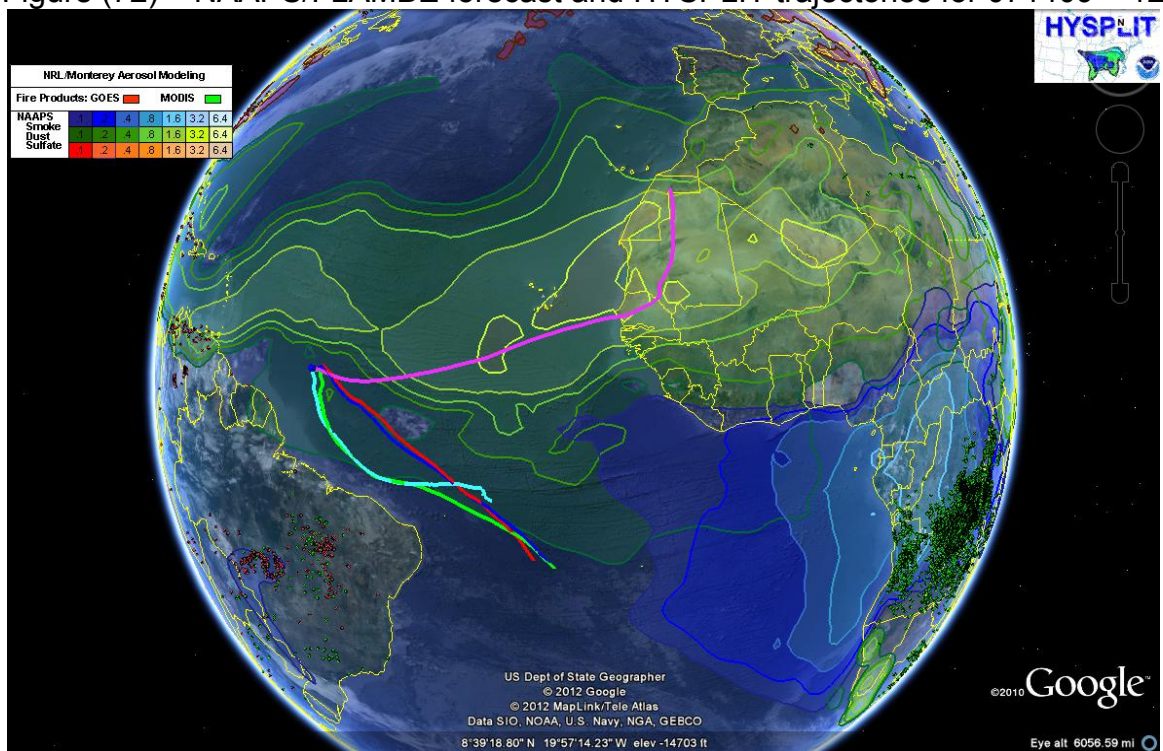


Figure (73) – NAAPS/FLAMBE forecast and HYSPLIT trajectories for 071409 – 18hrs

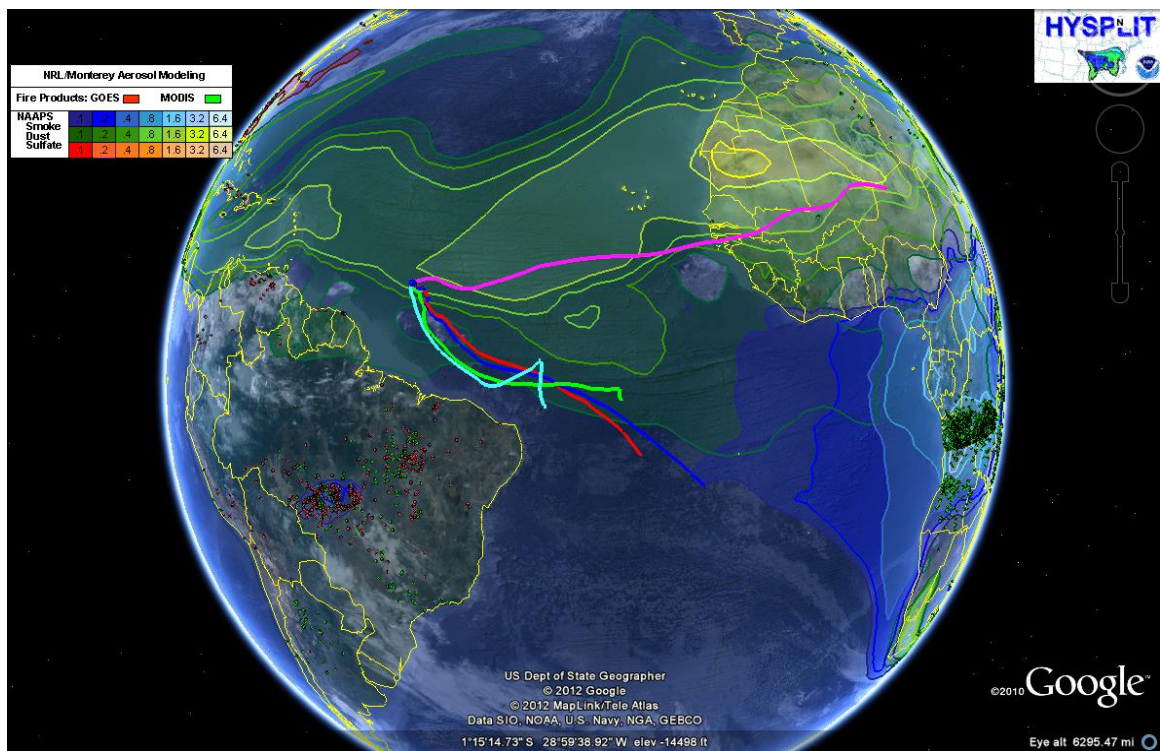


Figure (74) – NAAPS/FLAMBE forecast and HYSPLIT trajectories for 071509 – 00hrs

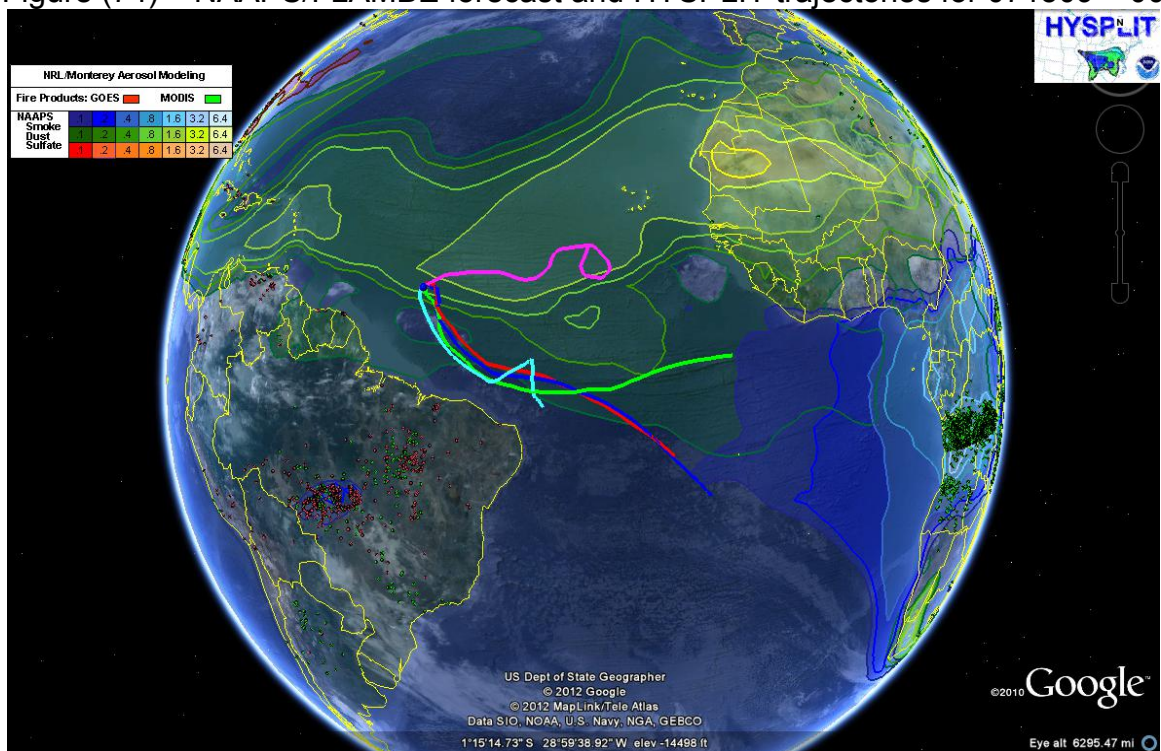


Figure (75) – NAAPS/FLAMBE forecast and HYSPLIT trajectories for 071509 – 06hrs

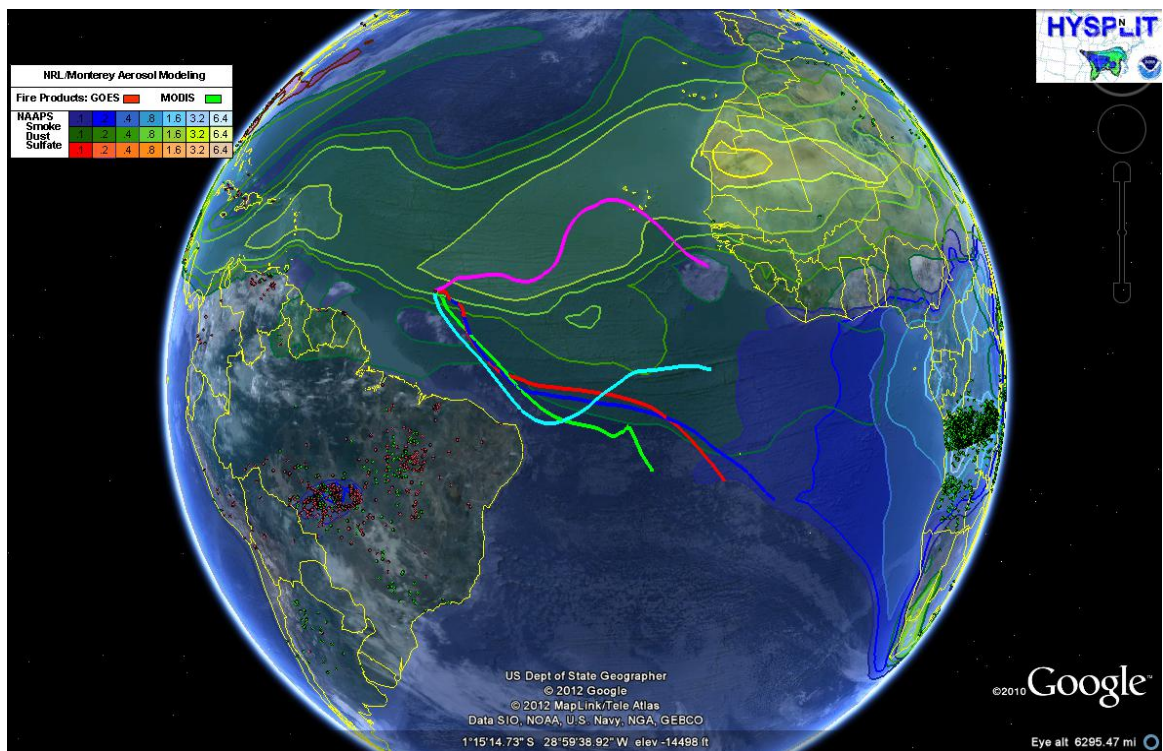


Figure (76) – NAAPS/FLAMBE forecast and HYSPLIT trajectories for 071509 – 12hrs



Figure (77) – NAAPS/FLAMBE forecast and HYSPLIT trajectories for 071509 – 18hrs

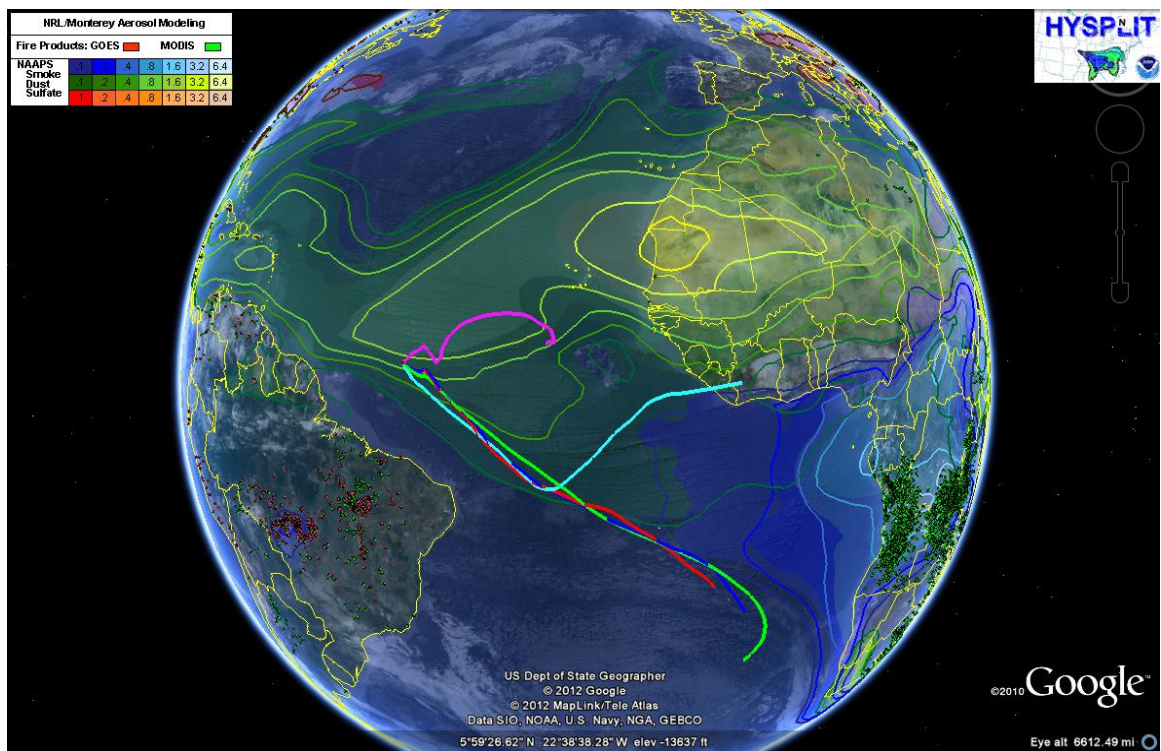


Figure (78) – NAAPS/FLAMBE forecast and HYSPLIT trajectories for 071609 – 00hrs

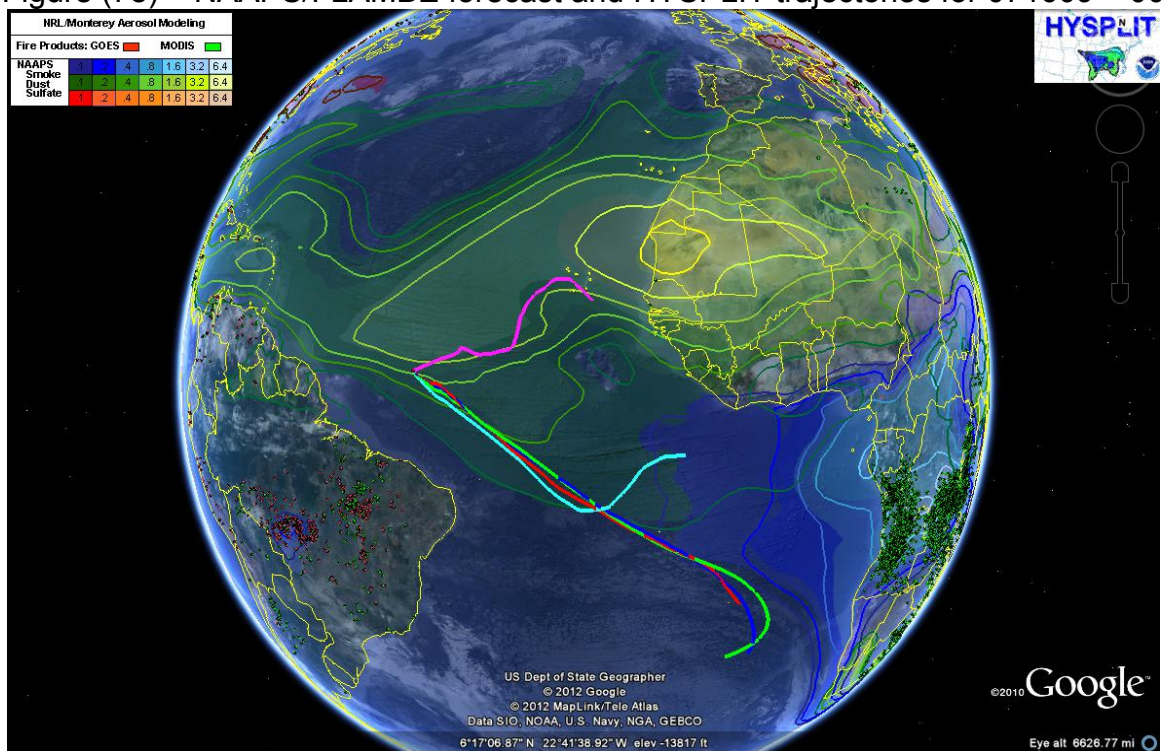


Figure (79) – NAAPS/FLAMBE forecast and HYSPLIT trajectories for 071609 – 06hrs

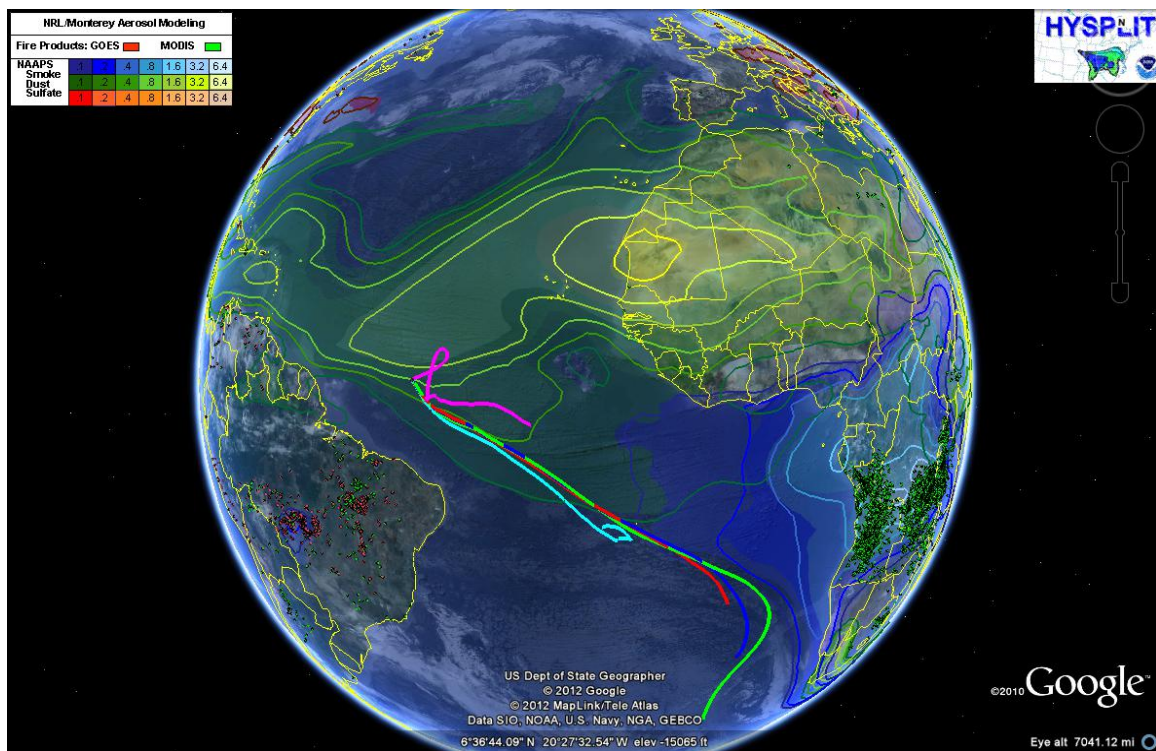


Figure (80) – NAAPS/FLAMBE forecast and HYSPLIT trajectories for 071609 – 12 hrs

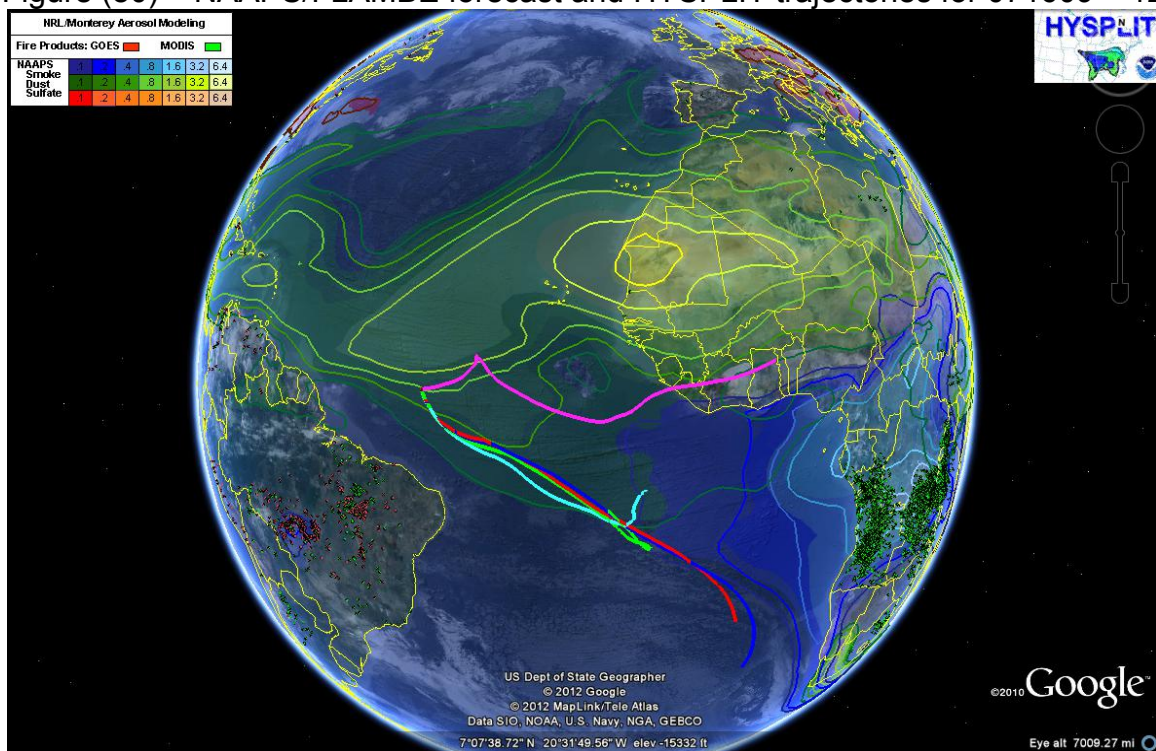


Figure (81) – NAAPS/FLAMBE forecast and HYSPLIT trajectories for 071609 – 18hrs

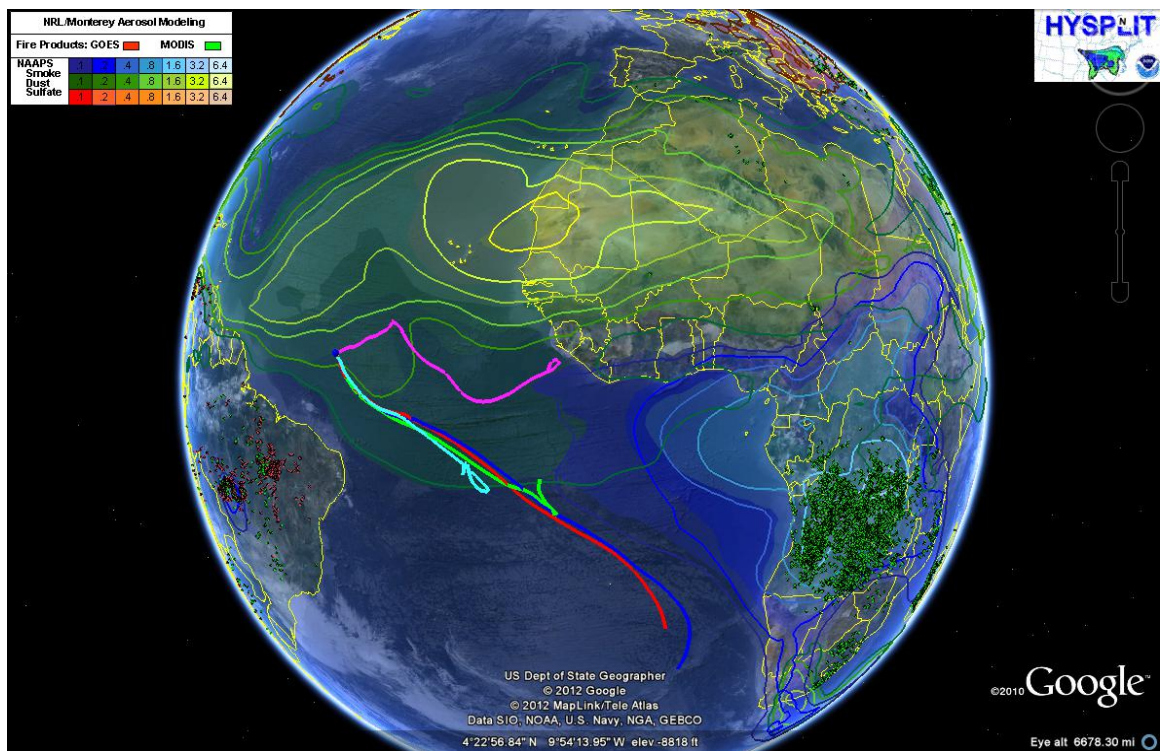


Figure (82) – NAAPS/FLAMBE forecast and HYSPLIT trajectories for 071709 – 00hrs

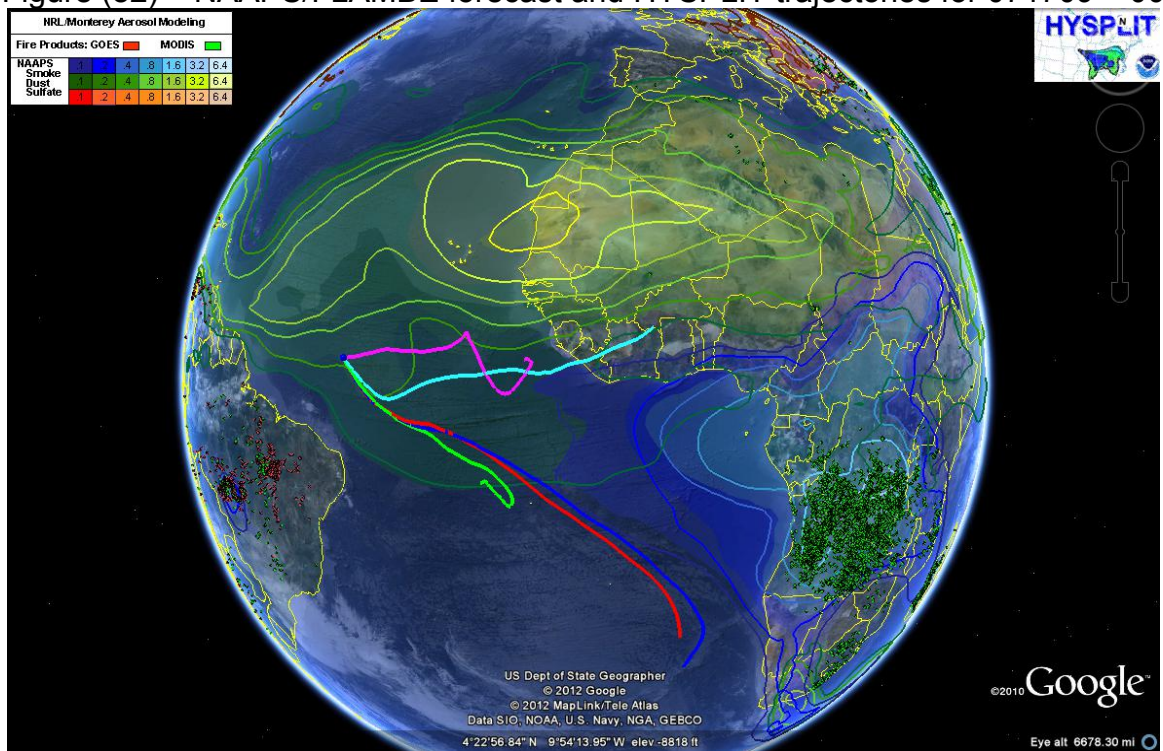


Figure (83) – NAAPS/FLAMBE forecast and HYSPLIT trajectories for 071709 – 06hrs

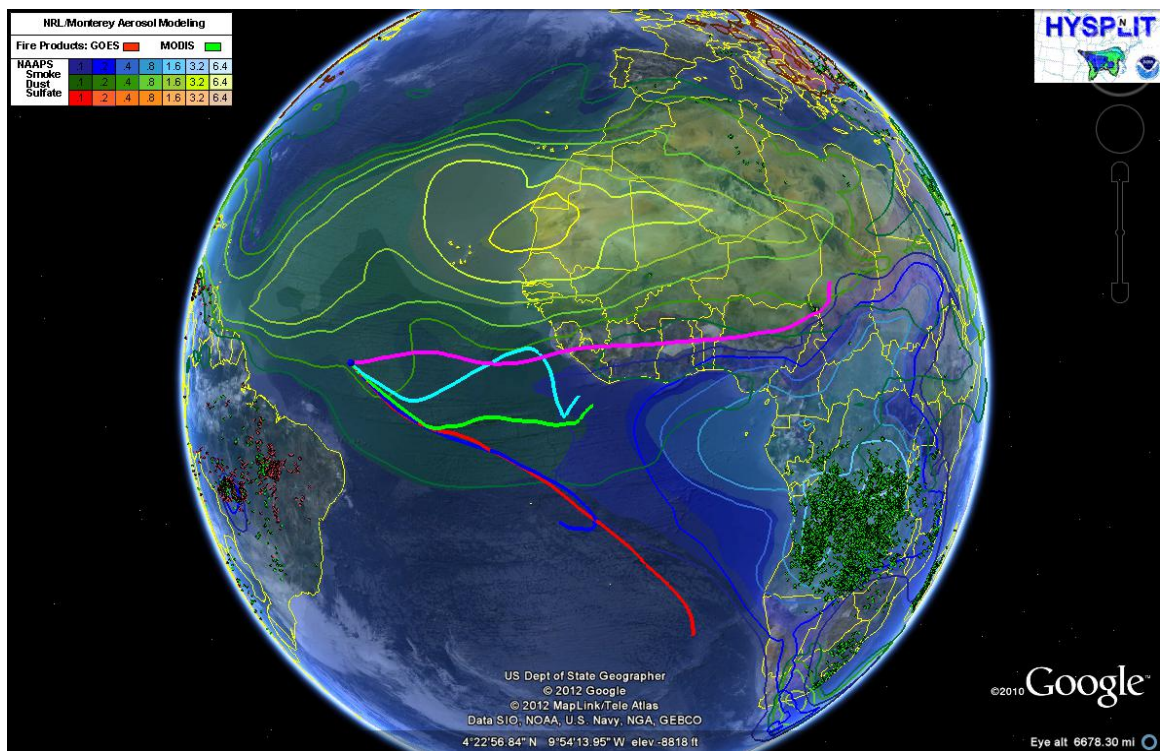


Figure (84) – NAAPS/FLAMBE forecast and HYSPLIT trajectories for 071709 – 12hrs

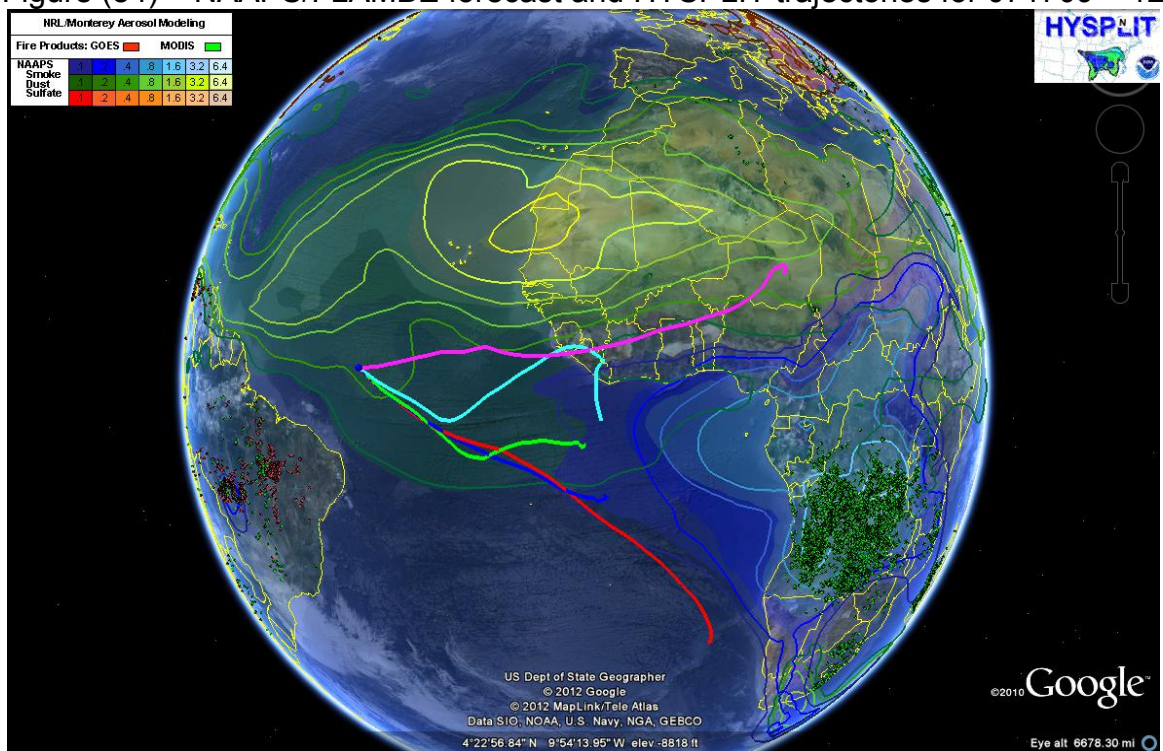


Figure (85) – NAAPS/FLAMBE forecast and HYSPLIT trajectories for 071709 – 18hrs

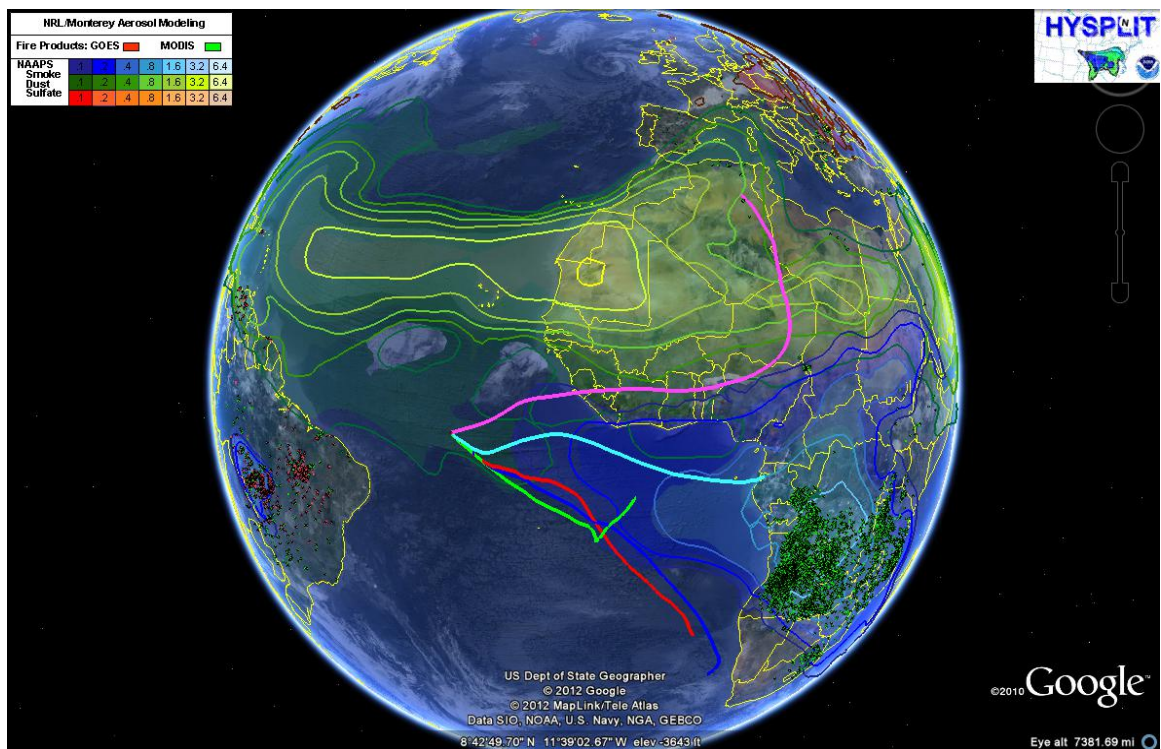


Figure (86) – NAAPS/FLAMBE forecast and HYSPLIT trajectories for 072009 – 00hrs

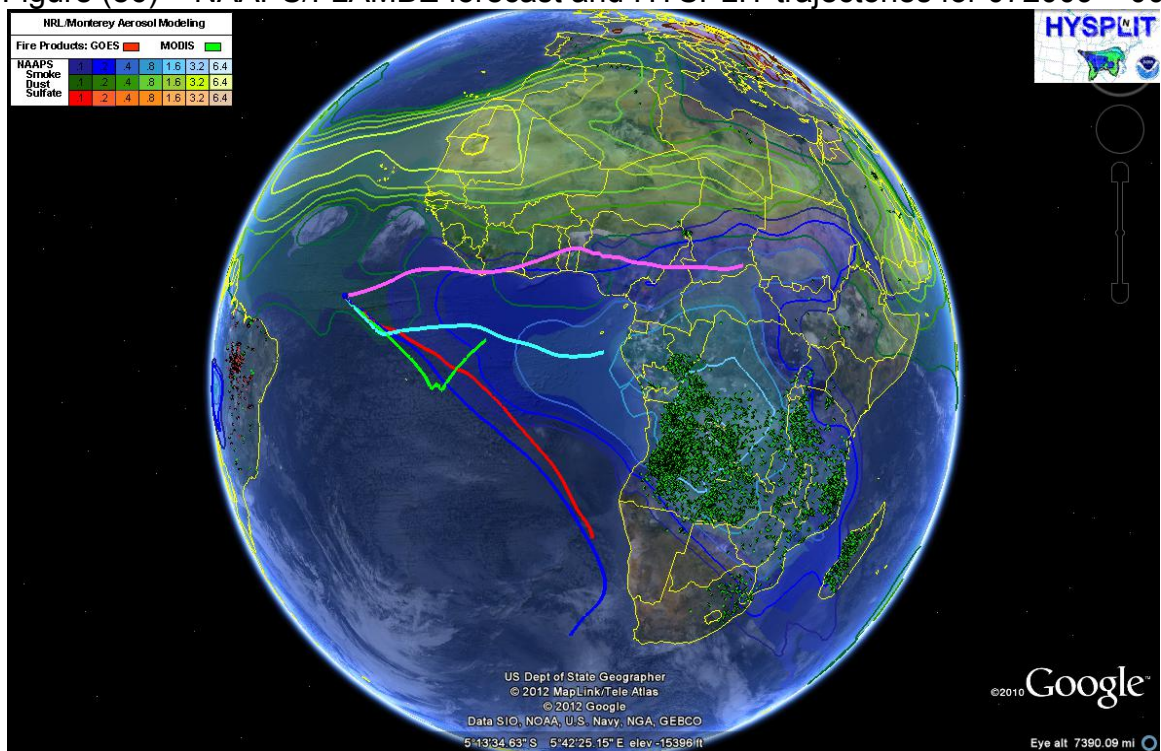


Figure (87) – NAAPS/FLAMBE forecast and HYSPLIT trajectories for 072009 – 06hrs

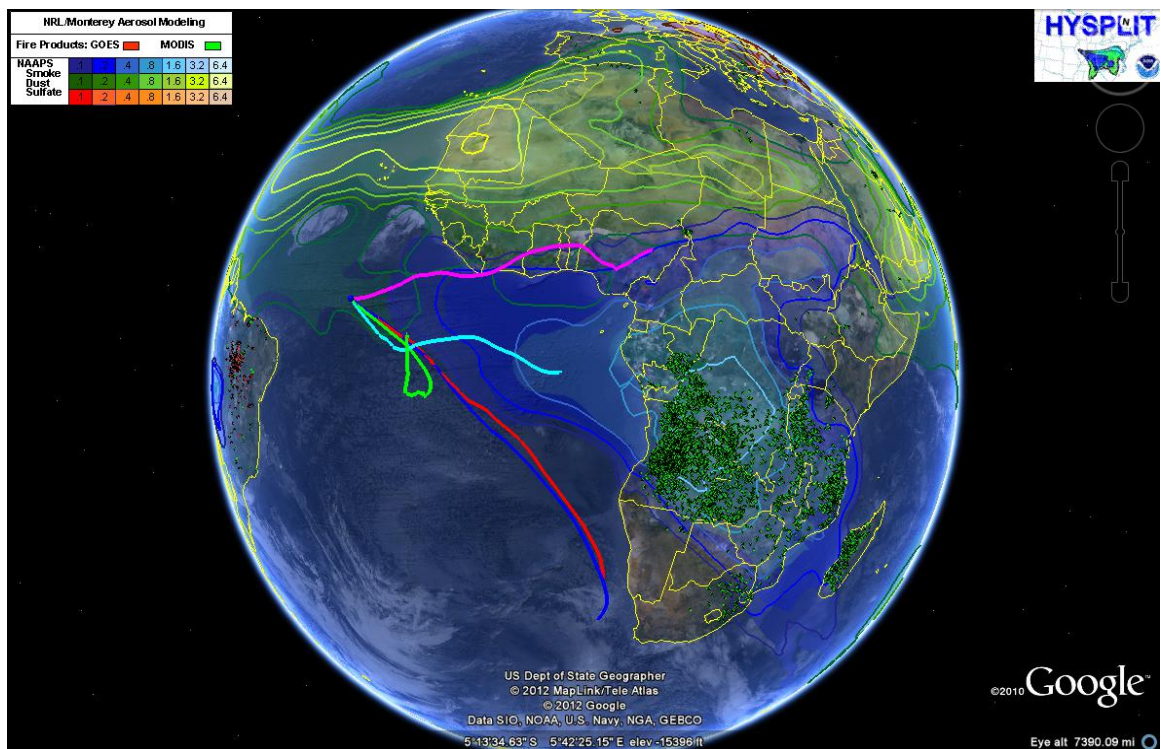


Figure (88) – NAAPS/FLAMBE forecast and HYSPLIT trajectories for 072009 – 12hrs

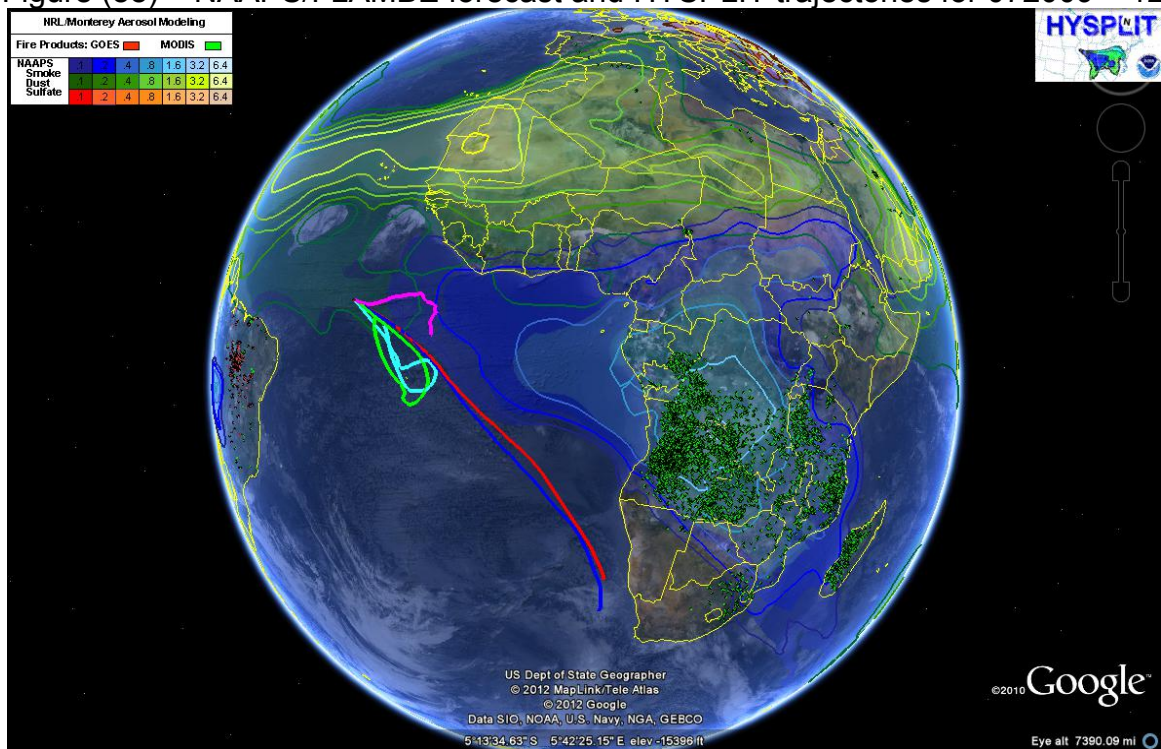


Figure (89) – NAAPS/FLAMBE forecast and HYSPLIT trajectories for 072009 – 18hrs

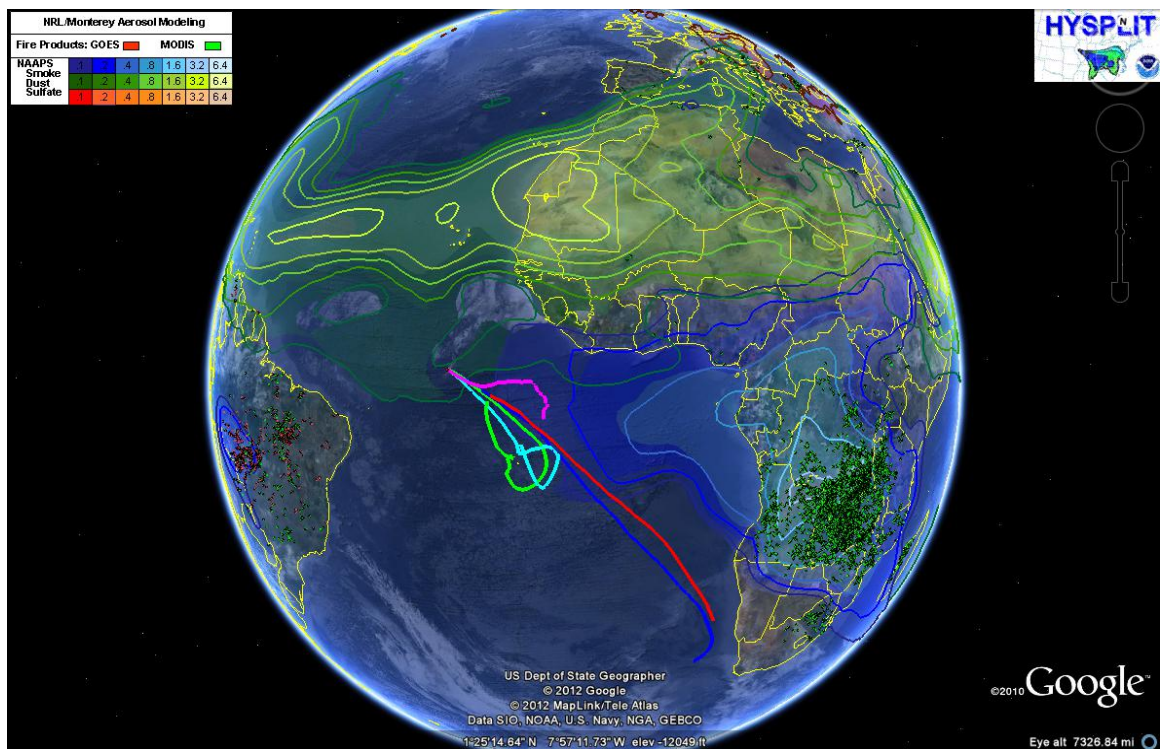


Figure (90) – NAAPS/FLAMBE forecast and HYSPLIT trajectories for 072109 – 00hrs

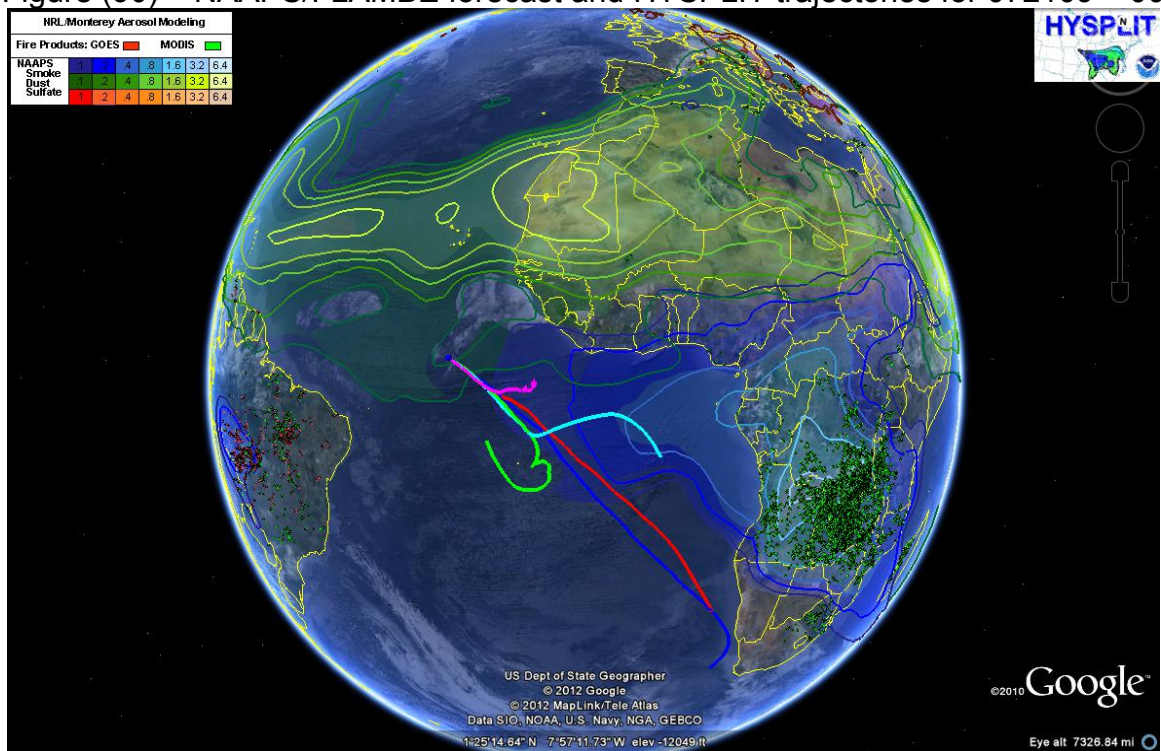


Figure (91) – NAAPS/FLAMBE forecast and HYSPLIT trajectories for 072109 – 06hrs

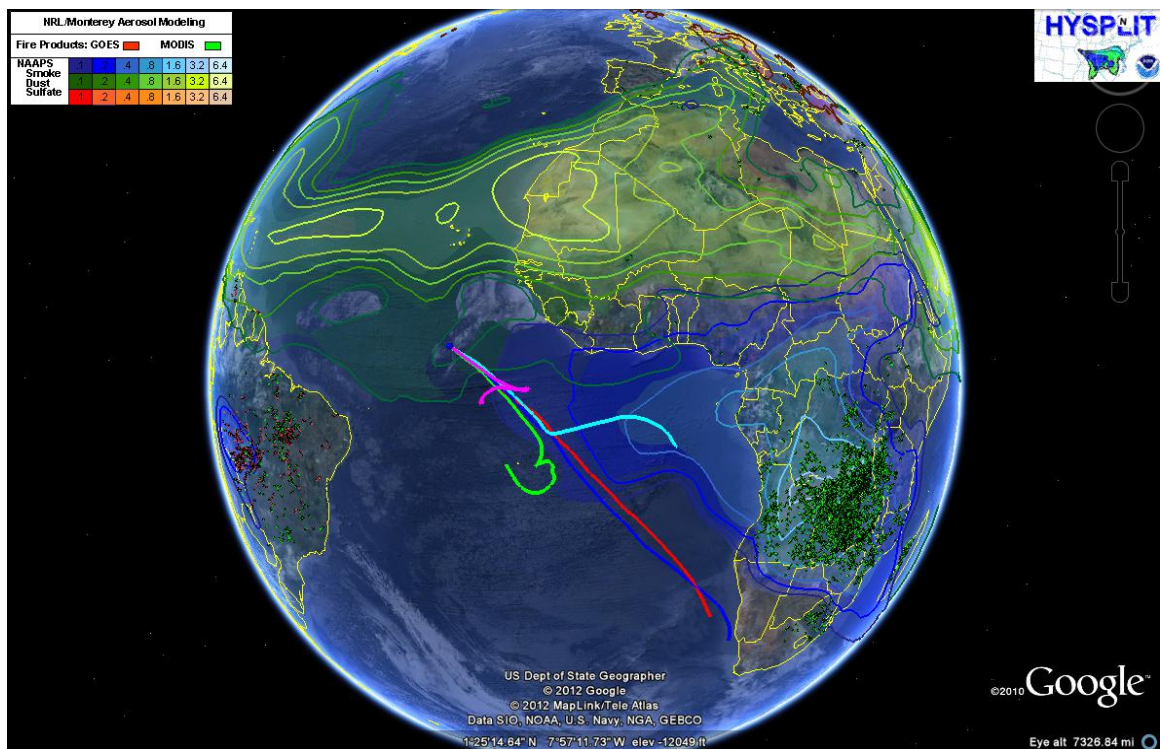


Figure (92) – NAAPS/FLAMBE forecast and HYSPLIT trajectories for 072109 – 12

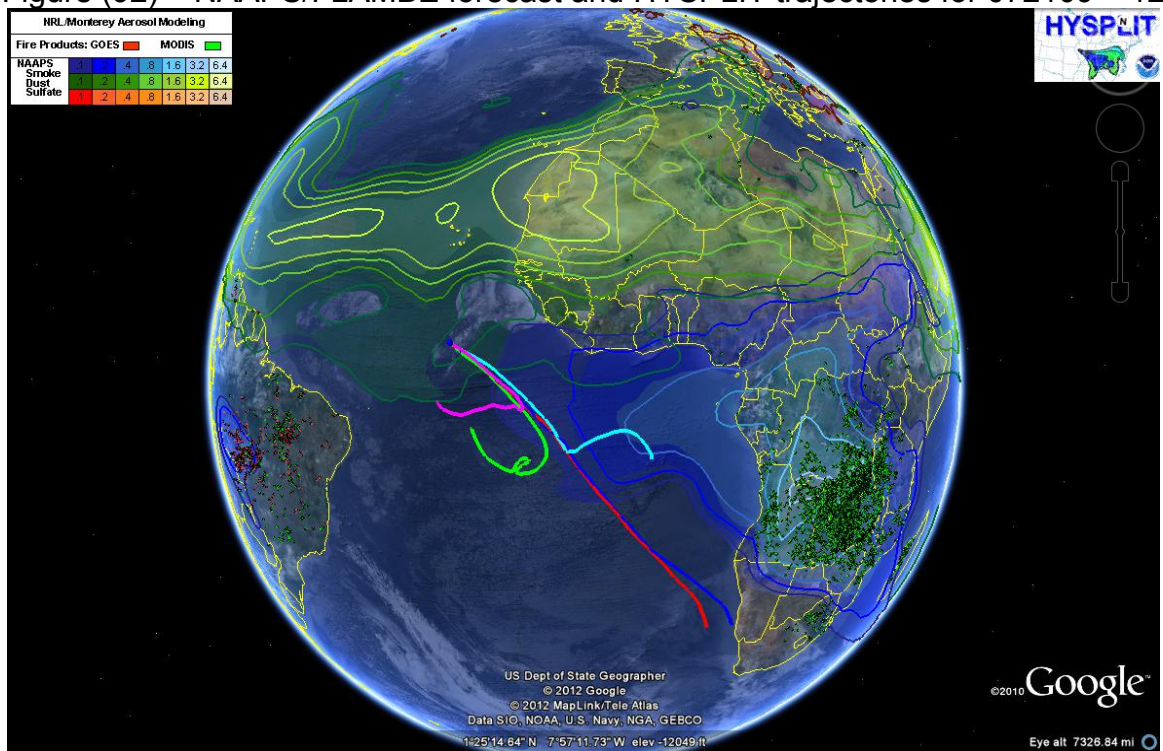


Figure (93) – NAAPS/FLAMBE forecast and HYSPLIT trajectories for 072109 – 18hrs

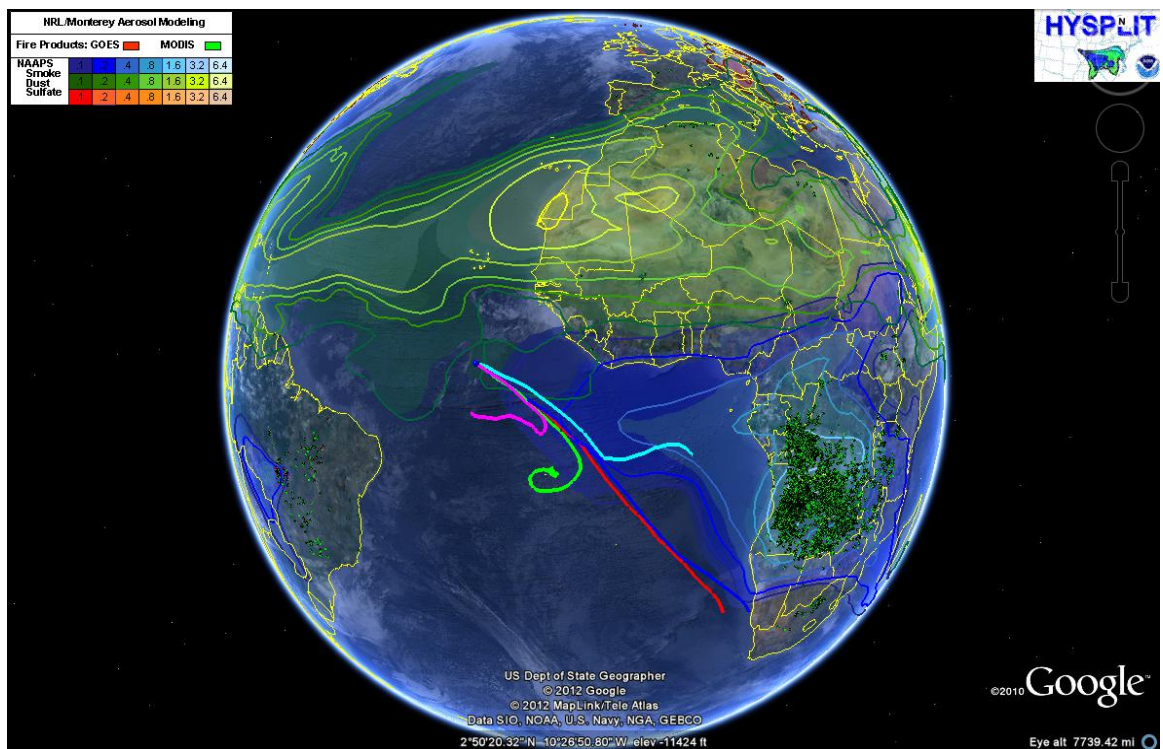


Figure (94) – NAAPS/FLAMBE forecast and HYSPLIT trajectories for 072209 – 00hrs

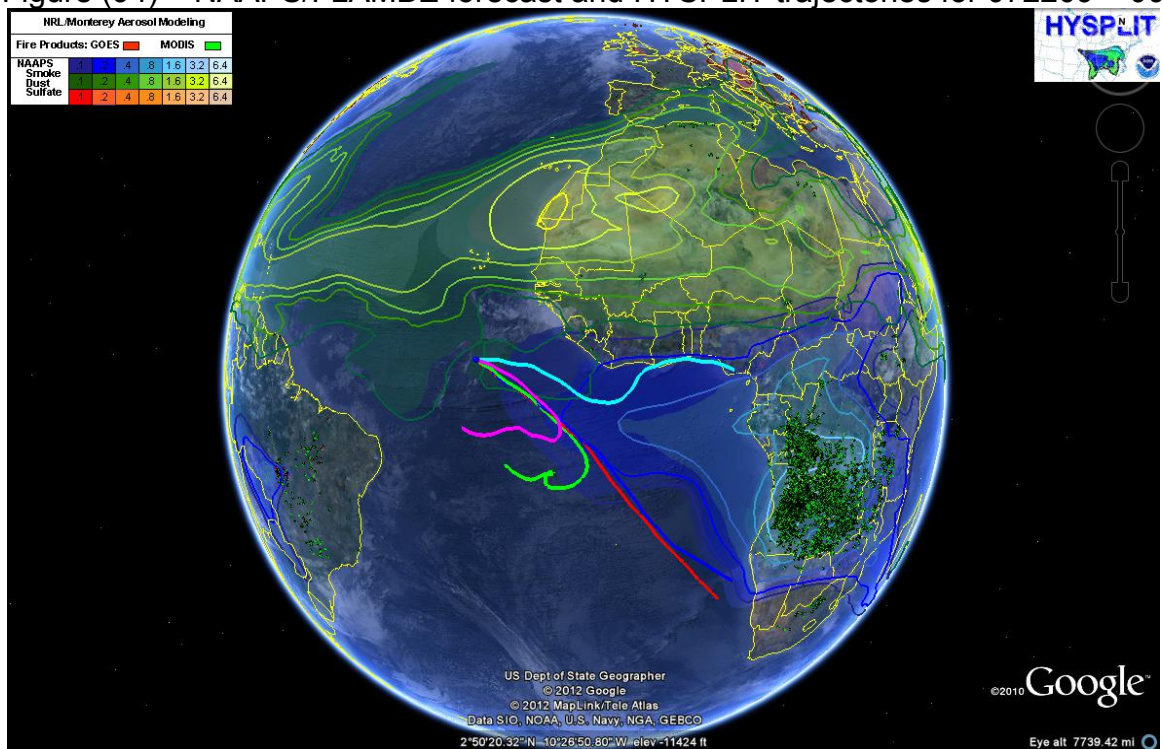


Figure (95) – NAAPS/FLAMBE forecast and HYSPLIT trajectories for 072209 – 06hrs

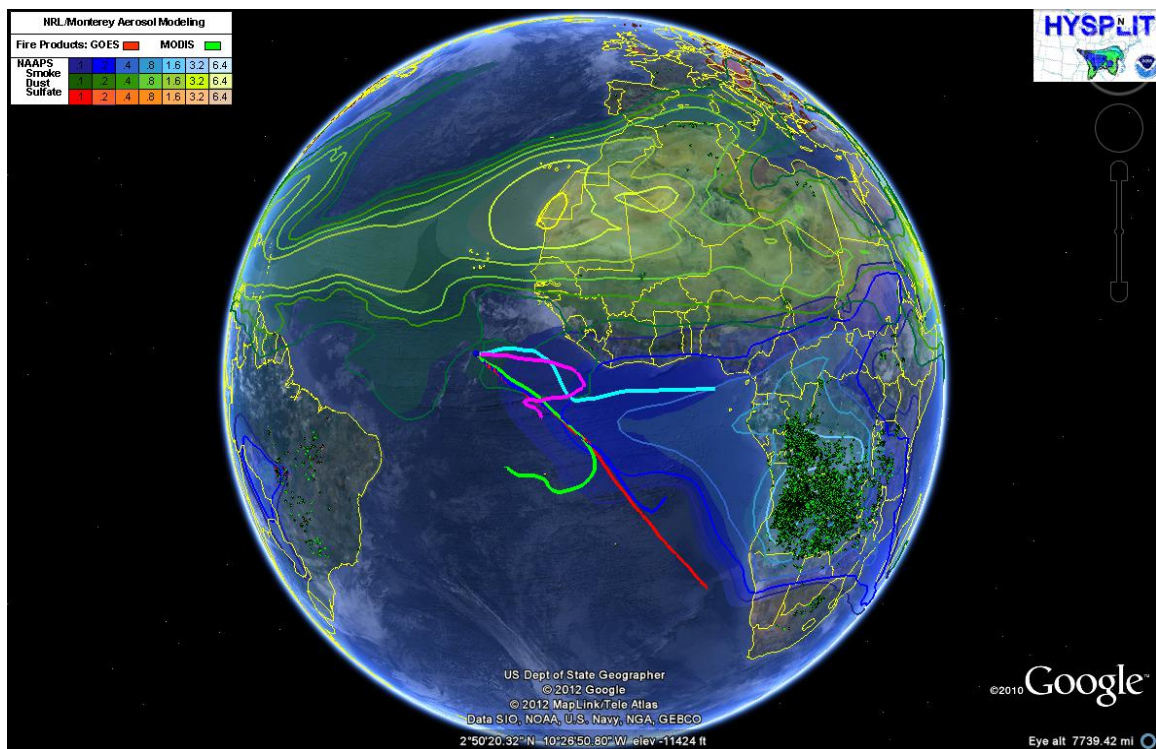


Figure (96) – NAAPS/FLAMBE forecast and HYSPLIT trajectories for 072209 – 12hrs

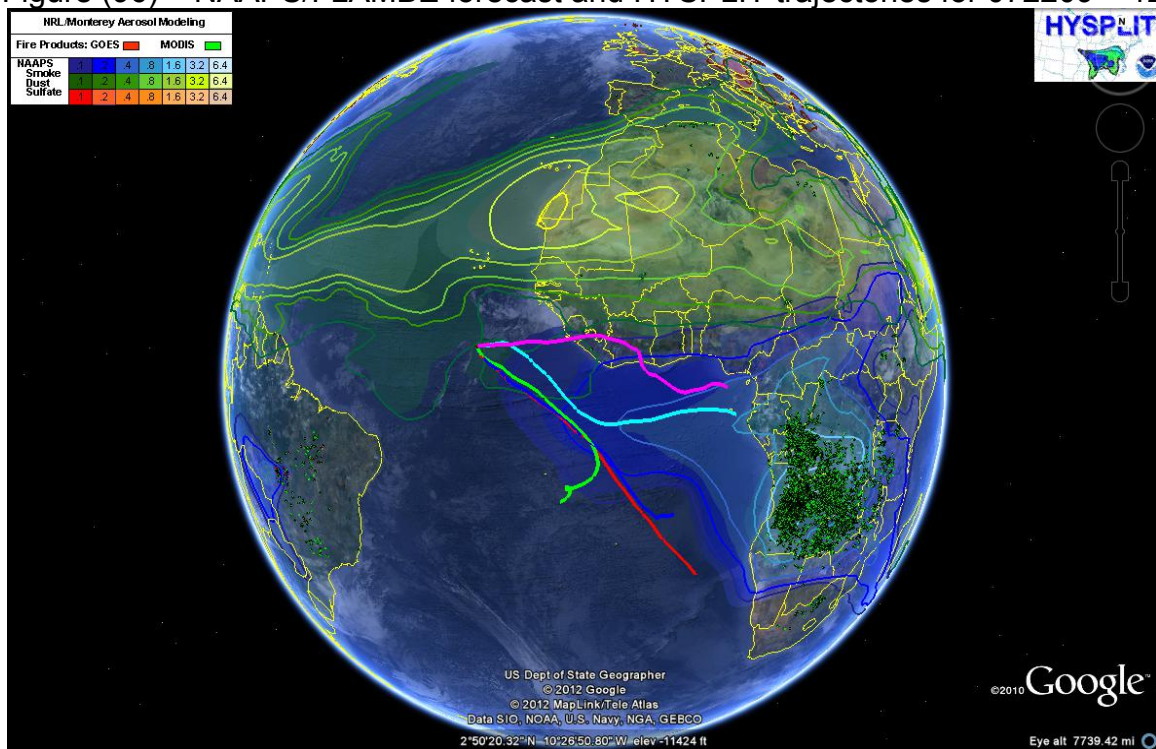


Figure (97) – NAAPS/FLAMBE forecast and HYSPLIT trajectories for 072209 – 18hrs

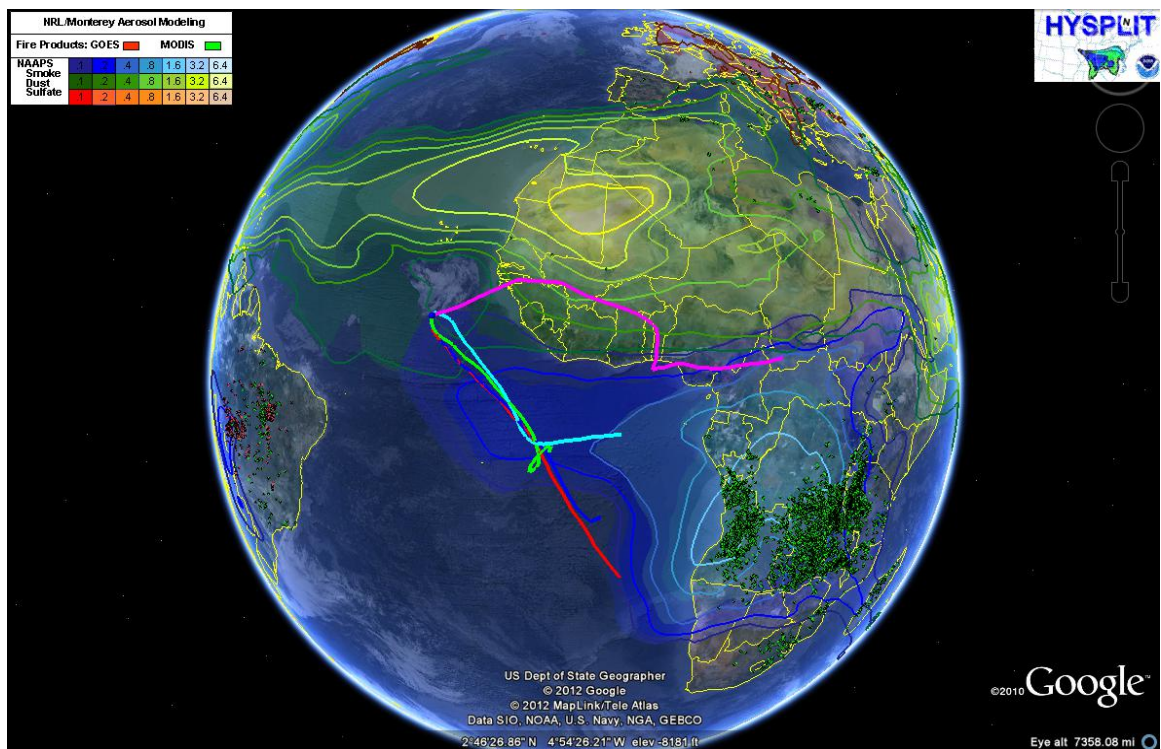


Figure (98) – NAAPS/FLAMBE forecast and HYSPLIT trajectories for 072309 – 00hrs

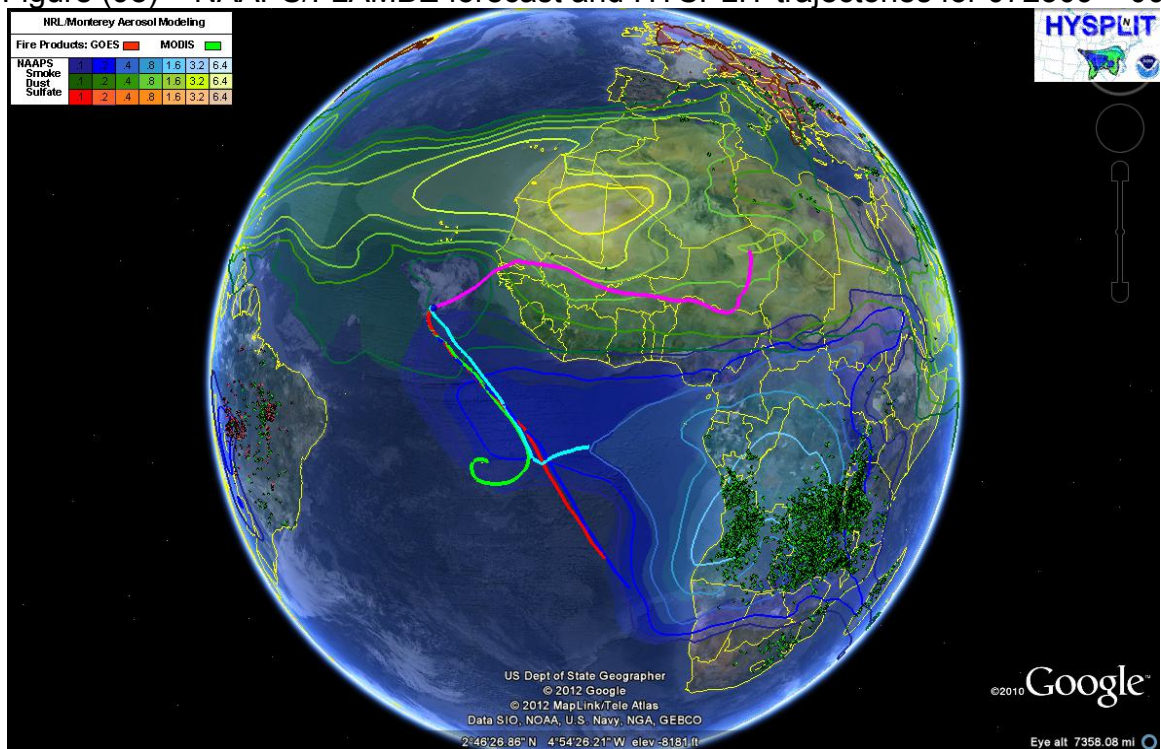


Figure (99) – NAAPS/FLAMBE forecast and HYSPLIT trajectories for 072309 – 06hrs

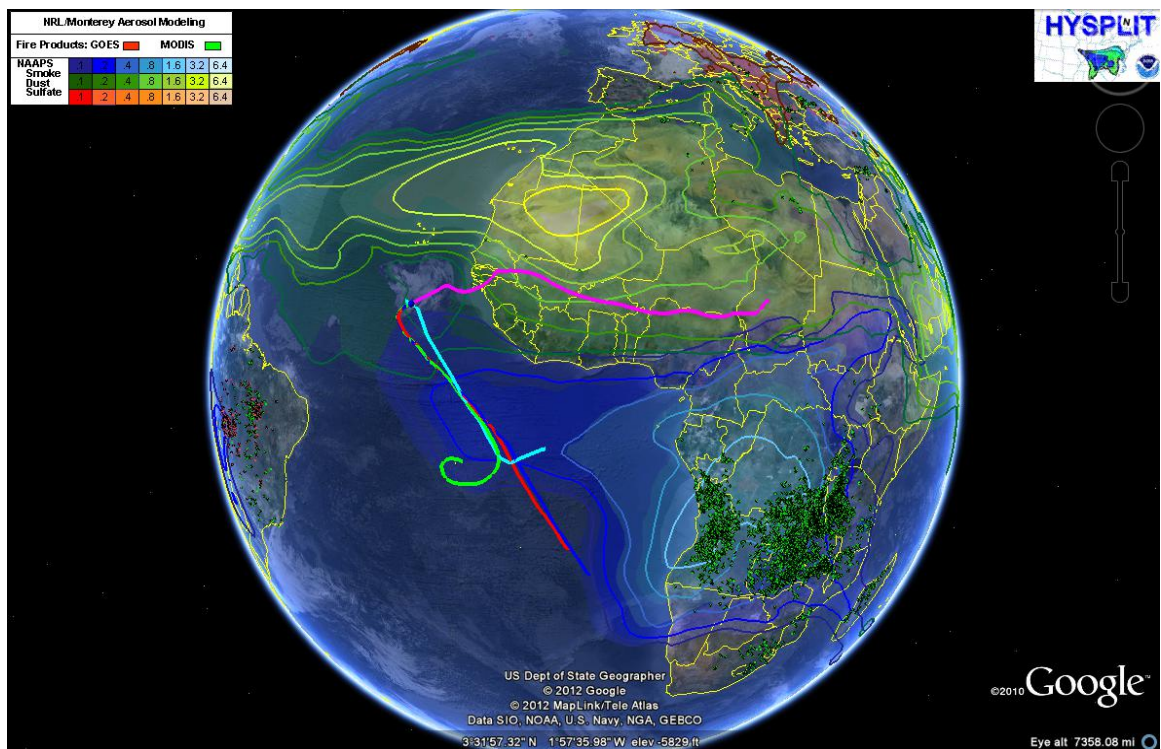


Figure (100) – NAAPS/FLAMBE forecast and HYSPLIT trajectories for 072309 – 12hrs

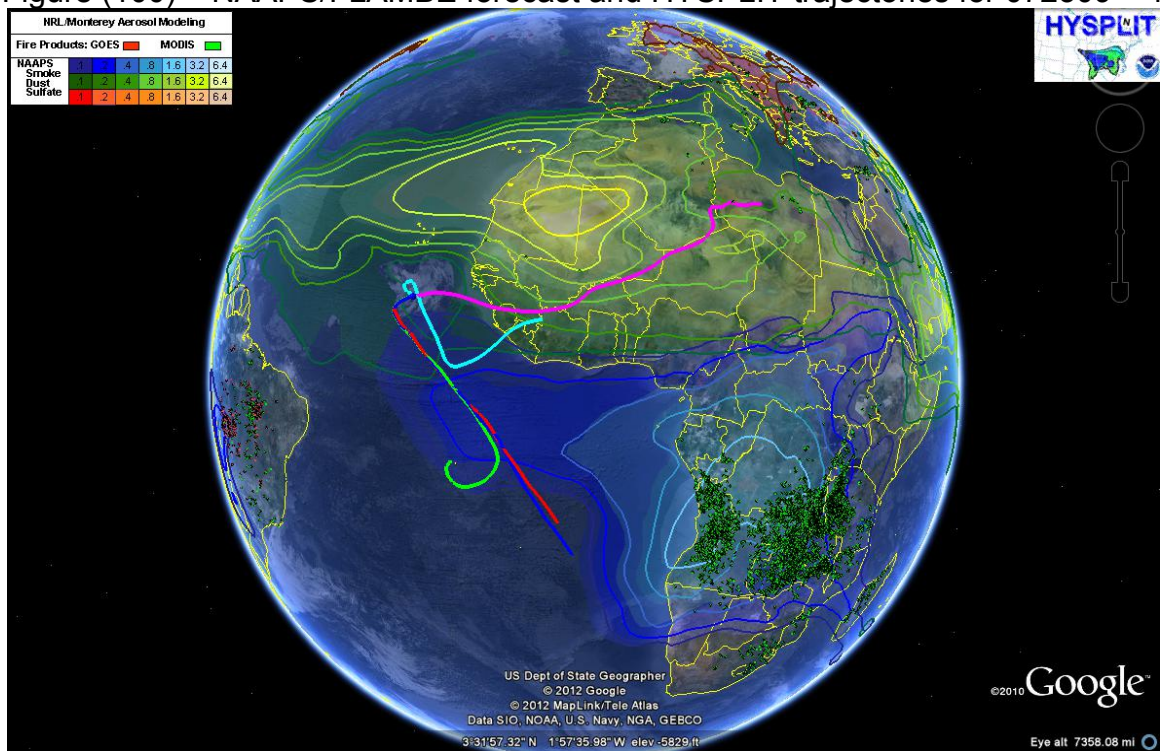


Figure (101) – NAAPS/FLAMBE forecast and HYSPLIT trajectories for 072309 – 18hrs

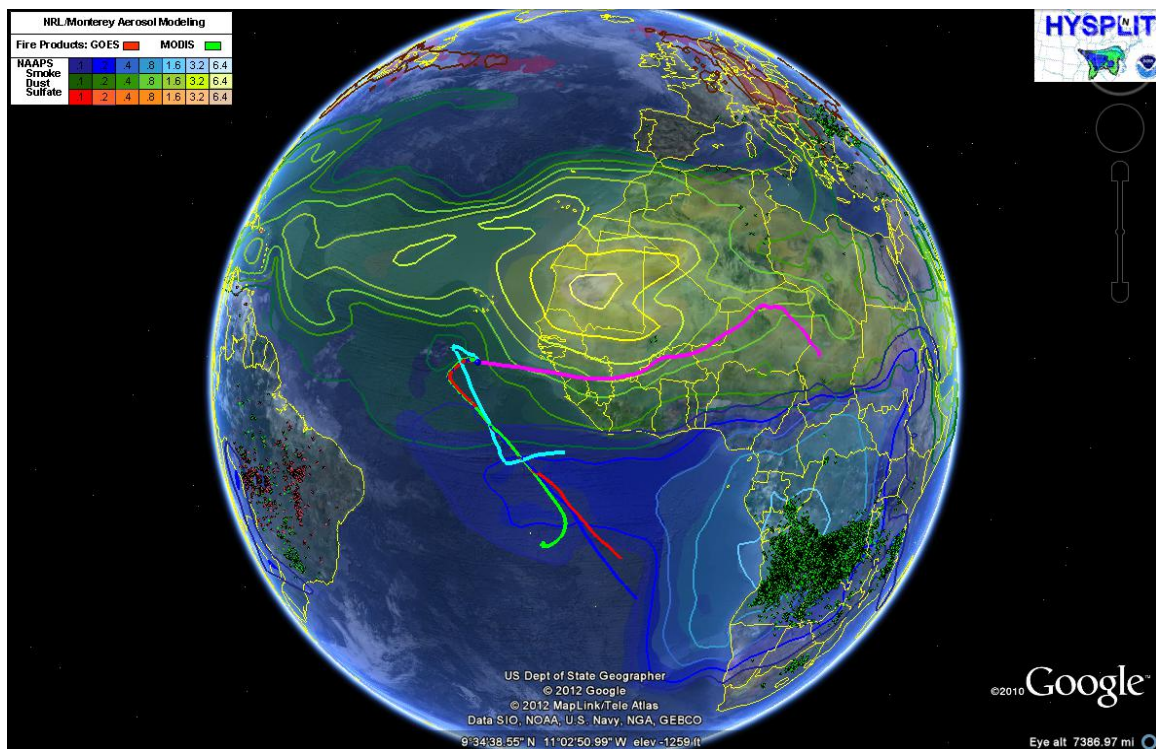


Figure (102) – NAAPS/FLAMBE forecast and HYSPLIT trajectories for 072409 – 00hrs

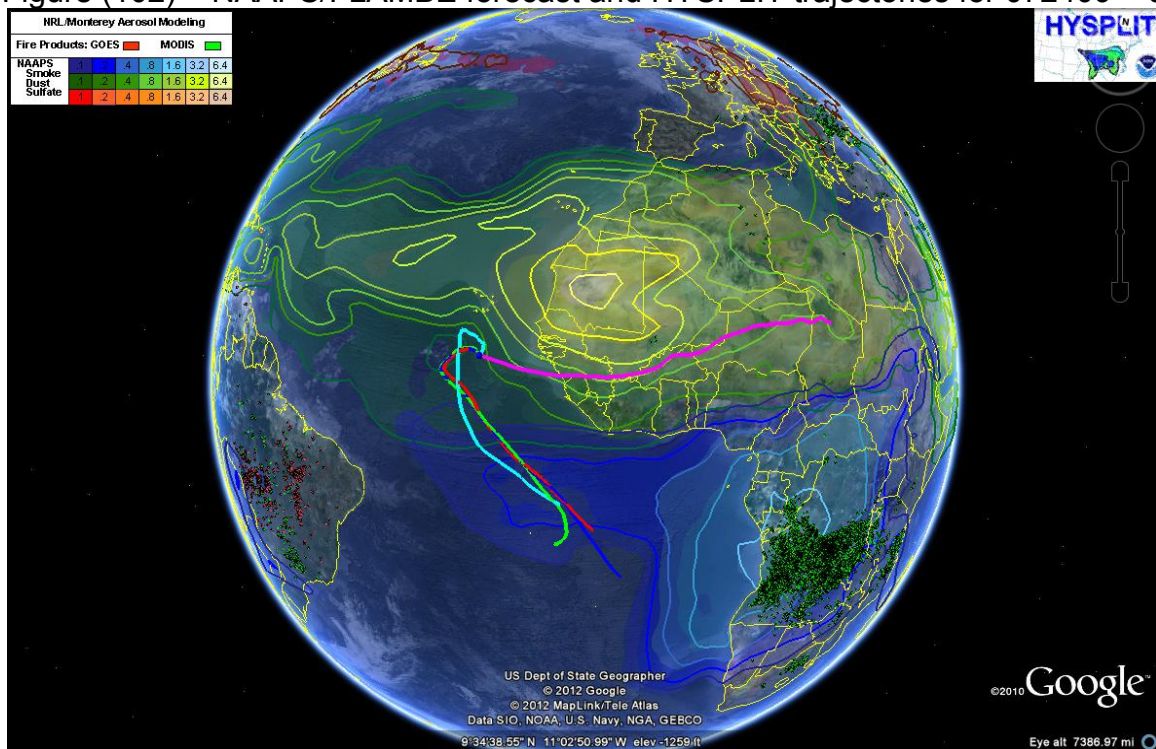


Figure (103) – NAAPS/FLAMBE forecast and HYSPLIT trajectories for 072409 – 06hrs

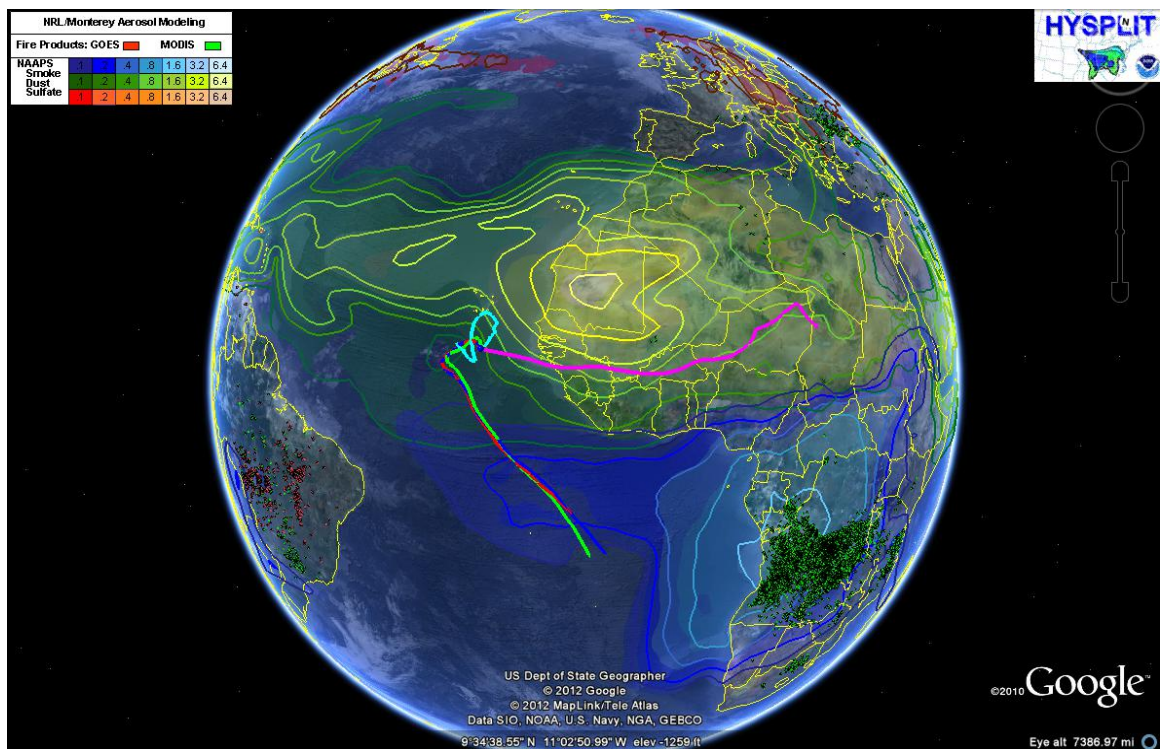


Figure (104) – NAAPS/FLAMBE forecast and HYSPLIT trajectories for 072409 – 12hrs

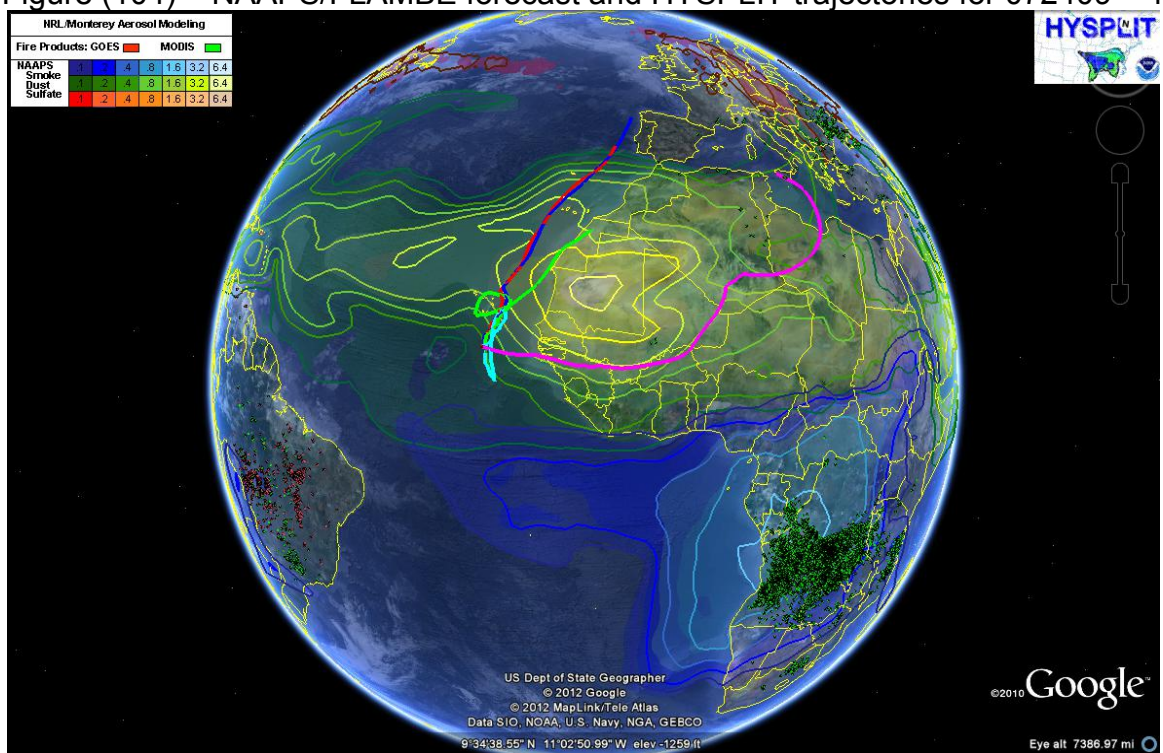


Figure (105) – NAAPS/FLAMBE forecast and HYSPLIT trajectories for 072409 – 18hrs

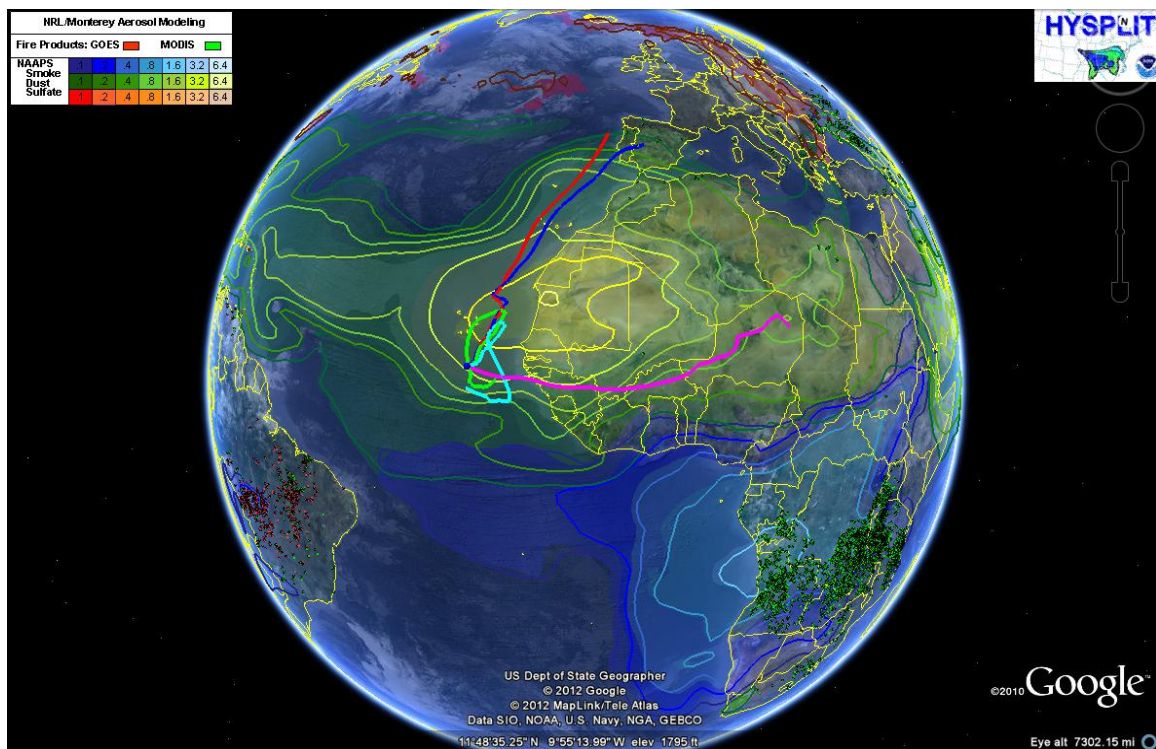


Figure (106) – NAAPS/FLAMBE forecast and HYSPLIT trajectories for 072509 – 00hrs

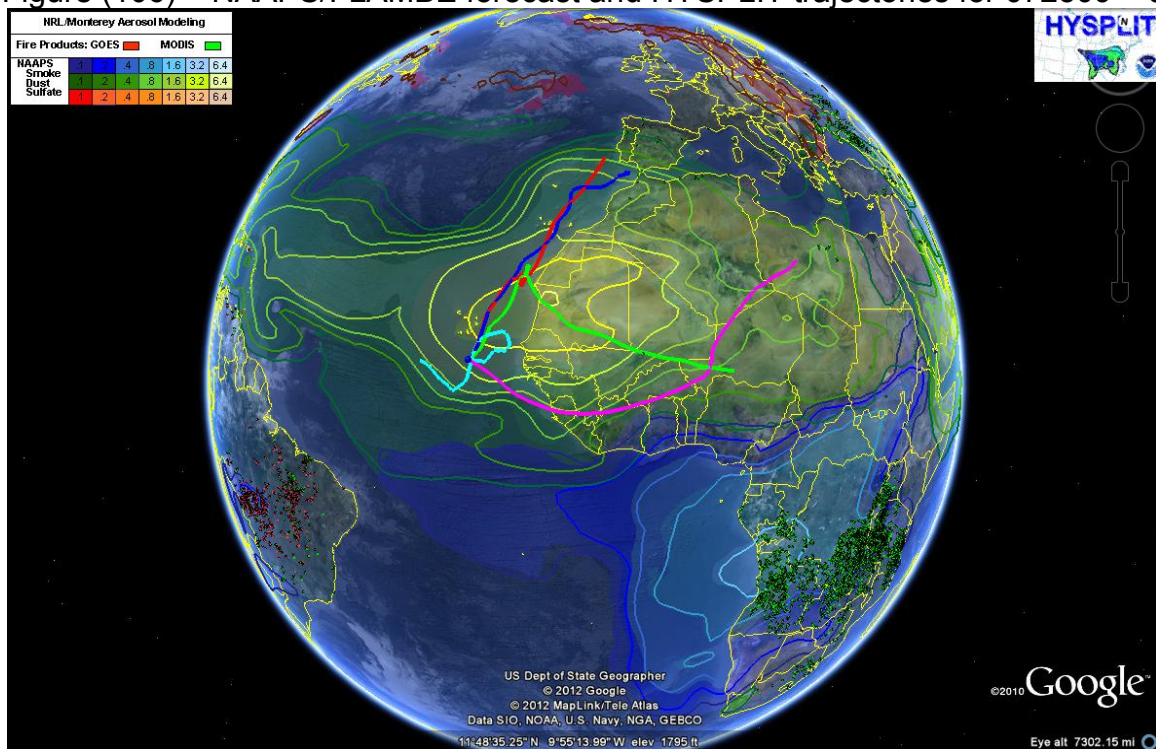


Figure (107) – NAAPS/FLAMBE forecast and HYSPLIT trajectories for 072509 – 06hrs

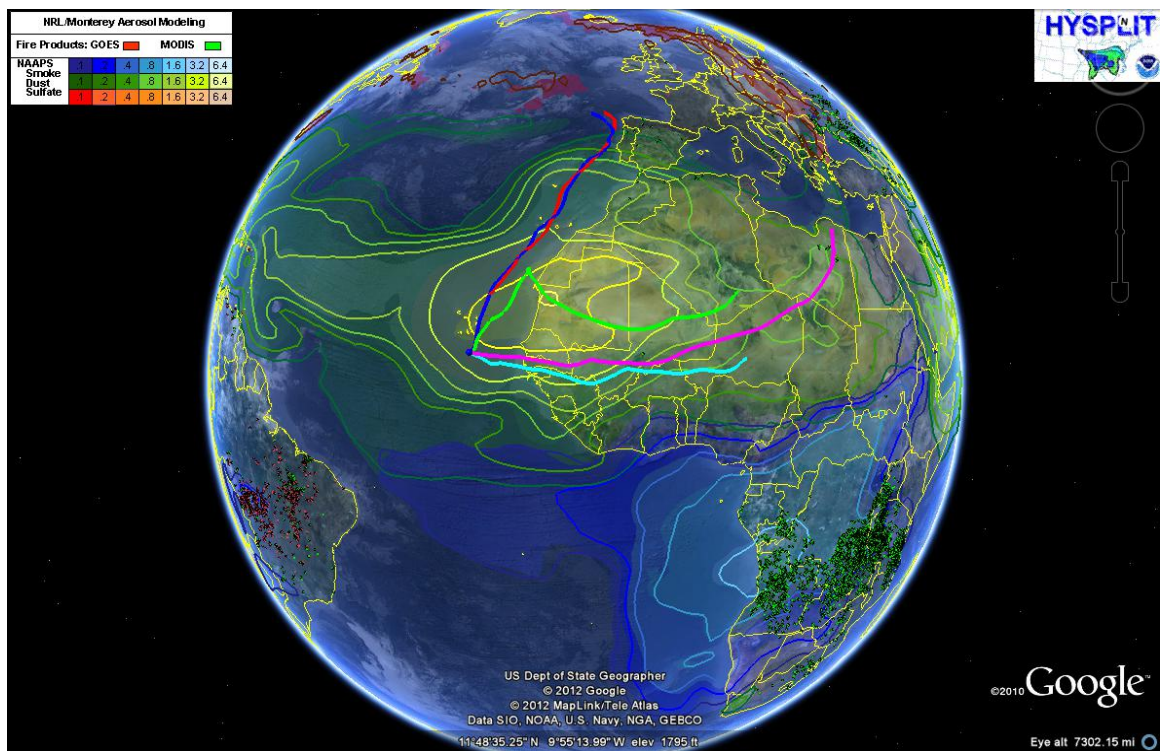


Figure (108) – NAAPS/FLAMBE forecast and HYSPLIT trajectories for 072509 – 12hrs

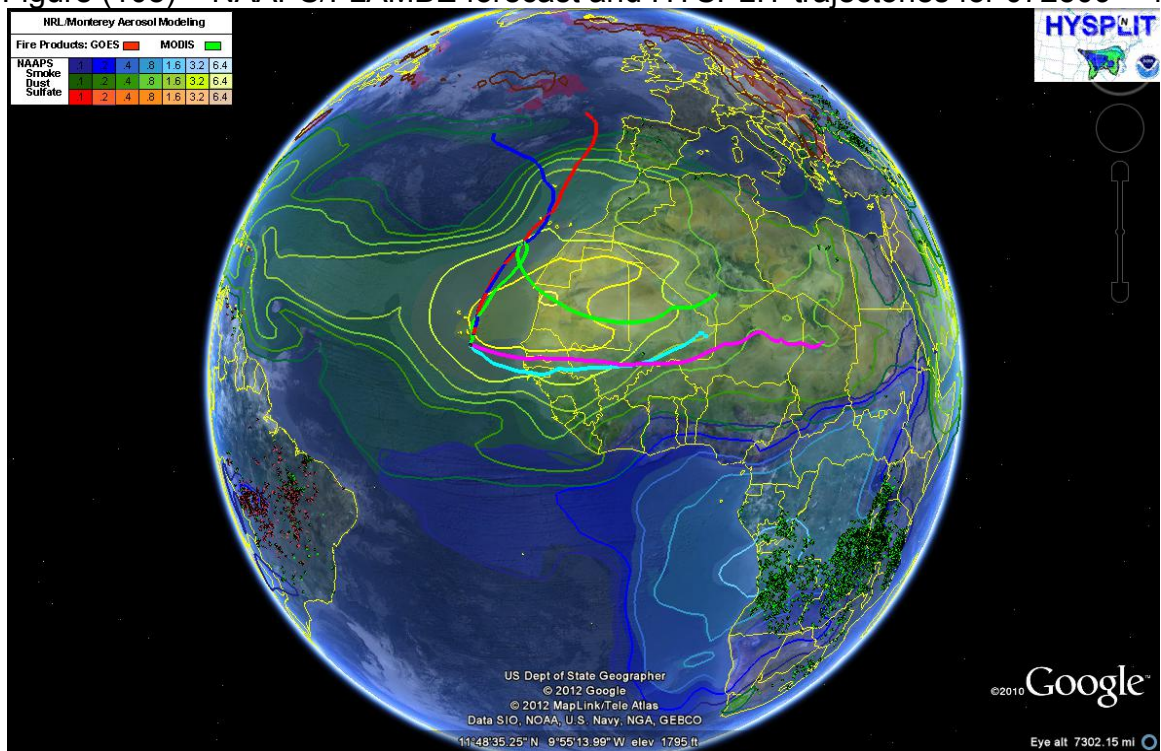


Figure (109) – NAAPS/FLAMBE forecast and HYSPLIT trajectories for 072509 – 18hrs

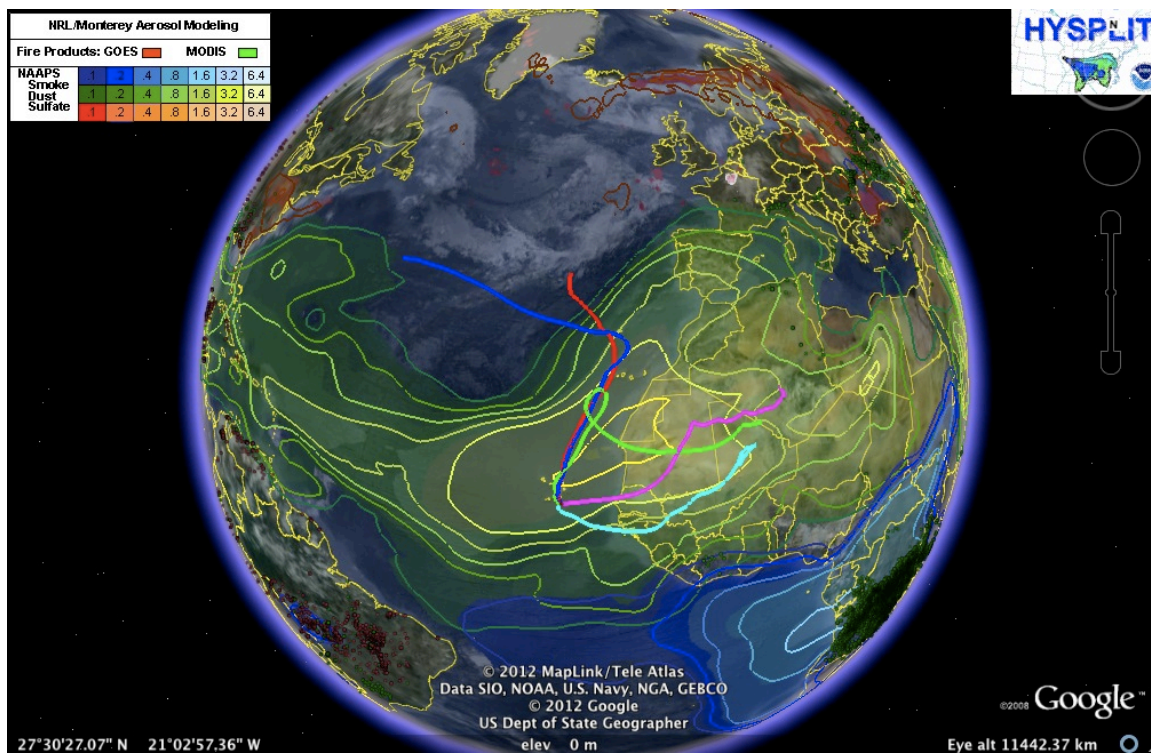


Figure (110) – NAAPS/FLAMBE forecast and HYSPLIT trajectories for 072609 – 00hrs

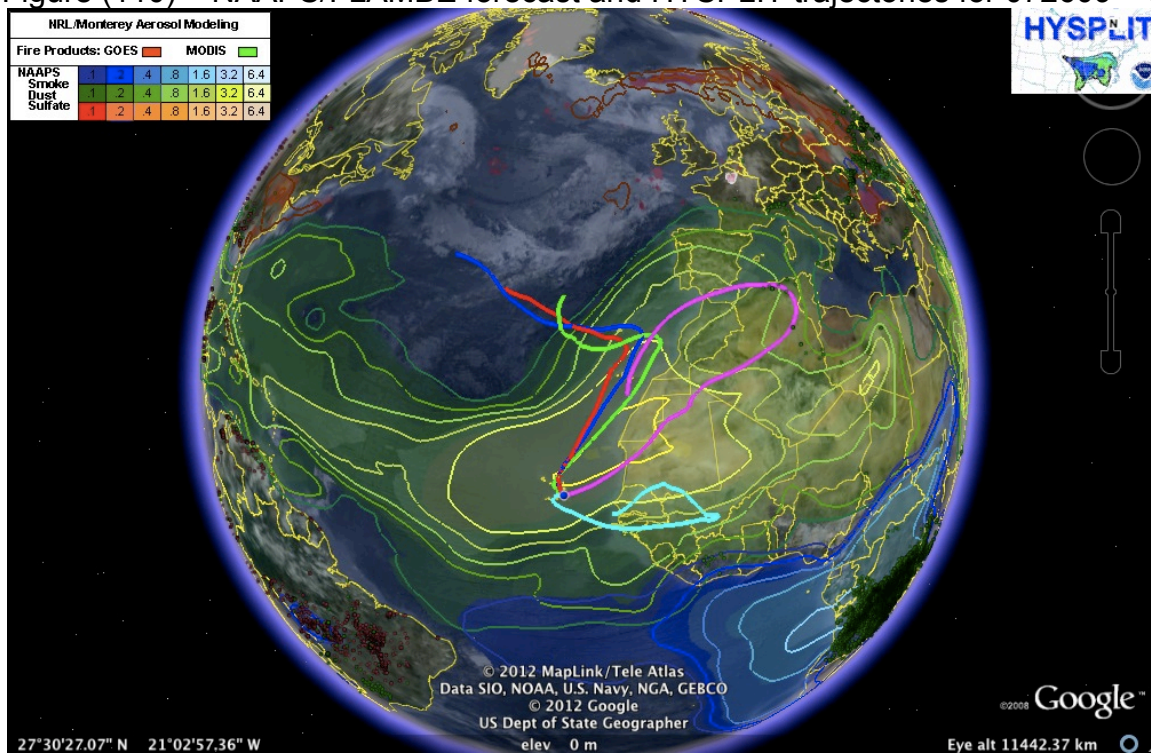


Figure (111) – NAAPS/FLAMBE forecast and HYSPLIT trajectories for 072609 – 06hrs

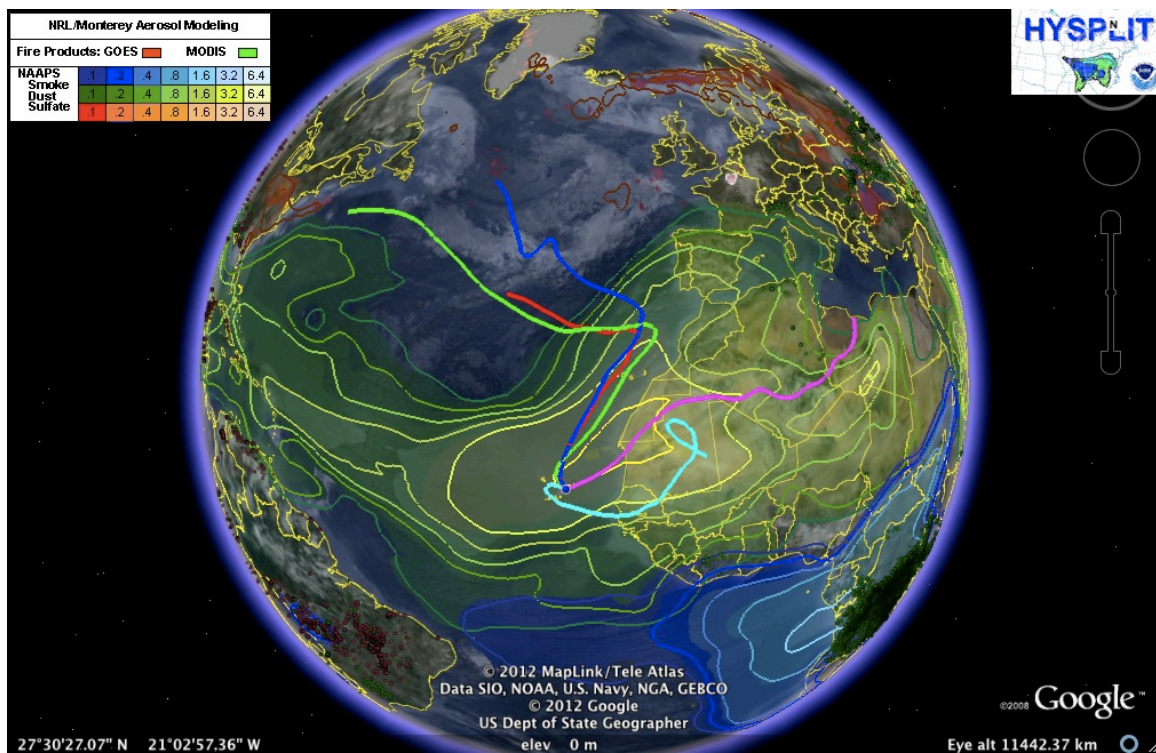


Figure (112) – NAAPS/FLAMBE forecast and HYSPLIT trajectories for 072609 – 12hrs

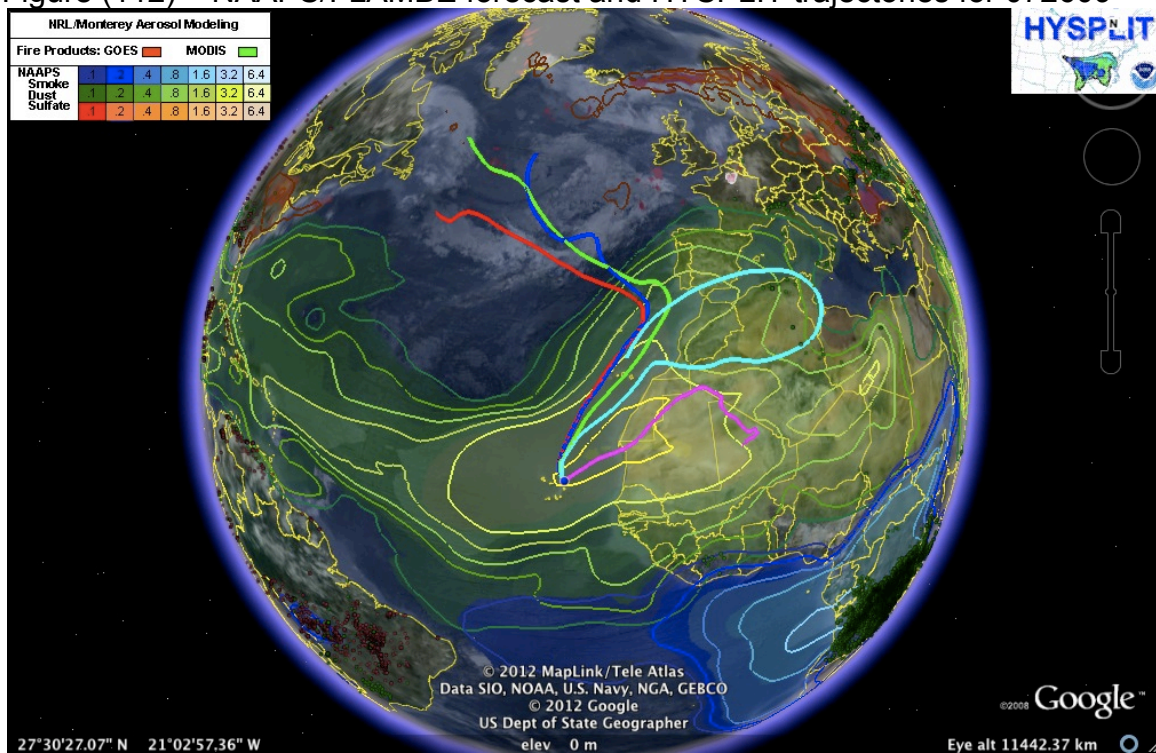


Figure (113) – NAAPS/FLAMBE forecast and HYSPLIT trajectories for 072609 – 18hrs

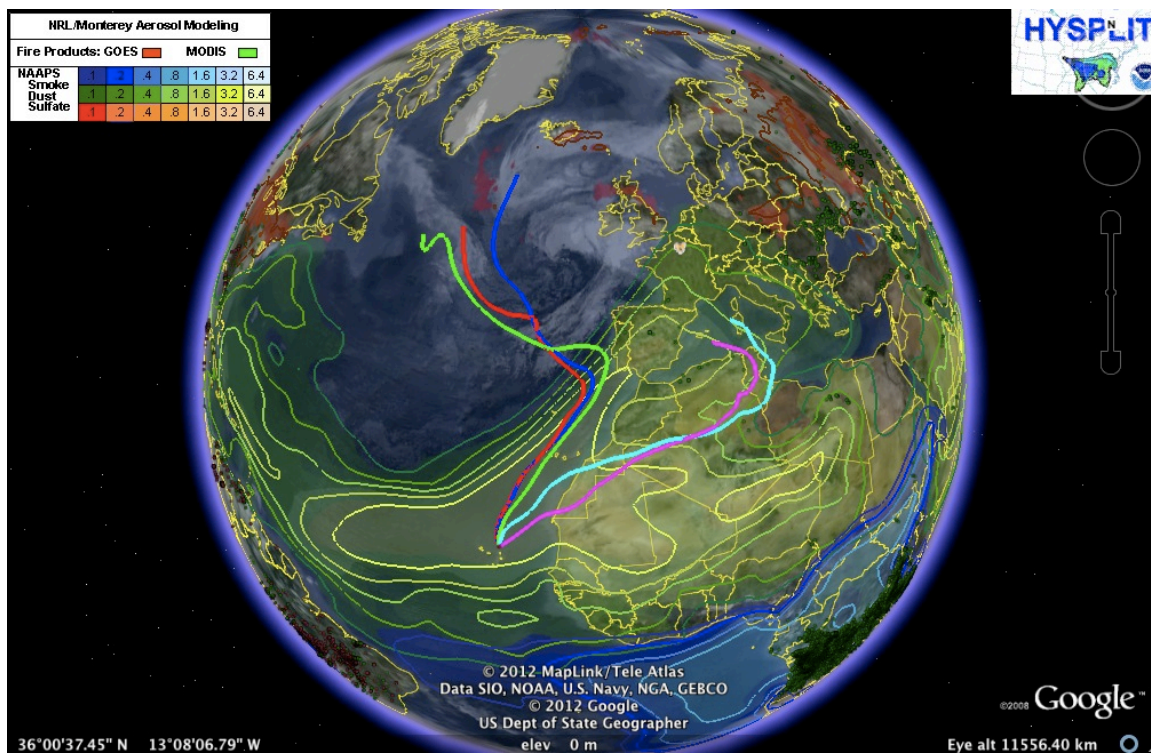


Figure (114) – NAAPS/FLAMBE forecast and HYSPLIT trajectories for 072709 – 00hrs

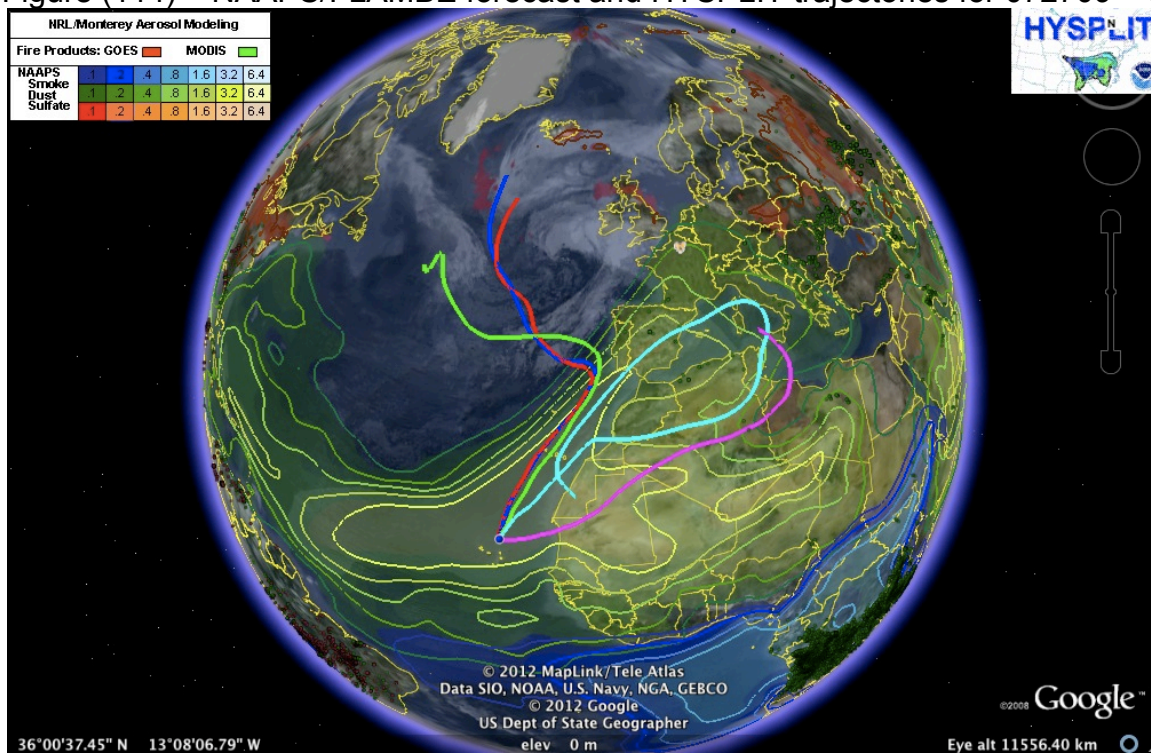


Figure (115) – NAAPS/FLAMBE forecast and HYSPLIT trajectories for 072709 – 06hrs

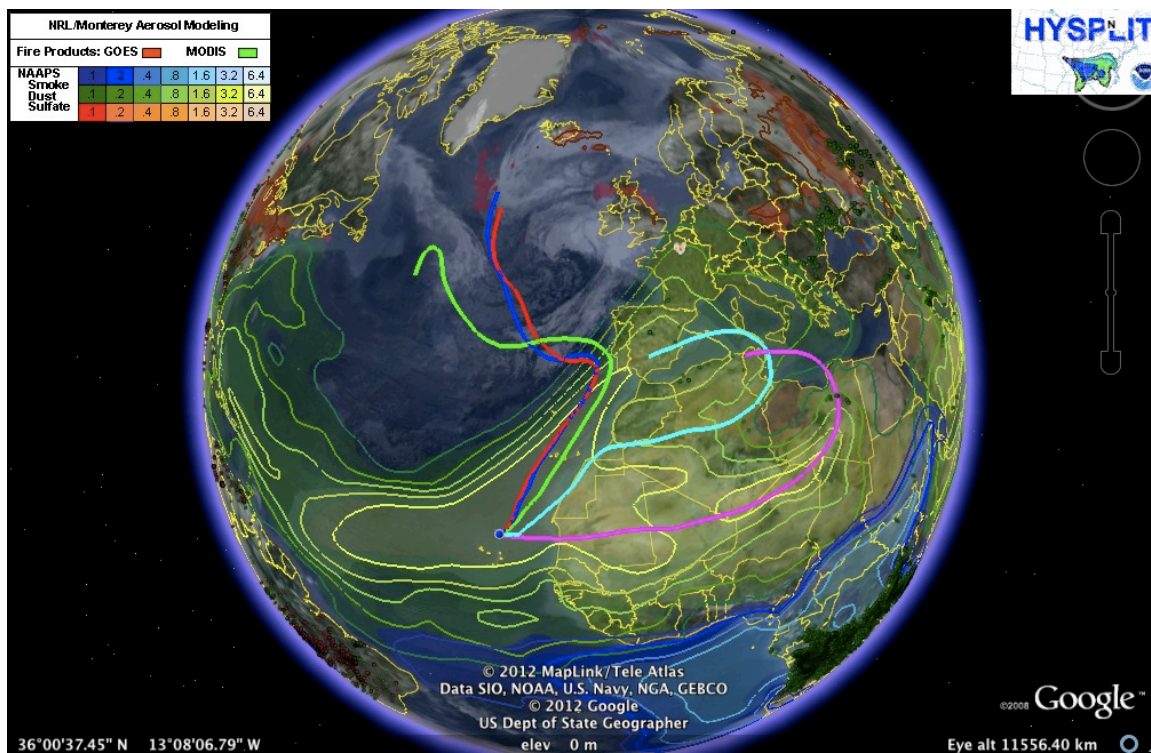


Figure (116) – NAAPS/FLAMBE forecast and HYSPLIT trajectories for 072709 – 12hrs

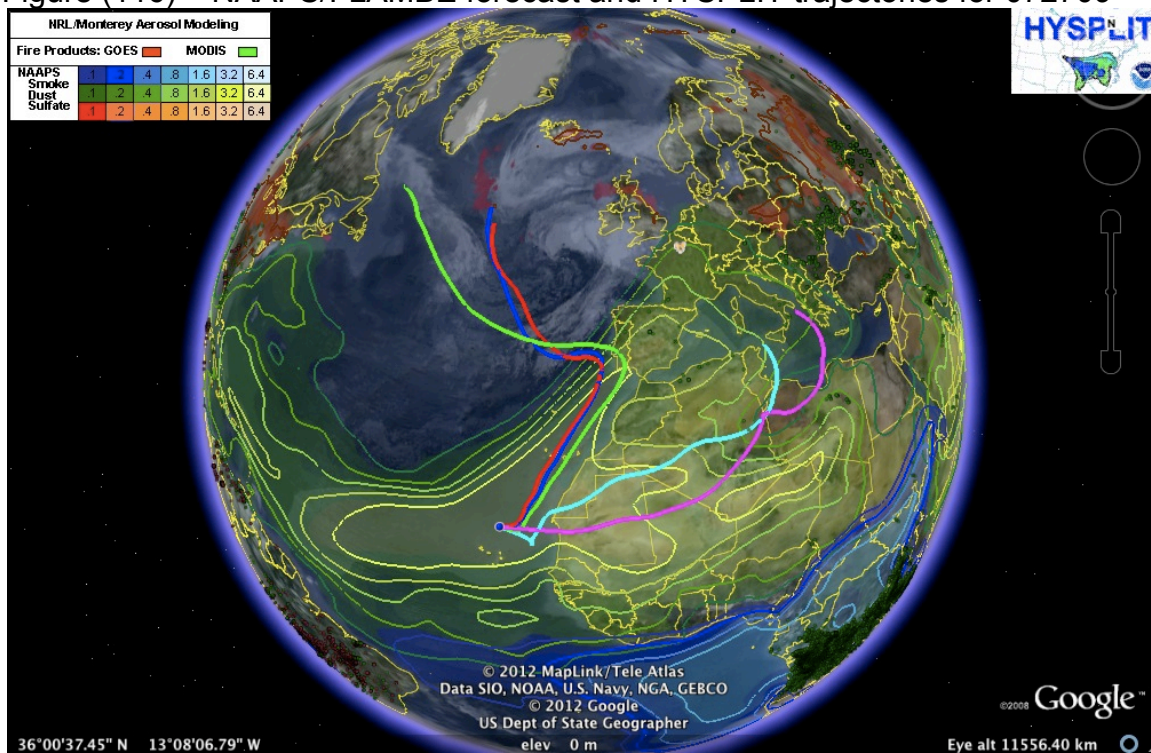


Figure (117) – NAAPS/FLAMBE forecast and HYSPLIT trajectories for 072709 – 18hrs

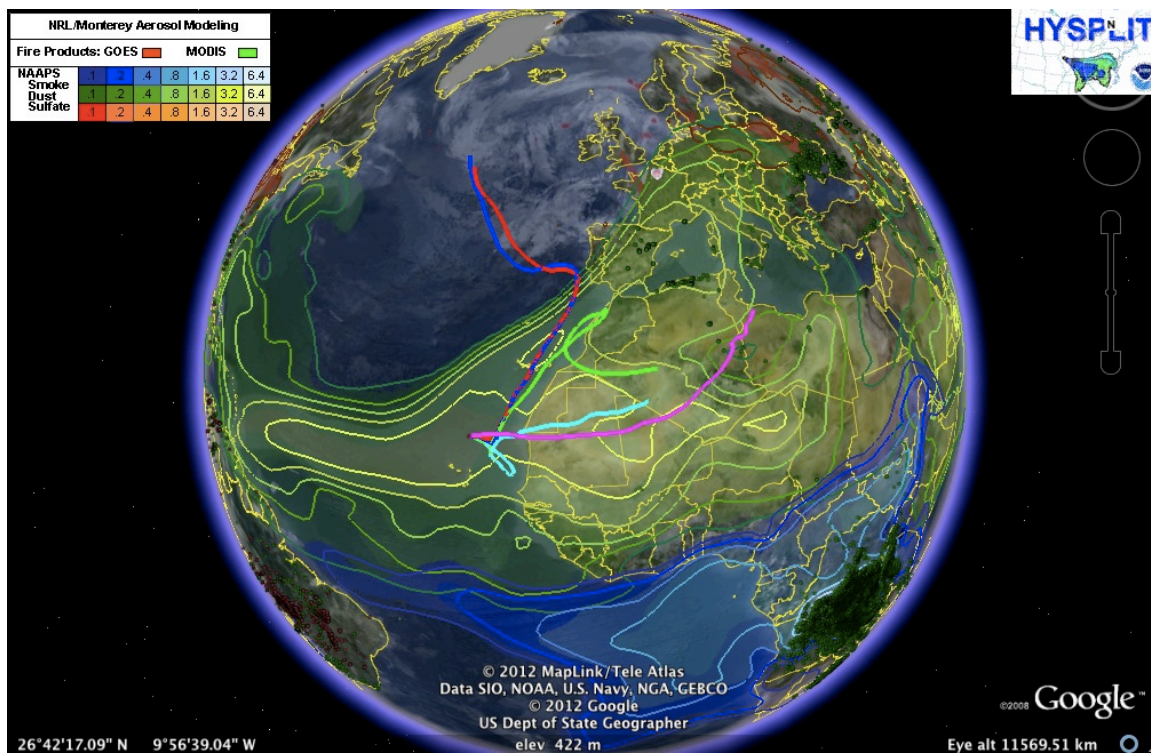


Figure (118) – NAAPS/FLAMBE forecast and HYSPLIT trajectories for 072809 – 00hrs

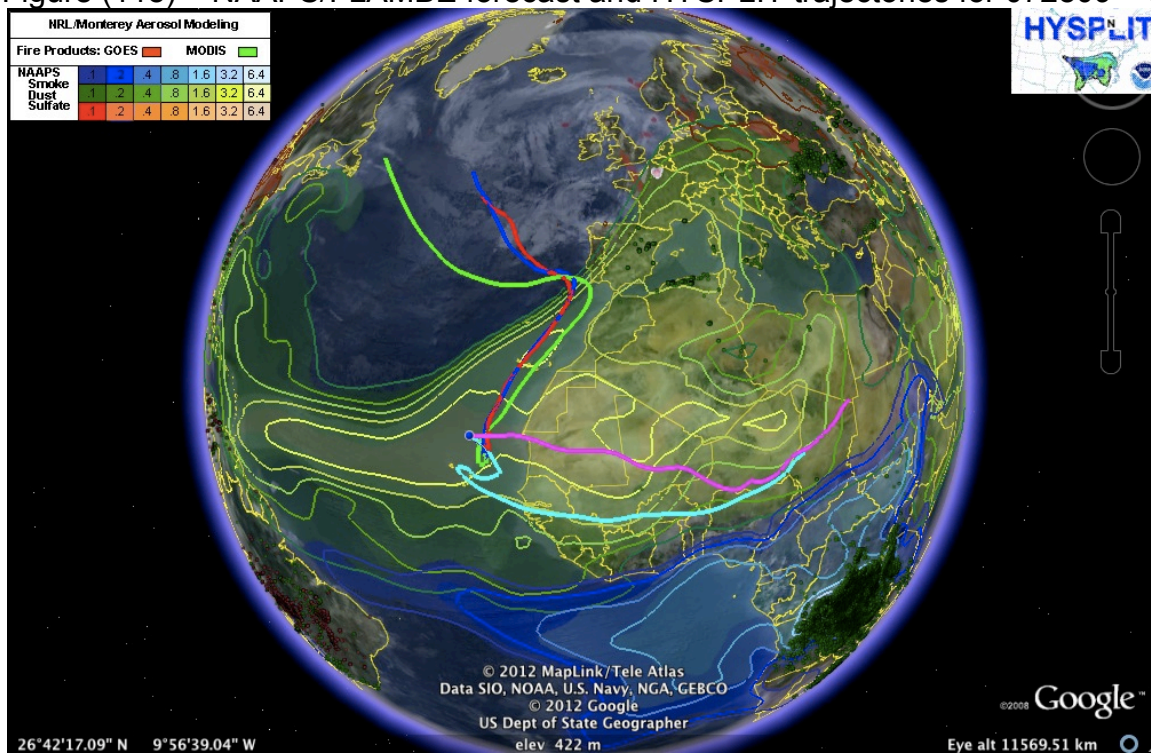


Figure (119) – NAAPS/FLAMBE forecast and HYSPLIT trajectories for 072809 – 06hrs

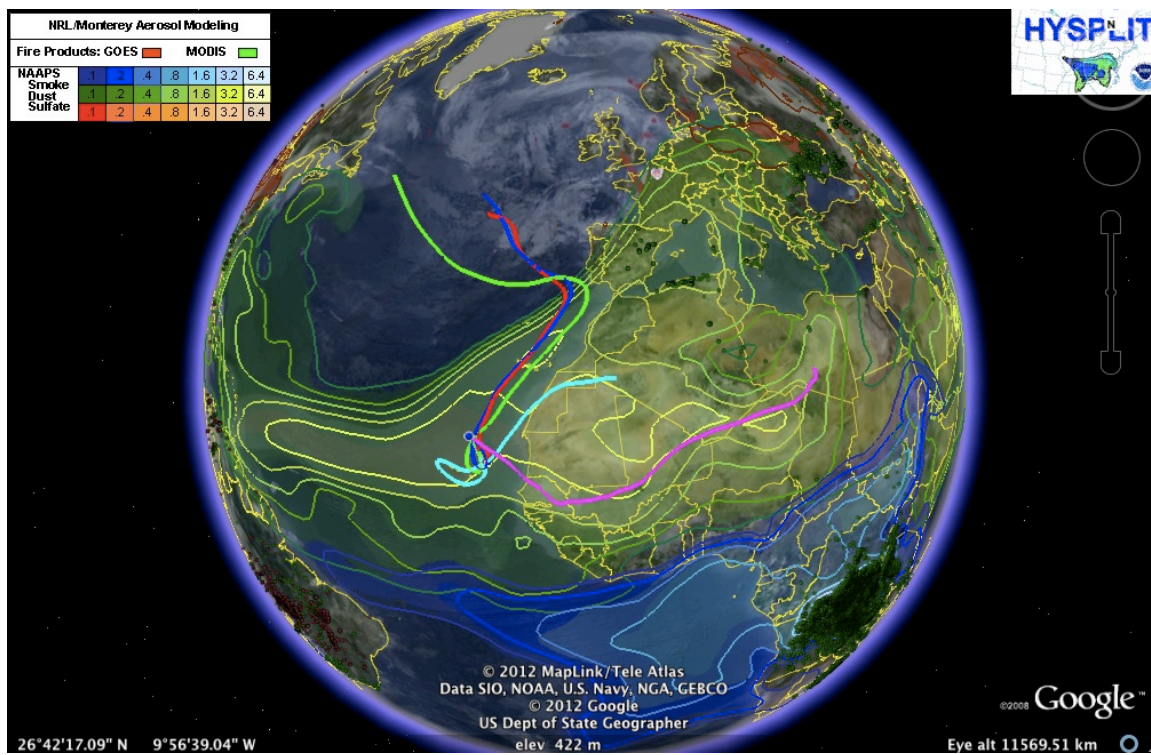


Figure (120) – NAAPS/FLAMBE forecast and HYSPLIT trajectories for 072809 – 12hrs

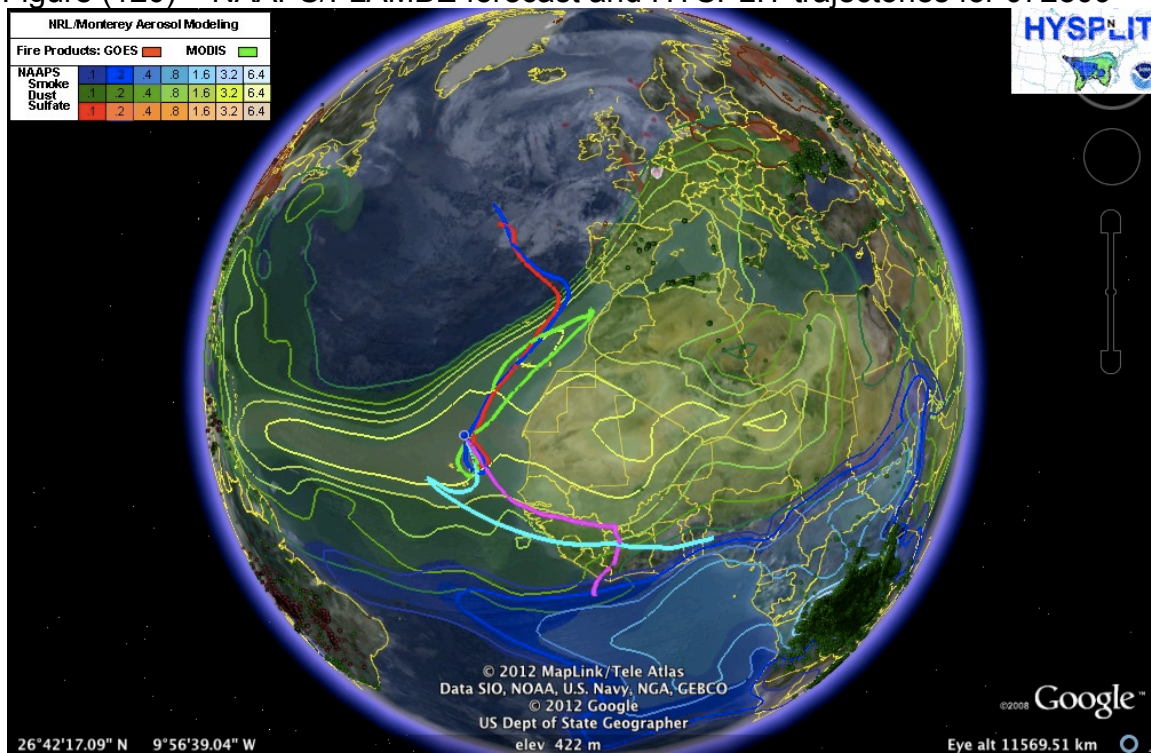


Figure (121) – NAAPS/FLAMBE forecast and HYSPLIT trajectories for 072809 – 18hrs

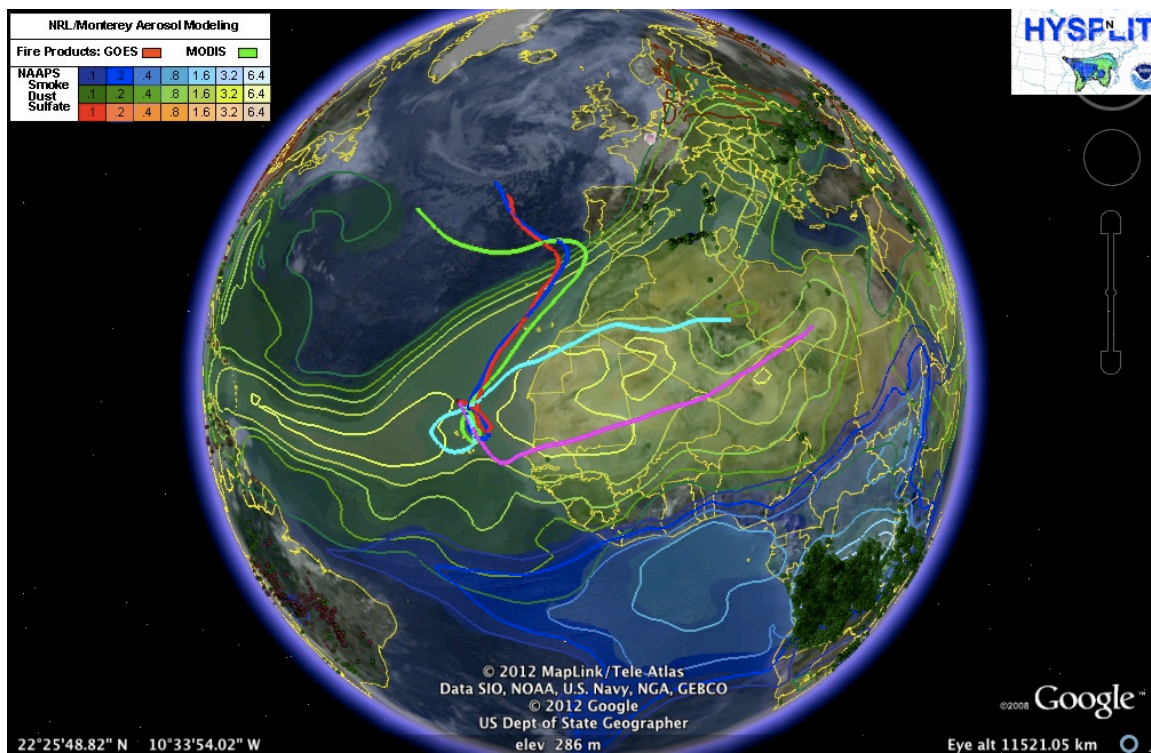


Figure (122) – NAAPS/FLAMBE forecast and HYSPLIT trajectories for 072909 – 00hrs

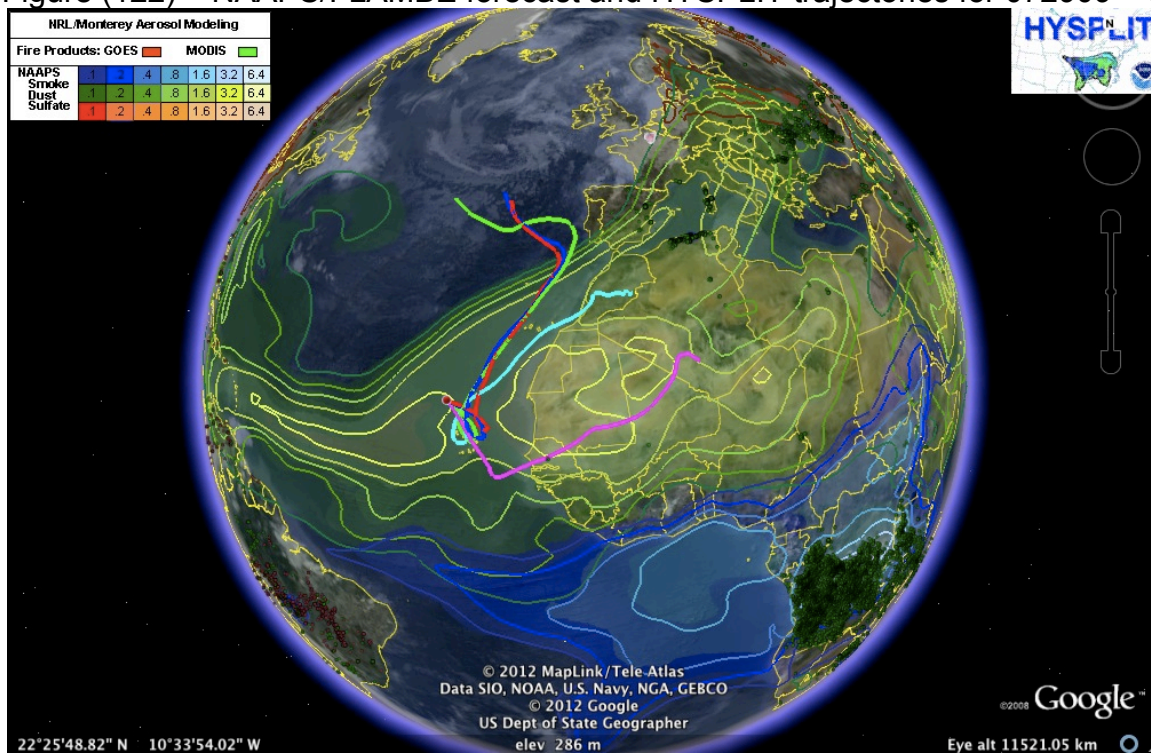


Figure (123) – NAAPS/FLAMBE forecast and HYSPLIT trajectories for 072909 – 06hrs

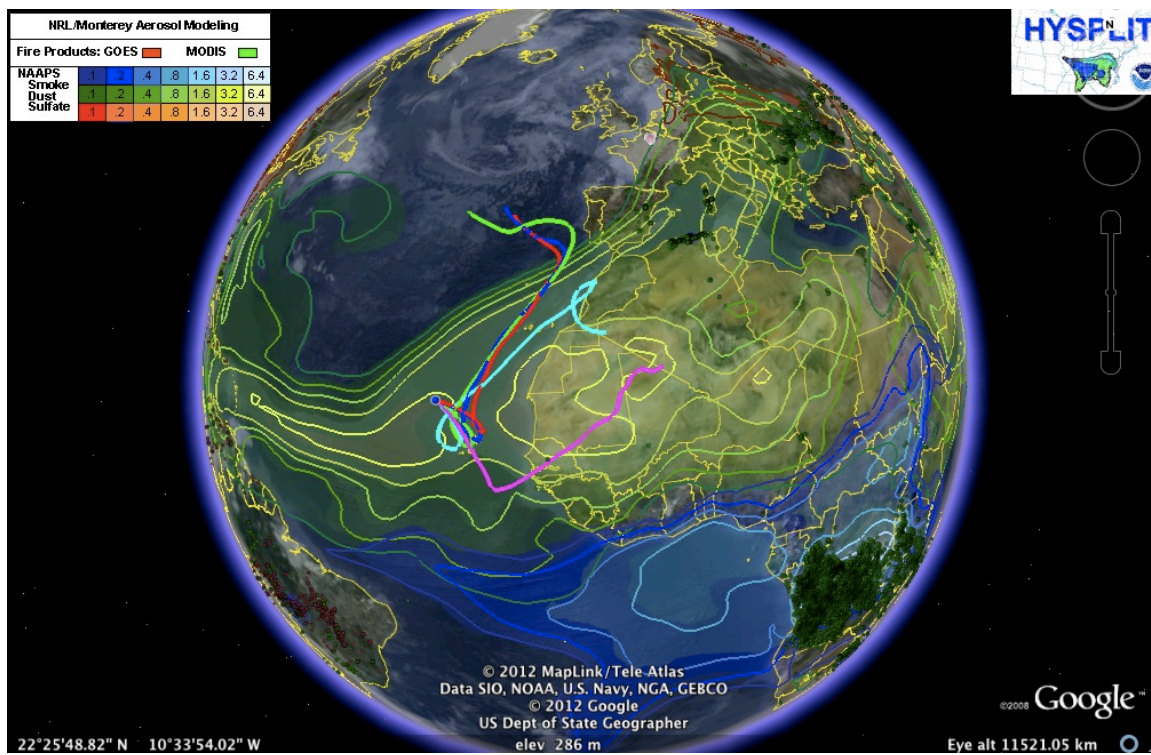


Figure (124) – NAAPS/FLAMBE forecast and HYSPLIT trajectories for 072909 – 12hrs

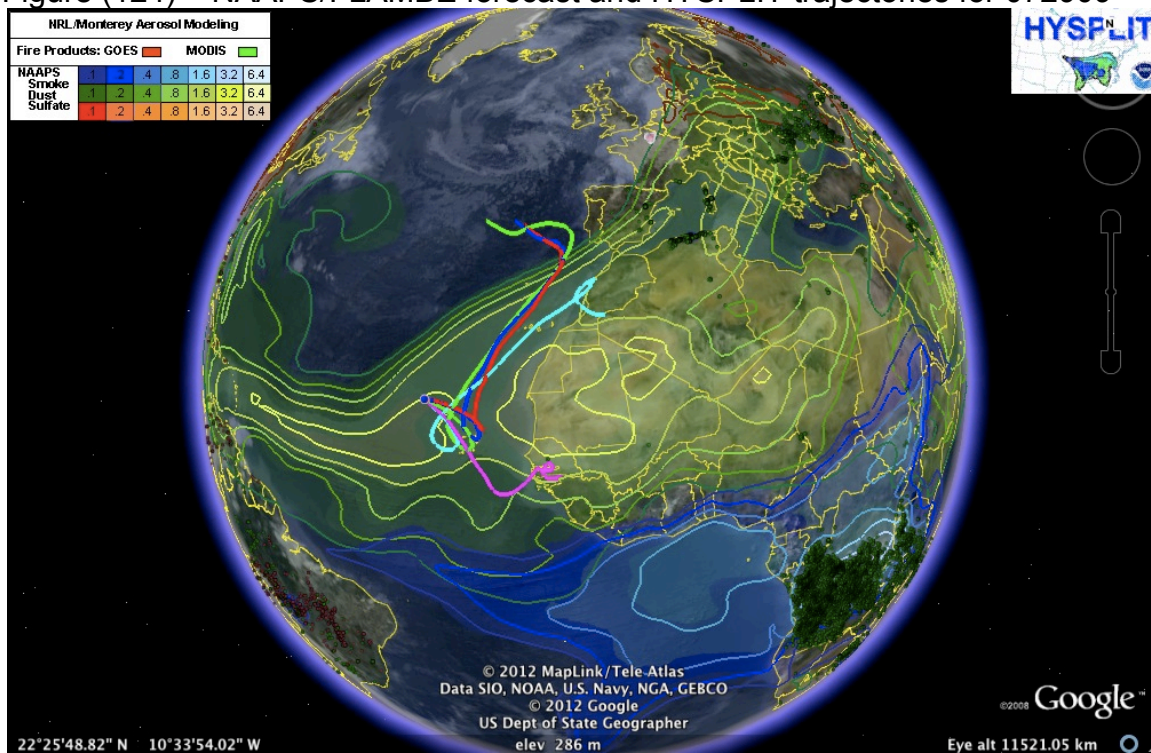


Figure (125) – NAAPS/FLAMBE forecast and HYSPLIT trajectories for 072909 – 18hrs

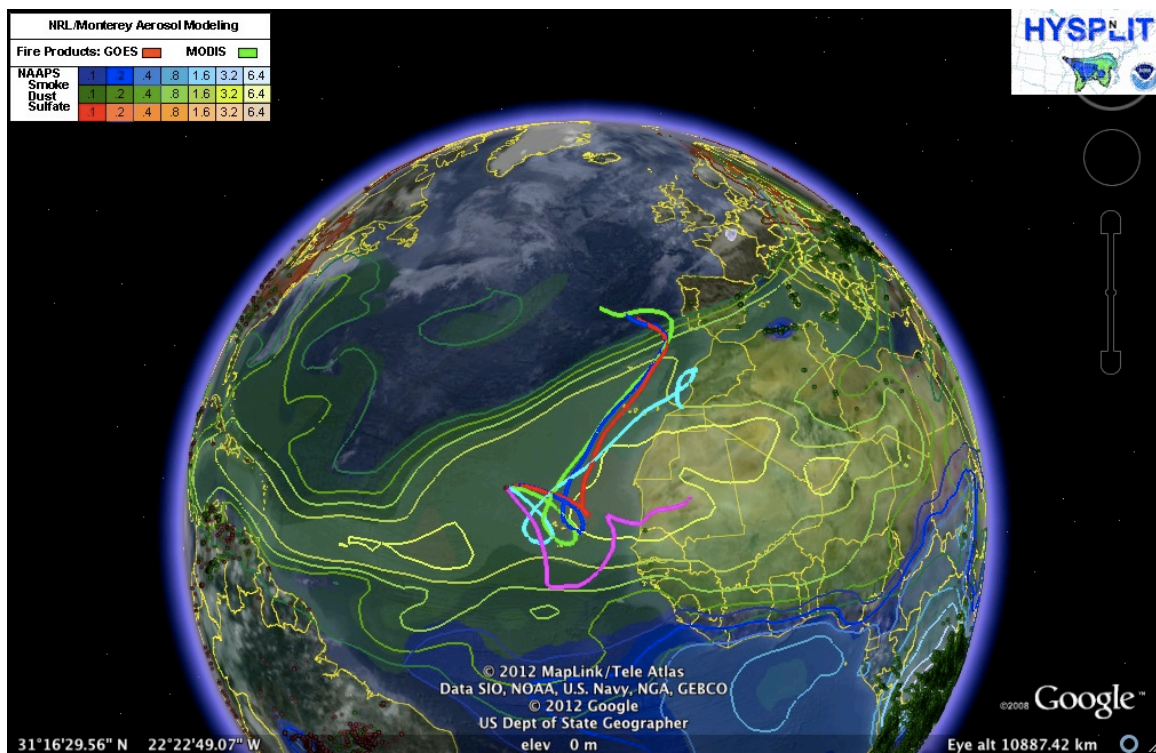


Figure (126) – NAAPS/FLAMBE forecast and HYSPLIT trajectories for 073009 – 00hrs

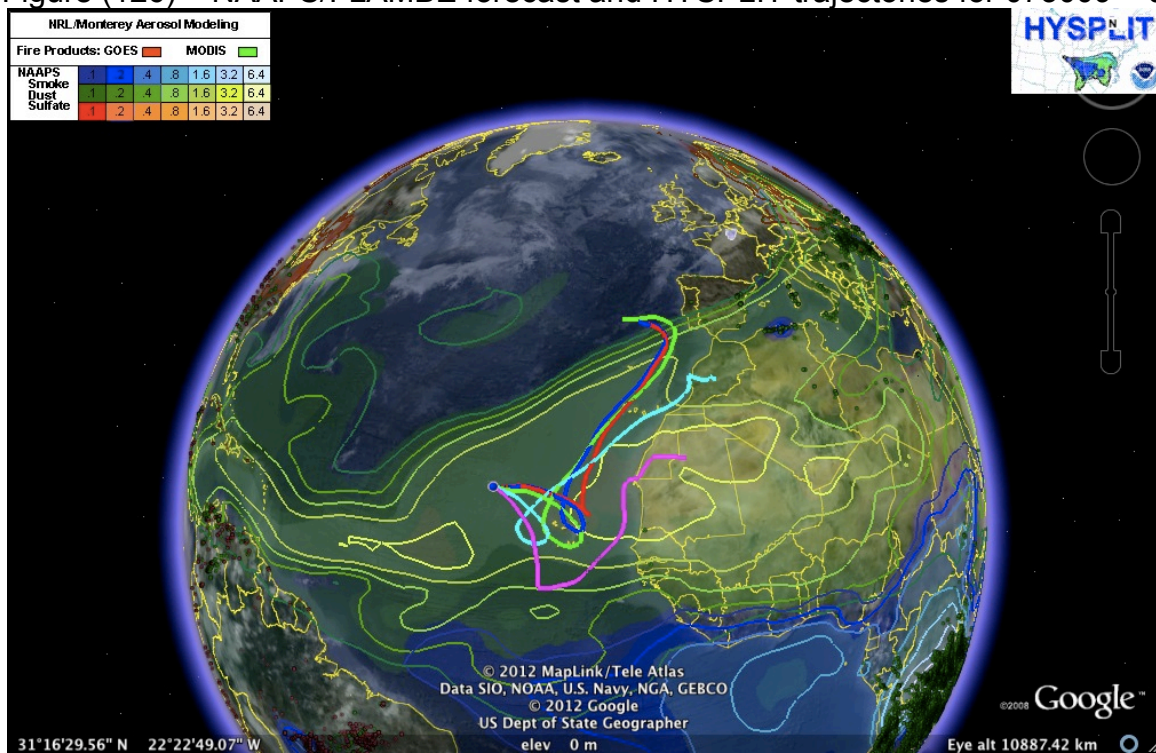


Figure (127) – NAAPS/FLAMBE forecast and HYSPLIT trajectories for 073009 – 06hrs

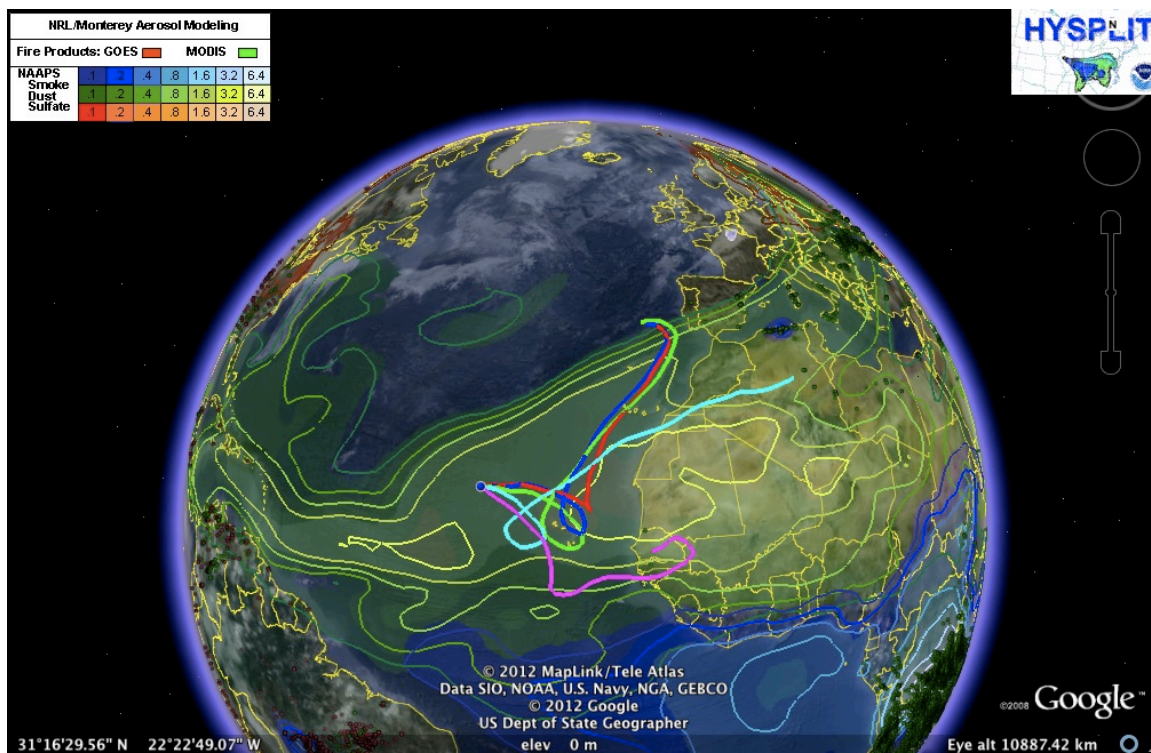


Figure (128) – NAAPS/FLAMBE forecast and HYSPLIT trajectories for 073009 – 12hrs

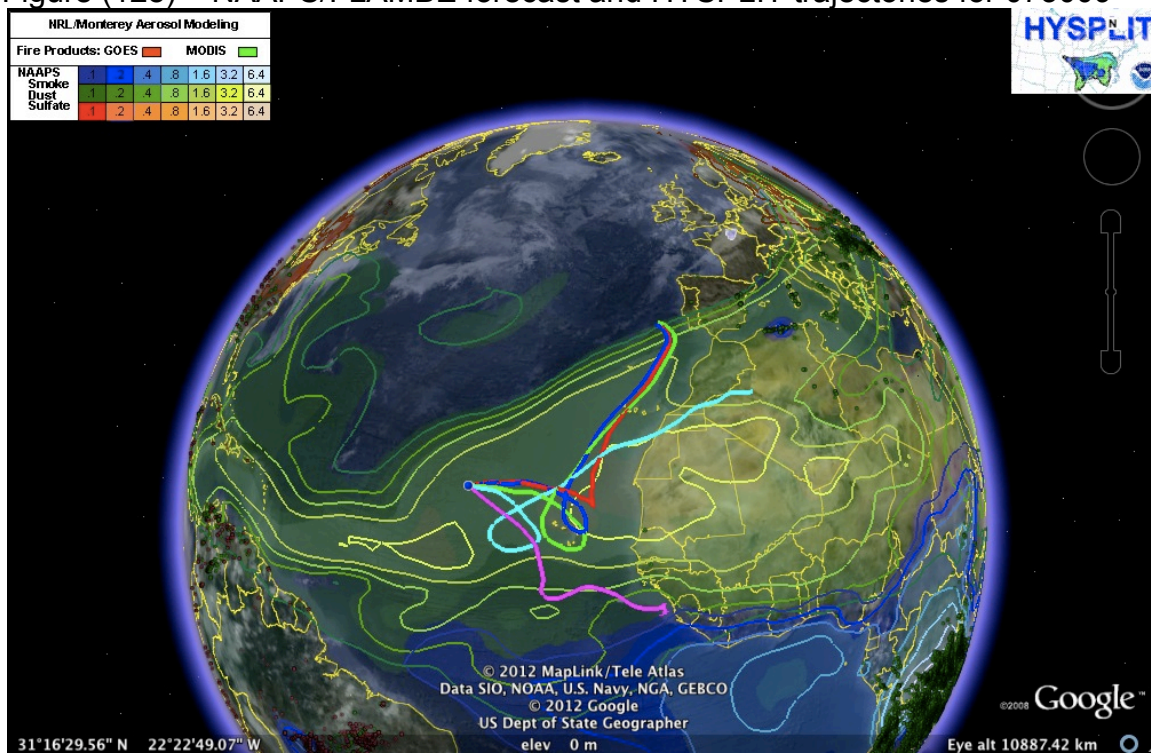


Figure (129) – NAAPS/FLAMBE forecast and HYSPLIT trajectories for 073009 – 18hrs

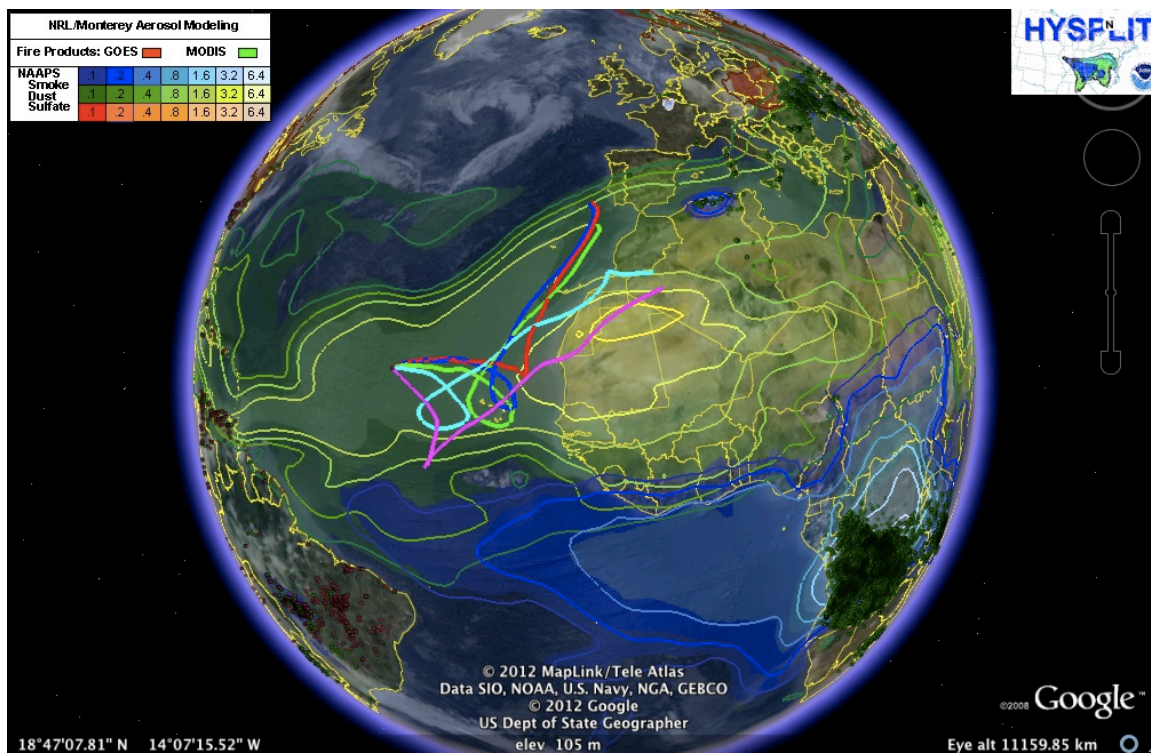


Figure (130) – NAAPS/FLAMBE forecast and HYSPLIT trajectories for 073109 – 00hrs

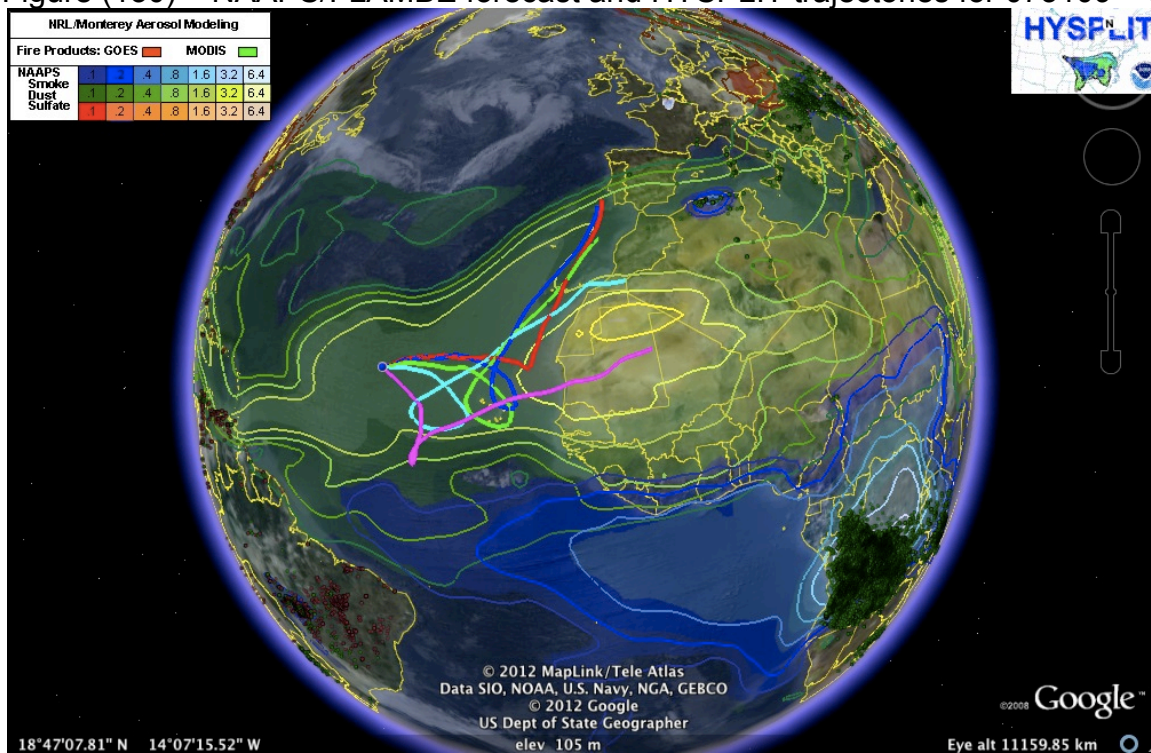


Figure (131) – NAAPS/FLAMBE forecast and HYSPLIT trajectories for 073109 – 06hrs

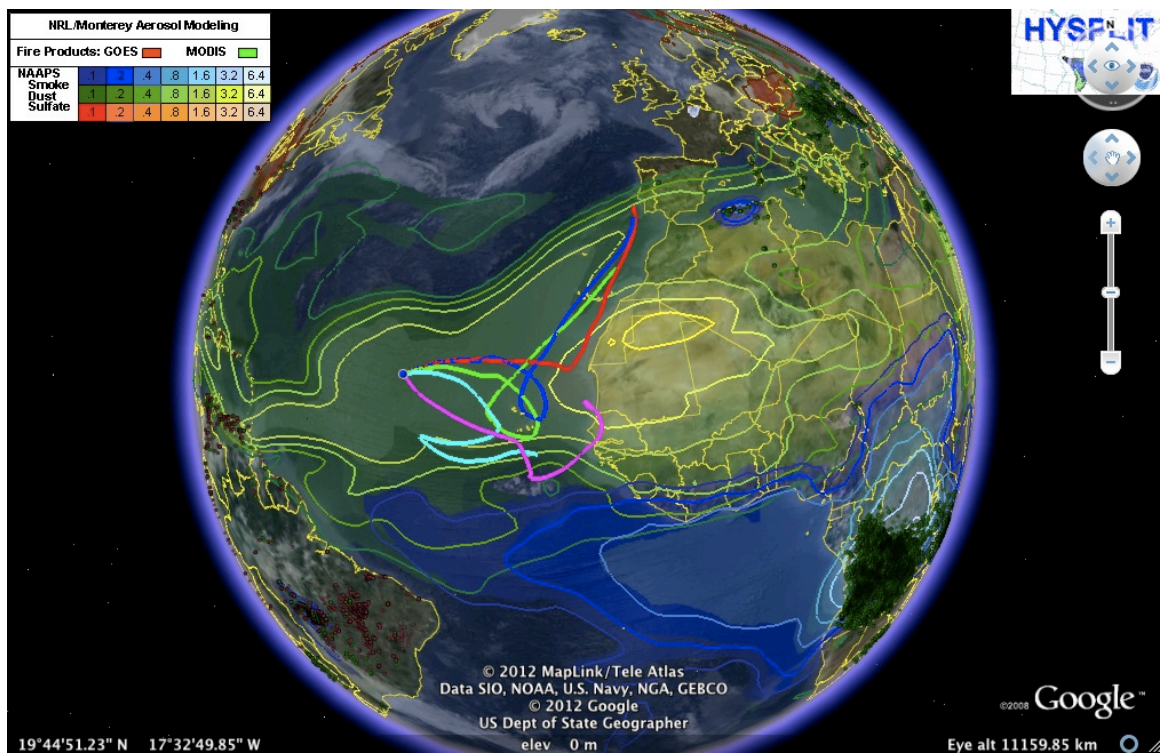


Figure (132) – NAAPS/FLAMBE forecast and HYSPLIT trajectories for 073109 – 12hrs

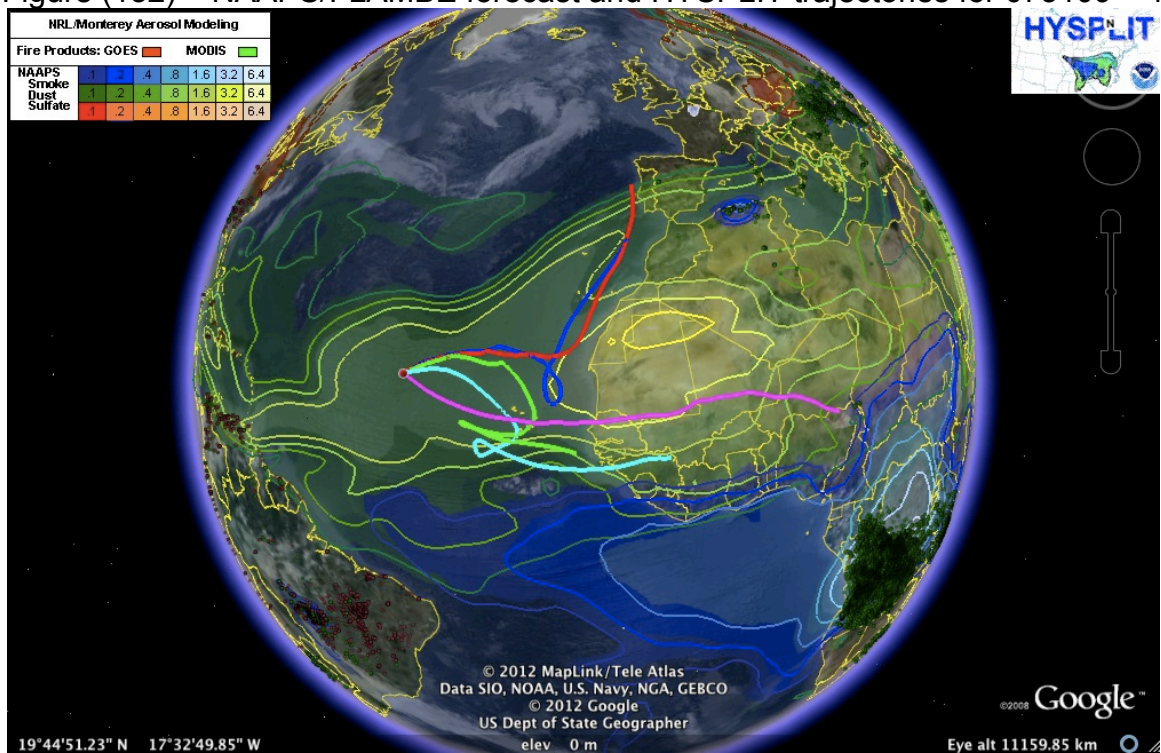


Figure (133) – NAAPS/FLAMBE forecast and HYSPLIT trajectories for 073109 – 18hrs

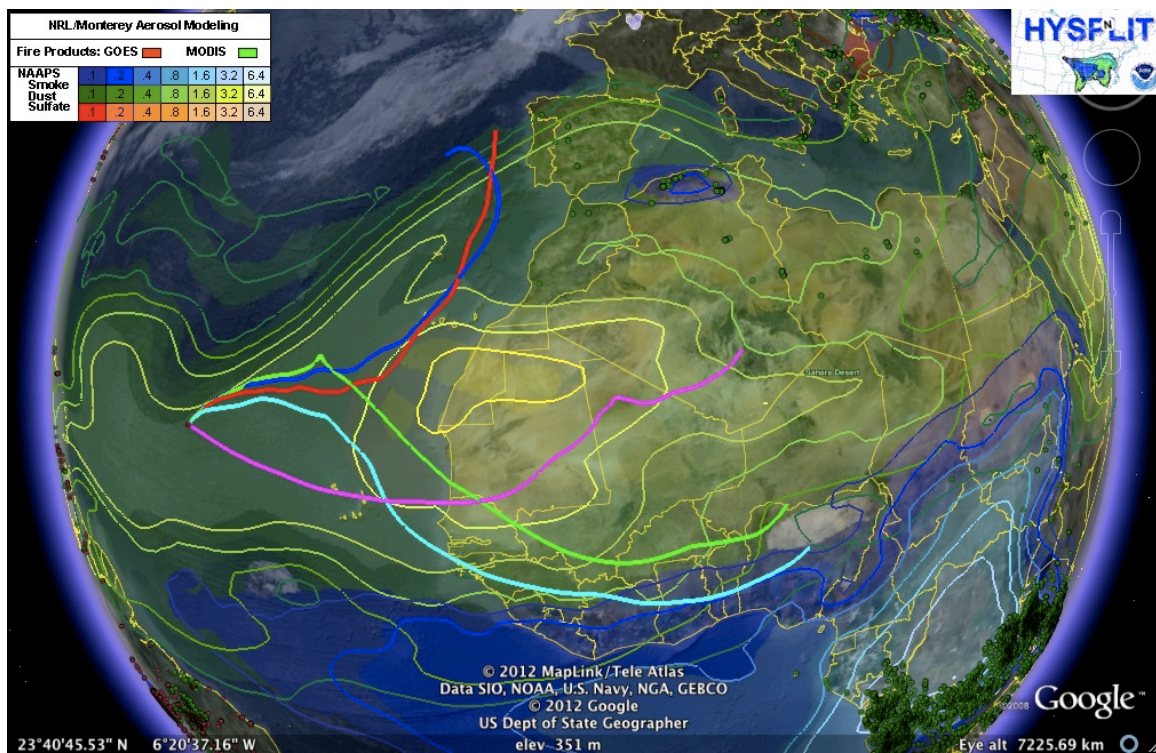


Figure (134) – NAAPS/FLAMBE forecast and HYSPLIT trajectories for 080109 – 00hrs

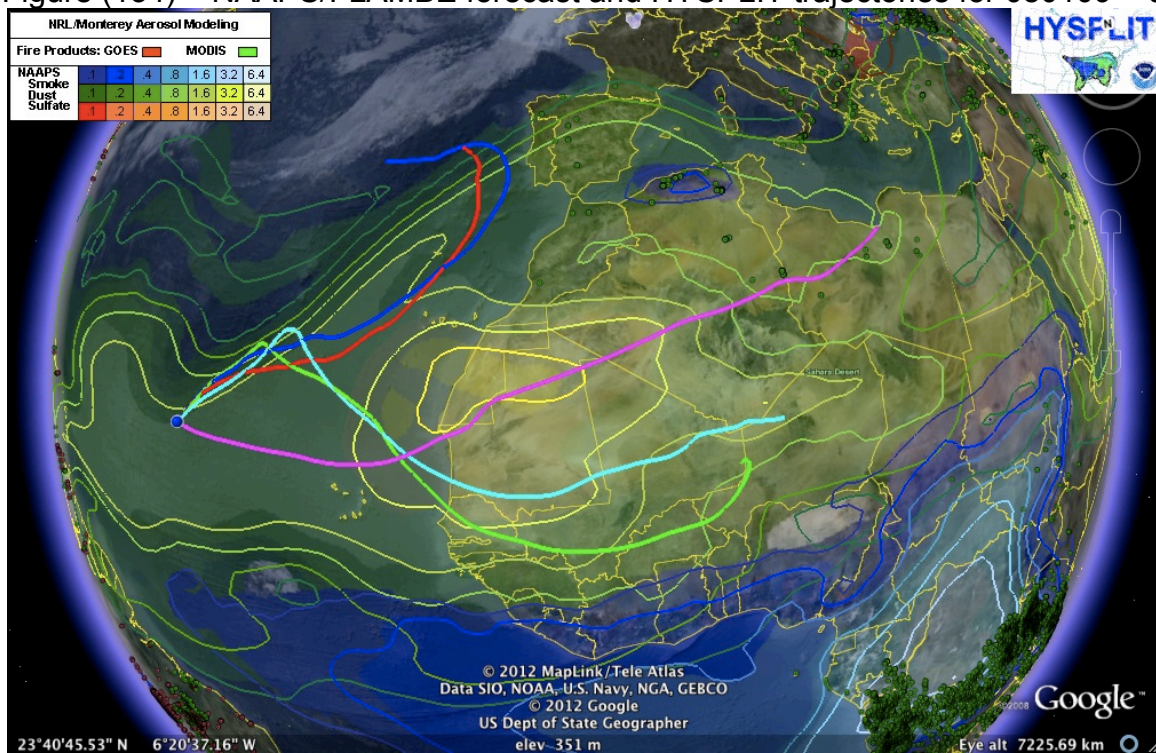


Figure (135) – NAAPS/FLAMBE forecast and HYSPLIT trajectories for 080109 – 06hrs

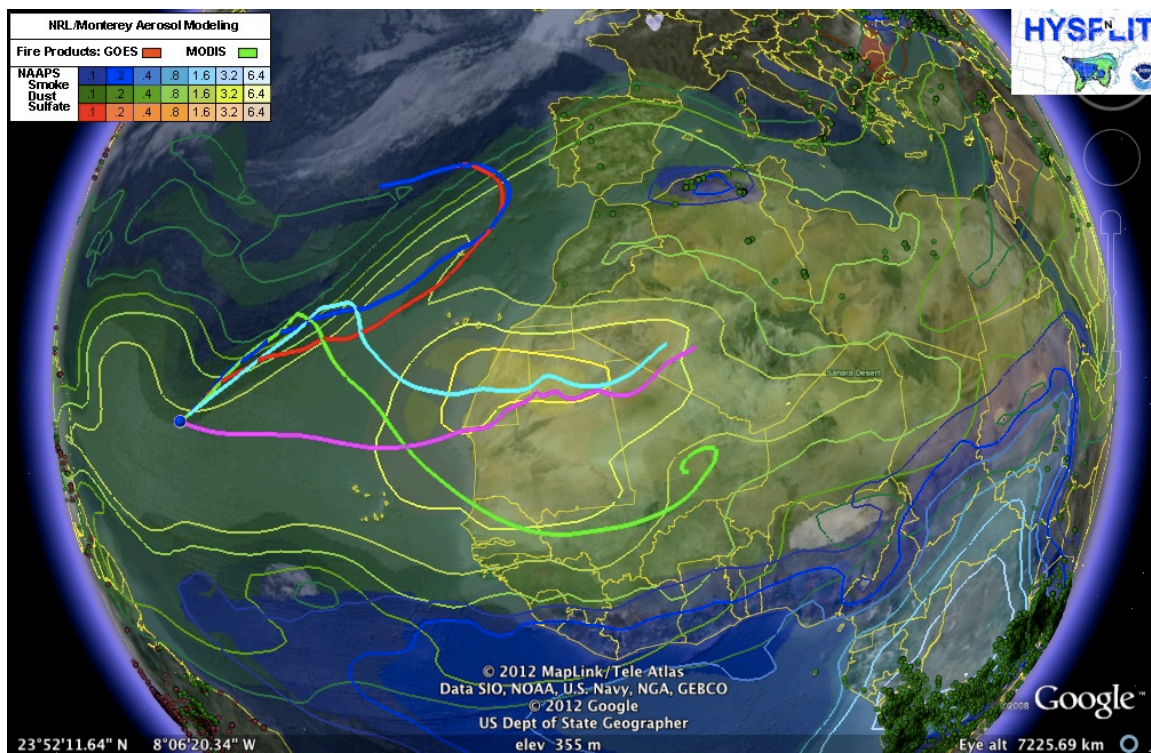


Figure (136) – NAAPS/FLAMBE forecast and HYSPLIT trajectories for 080109 – 12hrs

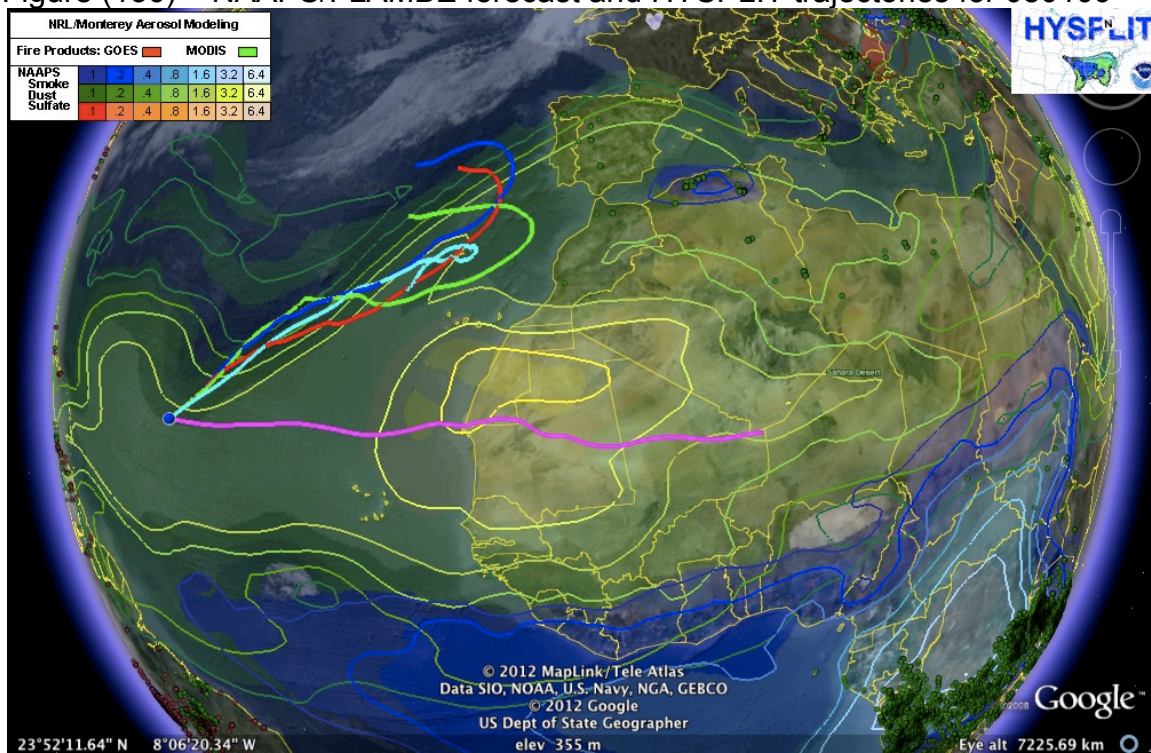


Figure (137) – NAAPS/FLAMBE forecast and HYSPLIT trajectories for 080109 – 18hrs

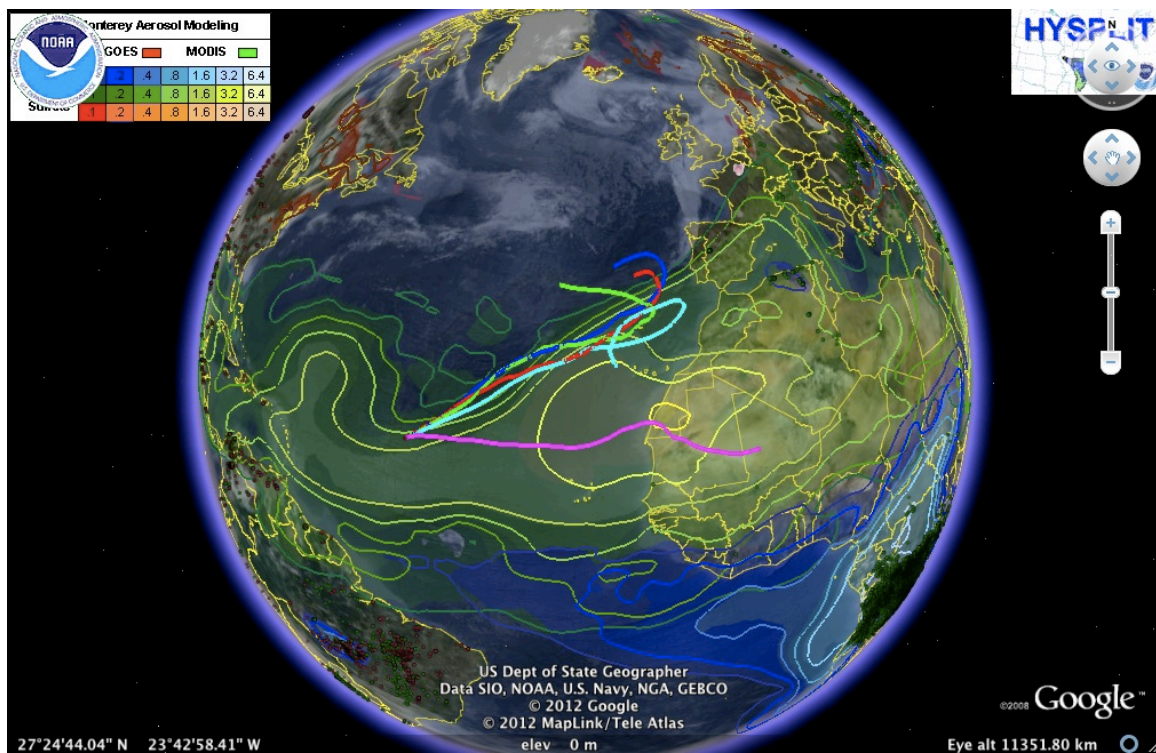


Figure (138) – NAAPS/FLAMBE forecast and HYSPLIT trajectories for 080209 – 00hrs

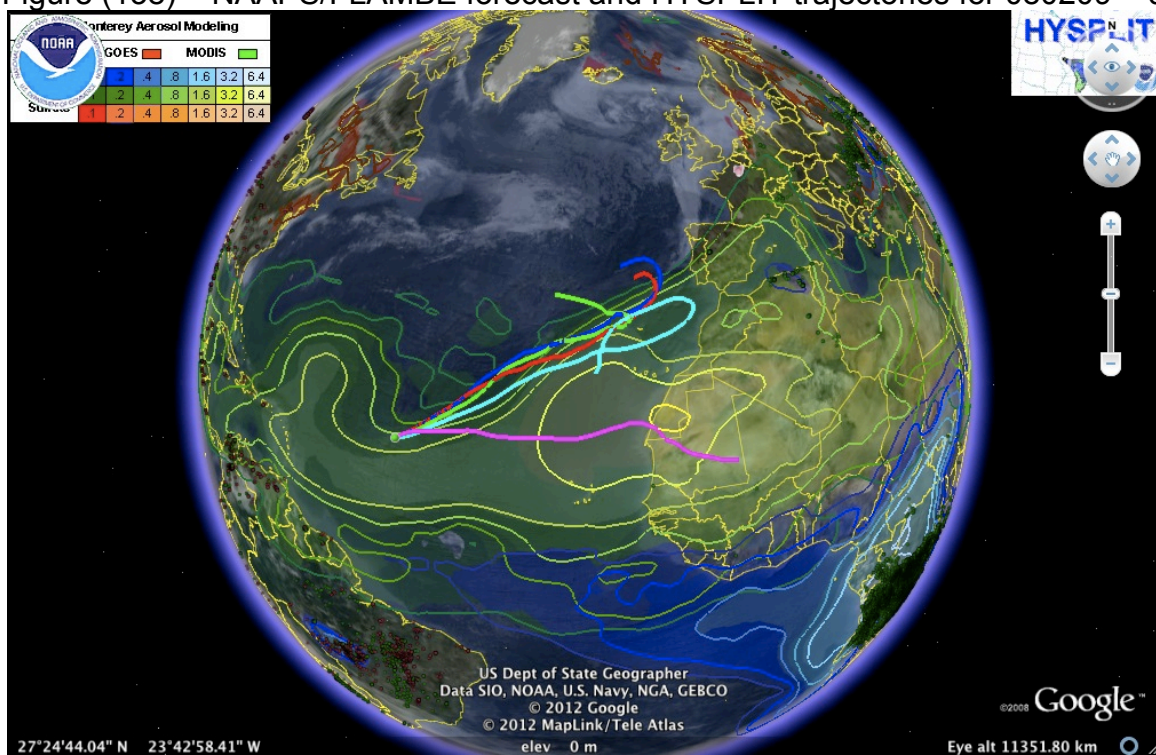


Figure (139) – NAAPS/FLAMBE forecast and HYSPLIT trajectories for 080209 – 06hrs

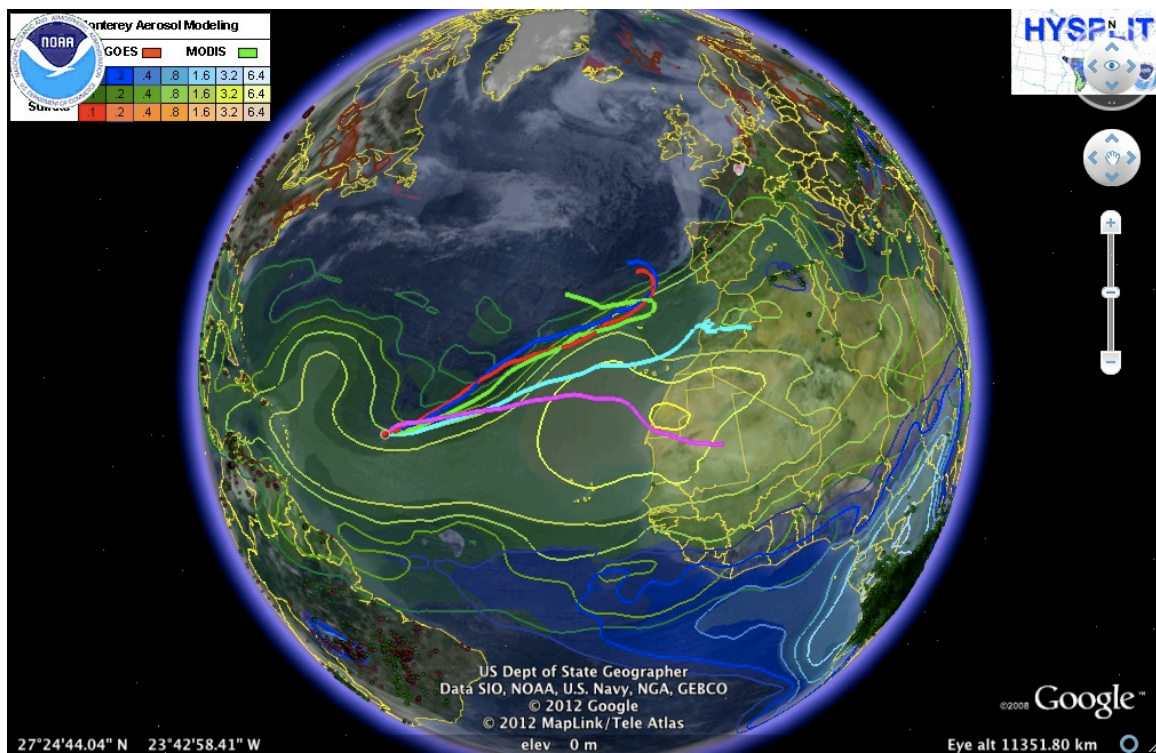


Figure (140) – NAAPS/FLAMBE forecast and HYSPLIT trajectories for 080209 – 12hrs

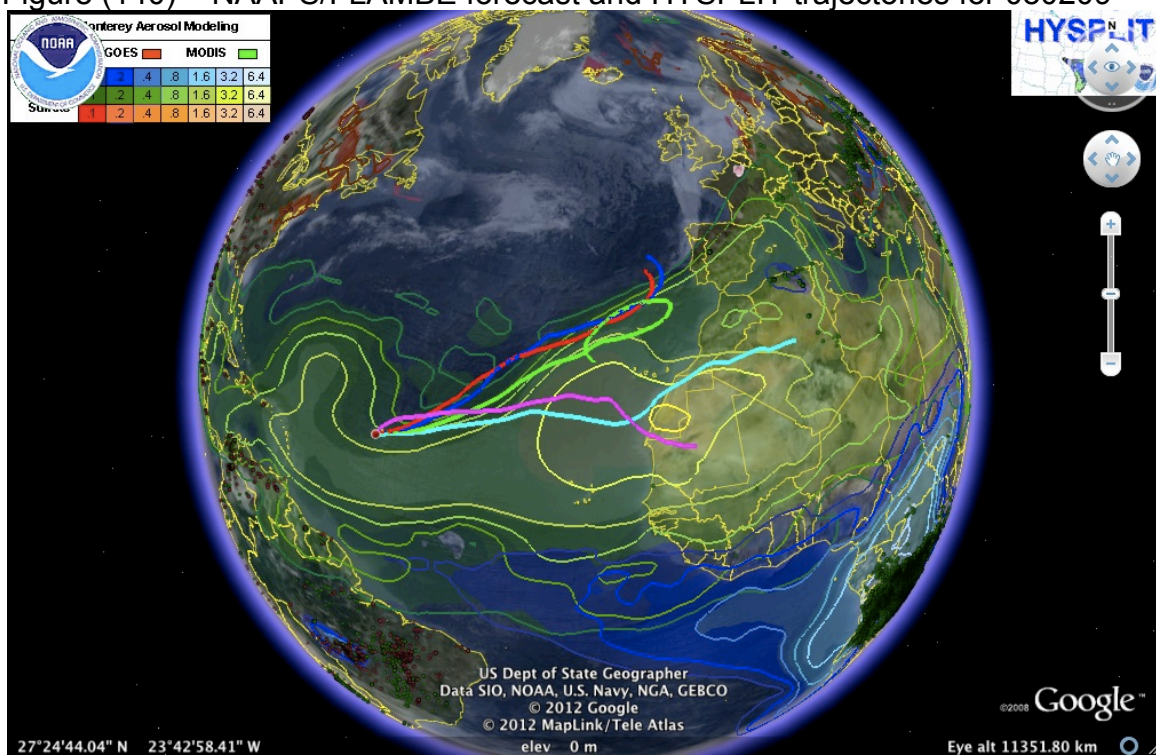


Figure (141) – NAAPS/FLAMBE forecast and HYSPLIT trajectories for 080209 – 18hrs

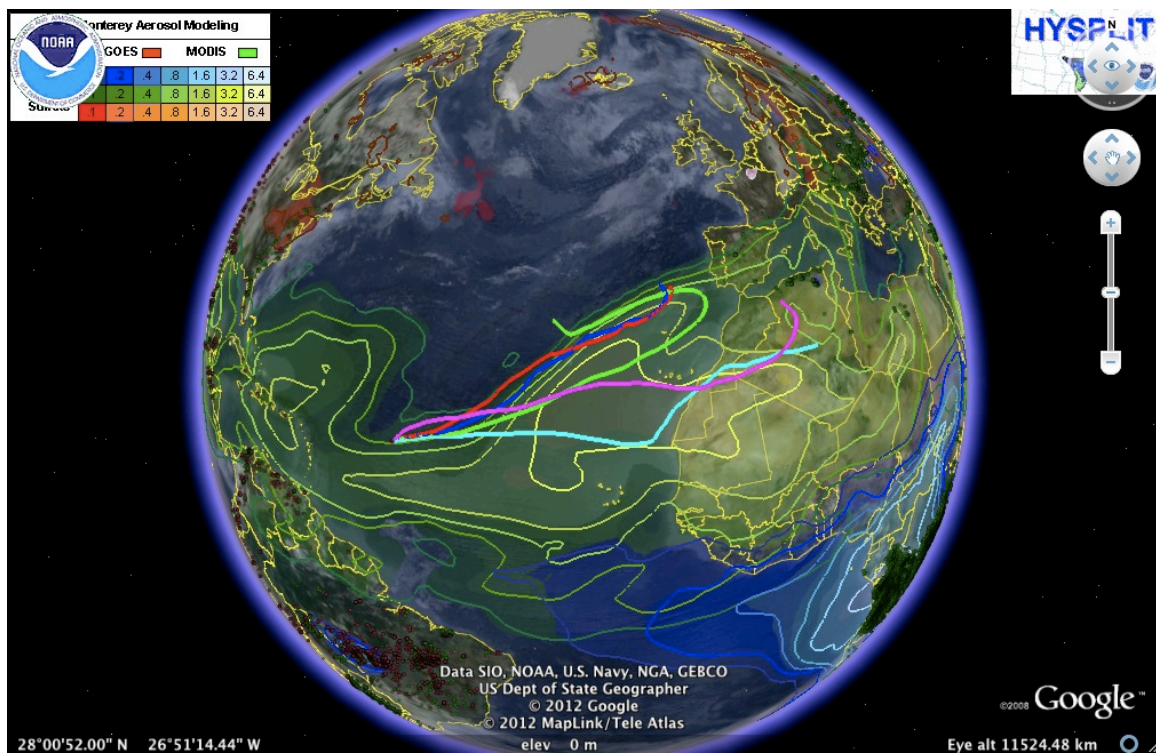


Figure (142) – NAAPS/FLAMBE forecast and HYSPLIT trajectories for 080309 – 00hrs

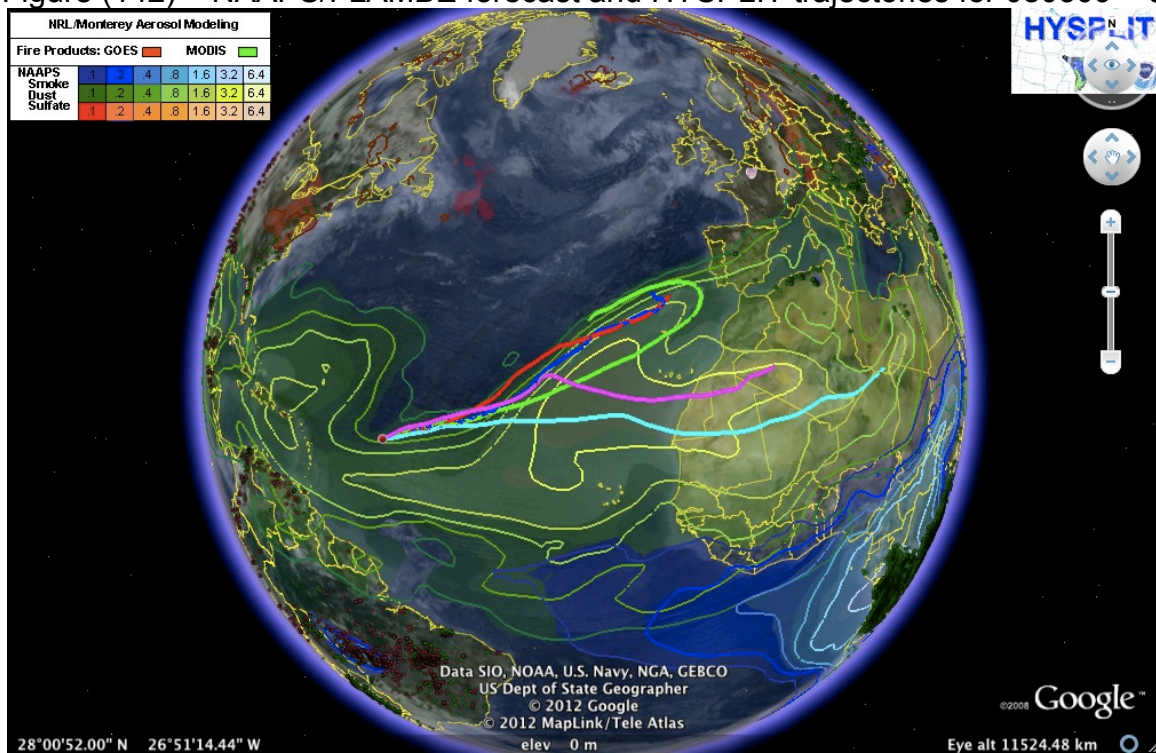


Figure (143) – NAAPS/FLAMBE forecast and HYSPLIT trajectories for 080309 – 06hrs

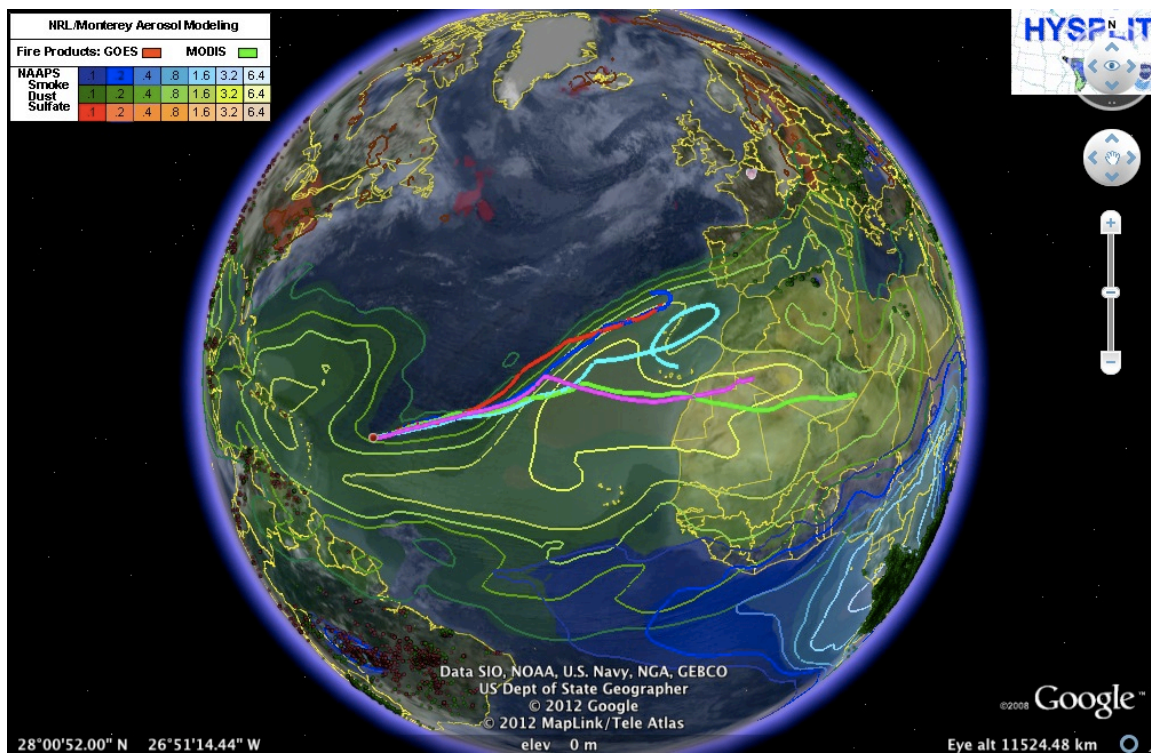


Figure (144) – NAAPS/FLAMBE forecast and HYSPLIT trajectories for 080309 – 12hrs

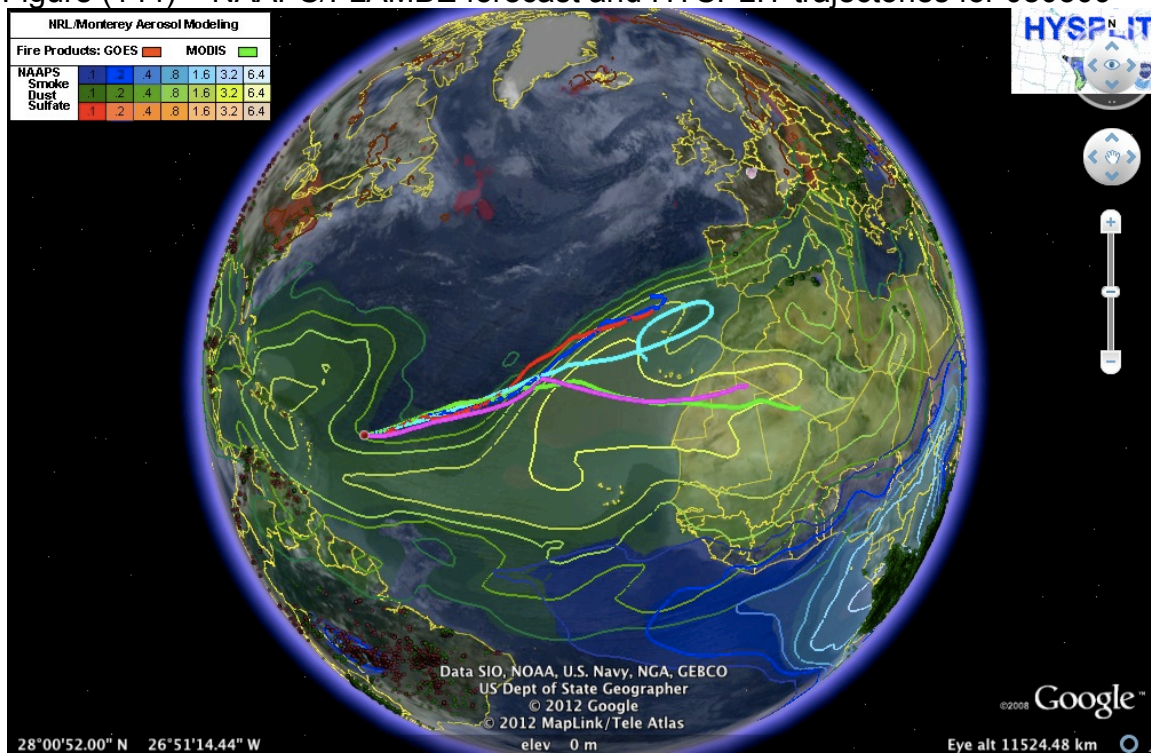


Figure (145) – NAAPS/FLAMBE forecast and HYSPLIT trajectories for 080309 – 18hrs

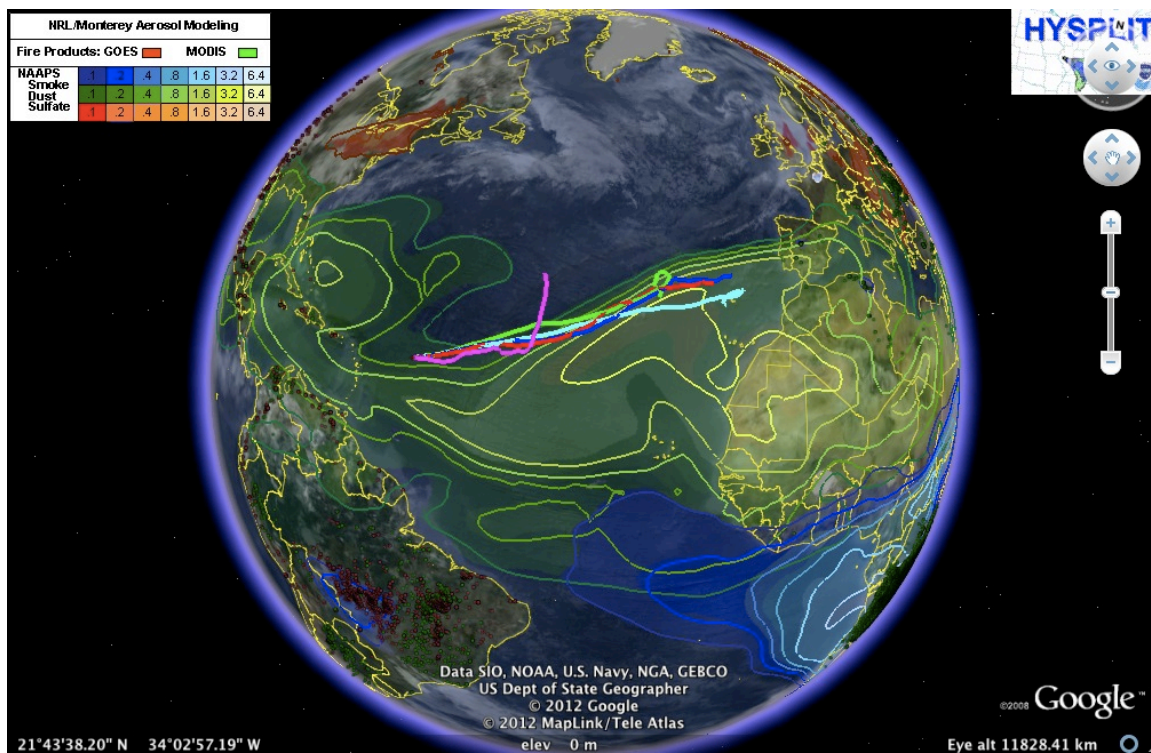


Figure (146) – NAAPS/FLAMBE forecast and HYSPLIT trajectories for 080409 – 00hrs

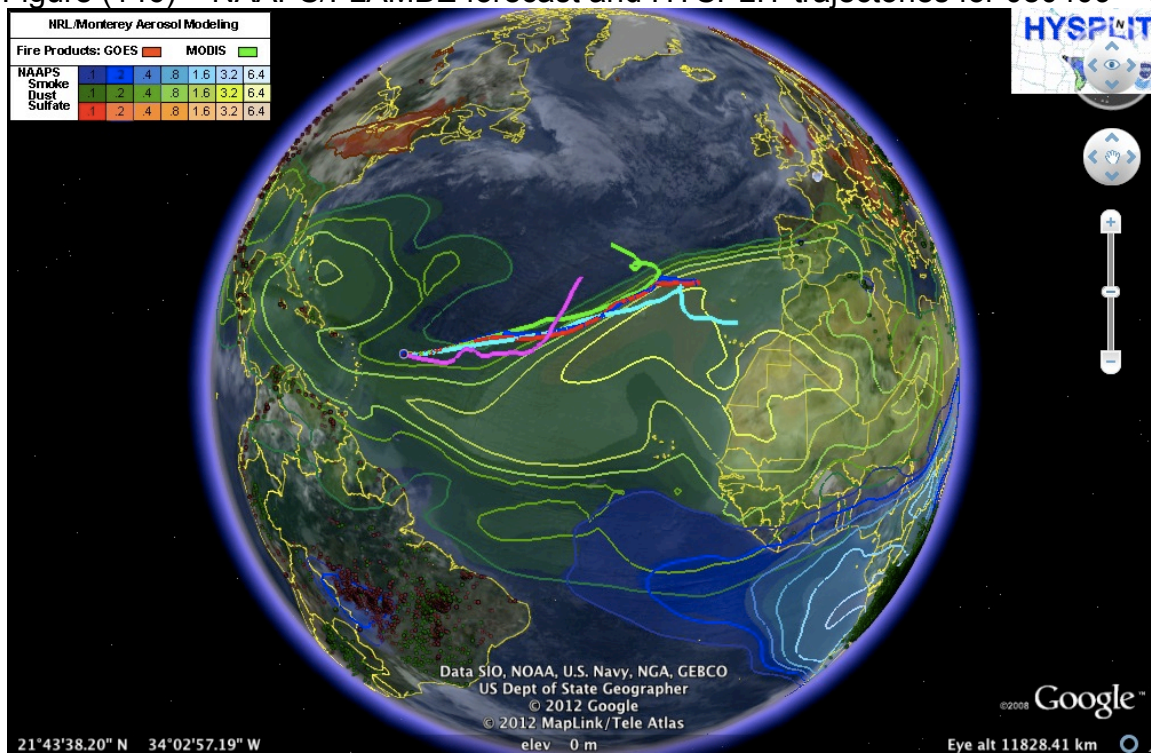


Figure (147) – NAAPS/FLAMBE forecast and HYSPLIT trajectories for 080409 – 06hrs

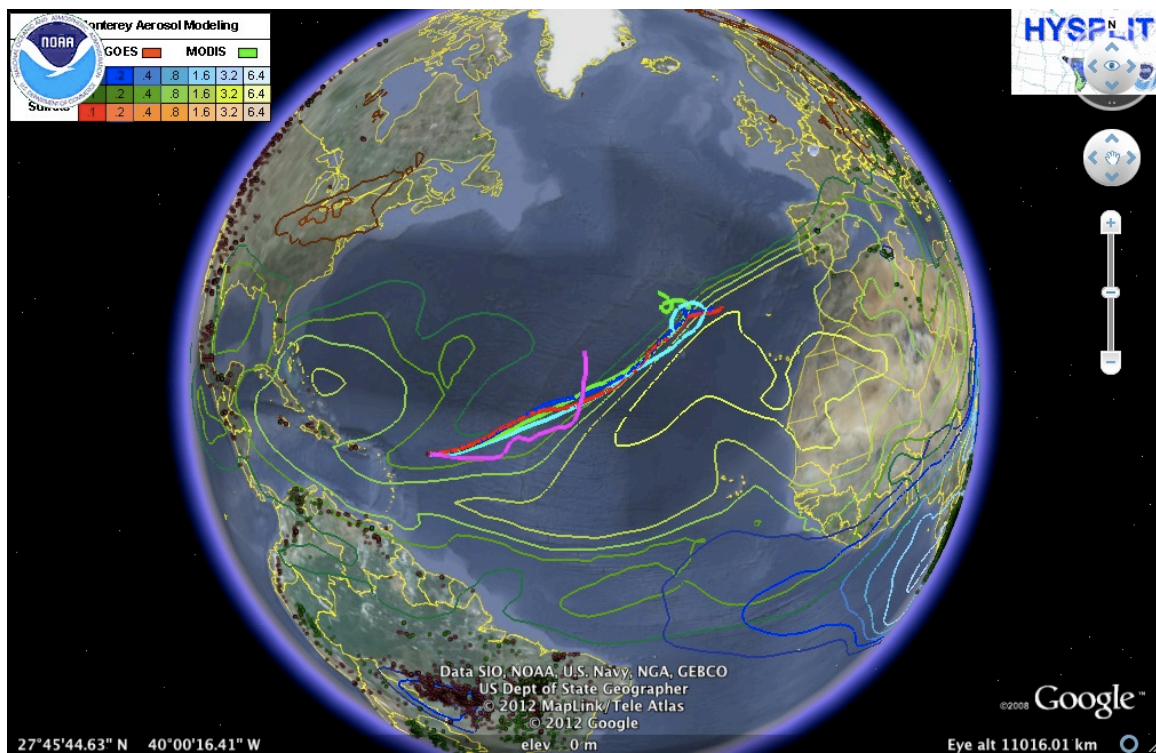


Figure (148) – NAAPS/FLAMBE forecast and HYSPLIT trajectories for 080409 – 12hrs

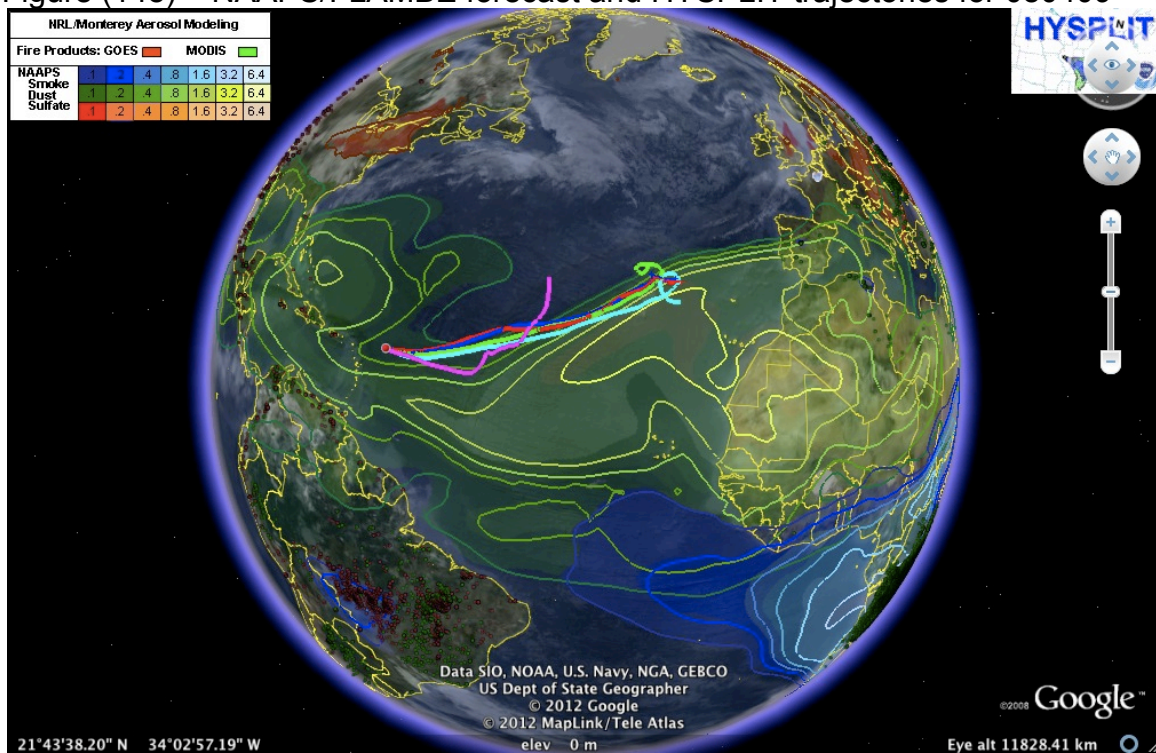


Figure (149) – NAAPS/FLAMBE forecast and HYSPLIT trajectories for 080409 – 18hrs

Curriculum Vita

Mariana Güereque was born in the city of Chihuahua, capital of the state of by the same name in Mexico. The eldest daughter of Eduardo Güereque and Guadalupe Lopez, she graduated from Preparatoria Federal por Cooperacion El Chamizal in Ciudad Juarez, Chihuahua, Mexico. She graduated from the University of Texas at El Paso with a Bachelor of Science in Environmental Science with a concentration in Hydrology, followed by a Master's of Science, also at UTEP, in Geological Sciences.

Permanent Address:

guereque@gmail.com